Universität Rostock

Traditio et Innovatio

Quantum Holonomies in Photonic Waveguide Systems

Dissertation

zur Erlangung des Grades
doctor rerum naturalium (Dr. rer. nat.)

am Institut für Physik
der Mathematisch-Naturwissenschaftlichen Fakultät
der Universität Rostock

vorgelegt von Julien Pinske, geb. am 29.07.1995 in Crivitz.

Betreuer: Prof. Dr. Stefan Scheel, Universität Rostock

Rostock, Februar 2023

https://doi.org/10.18453/rosdok_id00004349

Dieses Werk ist lizenziert unter einer
Creative Commons Namensnennung 4.0 International Lizenz.

Gutachter:

Prof. Dr. Stefan Scheel, Universität Rostock

Prof. Dr. Jan Sperling, Universität Paderborn

Prof. Dr. Jiannis Pachos, University of Leeds

Datum der Abgabe:

13. Februar 2023

Datum der Verteidigung:

23. Mai 2023

Abstract

The findings of gauge theory, both Abelian and non-Abelian, apply to areas beyond the theories of fundamental interactions. A gauge potential acting on a quantum state results in an evolution that is determined by a quantum holonomy. A striking feature of these geometric and topological proposals is that nontrivial quantum information processing can be performed even in the presence of a vanishing Hamiltonian, thus leading to desirable fault-tolerance features. The thesis at hand deals with the emergence of quantum holonomies in systems of coupled waveguides. Several proposals for their realisation in arrays of laser-written fused-silica waveguides are presented, including experimental results. I develop an operator-theoretic framework for the photon-number independent description of these optical networks. Finally, quantum holonomies will be embedded into schemes for measurement-based quantum computation, with the aim of approximating Jones polynomials.

Zusammenfassung

Die Erkenntnisse Abelscher und nicht-Abelscher Eichtheorien sind auf Problemstellungen anwendbar, welche sich über den Bereich moderner Quantenfeldtheorien hinaus erstrecken. Ein Eichpotential, welches auf einen Quantenzustand wirkt, führt zu einer Evolution, welche durch eine Quantenholonomie beschrieben wird. Eine bemerkenswerte Eigenschaft dieser geometrischen und topologischen Transformationen liegt in der Möglichkeit Quanteninformation unabhängig von dynamischen Einflüssen zu verarbeiten. Dies weist auf vielversprechende Fehlertoleranzeigenschaften dieser Transformationen hin. Die vorliegende Thesis untersucht die Konzipierung von Quantenholonomien in Systemen gekoppelter Wellenleiter. Eine Vielzahl möglicher Realisierungen mittels lasergeschriebener Wellenleiter in Quarzglas wird präsentiert und zugehörige experimentelle Ergebnisse erläutert. Die Entwicklung einer operatortheoretischen Darstellung für die photonenzahlunabhängige Beschreibung dieser optischen Netzwerke wird vorgenommen. Abschließend werden Quantenholonomien für die messinduzierte Quantenberechnung von Jones-Polynomen verwendet.

Contents

I. Prologue **1**

1.1. Introduction 1

1.2. Structure of the Thesis 4

II. Integrated Quantum Optics **5**

2.1. Integrated Photonic Waveguides 6

2.2. Quantised Electromagnetism in a Waveguide Array 10

III. Quantum Holonomies **15**

3.1. Adiabatic Geometric Phases 16

3.2. The Particle-Number Threshold 27

3.3. Nonadiabatic Geometric Phases 37

3.4. Geometric Aspects of Quantum Holonomies 42

3.5. Operator Formulation of Quantum Holonomies 45

IV. Holonomic Quantum Computation with Photons **55**

4.1. Elements of Quantum Information Theory 56

4.2. Linear Optical Quantum Computation 59

4.3. Holonomic Quantum Computation 62

4.4. Measurement-Based Quantum Computation 70

V. Braids and the Jones Polynomial **77**

5.1. The Jones Polynomial Algorithm 78

5.2. Jones Polynomials in Topological Quantum Field Theory 84

5.3. Quantum Calculation of Knot Invariants 86

VI. Summary and Conclusion **91**

6.1. Outlook 92

A. Supplementary Results **95**
A.1. Coupling and Overlap between Cylindrical Waveguides 95
A.2. Dark States of the Four-Mode Fully-Connected Graph 98
A.3. Details on the Operator Formulation of Quantum Holonomies 99
A.4. Unitary Representation of the Four-Strand Braid Group 103
A.5. Details on the Holonomic Manipulation of Graph States 106

B. Unpublished Manuscript **111**

Bibliography **127**

I | Prologue

The individuation of promising physical systems for implementing the "gauge-theoretic" quantum computer we have been discussing in this Letter is still an open problem that will require a deal of further investigations. [1]

P. Zanardi & M. Rasetti (1999)

1.1 Introduction

The emergence of quantum theory in the first half of the 20th century revised our understanding of Nature. The often counter-intuitive behaviour of quantum systems emerges when exploring increasingly smaller length and energy scales. Understanding these properties enabled a first technological revolution, transforming industrialised societies. The ongoing miniaturisation of modern technology — be it mechanical, electronic, or photonic — is limited through the regime in which such quantum effects become dominant.

Rather than seeing the occurrence of quantum-mechanical effects as a restriction, more recent developments put forward the idea to design and construct devices that harness these very effects to outperform contemporary means of information processing and communication [2]. In order to benefit from this quantum advantage [3], the superposition principle in individual systems, as well as quantum entanglement between multiple parties [4], can be put into action. The former allows computational operations to be applied in parallel and in particular renders larger coding space possible, while the latter is responsible for connecting the individual components of a quantum network such that multi-partite interactions enable algorithmic shortcuts. Early academic proposals include the search of large databases [5, 6], the efficient factorisation of prime numbers [7], and the simulation of increasingly complex quantum systems [8, 9]. Combining entanglement with the probabilistic nature of quantum measurements allows one to protect quantum channels against eavesdropping, thus enabling secure handling of classical and quantum information [10, 11]. By now, quantum information processing (QIP) matured into an industrialised field of research — marking a transition towards quantum engineering — where an increased interest on quantum machine learning [12], quantum programming languages [13], as well as the emergence of commercial start-ups [14] and (inter)national programs for building quantum computers, can be witnessed.

Fundamentally, the aforementioned ventures all rely on the precise control of quantum bits, aka qubits. Each physical architecture that is used to prepare, manipulate, and measure qubits comes with its own inherent and distinct benefits and drawbacks. Popular platforms are based on superconducting qubits [15], trapped ions [16], or quantum-dot-based quantum computers [17], each utilising different physical effects to perform QIP. Moreover, large quantum codes can be realised in cold atomic ensembles placed in optical lattices. These atoms can then be controlled and entangled using lasers, and a 10 000-atom quantum simulator has already been realised [18]. Less popular, but still relevant, approaches involve electron-on-helium qubits [19], cavity quantum electrodynamics [20], and nuclear magnetic resonance [21].

Arguably, the photon, the fundamental excitation of the quantised electromagnetic field, is one of the primary contestant for quantum computation (QC) and quantum communication [22]. Starting from early bulk-optical components, including beam splitters and phase shifters for linear transformations as well as nonlinear materials for the creation of entangled photons, quantum photonics matured into an industrialised area of research pursuing the design of integrated photonic platforms to achieve QC [23]. For example, these modern components include tailored optical fibres [24], silica-on-silicon chips [25], and laser-written waveguides [26]. Integrated photonic chips provide a high degree of interferometric stability, making it possible to sustain a substantial number of optical modes [27]. As photons rarely interact with each other, they are inherently robust towards distortions by neighbouring qubits (i.e., other photons). Still, interactions between photons are necessary to create an entangled quantum state. The therefore required nonlinearities can be designed, e.g., via quantum mechanical measurements [28, 29] or nonlinear optical chips [30].

Naturally, these microscopic systems are more sensitive to errors than classical platforms, so that the quest for providing reliable quantum systems significantly accelerated in recent years [31]. Even though pioneering experiments achieved error rates of less than one error in every 1 000 operations [32], viable and sustainable quantum algorithms require millions of operations, and even small perturbations can result in a fatal error. Besides great patience and care of experimentalists, there exist several theoretical tools for realising a passive protection against errors, including decoherence-free subspaces [33], dynamical decoupling [34], noiseless subsystem codes [35], and adiabatic QC [36]. In contrast to codes that actively correct errors [37, 38], these methods rely on an avoidance of errors by shielding the system against, e.g., environmental interactions, anticipated imperfections, and parametric fluctuations. The arguably most successful approach for achieving this is topological QC [39, 40], which is based on the preparation of quantum systems in a highly symmetric fashion. In other words, it addresses error correction already at the hardware level by making qubits agnostic towards a variety of errors. There are several strategies to ensure this. For instance, quantum systems in an effectively (2+1)-dimensional configuration space enable anyonic quasi-particle statistics [41] that exhibit sophisticated exchange symmetries beyond those of bosons and fermions. In this picture, quantum algorithms are performed by braiding the anyons (qubits) around each other. The final output of the QC does only depend on the specific sequence of braids but is independent of any local perturbation of the anyon's path. Witten pointed out that pair annihilation of anyons contains information on the knot formed by their world lines [42], hinting at a deep connection between topological quantum field theory and topics in modern mathematics [43].

On the other hand, topological codes do not aim at protecting individual qubits but rather structure the entire quantum computer in a way that provides a sort of global geometric protection. This idea goes back to Kitaev who first suggested this approach for a lattice of qubits with appropriate boundary conditions such that the system resembles a torus [44]. Therein, logical operations are applied to qubits in a toric code in the form of closed paths, tolerating all kinds of errors that deform the loop without breaking it. In the last decade, further generalisations, such as surface [45] and colour codes [46], were proposed. These are currently the best performing quantum codes at our disposal [31].

While a topological QC depends on a number of discrete variables, there are continuous transformations of quantum states that are closely related to the braiding of anyons. It was first noticed by Berry that in a slowly (adiabatically) changing quantum system, the initial state accumulates a phase that solely depends on the geometry of its path through state space [47]. Unlike dynamical phases, such a geometric phase cannot be removed by a rescaling of the energy. A famous example for this is the so-called Aharonov-Bohm effect [48, 49], in which the wave function of an electron traveling around a solenoidal magnetic field picks up a phase proportional to the flux through the surface enclosed by the trajectory of the electron. Pancharatnam studied this phenomenon in the context of polarisation optics [50] where it manifests itself in the interference of light. It was pointed out by Simon [51] that this purely geometric signature of a quantum evolution has to be attributed to adiabatic parallel transport of the state vector along a path in a projective Hilbert space. There exists a (conceptually) deep relation between geometric phases and the interactions that elementary particles experience in high-energy physics. Precisely speaking, both types of transformations can be attributed to the presence of a gauge potential that incorporates some intrinsic symmetry of the theory. Wilczek and Zee [52] noticed that states in an adiabatic subspace give rise to such a symmetry, because these cannot be distinguished by measurement of their energy (degenerate spectrum). They argued that this could potentially result in the emergence of non-Abelian (i.e., noncommuting) gauge potentials. In this case, the state after an evolution does not only acquire a geometric phase but differs from the initial one by a unitary matrix known as the quantum holonomy (non-Abelian geometric phase). Anandan and Aharonov showed that, under certain conditions, even nonadiabatic phase factors can be of purely geometric origin [53, 54]. The concept of holonomy, that is parallel transport along a closed loop, was first introduced by Cartan in 1926 [55, 56] within the context of Riemannian geometry. Therefore, holonomies might be viewed as the continuous differential-geometric counterpart to the braiding of anyons [57].

Based on these ideas borrowed from gauge theory, Zanardi and Rasetti proposed that a quantum-gate logic could be realised even on a subspace on which the Hamiltonian of a system vanishes completely [1]. Holonomic QC, both adiabatic [58, 59] and nonadiabatic [60], is an all-out geometric approach to QIP, in which holonomies play the role of the fundamental gate set from which quantum algorithms are to be implemented. Due to their geometric features, holonomic gates possess an inherent robustness towards fluctuations in the spectrum, timing errors, and local (parametric) perturbations [61, 62, 63]. Physical realisations of holonomic gates exist in systems of trapped ions [64, 65], superconducting qubits [66, 67], solid state spins in a diamond [68], and NMR-based systems [69]. Viewing this paradigm as a form of *gauge-theoretic* QC highlights the relation between the holonomy and the Wilson loop in lattice-gauge theory [70, 71]. The latter is an expression for the flow of a gauge potential through a spacetime plaquette. As holonomies are ubiquitous in physics, they might play a central role in the quantum simulation of quantum field theories, or loop-quantum gravity [72]. The latter is a background-independent approach to quantum field theory that incorporates gravitational effects.

In this thesis, I study the propagation of quantum light within networks of integrated photonic waveguides that realise a quantum holonomy. Main emphasis lies on the all-out geometric photon transfer between coupled modes. Several quantum photonic proposals for the generation of holonomies are presented [P1], even accounting for transverse mode overlap between strongly coupled waveguides [P2]. I show how arbitrary degeneracy can be realised in these systems. Moreover, I elucidate the relation between the holonomy and the number of photons involved in the evolution [P3]. Fabrication of these optical networks is considered in terms of laser-written fused-silica waveguides, and novel experimental results for quantum holonomies, both adiabatic and nonadiabatic, verify theoretical predictions to a high degree of accuracy [P4, P5]. An elegant operator formulation, based on a holonomic Heisenberg picture, enables analytical calculations even for large networks involving many photons [P6]. A possible road for building an all-out photonic holonomic quantum computer is devised using measurement-based design strategies [P7]. The paradigm is illustrated by showcasing a measurement-based version of the Hadamard test, which is a quantum algorithm estimating Jones polynomials.

1.2 Structure of the Thesis

I have endeavoured to write this thesis as coherent and self-containing as possible. Nevertheless, additional details and comments of more technical nature, in particular with regards to experimental setups, might be reserved for the published articles and prepared manuscripts [P1-P7].

The structure of the thesis is as follows. In Chapter II, the basic theory for the propagation of quantum light in systems of integrated photonic waveguides is presented. Particular emphasis lies on the description of networks of coupled waveguides in terms of a coupled-mode theory. Chapter III contains a discussion of quantum holonomies as a special class of unitaries. These quantities emerge in the context of adiabatic and nonadiabatic evolutions of quantum states that are confined to a subspace on which the Hamiltonian vanishes. Several proposals for their realisation in arrays of coupled waveguides are devised. Experimental results involving single and two-photon states are briefly presented. After this general discussion of quantum holonomies, Chapter IV is concerned with their usage in the holonomic processing of qubits. Photonic realisations of holonomic quantum gates are considered. For the case of nonadiabatic gates, I explicitly show how to combine holonomic QC with measurement-based QC resulting in a purely geometric manipulation of graph states. This hybrid approach can be utilised for the efficient quantum calculation of Jones polynomials. The design strategy for this algorithm is presented in Chapter V using a measurement-based version of the Hadamard test. Finally, Chapter VI contains a discussion of the results and some concluding remarks on the prospects of all-out photonic QIP in terms of holonomies.

II | Integrated Quantum Optics

The field of optics — that is the study of light and its interaction with matter — constitutes the backbone of many modern technologies including telecommunication devices, medical equipment, as well as sensitive measurement instruments, to name but a few. Classically, light is viewed as an electromagnetic wave propagating through space according to Maxwell's equations. Einstein [73] and Planck [74] challenged this well established notion at the beginning of the 20th century with their discovery of the *light quanta*, nowadays more commonly referred to as the photon. Photons, being the fundamental excitations of the quantised electromagnetic field, became one of the primary subjects of interest in the field of quantum optics. Since then, promising experiments in optical networks were conducted, verifying the potential for low-decoherence and high-control setups. Specifically, it is possible to create multi-photon entangled states [75, 76, 77] and induce quantum correlations that are without any classical counterpart [78, 79].

However, when based on mirrors, phase shifters, and beam splitters, the scalability of these experiments is strongly restricted, due to thermal fluctuations and mechanical vibrations. This results in an interferometric instability that limits the size of the overall setup. This apparent loss of coherence can be addressed by utilising integrated optical structures such as optical fibres or photonic waveguides. In this thesis, I will be primarily concerned with the latter implementation. Systems of photonic waveguides were already studied in 1970 [80] and by now, these structures allow for the controlled coupling of numerous modes within a photonic *pocket lab* [81].

Describing the light field in such structures in terms of a collection of individual modes, each being tightly localised around a waveguide, allows for an extremely elegant theoretical description of the ongoing dynamics. This approach is known as coupled-mode theory. Since its inception in electromagnetic systems [82, 83], coupled-mode theory has become a well-established tool in the description of waveguide structures, optical fibre networks, and a plethora of other optoelectronic structures [84, 85].

In this chapter, the basic theory of light propagation in integrated photonic waveguides is outlined. Particular attention lies on fused-silica laser-written waveguides. After reviewing the classical theory in Sec. 2.1, Sec. 2.2 contains a canonical quantisation of the coupled-mode equations allowing for the study of multi-photon dynamics in an array of coupled waveguides. Both the overlap between (nonorthogonality of) adjacent modes and photon loss, due to a bending of waveguides, are addressed.

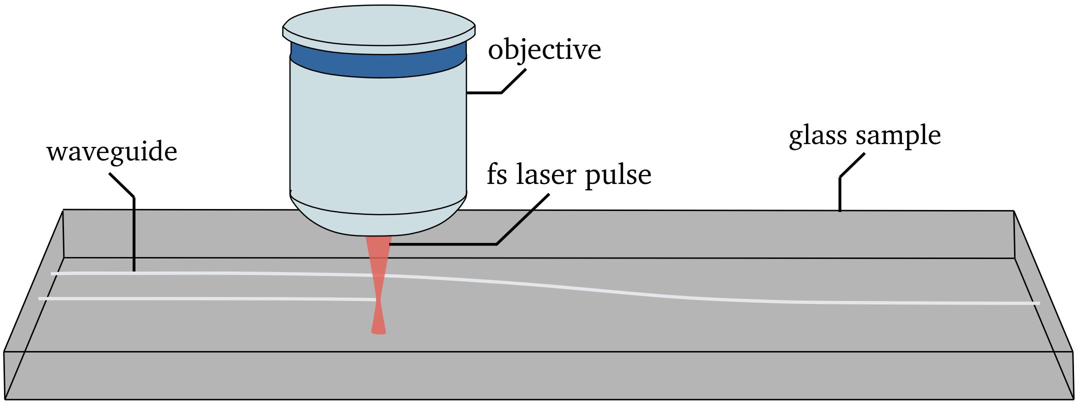

Figure 1.: Fabrication of fused-silica waveguides using the femtosecond (fs) laser-writing technique. A high-intensity laser pulse alters the molecular structure of the glass sample, thus resulting in a local change of the refractive-index profile along which light is guided.

2.1 Integrated Photonic Waveguides

As we are concerned with the propagation of light in dielectric materials, the starting point of any discussion must be the macroscopic Maxwell equations without free charges or currents

$$\begin{aligned} \nabla\cdot\boldsymbol{D}(\boldsymbol{r},t) &= 0, & \nabla\times\boldsymbol{E}(\boldsymbol{r},t) &= -\partial_t\boldsymbol{B}(\boldsymbol{r},t),\\ \nabla\cdot\boldsymbol{B}(\boldsymbol{r},t) &= 0, & \nabla\times\boldsymbol{H}(\boldsymbol{r},t) &= \partial_t\boldsymbol{D}(\boldsymbol{r},t). \end{aligned}$$

For a linear and isotropic medium the constitutive equations between the microscopic fields $\boldsymbol{E}$, $\boldsymbol{B}$ and macroscopic fields $\boldsymbol{D}$, $\boldsymbol{H}$ are

$$\boldsymbol{D}(\boldsymbol{r},t) = \varepsilon(\boldsymbol{r})\boldsymbol{E}(\boldsymbol{r},t), \qquad \boldsymbol{H}(\boldsymbol{r},t) = \mu^{-1}\boldsymbol{B}(\boldsymbol{r},t). \tag{2.1}$$

In Eq. (2.1), I allowed for an inhomogeneous medium with spatially varying permittivity $\varepsilon(\boldsymbol{r}) = \varepsilon_0\varepsilon_\mathrm{r}(\boldsymbol{r})$, while the permeability $\mu = \mu_0$ is considered to be constant to satisfactory precision. Taking the curl of Faraday's law $\nabla\times\boldsymbol{E} = -\partial_t\boldsymbol{B}$, making use of the Grassmann identity $\nabla\times\nabla\times = \nabla(\nabla\cdot\,) - \nabla^2$, while minding $\mu^{-1}\nabla\times\boldsymbol{B} = \varepsilon\partial_t\boldsymbol{E}$, leads to an inhomogeneous wave equation

$$\nabla^2\boldsymbol{E} - \nabla(\nabla\cdot\boldsymbol{E}) = \frac{\varepsilon_\mathrm{r}}{c^2}\partial_t^2\boldsymbol{E}, \tag{2.2}$$

where ∇^2 denotes the Laplacian and $c = 1/\sqrt{\mu_0\varepsilon_0}$ is the vacuum speed of light.

Suppose that the material under investigation consist of a host medium with constant refractive index n_0 and a weak inhomogeneity Δn given by the index contrast, i.e., $\varepsilon_\mathrm{r}(\boldsymbol{r}) = n^2(\boldsymbol{r})$ with $n(\boldsymbol{r}) = n_0 + \Delta n(\boldsymbol{r})$. The assumption of a weakly modulated index contrast is certainly satisfied for femtosecond laser-written waveguides in fused-silica [26, 86] (Fig. 1), where $10^{-3} < \Delta n < 10^{-8}$ [87, 88], but does not necessarily hold in other structures such as silica-on-silicon waveguides [25] or lithium-niobate based systems [89]. Making use of the assumption, one gets $\boldsymbol{\nabla} \cdot \boldsymbol{E} \approx \varepsilon^{-1} \boldsymbol{\nabla} \cdot \boldsymbol{D} = 0$, turning Eq. (2.2) into a homogeneous wave equation. Moreover, the vector character of the Helmholtz equation can be neglected by factoring out a constant unit vector $\boldsymbol{\nu}$, because polarization effects at the interface of a waveguide become unimportant, so that scalar wave theory can be applied [90, 91]. Hence, $\boldsymbol{E}(\boldsymbol{r}, t) = E(\boldsymbol{r})\mathrm{e}^{\mathrm{i}(kz-\omega t)}\boldsymbol{\nu}$ for a monochromatic plane wave that predominantly propagates in z-direction. Here, $k = n_0\omega/c$ is the wave vector amplitude in the ambient medium. Employing the paraxial wave approximation that states that the change of the amplitude $E(\boldsymbol{r})$ over one wavelength is negligible (slowly varying envelope $\partial_z^2 E \approx 0$) and remembering that $n^2(\boldsymbol{r}) \approx n_0^2 + 2n_0\Delta n(\boldsymbol{r})$ in good approximation, we finally arrive at the paraxial Helmholtz equation for the electric field

$$\mathrm{i}\lambda\!\!\!^{-}\partial_z E(\boldsymbol{r}) + \frac{\lambda\!\!\!^{-2}}{2n_0}\boldsymbol{\nabla}_\perp^2 E(\boldsymbol{r}) + \Delta n(\boldsymbol{r})E(\boldsymbol{r}), = 0 \tag{2.3}$$

where $\lambda\!\!\!^{-} = \lambda/2\pi = n_0/k$ was introduced, and $\boldsymbol{\nabla}_\perp^2 = \partial_x^2 + \partial_y^2$ is the Laplacian for the transverse plane.

2.1.1 Coupled-mode theory

For an array of M waveguides, the refractive-index contrast can be modelled as $\Delta n(\boldsymbol{r}) = \sum_{k=1}^{M} \Delta n_k(\boldsymbol{r})$, with Δn_k being the index profile of the kth waveguide. For the moment radiation losses (coupling to continuum modes of the host material) will be neglected. The overall electric field may then be expanded in terms of tight-binding modes only, viz.

$$E(\boldsymbol{r}) = \sum_{k=1}^{M} \alpha_k(z) w_k(\boldsymbol{r}) \mathrm{e}^{\mathrm{i}\beta_k z}, \tag{2.4}$$

where w_k is the transverse field mode that is localized around the waveguide Δn_k (Fig. 2), and α_k is the corresponding longitudinal field amplitude determining the dynamics of the light field. The parameter β_k denotes the propagation constant of the individual waveguide.

In the following, it is assumed that the shape of the transverse field w_k remains constant throughout the propagation. This appears to be valid whenever the fabrication process is stable and in particular β_k should be constant along the propagation direction. However, because the position of the waveguides might vary along the z-axis, the corresponding mode has to follow, i.e., $w_k(\boldsymbol{r}) = w_k(x - x_k(z), y - y_k(z))$, where (x_k, y_k) marks the center of the kth waveguide. On the other hand, in any typical setup the waveguide position changes only gradually over the propagation length (paraxial approximation), that is $\partial_z x_k \approx \partial_z y_k \approx 0$ [92, P2]. Hence, one can safely assume $w_k(\boldsymbol{r}) \approx w_k(\boldsymbol{r}_\perp)$ depends only on the transverse coordinates $\boldsymbol{r}_\perp = (x, y)$. In the absence of any neighbouring waveguides, the kth transverse mode satisfies its own Helmholtz equation

$$\frac{\lambda\!\!\!^{-2}}{2n_0}\boldsymbol{\nabla}_\perp^2 w_k(\boldsymbol{r}_\perp) + \Delta n_k(\boldsymbol{r}) w_k(\boldsymbol{r}_\perp) = 0. \tag{2.5}$$

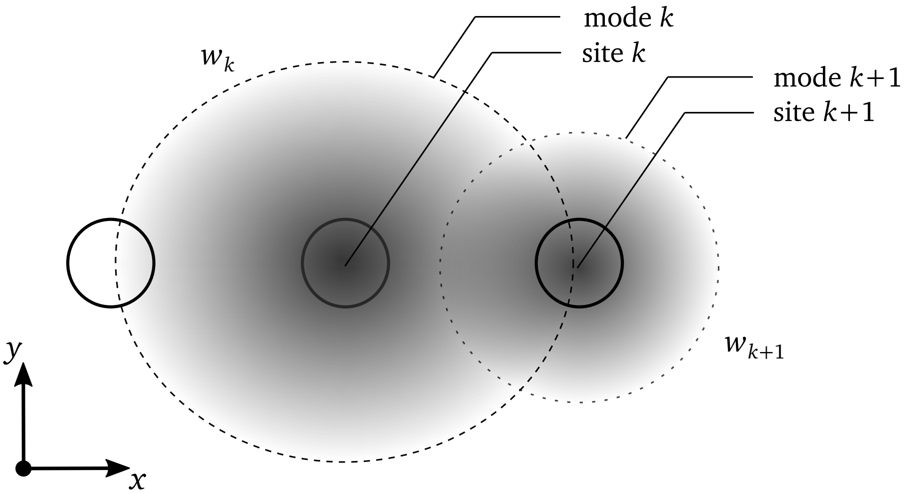

Figure 2.: Schematic front view of coupled waveguides (black circles). Each site k supports a fundamental transverse mode w_k (shaded areas). The modes extend towards the nearest neighbouring sites. Taken from Ref. [P2].

For simplicity, it is assumed that each waveguide supports only its first transverse mode. This is not too limiting of an assumption, because monomode operation and mode synchronism are often required as operating conditions [91].

Inserting the ansatz (2.4) into Eq. (2.3) and making use of Eq. (2.5) leads to

$$\sum_{k=1}^{M}\Big(\mathrm{i}\bar{\lambda}\partial_z\alpha_k w_k + \bar{\lambda}\beta_k\alpha_k w_k + \sum_{\substack{m=1\\ m\neq k}}^{M}\Delta n_m\alpha_k w_k\Big) = 0. \tag{2.6}$$

When multiplying Eq. (2.6) with w_j^* and integrating over the entire (x, y)-plane S_∞, an overlap of the transverse fields with the surrounding waveguides induces transfer of light between the modes (Fig. 2). We recognise two different contributions that occur in Eq. (2.6) after contraction, namely

$$\kappa_{kj} = \frac{1}{\bar{\lambda}}\sum_{\substack{m=1\\ m\neq k}}^{M}\int_{S_\infty}\Delta n_m w_j^* w_k \mathrm{d}^2\boldsymbol{r}_\perp, \qquad \sigma_{kj} = \int_{S_\infty} w_j^* w_k \mathrm{d}^2\boldsymbol{r}_\perp. \tag{2.7}$$

Here, $\kappa_{kj} \approx \frac{1}{\bar{\lambda}}\int \Delta n_j w_j^* w_k \mathrm{d}^2\boldsymbol{r}_\perp$ is the evanescent coupling between the waveguides j and k and σ_{kj} describes the overlap of their respective transverse modes. In particular, there is also a self-coupling $\nu_k = \kappa_{kk}$ due to the presence of other waveguides around the kth mode. The latter is usually the smallest contribution to the propagation and will therefore be neglected in the following discussion, i.e., $\nu_k \approx 0$. This can be justified using Fig. 3. (a) where these quantities were computed for two cylindrical waveguides as a function of their separation. For such highly symmetric step-index waveguides an analytical expression for the transverse mode $w_j(\boldsymbol{r}_\perp)$ can be given in terms of Bessel functions [93]. Details on the

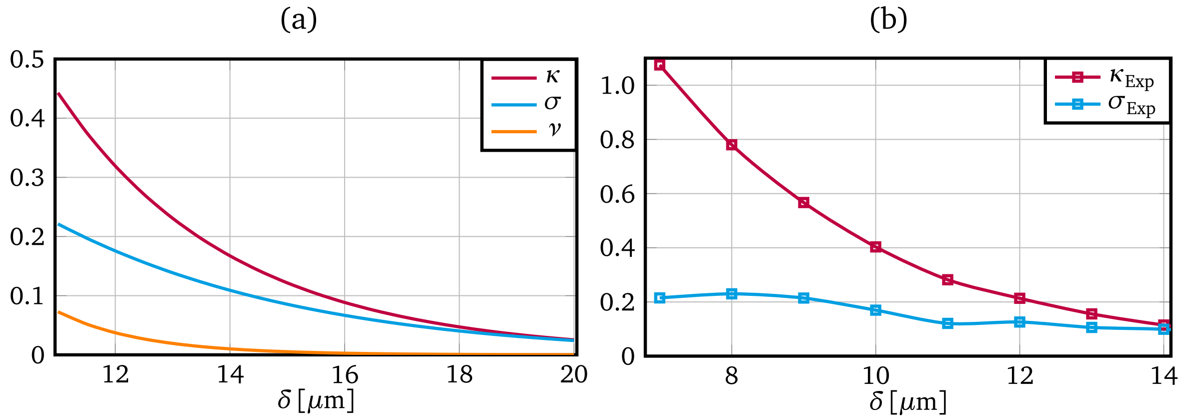

Figure 3.: (a) Coupling κ in mm^{-1}, overlap σ, and self-coupling ν in mm^{-1} between two adjacent waveguides as a function of their separation δ. The results are shown for cylindrical waveguides of radius $R = 4.8\,\mu$m with bulk index $n_0 = 1.452$ and weak contrast $\Delta n = 6.53 \times 10^{-4}$ for the inside of each waveguide. The wavelength of the considered light beam is $\lambda = 633\,$nm. Taken from Ref. [P2]. (b) Coupling κ_{Exp} in mm^{-1} and overlap σ_{Exp} between two fused-silica laser-written waveguides as a function of their separation δ.

calculation can be found in Appendix A.1. In Fig. 3. (b) coupling and overlap between two laser-written waveguides in fused silica are plotted. Markers in the plot label values of κ_{Exp} and σ_{Exp} extracted from an intensity measurement[1].

Given the definitions from Eq. (2.7), the coupled-mode equations become [91, 94]

$$\sum_{k=1}^{M} \left(\mathrm{i}\sigma_{kj}\partial_z \alpha_k + \kappa_{kj}\alpha_k + \beta_k \sigma_{kj}\alpha_k \right) = 0. \tag{2.8}$$

This form of the paraxial Helmholtz equation resembles a discrete Schrödinger equation. Equation (2.8) can be reformulated as the matrix equation $\boldsymbol{\Sigma}\partial_z \boldsymbol{\alpha} = \mathrm{i}\mathbf{K}\boldsymbol{\alpha}$, with $(\mathbf{K})_{jk} = \kappa_{jk} + \beta_k \sigma_{jk}$ and $(\boldsymbol{\Sigma})_{jk} = \sigma_{jk}$ being the coupling and power matrix, respectively. Because $\mathbf{K}$ and $\boldsymbol{\Sigma}$ do not commute in general, the matrix $\boldsymbol{\Sigma}^{-1}\boldsymbol{K}$ governing the propagation is not necessarily Hermitian, and $\left(\boldsymbol{\alpha}^{\mathrm{T}}\right)^{*}\boldsymbol{\alpha}$ would not be conserved throughout the propagation. Nevertheless, the modified intensity distribution $\left(\boldsymbol{\alpha}^{\mathrm{T}}\right)^{*}\boldsymbol{\Sigma}\boldsymbol{\alpha}$ remains constant along z.

2.1.1.1 Normal-mode expansion

The non-Hermitian nature of the coupled-mode equations (2.8) can be lifted by transforming to a set of longitudinal normal modes $(\boldsymbol{b})_k = b_k(z)$ (also known as supermodes [91]). Even though our analysis did not start from power-orthogonal modes, conservation of energy demands that such normal modes exist [85]. Obviously, in contrast to the waveguide mode α_k, the associated normal mode b_k will contain contributions from adjacent waveguides.

---

[1] The experiment was conducted by Johannes Bentzien from the Experimental Solid-State Optics group under Professor Alexander Szameit.

More generally, their relation is given by the conserved quantity $\left(\boldsymbol{b}^{\mathrm{T}}\right)^{*}\boldsymbol{b} = \left(\boldsymbol{\alpha}^{\mathrm{T}}\right)^{*}\boldsymbol{\Sigma}\boldsymbol{\alpha}$. Moreover, because the power matrix $\boldsymbol{\Sigma}$ is positive definite, there exists a (non-unique) matrix $\mathbf{Q}$ such that $\boldsymbol{\Sigma} = \left(\mathbf{Q}^{\mathrm{T}}\right)^{*}\mathbf{Q}$. Once such a factorisation is known, the normal modes are obtained from $\boldsymbol{b} = \mathbf{Q}\boldsymbol{\alpha}$. With respect to the normal modes, Eq. (2.8) can be written as [85]

$$\partial_z \boldsymbol{b} = \mathrm{i}\mathbf{H}\boldsymbol{b},$$

where $\mathbf{H}$ is given by [85]

$$\mathbf{H} = \left(\left(\mathbf{Q}^{-1}\right)^{\mathrm{T}}\right)^{*}\mathbf{K}\mathbf{Q}^{-1}, \tag{2.9}$$

which is Hermitian, because the coupling matrix is Hermitian, i.e., $\mathbf{K} = \left(\mathbf{K}^{\mathrm{T}}\right)^{*}$. From similarity with Eq. (2.9) it follows that the non-Hermitian matrix $\boldsymbol{\Sigma}^{-1}\mathbf{K}$ can always be diagonalised with real spectrum. The matrix $\mathbf{H}$ might be viewed as a generalised coupling matrix mediating population transfer between the normal modes. However, its off-diagonal elements have a fundamentally different distance behaviour as the usual evanescent couplings κ_k. This distortion due to nonorthogonality was observed experimentally in Refs. [95, 96] by means of a fluorescence measurement. As this kind of measurement highlights the non-Hermitian nature of Eq. (2.8), it can potentially be utilised to simulate the dynamics of a $\mathcal{PT}$-symmetric Hamiltonian [97] without gain and loss, a field of research that attracted substantial interest in recent years [98].

2.1.1.2 Orthogonal coupled-mode theory

The nonorthogonality of transverse modes can be neglected if the distance between adjacent waveguides is sufficiently large, i.e., $\sigma_{kj} \approx 0$ for $j \neq k$ and $\sigma_{kk} = 1$ by normalisation. Then one works in the regime of an orthogonal coupled-mode theory [26, 84]. In this case, the coupled-mode equations (2.8) simplify to

$$\mathrm{i}\partial_z \alpha_k + \beta_k \alpha_k + \sum_{j=1}^{M} \kappa_{jk}\alpha_j = 0. \tag{2.10}$$

Hence, the normal modes approximately coincide with modes of the individual waveguides, that is $\boldsymbol{b} \approx \boldsymbol{\alpha}$ and $\left(\boldsymbol{\alpha}^{\mathrm{T}}\right)^{*}\boldsymbol{\alpha}$ is conserved throughout the propagation, thus resembling the intensity of a coherent light beam propagating through the M-mode network.

2.2 Quantised Electromagnetism in a Waveguide Array

The quantisation of a classical field theory can be conducted in several different ways, which all aim at establishing a consistent quantum theory [99]. Fundamental excitations of the fields then present the elementary particles of the theory, for example, photons in the case of the electromagnetic field. Let us proceed with a canonical quantisation of the orthogonal coupled-mode equations (2.10) governing the propagation of a classical light field in an array of waveguides. This is achieved by promoting the amplitude $\alpha_k(z)$ in the

kth spatial mode to a Hilbert-space operator $\hat{a}_k(z)$ satisfying equal-z commutation relations

$$[\hat{a}_j(z), \hat{a}_k(z)] = 0, \qquad [\hat{a}_j(z), \hat{a}_k^\dagger(z)] = \delta_{jk}, \qquad [\hat{a}_j^\dagger(z), \hat{a}_k^\dagger(z)] = 0. \tag{2.11}$$

The operators $\hat{a}_k^\dagger(z)$ and $\hat{a}_k(z)$ describe the creation and annihilation of a photon in the kth waveguide that passes the area at z (at the time $t = z/c$), respectively. Postulating an M-mode vacuum state $|\mathbf{0}\rangle = \bigotimes_{k=1}^{M} |0_k\rangle$, photon-number states (Fock states) are introduced by applying products and powers of bosonic creation operators to the vacuum[2]. After the quantisation, the coupled-mode equations (2.10) become

$$\mathrm{i}\partial_z \hat{a}_k(z) + \beta_k \hat{a}_k(z) + \sum_{j=1}^{M} \kappa_{jk}(z)\hat{a}_j(z) = 0.$$

A comparison with the Heisenberg equation of motion $\partial_z \hat{a}_k = \mathrm{i}[\hat{a}_k, H]$ for the kth bosonic mode only allows a Hamiltonian of the form[3] [100]

$$H = \sum_{\substack{j,k=1\\ j\neq k}}^{M} \left(\kappa_{jk}\hat{a}_j\hat{a}_k^\dagger + \kappa_{jk}^*\hat{a}_j^\dagger\hat{a}_k\right) + \sum_{k=1}^{M} \beta_k \hat{n}_k, \tag{2.12}$$

where the commutation relations (2.11) were used, while demanding Hermiticity of H. In the above equation, $\hat{n}_k = \hat{a}_k^\dagger \hat{a}_k$ denotes the number operator of the kth bosonic mode.

Because in the coupled-mode equations the propagation length z plays a similar role as the time parameter t in a free-space quantisation, the Hamiltonian does not correspond to the energy observable but is given in units of inverse length. Strictly speaking, it therefore corresponds to the momentum operator (with $\hbar = 1$) satisfying an analogous Heisenberg equation of motion as used above [100, 101].

While a canonical quantisation of the free-space electromagnetic field leads to a continuous set of infinitely-many uncoupled harmonic oscillators [102], the Hamiltonian (2.12) describes a discrete (and finite) collection of coupled harmonic oscillators. Even though the given derivation was carried through for a network of weak-index contrast waveguides, coupled-mode Hamiltonians of the form (2.12) can arise in a variety of different settings, including bulk-optical setups (beam splitters and phase shifters), high-index contrast waveguides [103], and even optomechanical oscillators [104]. These are formally summarised as multi-port systems or linear-optical networks [105].

The Hamiltonian (2.12) is bilinear in the creation and annihilation operators. It can therefore be written as $H = \hat{\boldsymbol{a}}^\dagger \mathbf{K} \hat{\boldsymbol{a}}$, where $\mathbf{K}$ is the classical coupling matrix of the M-mode network. The structure of these systems leads their dynamical evolution to be completely determined by the transfer matrix $\mathcal{U} = \mathrm{e}^{\mathrm{i}\mathbf{K}(z_\mathrm{f}-z_0)}$ (scattering matrix) of the network [105], i.e.,

---

[2] For the sake of brevity, the notation $|n_j n_k\rangle = |0, \ldots, n_j, 0, \ldots, 0, n_k, 0, \ldots, 0\rangle$ is often used throughout the thesis. The total number of modes in a system will always be clear from the context.

[3] Throughout the thesis, Hilbert-space operators will be denoted by capital letters, with the exception of the bosonic operators $\hat{a}_k$, $\hat{n}_k = \hat{a}_k^\dagger \hat{a}_k$ acting on Fock space, which instead are equipped with a hat.

$$\hat{\boldsymbol{a}}(z_{\mathrm{f}}) = \mathcal{U}\big[\hat{\boldsymbol{a}}(z_0)\big].$$

Once the modes at the end of the propagation $\hat{\boldsymbol{a}}(z_{\mathrm{f}})$ are known, the propagation of any multi-photon state can immediately be given. In particular, the overall photon number in linear optical setups is preserved throughout evolution. In the context of quantum field theory, the Hamiltonian (2.12) is sometimes referred to as a noninteracting model [99], because the presence of additional photons in a mode does not influence the photon's propagation.

2.2.1 Photon loss

So far photon loss was neglected in the discussion. In any realistic scenario such losses will occur for various reasons, including absorption by the ambient medium [106], scattering centers [107] due to abrupt modulation of the refractive-index profile, and bending losses due to changes in the waveguide position along z. I conclude this chapter by briefly discussing how photon loss can be introduced heuristically by referring to a system-environment approach [108]. This is necessary as a full characterisation of a waveguide network and its surroundings would introduce coupling to a continuum of modes, making diagonalisation of the corresponding Hamiltonian impossible.

In order to avoid such complications, we shall assume that the overall Hamiltonian

$$H = H_{\mathrm{S}} + H_{\mathrm{R}} + H_{\mathrm{I}},$$

consists of the system part H_{S}, the reservoir or environment H_{R}, and an interaction H_{I} between them that is reasonably weak [Fig. 4. (a)]. To make this precise, the quantum state ϱ of the combined system is assumed to propagate as a product

$$\varrho(z) \approx \varrho_{\mathrm{S}}(z) \otimes \varrho_{\mathrm{R}}(0). \tag{2.13}$$

Here, $\varrho_{\mathrm{S}}(z) = \mathrm{Tr}_{\mathrm{R}}\varrho(z)$ is the reduced density operator of the system. Equation (2.13) has the physical interpretation of an interaction that is strong enough to distort the state of the system, but does not alter the reservoir throughout the propagation. Uncertainty in our knowledge about the state of the system, due to a leakage (amplification) of the wave function into (by) the environment, is formally known as decoherence. In this case, the state of the system cannot be given by a pure state, i.e., a Hilbert-space vector. The factorisation (2.13) is known as the Born approximation and appears to be justified in systems of coupled waveguides, because the loss of a few photons does not alter the ambient medium in any meaningful way.

Additionally, the Markov approximation will be employed, which states that the future propagation of the state $\varrho(z)$ is only affected by its state in the present. This is often described as removing any memory effects from the evolution. Hence, scattered photons are assumed to be irrevocably lost from the network. Under the given assumptions, explicit quantum master equations can be derived for the propagation of a quantum state of light [108, 109].

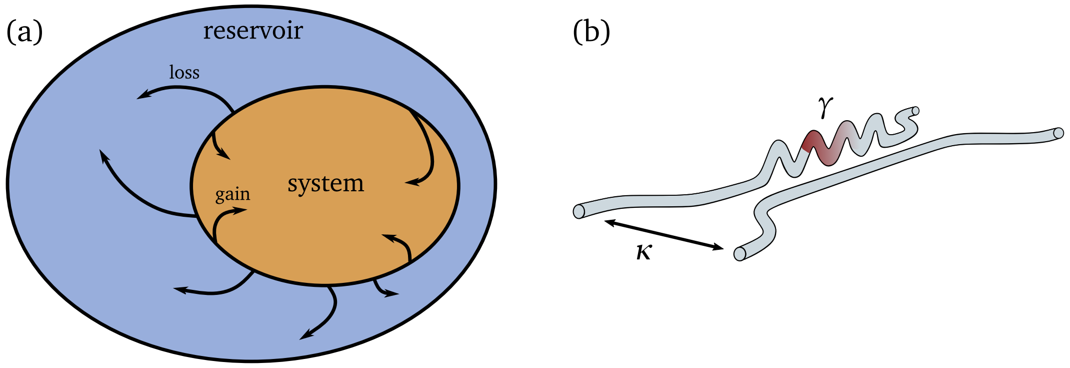

Figure 4.: (a) In an open system approach the overall Hilbert space is partitioned into environmental and the system's degrees of freedom. Their separate dynamics are induced by the Hamiltonians H_R and H_S, respectively. The influence of the reservoir onto the system is described by the interaction part H_I. (b) Illustration of photon loss due to a bending of waveguides.

For a system of M lossy photonic waveguides the dynamics are governed by

$$\partial_z \varrho = \mathrm{i}\big[\varrho, H_\mathrm{S}\big] + \sum_{k=1}^{M} \gamma_k \big(2\hat{a}_k \varrho \hat{a}_k^\dagger - \hat{n}_k \varrho - \varrho \hat{n}_k\big), \tag{2.14}$$

where $\gamma_k(z)$ are Markovian dissipators describing photon loss in the kth bosonic mode and H_S is the coupled-mode Hamiltonian (2.12). The z-dependence of the loss rate γ_k is no deterrent to the Born-Markov approximation (neither is the z-dependence of the couplings), as long as they are slowly varying[4].

The specific form of the dissipators γ_k might be derived from first principles by referring to a microscopic model for the system-reservoir interaction, or are retrieved from phenomenological arguments, e.g., interpolation with experimental data. For instance, absorption within a waveguide can be modelled in terms of a constant loss rate γ_k (absorption coefficient) that is specified by the given material. On the other hand, describing photon loss due to a bending of waveguides [Fig. 4. (b)] is a more subtle task. Following the approach from Ref. [112], this type of loss depends on the Gaussian radius of curvature

$$r_k(z) = \frac{\left(1 + \left[\partial_z x_k(z)\right]^2\right)^{\frac{3}{2}}}{|\partial_z^2 x_k(z)|},$$

---

[4] One could imagine a situation in which the waveguide position is modulated rapidly oscillating, thus rendering a reentering of scattered photons into the waveguide possible. The study of such systems would demand for a post-Markovian [110] or non-Markovian [111] analysis of the underlying dynamics.

where $x_k(z)$ is the position of the kth waveguide (measured from the center). The lose rate is of the form

$$\gamma_k(z) = K_1 \mathrm{e}^{-K_2 r_k(z)},$$

with material parameters K_1 and K_2 [113].

2.2.1.1 *Bending losses in the three-waveguide coupler*

For the purpose of illustration, consider an array of three waveguides. The outer modes W and E interact solely with the central one C via the evanescent coupling κ_W and κ_E, respectively. In other words, the outer modes are assumed to have negligible next-nearest neighbour (second-order) coupling. The tight-binding Hamiltonian of the system reads

$$H_\mathrm{S}(z) = \kappa_\mathrm{W}(z)\big(\hat{a}_\mathrm{W}\hat{a}_\mathrm{C}^\dagger + \hat{a}_\mathrm{W}^\dagger\hat{a}_\mathrm{C}\big) + \kappa_\mathrm{E}(z)\big(\hat{a}_\mathrm{E}\hat{a}_\mathrm{C}^\dagger + \hat{a}_\mathrm{E}^\dagger\hat{a}_\mathrm{C}\big).$$

For simplicity, let the central mode C remain at its position. Then, the z-dependent couplings $\kappa_k(z)$ imply a change of the waveguide position $x_k(z)$ of the outer modes $k = \mathrm{W,E}$. The relation between the coupling and the distance to the central waveguide can be approximated by an exponential behaviour $\kappa_k(z) = K_3 \mathrm{e}^{-K_4 x_k(z)}$, with material parameters K_3 and K_4. Once the geometry $(x_\mathrm{W}, x_\mathrm{E})$ is known, couplings and photon loss can be calculated.

Injecting a single photon into the setup, the Master equation (2.14) can be written down explicitly with respect to the number states $|\mathbf{0}\rangle$ and $\hat{a}_j^\dagger|\mathbf{0}\rangle$, with $j = \mathrm{W,C,E}$. The propagated state $\varrho(z)$ can be obtained by numerical solution of the system of first-order differential equations

$$\begin{aligned}
\partial_z \varrho_\mathrm{WW} &= -2\,\mathrm{Im}(\kappa_\mathrm{W}\varrho_\mathrm{WC}) - 2\gamma_\mathrm{W}\varrho_\mathrm{WW}, & \partial_z \varrho_\mathrm{EW} &= \mathrm{i}(\kappa_\mathrm{W}\varrho_\mathrm{EC} - \kappa_\mathrm{E}\varrho_\mathrm{WC}^*) - (\gamma_\mathrm{W} + \gamma_\mathrm{E})\varrho_\mathrm{EW},\\
\partial_z \varrho_\mathrm{EE} &= -2\,\mathrm{Im}\big(\kappa_\mathrm{E}\varrho_\mathrm{EC}\big) - 2\gamma_\mathrm{E}\varrho_\mathrm{EE}, & \partial_z \varrho_\mathrm{WC} &= \mathrm{i}\big(\kappa_\mathrm{W}(\varrho_\mathrm{WW} - \varrho_\mathrm{CC}) + \kappa_\mathrm{E}\varrho_\mathrm{EW}^*\big) - \gamma_\mathrm{W}\varrho_\mathrm{WC},\\
\partial_z \varrho_\mathrm{CC} &= 2\,\mathrm{Im}(\kappa_\mathrm{W}\varrho_\mathrm{WC} + \kappa_\mathrm{E}\varrho_\mathrm{EC}), & \partial_z \varrho_\mathrm{EC} &= \mathrm{i}\big(\kappa_\mathrm{E}(\varrho_\mathrm{EE} - \varrho_\mathrm{CC}) + \kappa_\mathrm{W}\varrho_\mathrm{EW}\big) - \gamma_\mathrm{E}\varrho_\mathrm{EC},\\
\partial_z \varrho_{00} &= 2\gamma_\mathrm{W}\varrho_\mathrm{WW} + 2\gamma_\mathrm{E}\varrho_\mathrm{EE},
\end{aligned} \tag{2.15}$$

where $\mathrm{Im}(\,\cdot\,)$ stands for the imaginary part of a function. Note that the central waveguide is lossless (i.e., $\gamma_\mathrm{C} = 0$) as its position is not altered throughout the propagation. In Sec. 4.3.2, the three-waveguide coupler will be utilised for the manipulation of quantum information. Solutions of Eq. (2.15) quantify the accumulation of errors due to photon loss.

III | Quantum Holonomies

Symmetries are fundamental to any physical theory — both classical and quantum. They characterise what can be changed about a system without affecting any of its properties. Prominent examples for this are the translation invariance in homogeneous spaces and the invariance under rotations in isotropic or spherical systems. On the other hand, not all physical systems can be in complete symmetry, as then the entire universe would ultimately be static.

The occurrence of symmetries is closely linked to the emergence of gauge potentials. The potential's behaviour under a gauge transformation is such that physical observables remain unaffected. The set of all such transformations is aptly called the symmetry group. The theories of fundamental interactions draw heavily from this notion of gauge symmetry. For instance, electrodynamics is founded on the invariance of the electromagnetic field under certain changes of the vector potential, which are associated with an Abelian U(1) gauge symmetry. In contrast, the weak and strong interactions are both understood as non-Abelian gauge theories with symmetry groups SU(2) and SU(3), respectively [114].

It took a considerable amount of time until Wilczek and Zee noticed that any quantum system (with a d-fold degenerate subspace) can potentially give rise to a U(d) gauge symmetry [52]. More precisely, if the physical parameters of the system are varied slowly then, in the adiabatic limit [115], the system's evolution is governed by a gauge potential, instead of its Hamiltonian. The presence of a gauge potential manifests itself in the difference between the initial state of a system and the final output after evolution. This difference is given by a unitary operator that only depends on the path the quantum state has taken through Hilbert space, and is known as a quantum holonomy (non-Abelian geometric phase). The concept was extended by Anandan and Aharonov, who showed that even nonadiabatic evolutions can remain purely geometric in their characteristics [53, 54].

In this chapter, I will lay out the theory of quantum holonomies in bosonic systems. Starting with the study of adiabatic quantum holonomies in Sec. 3.1, a compendium on how to design these transformations in terms of coupled waveguides is given, including experimental results. Section 3.2 explores the relation between holonomies and the number of particles participating in an evolution. In Sec. 3.3, nonadiabatic quantum holonomies are examined and their emergence in systems of coupled waveguides is discussed. The relation between gauge potentials and parallel transport is briefly elucidated in Sec. 3.4. Finally, an operator formalism, which allows for an elegant photon-number independent description of quantum holonomies is developed in Sec. 3.5.

3.1 Adiabatic Geometric Phases

All quantum field theories that have proven successful in describing real world phenomena are non-Abelian gauge theories [114]. The variety of different (gauge) transformations under which the relevant physics stay unaffected constitute a symmetry group. Quantum mechanics itself gives rise to symmetries in simple dynamical systems. The evolution of a quantum state $|\Psi\rangle$ is given by Schrödinger's equation ($\hbar = 1$ throughout the thesis)

$$\mathrm{i}\partial_t \, |\Psi(t)\rangle = H(t) \, |\Psi(t)\rangle \,, \tag{3.1}$$

where $H(t)$ denotes the Hamiltonian of the quantum system. If the system is initially in the state $|\Psi(0)\rangle$, then after a time period T, the wave packet evolves into $|\Psi(T)\rangle = U(T) \, |\Psi(0)\rangle$, being a formal solution to Eq. (3.1). Conservation of the overall probability, that is $\langle\Psi(t)|\Psi(t)\rangle = 1$ at every instant $t \in [0, T]$, demands for $U(t)$ to be a unitary operator, i.e., $U^\dagger = U^{-1}$. An explicit form of the time-evolution operator is given in terms of a time-ordered matrix exponential (Dyson series)

$$U(T) = \hat{\mathbf{T}} \exp\left(-\mathrm{i} \int_0^T H(t) \mathrm{d}t \right).$$

Solutions to Eq. (3.1) are in general complex [116], but measurement outcomes are determined by absolute values of the wave function. Hence, any knowledge of a phase factor in $|\Psi\rangle$ can be discarded[1]. It follows that one can replace $|\Psi(t)\rangle$ by $\mathrm{e}^{\mathrm{i}\Lambda(t)} \, |\Psi(t)\rangle$ without changing any of the physics. This is the most simple example of a U(1) gauge symmetry.

More intriguing symmetries are found in systems of specific configuration. Let therefore $H(t)$ be the time-dependent Hamiltonian of a quantum system. The system shall be expressible in terms of local control parameters κ_μ, $\mu = 1, \ldots, D$. Depending on the underlying physics the set $\{\kappa_\mu\}_\mu$ might include external driving fields, subsystem couplings or hopping probabilities between different states. In this picture, a time evolution of the system is associated with a specific path $C(t)$ in the D-dimensional parameter space $\mathscr{M}$ (control manifold) containing all possible configurations of the system. Furthermore, assume that the Hamiltonian supports a d-fold degenerate subspace $\mathscr{H}_0$ with energy $\varepsilon_0 = 0$ and a nonvanishing gap $\Delta\varepsilon$ that separates it from adjacent eigenenergies. The subspace $\mathscr{H}_0$ is spanned by the zero-eigenvalue eigenstates $|\psi_a(t)\rangle$, $a = 1, \ldots d$, in many contexts referred to as *dark states* [64, 117, 118]. If one changes the parameters $\boldsymbol{\kappa}(t) = (\kappa_\mu(t))_\mu$ slowly compared to the inverse energy gap $\Delta\varepsilon$, then the evolution is said to be adiabatic [115]. Precisely speaking, the condition $\Delta\kappa_\mu/\Delta t \ll \Delta\varepsilon$ must be valid at every instant in time. Hence, level crossing between ε_0 and adjacent eigenenergies is strictly prohibited, as this would entail $\Delta\varepsilon \to 0$. This implies that there is no transfer of population into states of different energy. However, the transfer of population within the degenerate subspace $\mathscr{H}_0$ is still possible.

In the adiabatic limit, a collection of evolving orthonormal states $\{|\eta_a(t)\rangle\}_{a=1}^d$ prepared in $\mathscr{H}_0$ at $t = 0$, has to reside in this subspace. The evolving states, governed by Schrödinger's equation, then satisfy $\langle \eta_b | \partial_t | \eta_a \rangle = 0$, because of $\varepsilon_0 = 0$. The expression can be expanded in terms of a superposition of the eigenstates, i.e., $|\eta_a(t)\rangle = U(t)\,|\psi_a(t)\rangle$ with $U(t)$ acting solely on $\mathscr{H}_0$. Subsequent differentiation yields

---

[1] Nevertheless, such information can become relevant in interference experiments, such as double-slit experiments or Mach-Zehnder interferometers, to name a few.

$$\left(U^\dagger \partial_t U\right)_{ab} = (A_t)_{ba},$$

where $(A_t)_{ba} = \langle \psi_a | \partial_t | \psi_b \rangle$ is an anti-Hermitian $d \times d$ matrix, i.e., $(A_t)^*_{ba} = -(A_t)_{ab}$. As the evolution resides in a single eigenspace, the time-evolution operator U is independent of fluctuations in the spectrum of $H(t)$.

If the configuration is driven in a cyclic manner, i.e., $\boldsymbol{\kappa}(0) = \boldsymbol{\kappa}(T)$, integration is performed along a loop C in $\mathscr{M}$. The time-evolution operator acting on the subspace becomes a quantity of the loop only, that is known as a quantum holonomy (non-Abelian geometric phase)

$$U_A(C) = \hat{\mathbf{P}} \exp \oint_C A, \tag{3.2}$$

where $A = \sum_\mu A_\mu \mathrm{d}\kappa_\mu$ is the adiabatic connection [52]. Its components are computed from the eigenstates via

$$(A_\mu)_{ba} = \langle \psi_a | \partial_\mu | \psi_b \rangle\,, \tag{3.3}$$

with $\partial_\mu = \partial / \partial \kappa_\mu$ being a shorthand. In Eq. (3.2), the path ordering symbol $\hat{\mathbf{P}}$ accounts for the noncommuting nature of the connection, i.e., $[A_\mu, A_\nu] \neq 0$ in general. The path-ordering prescription makes an immediate evaluation of Eq. (3.2) generally unfeasible. Nevertheless, there are always parameter plaquettes that satisfy the path ordering automatically [40, 119].

Note that the explicit form of an eigenstate $|\psi_a\rangle \in \mathscr{H}_0$ is not unique. While the d-dimensional subspace $\mathscr{H}_0$ is unaffected by a change of basis $|\psi^g_c\rangle = \sum_a g_{ca}\,|\psi_a\rangle$ for arbitrary $g \in \mathrm{U}(d)$, the connection (3.3) becomes

$$A^g_\mu = g A_\mu g^\dagger - g \partial_\mu g^\dagger,$$

which is the transformation behaviour of a $\mathrm{U}(d)$ gauge theory, familiar from the theories of elementary particles [114]. Under such a change of basis the holonomy (3.2) transforms in a gauge covariant manner, that is

$$U^g_A(C) = g U_A(C) g^\dagger.$$

Quantities which transform gauge covariantly preserve their spectral properties, and in particular leave expectation values unchanged [114]. Moreover, a gauge-invariant quantity — the Wilson loop — can always be constructed, that is $W_C = \mathrm{Tr}\{U_A(C)\}$. It is immediately clear, that $|W_C| = d$ for a collection of Abelian subsystems, i.e., $U_A(C) = \mathrm{e}^{\mathrm{i}\phi(C)}\mathbb{1}$ with $\phi(C)$ being a scalar [120]. I should stress, that holonomies can be matrix-valued while still being Abelian, i.e., $U_A(C_1)U_A(C_2) = U_A(C_2)U_A(C_1)$ for arbitrary loops C_1 and C_2 in $\mathscr{M}$.

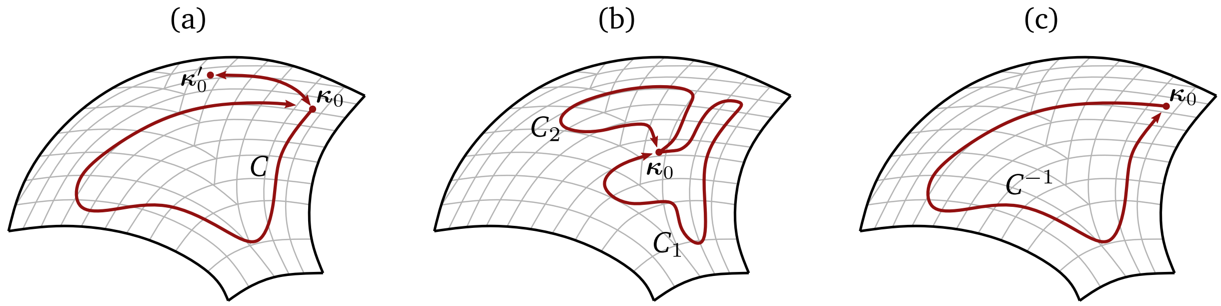

Figure 5.: Closed parameter variations resemble loops in the parameter space $\mathscr{M}$. (a) The base point $\boldsymbol{\kappa}_0$ of a loop can be moved to $\boldsymbol{\kappa}_0'$ by employing a path that is traversed forwards and backwards at the beginning and at the end of the loop, respectively. (b) Composition of two subsequent loops C_1 and C_2 at the base point $\boldsymbol{\kappa}_0$. (c) The inverse of a loop C is obtained when traversing the same loop but with opposite orientation, i.e., backwards.

3.1.1 Properties of quantum holonomies

Quantum holonomies have a number of intriguing properties [40] that can be derived from Eq. (3.2).

(a) Remaining at rest at a point $\boldsymbol{\kappa}_0$ in the parameter space $\mathscr{M}$ amounts to a trivial action on the subspace $\mathscr{H}_0$, i.e., $U_A(C_0) = \mathbb{1}$ with $C_0(t) = \boldsymbol{\kappa}_0$.

(b) Given a composition of two loops

$$(C_2 \circ C_1)(t) = \begin{cases} C_1(t), & t \leq \frac{T}{2}, \\ C_2(t), & t > \frac{T}{2}, \end{cases}$$

a sequence of unitaries is induced, i.e., $U_A(C_2 \circ C_1) = U_A(C_2)U_A(C_1)$.

(c) Traversing the loop C with reversed orientation (i.e., backwards) yields the inverse transformation, i.e., $U_A(C^{-1}) = U_A^{-1}(C)$ for $C^{-1}(t) = C(T-t)$.

(d) As long as adiabaticity holds, the rate at which the loop is traversed does not change the unitary operator, i.e., $U_A(C_f) = U_A(C)$ with $C_f(t) = C(f(t))$ and f is any diffeomorphism of $[0, T]$.

Finally, it should be emphasised that the holonomy $U_A(C)$ only depends on the area enclosed by the loop C (up to orientation) and is therefore invariant even under strong deformations [62]. It follows that, the transformation is independent of the chosen base point $\boldsymbol{\kappa}_0$ at which the loop C starts and ends. The proof of this statement is illustrated in Fig. 5. (a), where the base point is moved from $\boldsymbol{\kappa}_0$ to $\boldsymbol{\kappa}_0'$, the loop C is traversed, and then $\boldsymbol{\kappa}_0'$ is moved back to $\boldsymbol{\kappa}_0$. The first and last step cancel each other out, because moving the base point does not enclose any area. Furthermore, the properties (b) and (c) are illustrated in Fig. 5. (b) and (c), respectively.

3.1.2 The holonomy group

By traversing different loops in $\mathscr{M}$ one can potentially access a variety of different unitaries $U_A(C)$. The set of all such transformations forms the holonomy group

$$\mathrm{Hol}(A) = \left\{ U_A(C) \,\middle|\, C(0) = C(T) = \boldsymbol{\kappa}_0 \right\}.$$

It is a subgroup of the unitary group $\mathrm{U}(d)$ [check properties (a) to (c)], and due to the previous argument [Fig. 5. (a)] it is independent of the chosen base point $\boldsymbol{\kappa}_0 \in \mathscr{M}$. If it is possible to design any unitary matrix by driving a sequence of loops in $\mathscr{M}$, $\mathrm{Hol}(A)$ coincides with the entire unitary group $\mathrm{U}(d)$, and the connection A is said to be *irreducible*.

A convenient way to assess whenever this is fulfilled, is given by the local curvature F (non-Abelian field strength) whose anti-symmetric components ($F_{\mu\nu} = -F_{\nu\mu}$) are given by

$$F_{\mu\nu} = \partial_\mu A_\nu - \partial_\nu A_\mu + [A_\mu, A_\nu]. \tag{3.4}$$

It is related to the holonomy via the (non-Abelian) Stokes theorem $\iint_{\mathscr{D}} F = \oint_C A$, where $\mathscr{D} \subset \mathscr{M}$ is the area enclosed by the loop C [119, 121]. The curvature[2] measures how much the eigenstates $|\psi_a(\boldsymbol{\kappa})\rangle$ in $\mathscr{H}_0$ change under variation of the parameters κ_μ in $\mathscr{M}$.

According to a statement from differential geometry [121], if there are d^2 linear-independent matrices $F_{\mu\nu}$, it is possible to design any element of the unitary group $\mathrm{U}(d)$ in terms of holonomies, a result known as the Ambrose-Singer theorem [123]. In this case, the components $F_{\mu\nu}$ are the (infinitesimal) generators of the holonomy group $\mathrm{Hol}(A) = \mathrm{U}(d)$ [114]. However, in general, the number of linear-independent $F_{\mu\nu}$ gives only a lower bound to the dimension of $\mathrm{Hol}(A)$. In this context, dimension refers to the degrees of freedom that completely determine an element in a group. For instance, a unitary matrix in $\mathrm{U}(d)$ is completely characterised by specifying d^2 real numbers, i.e., $\dim \mathrm{U}(d) = d^2$. In order to obtain all the generators of $\mathrm{Hol}(A)$ we have to compute the algebra spanned by the curvature and its higher-order covariant derivatives[3] [124, 125]

$$\nabla_\sigma F_{\mu\nu}, \quad \nabla_\delta \nabla_\sigma F_{\mu\nu}, \quad \nabla_\epsilon \nabla_\delta \nabla_\sigma F_{\mu\nu}, \quad \ldots$$

where the derivative operator is defined as

$$\nabla_\sigma = \partial_\sigma + [A_\sigma, \cdot\,].$$

---

[2] It is not uncommon to refer to $F_{\mu\nu}$ as the curvature of the parameter space $\mathscr{M}$. This is somewhat misleading, as the $F_{\mu\nu}$ depends not only on the physical parameters $(\kappa_\mu)_\mu$ but on the form of eigenstates as well. Nevertheless, the name has merit to it, because the curvature (3.4) depends on the chosen gauge, and a gauge transformation merely reparametrises the points in $\mathscr{M}$. Technically speaking, $F_{\mu\nu}$ is a local representation of the curvature two-form of the $\mathrm{U}(d)$-principal bundle $\{\mathscr{H}_0(\boldsymbol{\kappa})\}_{\boldsymbol{\kappa} \in \mathscr{M}} \to \mathscr{M}$ on the base manifold $\mathscr{M}$ [122]. At each point $\boldsymbol{\kappa}$ in $\mathscr{M}$ there is a (typical) fibre $\mathscr{H}_0(\boldsymbol{\kappa})$.

[3] There is an intuitive, but by no means rigorous, analogy for this. Similar to a Taylor polynomial, which is a local approximation of a (globally defined) function, the curvature $F^g_{\mu\nu} = g F_{\mu\nu} g^\dagger$ is only valid on a local patch of $\mathscr{M}$ [a specific gauge $g \in \mathrm{U}(d)$]. Adding higher-order (covariant) derivatives to the Taylor polynomial (curvature algebra) improves the approximation.

In the mathematical literature, this is sometimes referred to as Chow's theorem [126]. Clearly, if the connection A_σ is Abelian, then $\nabla_\sigma = \partial_\sigma$, and the (linear) span of the matrices $\{F_{\mu\nu}, \partial_\sigma F_{\mu\nu}, \dots\}_{\mu\nu\sigma\dots}$ is one-dimensional. One concludes that $\mathrm{Hol}(A)$ is an Abelian subgroup of $\mathrm{U}(d)$, and the connection is reducible (for $d > 1$). Despite the fact that the above analysis does not provide an explicit prescription for designing unitary transformations, there existential nature makes them suitable for estimating the general potency of a quantum system to generate holonomies. In Chapter IV, we will encounter that the notion of an irreducible connection is tightly linked to the demand for computational universality in holonomic QC.

3.1.3 Quantum photonic realisation of a U(2) holonomy

In order to harness the concept of holonomy in systems of coupled waveguides (see Chapter II), a structure has to be designed that provides the necessary degeneracy. One suitable setup is a tripod arrangement of waveguides [127], illustrated in Fig. 6. (a). Here each of three outer modes (denoted as W, E, and A) interacts solely with the central one C. The strength of the interaction is described by the real-valued couplings $\kappa_k = \kappa_k^*$ for $k = \mathrm{W}, \mathrm{E}, \mathrm{A}$. The tripod structure was already employed for the generation of geometric phases using a coherent light beam [128], and a non-Abelian braiding of photonic modes was performed in Ref. [129] using a single photon. Similar proposals exist for neutral atoms [117] and trapped ions [64].

Within an orthogonal coupled-mode theory, the system's Hamiltonian reads [P1]

$$H(z) = \sum_{k \in \{\mathrm{W},\mathrm{E},\mathrm{A}\}} \kappa_k(z)\big(\hat{a}_k \hat{a}_{\mathrm{C}}^\dagger + \hat{a}_k^\dagger \hat{a}_{\mathrm{C}}\big).$$

If a single photon is subjected to the structure, the system gives rise to two dark states

$$\begin{aligned} |d_1\rangle &= \sin\theta\,|1_{\mathrm{E}}\rangle - \cos\theta\,|1_{\mathrm{A}}\rangle\,, \\ |d_2\rangle &= \cos\vartheta\,|1_{\mathrm{W}}\rangle - \cos\theta\sin\vartheta\,|1_{\mathrm{E}}\rangle - \sin\theta\sin\vartheta\,|1_{\mathrm{A}}\rangle\,. \end{aligned}$$

In the above, the parametrisation $\theta = \arctan(\kappa_{\mathrm{A}}/\kappa_{\mathrm{E}})$ and $\vartheta = \arctan\big(\kappa_{\mathrm{W}}/\sqrt{\kappa_{\mathrm{E}}^2 + \kappa_{\mathrm{A}}^2}\big)$ was utilised. A straight-forward calculation of the connection (3.3) leads to $(A_\theta)_{21} = \sin\vartheta = -(A_\theta)_{12}$ as the only nonvanishing component, and therefore path ordering becomes obsolete. A subsequent evaluation of the matrix exponential in Eq. (3.2) results in the quantum holonomy

$$U_A(C) = \begin{bmatrix} \cos\phi_C & -\sin\phi_C \\ \sin\phi_C & \cos\phi_C \end{bmatrix}, \tag{3.5}$$

with $\phi_C = \oint_C \sin\vartheta \mathrm{d}\vartheta$ being a geometric phase.

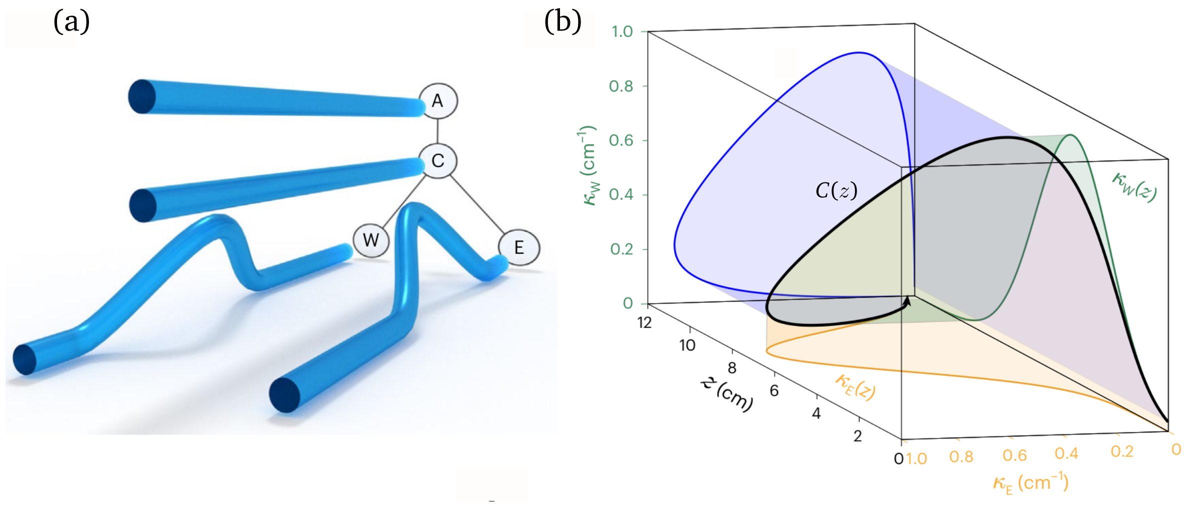

Figure 6.: (a) Tripod arrangement of photonic waveguides fabricated by the femtosecond laser-writing technique. The outer modes of the system interact solely with the central waveguide. The figure shows the realisation of a quantum holonomy via Gaussian coupling pulses. (b) The strength of these interactions is described by the respective couplings κ_μ. The desired loop C (blue) is implemented by parametrising the couplings along the spatial coordinate $0\,\text{cm} \leq z \leq 12\,\text{cm}$ which indicates the longitudinal position within the sample. In this setting, κ_W (green) and κ_E (yellow) follow Gaussian profiles, while κ_A is kept constant. Adapted from Ref. [P4].

For the experiments[4] reported in Ref. [P4], the Gaussian coupling configuration

$$\kappa_\mathrm{E}(z) = \Omega \exp\left(-\frac{(z-\bar{z}+\tau)^2}{Z^2}\right), \qquad \kappa_\mathrm{W}(z) = \Omega \exp\left(-\frac{(z-\bar{z}-\tau)^2}{Z^2}\right), \tag{3.6}$$

was designed. In the above, $\Omega = 0.9\,\text{cm}^{-1}$, $Z = 2.5\,\text{cm}$, $\bar{z} = 6\,\text{cm}$, and $\tau = 1.5\,\text{cm}$, while $\kappa_\mathrm{A} = 1.1\,\text{cm}^{-1}$ remains constant. Variation of the couplings is shown in Fig. 6. (b). These (approximately) form a loop C in the coupling space $\mathscr{M}$. The entire glass sample consists of a 12 cm long holonomy, followed by a 3 cm fan-out.

Due to the finite propagation length, adiabaticity can never be satisfied perfectly. This results in a population of the nondegenerate bright states

$$|b_\pm\rangle = \frac{1}{\sqrt{2}}\big(\sin\vartheta\,|1_\mathrm{W}\rangle + \cos\theta\cos\vartheta\,|1_\mathrm{E}\rangle + \sin\theta\cos\vartheta\,|1_\mathrm{A}\rangle \pm |1_\mathrm{C}\rangle\big),$$

having energy $\varepsilon_\pm = \pm\sqrt{\kappa_\mathrm{E}^2 + \kappa_\mathrm{W}^2 + \kappa_\mathrm{A}^2}$. This leads to a dynamical evolution that deviates from the holonomy (3.5). In the tripod structure, diabatic effects (nonadiabatic coupling) manifest themselves in photons occupying the central mode C, as this can only be due to the excitation of bright states. An appropriate measure of how severely the diabatic effects harm the generation of geometric phases is the (expected) fidelity[5] $\overline{F}(U,\mathcal{N})$ between the desired unitary U, ideally to be realised, and the noisy quantum operation $\mathcal{N}$. In any realistic scenario, the map $\mathcal{N}$ does not only contain diabatic errors, but photon losses, imprecision in the physical setup (e.g., in the couplings), errors due to a fan-out at the end of the propagation, etc.

---

[4] The experimental results reported in Refs. [P4, P5] were obtained by Vera Neef from the Experimental Solid-State Optics group under Professor Alexander Szameit. The theoretical analysis of these waveguide structures is due to myself.

After preparing a single photon in one of the dark states $|D_1(\boldsymbol{\kappa}_0)\rangle = |1_\mathrm{W}\rangle$ or $|D_2(\boldsymbol{\kappa}_0)\rangle = |1_\mathrm{E}\rangle$ at $\boldsymbol{\kappa}_0 = (0,0,\kappa)$, that is the photon is at the front facet of the East or West wing of the tripod, performing repeated measurements on the output state using single-photon (avalanche-photo diode) detectors allows one to extract the fidelity[6]. The architecture realises a quantum holonomy with $\overline{F} = 99.7\,\%$ showing excellent agreement between theory and experiment [P4].

3.1.4 Quantum photonic realisation of a U(3) holonomy

The coupling design (3.6), realising the parameter loop C employed in the experiment, can be viewed as an all-out optical STIRAP (**sti**mulated **R**aman **a**diabatic **p**assage) scheme. STIRAP has its origin in atomic systems [131], where light-matter interactions (so-called Rabi couplings) are induced slowly varying by means of an external laser field, thus resulting in adiabatic population transfer between the degenerate ground states of an atom. However, photonic systems have a distinct advantage over these atomic implementations, namely a single (bosonic) mode can contain multiple photons.

Therefore, let us turn to a situation in which two indistinguishable photons are injected into the optical tripod arrangement. Remarkably, upon sending a second photon into the tripod, degeneracy increases, that is the tripod system possesses a four-fold degenerate dark subspace spanned by the two-photon dark states

$$\begin{aligned}
|D_1\rangle &= \sin^2\theta\,|2_\mathrm{E}\rangle - \sqrt{2}\sin\theta\cos\theta\,|1_\mathrm{E}1_\mathrm{A}\rangle + \cos^2\theta\,|2_\mathrm{A}\rangle\,,\\
|D_2\rangle &= \frac{1}{\sqrt{2}}\sin\theta\cos\theta\sin\vartheta\big(\,|2_\mathrm{A}\rangle - |2_\mathrm{E}\rangle\,\big) + \cos\vartheta\big(\sin\theta\,|1_\mathrm{E}1_\mathrm{W}\rangle - \cos\theta\,|1_\mathrm{A}1_\mathrm{W}\rangle\,\big)\\
&\quad + \sin\vartheta\cos(2\theta)\,|1_\mathrm{E}1_\mathrm{A}\rangle\,,\\
|D_3\rangle &= \cos^2\vartheta\,|2_\mathrm{W}\rangle - \sqrt{2}\sin\vartheta\cos\vartheta\big(\cos\theta\,|1_\mathrm{E}1_\mathrm{W}\rangle + |1_\mathrm{W}1_\mathrm{A}\rangle\,\big)\\
&\quad + \sin^2\vartheta\big(\sin^2\theta\,|2_\mathrm{A}\rangle + \cos^2\theta\,|2_\mathrm{E}\rangle\,\big) + \sqrt{2}\sin\theta\cos\theta\sin^2\vartheta\,|1_\mathrm{E}1_\mathrm{A}\rangle\,,
\end{aligned}$$

---

[5] The expected fidelity between U and $\mathcal{N}$ is defined as [130]

$$\overline{F}(U,\mathcal{N}) = \frac{1}{K}\sum_{k=1}^{K} F(U\,|\psi_k\rangle\,,\varrho_k) = \frac{1}{K}\sum_{k=1}^{K}\langle\psi_k|\,U^\dagger\mathcal{N}\big(\,|\psi_k\rangle\,\langle\psi_k|\,\big)U\,|\psi_k\rangle\,.$$

Summation is carried out over an ensemble of K input states $|\psi_k\rangle$. The fidelity has an operational interpretation of how close the desired states $U\,|\psi_k\rangle$ are to the obtained output $\varrho_k = \mathcal{N}\big(\,|\psi_k\rangle\,\langle\psi_k|\,\big)$.

[6] In the experiment, photon counts at the output facet of the central mode C were removed from the statistic, thus correcting part of the diabatic error by post processing.

$$
\begin{aligned}
|D_4\rangle = {} & \frac{1}{\sqrt{2}}\sin^2\vartheta\,|2_{\mathrm{W}}\rangle + \sin\vartheta\cos\vartheta\big(\cos\theta\,|1_{\mathrm{W}}1_{\mathrm{E}}\rangle + \sin\theta\,|1_{\mathrm{W}}1_{\mathrm{A}}\rangle\big) \\
& + \frac{1}{\sqrt{2}}\cos^2\vartheta\big(\cos^2\theta\,|2_{\mathrm{E}}\rangle + \sin^2\theta\,|2_{\mathrm{A}}\rangle\big) + \sin\theta\cos\theta\cos^2\vartheta\,|1_{\mathrm{E}}1_{\mathrm{A}}\rangle - \frac{1}{\sqrt{2}}|2_{\mathrm{C}}\rangle\,.
\end{aligned}
$$

With the explicit form of the dark states at hand, determining the connection amounts to a straight-forward calculation, that leads to

$$
A_\theta = \begin{bmatrix} 0 & -\sqrt{2}\sin\vartheta & 0 & 0 \\ \sqrt{2}\sin\vartheta & 0 & -\sqrt{2}\sin\vartheta & 0 \\ 0 & \sqrt{2}\sin\vartheta & 0 & 0 \\ 0 & 0 & 0 & 0 \end{bmatrix},
$$

while $A_\vartheta = 0$ again. A quantum holonomy is obtained by driving through a loop C in $\mathscr{M}$. Evaluating Eq. (3.2) gives

$$
U_A(C) = \begin{bmatrix} \cos^2\phi_C & -\sqrt{2}\sin\phi_C\cos\phi_C & \sin^2\phi_C & 0 \\ \sqrt{2}\sin\phi_C\cos\phi_C & \cos(2\phi_C) & -\sqrt{2}\sin\phi_C\cos\phi_C & 0 \\ \sin^2\phi_C & \sqrt{2}\sin\phi_C\cos\phi_C & \cos^2\phi_C & 0 \\ 0 & 0 & 0 & 1 \end{bmatrix}, \tag{3.7}
$$

with ϕ_C being the same geometric phase factor as in the single-photon case (3.5).

Unlike the propagation of a single photon, here the holonomy reveals a block structure in which one of the dark states decouples. In Ref. [132], an intuitive explanation for this block structure was given, referring to the fact that $|D_4\rangle$ involves photons in central mode similar to a bright state. It might therefore be prohibited to participate in the adiabatic propagation even though it has eigenenergy zero. In Sec. 3.5, I give a more rigorous argument by looking at the adiabatic evolution of bosonic modes, instead of photon-number states. This will lead to an operator version of the adiabatic theorem [P6] that clarifies the block structure of the holonomy (3.7).

The two-photon experiments were performed using the same waveguide structure, that is the tripod arrangement with the coupling design (3.6). The results were reported in Ref. [P4] as well. As theoretical predictions rely on the assumption of an indistinguishable photon pair to be prepared as an input, a HOM-dip experiment was performed showing a visibility of 95 %. Two-photon measurements were realised by combining the single-photon detectors with fibre beam splitters at the output facet of the tripod. This amounts to preparing a set of projectors that can distinguish between the number states

$$
|D_1(\boldsymbol{\kappa}_0)\rangle = |2_{\mathrm{E}}\rangle\,, \quad |D_2(\boldsymbol{\kappa}_0)\rangle = |1_{\mathrm{E}}1_{\mathrm{W}}\rangle\,, \quad |D_3(\boldsymbol{\kappa}_0)\rangle = |2_{\mathrm{W}}\rangle\,.
$$

Thus, the fidelity can be retrieved from the measurement data, that is $\overline{F} = 99.7\,\%$, again being in excellent agreement with the theoretical predictions [P4].

Note that the energy gap between the dark and bright states is the same as for a single-photon, i.e., $\varepsilon_\pm = \pm\sqrt{\kappa_{\mathrm{E}}^2 + \kappa_{\mathrm{W}}^2 + \kappa_{\mathrm{A}}^2}$. However, for two photons, the bright states themselves belong to a two-fold degenerate eigenspace

$$\begin{aligned}
|B_{\pm,1}\rangle &= \frac{1}{\sqrt{2}}\sin\theta\sin\vartheta\,|1_{\mathrm{W}}1_{\mathrm{E}}\rangle + \sin\theta\cos\theta\cos\vartheta\,|2_{\mathrm{E}}\rangle - \frac{1}{\sqrt{2}}\cos(2\theta)\cos\vartheta\,|1_{\mathrm{E}}1_{\mathrm{A}}\rangle \pm \sin\theta\,|1_{\mathrm{E}}1_{\mathrm{C}}\rangle \\
&\quad - \frac{1}{\sqrt{2}}\sin\vartheta\cos\theta\,|1_{\mathrm{W}}1_{\mathrm{A}}\rangle - \sin\theta\cos\theta\cos\vartheta\,|2_{\mathrm{A}}\rangle \mp \frac{1}{\sqrt{2}}\cos\theta\,|1_{\mathrm{A}}1_{\mathrm{C}}\rangle\,, \\
|B_{\pm,2}\rangle &= \sin\vartheta\cos\vartheta\big(\,|2_{\mathrm{W}}\rangle - \cos^2\theta\,|2_{\mathrm{E}}\rangle - \sin^2\theta\,|2_{\mathrm{E}}\rangle\,\big) + \frac{\cos(2\vartheta)}{\sqrt{2}}\big(\cos\theta\,|1_{\mathrm{W}}1_{\mathrm{E}}\rangle + \sin\theta\,|1_{\mathrm{W}}1_{\mathrm{A}}\rangle\,\big) \\
&\quad - \sqrt{2}\sin\theta\cos\theta\sin\vartheta\cos\vartheta\,|1_{\mathrm{E}}1_{\mathrm{A}}\rangle \pm \frac{1}{\sqrt{2}}\cos\vartheta\,|1_{\mathrm{W}}1_{\mathrm{C}}\rangle \mp \frac{1}{\sqrt{2}}\sin\vartheta\cos\theta\,|1_{\mathrm{E}}1_{\mathrm{C}}\rangle \\
&\quad \mp \frac{1}{\sqrt{2}}\sin\theta\sin\vartheta\,|1_{\mathrm{A}}1_{\mathrm{C}}\rangle\,.
\end{aligned} \tag{3.8}$$

I denote the two remaining eigenstates of the system as the second-order bright states

$$\begin{aligned}
|B_{\pm 2}\rangle &= \frac{1}{2}\sin^2\vartheta\,|2_{\mathrm{W}}\rangle + \frac{1}{\sqrt{2}}\sin\vartheta\cos\vartheta\big(\cos\theta\,|1_{\mathrm{W}}1_{\mathrm{E}}\rangle + \sin\theta\,|1_{\mathrm{W}}1_{\mathrm{A}}\rangle\,\big) \pm \frac{1}{\sqrt{2}}\sin\vartheta\,|1_{\mathrm{W}}1_{\mathrm{C}}\rangle \\
&\quad + \frac{1}{2}\cos^2\vartheta\big(\cos^2\theta\,|2_{\mathrm{E}}\rangle + \sin^2\theta\,|2_{\mathrm{A}}\rangle\,\big) + \frac{1}{\sqrt{2}}\sin\theta\cos\theta\sin\vartheta\cos\vartheta\,|1_{\mathrm{E}}1_{\mathrm{A}}\rangle \\
&\quad + \frac{1}{\sqrt{2}}\cos\vartheta\big(\cos\theta\,|1_{\mathrm{E}}1_{\mathrm{C}}\rangle + \sin\theta\,|1_{\mathrm{A}}1_{\mathrm{C}}\rangle\,\big) + \frac{1}{2}\,|2_{\mathrm{C}}\rangle\,,
\end{aligned}$$

as they have nondegenerate eigenenergies $\varepsilon_{\pm 2} = \pm 2\sqrt{\kappa_{\mathrm{E}}^2 + \kappa_{\mathrm{W}}^2 + \kappa_{\mathrm{A}}^2}$. When preparing two photons in the dark subspace, nonadiabatic coupling to these states is strongly suppressed by an energy gap that is twice as big.

3.1.5 Degeneracy of the photonic star graph

The previous discussion can be viewed as the special case of a star graph Hamiltonian to which N photons are subjected. In the *photonic star graph*, shown in Fig. 7. (a), $M-1$ bosonic modes couple exclusively to the mode M [P1]. The isodegenerate Hamiltonian of the system reads

$$H = \sum_{k=1}^{M-1}\big(\kappa_k \hat{a}_k \hat{a}_M^\dagger + \kappa_k^* \hat{a}_k^\dagger \hat{a}_M\big). \tag{3.9}$$

For $M = 4$, one recovers the tripod structure. It is clear that an implementation in terms of waveguides becomes unfeasible when the number of modes becomes large, as placing more and more waveguides around a central one will inevitably result in a coupling between the outer modes [P1].

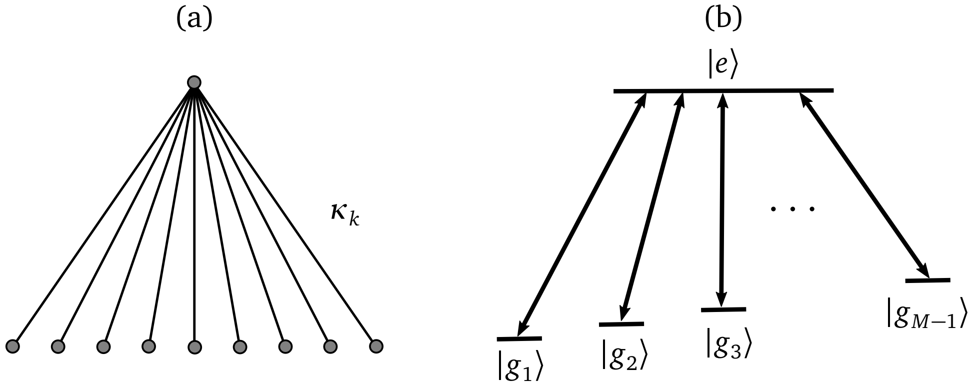

Figure 7.: (a) Depiction of the photonic star graph. The kth outer mode ($k=1,\dots,M-1$) interacts solely with the central one via the coupling κ_k. (b) Term scheme of an atomic M-pod system in which $M-1$ ground states $|g_k\rangle$ couple to an excited state $|e\rangle$.

Consider N photons to be subjected to the star graph. Formally, this corresponds to the Hamiltonian (3.9) acting on the N-photon Fock layer

$$\mathscr{F}_N = \left\{ |n_1, n_2 \dots\rangle \;\middle|\; \sum_{k=1}^{M} n_k = N \right\}.$$

Represented in the basis $\mathscr{F}_N$, the Hamiltonian defines a matrix $H|_{\mathscr{F}_N}$ on a reduced Hilbert space having dimension $\binom{N+M-1}{N} = \frac{(N+M-1)!}{N!(M-1)!}$, which is the number of possibilities to distribute N indistinguishable photons on M labelled waveguides [P1].

By diagonalisation of the matrix $H|_{\mathscr{F}_N}$ one finds a decomposition of the total Hilbert space $\mathscr{H}$ of the system into orthogonal eigenspaces, viz.

$$\mathscr{H} = \mathscr{H}_0 \oplus \mathscr{H}_+ \oplus \mathscr{H}_- \oplus \dots \oplus \mathscr{H}_{+N} \oplus \mathscr{H}_{-N},$$

where $\mathscr{H}_0$ is its dark subspace, and $\mathscr{H}_{\pm n}$ is the eigenspace with energy

$$\varepsilon_{\pm n} = \pm n \sqrt{|\kappa_1|^2 + \dots + |\kappa_{M-1}|^2} = \pm n \varepsilon$$

for $n = 1, \dots, N$. We observe that higher-order bright states emerge, when more photons are subjected to the system. The degeneracy $d_{\pm n}$ of these subspaces depends on the number of modes M and photons N, but is the same at each point $\boldsymbol{\kappa} \neq \mathbf{0}$ in the coupling space $\mathscr{M}$. In particular, one can fix $\boldsymbol{\kappa}_0 = (0, \dots, 0, \kappa)$ such that the Hamiltonian (3.9) reduces to

$$H(\boldsymbol{\kappa}_0) = \kappa(\hat{a}_{M-1}\hat{a}_M^\dagger + \hat{a}_{M-1}^\dagger \hat{a}_M).$$

In this simplified setting, counting the number of dark states $\prod_j \sqrt{n_j!}^{-1} \left(\hat{a}_j^\dagger\right)^{n_j} |\mathbf{0}\rangle$ in the N photon case amounts to counting the number of possibilities to distribute N photons onto the modes $\hat{a}_j^\dagger$ for $j = 1, \dots, M-2$. There are $\binom{N+M-3}{N}$ ways of distributing all photons over these modes. Additionally, having a simultaneous excitation of the modes

$$\frac{1}{\sqrt{2}}(\hat{a}^\dagger_{M-1} + \hat{a}^\dagger_M), \qquad \frac{1}{\sqrt{2}}(\hat{a}^\dagger_{M-1} - \hat{a}^\dagger_M), \tag{3.10}$$

produces dark states as well, when applied to the vacuum $|\mathbf{0}\rangle$. As this involves two photons, there are $\binom{N-2+M-3}{N-2}$ ways to distribute the remaining $N-2$ photons over the modes $\hat{a}^\dagger_j$. The argument continues. Even numbers n of photons are equally distributed to the pair of modes (3.10), while the remaining $N-n$ are distributed over the modes $\hat{a}^\dagger_j$ for $j = 1, \dots, M-2$. Hence, there are two distinct cases, N odd or even, for which one finds two formulas for the total number of dark states $d_0(N,M) = \dim \mathscr{H}_0$, that is [P1]

$$d_0(N,M) = \begin{cases} \sum_{n=1}^{\frac{N}{2}} \binom{2n+M-3}{2n}, & \text{if } N \text{ even}, \\ \sum_{n=0}^{\frac{N-1}{2}} \binom{2n+1+M-3}{2n+1}, & \text{if } N \text{ odd}. \end{cases}$$

The proof can be extended to (higher-order) bright states. When counting the number of bright states with energy $\pm n\varepsilon$, one first has to put n photons in one of the modes (3.10), and then distribute the rest as if to create a dark state. Thus, for bright states with energy $\pm n\varepsilon$, there are $d_{\pm n}(N,M) = d_0(N-n,M)$ possibilities [P1].

In Fig. 8, the resulting spectral structure is schematically shown for selected values of N and M. Clearly, the addition of more photons drastically increases the dimensions of subspaces on which potentially more intriguing (higher-dimensional) holonomies can be generated. If one considers only a single photon, i.e., $N = 1$, then the star graph has $M-2$ dark states and two nondegenerate bright states. This is mathematically equivalent to the atomic M-pod scheme from Ref. [117], where $M-1$ electronic ground states couple to the electromagnetic field only via a single excited state [Fig. 7. (b)]. Due to the fermionic nature of electrons, degeneracy can only be increased by providing additional energy levels (i.e., increasing M). In contrast, the photonic star graph allows for more degenerate subspaces by virtue of providing additional photons as well (i.e., increasing N).

In conclusion, it was shown that the star graph arrangement provides the necessary degeneracy for the generation of quantum holonomies that belong to the group $\mathrm{U}(d_0(N,M))$, when N indistinguishable photons are injected into the setup.

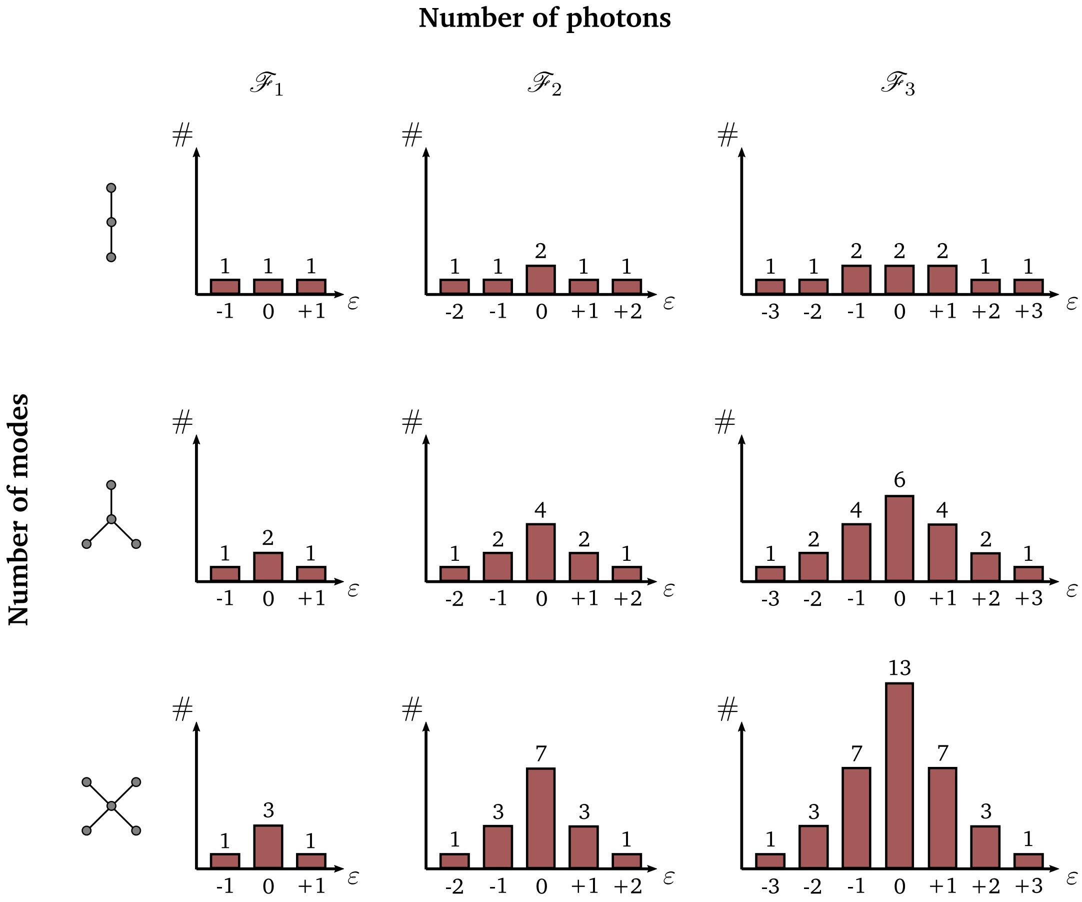

Figure 8.: Spectral properties of the photonic star graph filled with N photons. The number of eigenstates (#) is depicted over the energy (in multiples of ε) for $M = 3, 4, 5$ and $N = 1, 2, 3$. Additional waveguides lead to an increase in the degeneracy. The degeneracy of the lowest energy (magnitude-wise) increases the most, while the two highest (magnitude-wise) eigenenergies are nondegenerate. In comparison, increasing the number of photons in the system not only increases degeneracy but gives rise to two additional nondegenerate eigenenergies. Adapted from Ref. [P1].

3.2 The Particle-Number Threshold

We witnessed a remarkable increase in degeneracy of a (bosonic) quantum system upon subjecting more particles. Naively, one might assume that in this way arbitrarily complicated unitary transformations can be utilised for the manipulation of photon-number states. This is not the case. For once, this is clear from intuition as the parameter space $\mathscr{M}$ is independent of the particle number. Hence, a finite supply of physically accessible couplings cannot allow for the manipulation of arbitrary combinations of photon-number states. Secondly, it was already shown for the tripod structure (Sec. 3.1.3 and Sec. 3.1.4) that, when moving from a single photon to two indistinguishable photons, its dark subspace gave rise to a holonomy (3.7) revealing a submatrix structure. The analysis so far hints at a more general question [P3]. What is the number of particles N an experimentalist should subject to a quantum system in order to generate the most versatile set of quantum holonomies?

To be precise, the terminology *most versatile set* refers to the holonomy group of highest dimension. The question of how many different unitaries can be harnessed by driving loops through $\mathscr{M}$ is therefore closely related to computational universality [133], which holds if $\mathrm{Hol}(A) = \mathrm{U}(d)$. In this section, quantum holonomies are studied in relation to the number of particles involved in the evolution. In the following, this issue is motivated through illustrative examples following Ref. [P3].

3.2.1 Three-waveguide coupler

Consider an array consisting of three waveguides. The outer modes $\hat{a}_{\mathrm{W}}$ and $\hat{a}_{\mathrm{E}}$ experience coupling to the central mode $\hat{a}_{\mathrm{C}}$. Within an orthogonal coupled-mode theory the Hamiltonian of the system reads

$$H = \sum_{k \in \{\mathrm{W},\mathrm{E}\}} \left(\kappa_k \hat{a}_k \hat{a}_{\mathrm{C}}^\dagger + \kappa_k^* \hat{a}_k^\dagger \hat{a}_{\mathrm{C}} \right). \tag{3.11}$$

The Hamiltonian is equivalent to the star graph for $M = 3$.

Suppose a single photon is injected into one of the outer modes (W or E) of the optical setup, with complex[7] couplings $\kappa_{\mathrm{W}}(z)$ and $\kappa_{\mathrm{E}}(z)$ varying slowly compared to the minimal energy gap $\sqrt{|\kappa_{\mathrm{W}}|^2 + |\kappa_{\mathrm{E}}|^2}$. In the adiabatic limit, the photon remains in the dark state

$$|d\rangle = \sin\theta \, |1_{\mathrm{W}}\rangle - \cos\theta \, \mathrm{e}^{\mathrm{i}\varphi} \, |1_{\mathrm{E}}\rangle ,$$

where $\tan\theta = |\kappa_{\mathrm{E}}|/|\kappa_{\mathrm{W}}|$ and $\varphi = \arg(\kappa_{\mathrm{W}})$. The only nonvanishing component of the connection is $A_\varphi = \mathrm{i}\cos^2\theta$. The curvature is readily obtained to $F_{\theta\varphi} = \sin(2\theta)$. After traversing a loop C in the (θ, φ) plane, the output state $|\Psi(z_{\mathrm{f}})\rangle = \mathrm{e}^{\mathrm{i}\phi(C)} |\Psi(z_0)\rangle$ accumulates the geometric phase

$$\phi(C) = \iint_{\mathscr{D}} \sin(2\theta) \mathrm{d}\varphi \mathrm{d}\theta, \tag{3.12}$$

with $\mathscr{D}$ being the area enclosed by the loop C.

Subjecting a second (indistinguishable) photon to the setup, leads to the two dark states

$$\begin{aligned} |D_1\rangle &= \sin^2\theta \, |2_{\mathrm{W}}\rangle - \sqrt{2} \sin\theta \cos\theta \, \mathrm{e}^{\mathrm{i}\varphi} \, |1_{\mathrm{W}} 1_{\mathrm{E}}\rangle + \cos^2\theta \, \mathrm{e}^{2\mathrm{i}\varphi} \, |2_{\mathrm{E}}\rangle , \\ |D_2\rangle &= \frac{1}{\sqrt{2}} \Big(\sin^2\theta \, |2_{\mathrm{E}}\rangle + \cos^2\theta \, \mathrm{e}^{-2\mathrm{i}\varphi} \, |2_{\mathrm{W}}\rangle - |2_{\mathrm{c}}\rangle \Big) + \sqrt{2} \sin\theta \cos\theta \, \mathrm{e}^{-\mathrm{i}\varphi} \, |1_{\mathrm{W}} 1_{\mathrm{E}}\rangle . \end{aligned}$$

Consequently, A_φ is now a matrix-valued quantity. At first glance, one might expect that this enables the generation of non-Abelian holonomies. However, a calculation of the holonomy yields

---

[7] A complex coupling strength κ_μ can be engineered using varying detuning [135, 136].

$$U_A(C) = \begin{bmatrix} \mathrm{e}^{2\mathrm{i}\phi(C)} & 0 \\ 0 & \mathrm{e}^{-2\mathrm{i}\phi(C)} \end{bmatrix}. \tag{3.13}$$

It is immediately clear from the diagonal form of the matrix (3.13) that the holonomy belongs to an Abelian subgroup of U(2). Hence, even though degeneracy of the system would render the generation of noncommuting transformations possible, the holonomy group is still Abelian. Technically speaking, the evaluation of the holonomy group on the two-photon Fock layer induces a reducible representation of the group $\mathrm{Hol}(A) = \mathrm{U}(1)$.

3.2.2 Four-mode fully-connected graph

As a second example, showing more intriguing behaviour, consider the four-mode fully-connected graph depicted in Fig. 9. The graph consists of four bosonic modes each interacting with all other modes in the graph. In terms of waveguides, this means we have to utilise more than just nearest-neighbour coupling[8].

Generally, it is not expected that such Hamiltonians give rise to a degenerate spectrum when arbitrary configurations $\boldsymbol{\kappa} \in \mathscr{M}$ are considered. This is due to the reason that nondegeneracy is the generic case, while degeneracy requires some form of symmetry [1]. Nonetheless, it is possible to construct specific configurations that lead to a degenerate subspace [58, 59]. Therefore, let H_0 be a Hamiltonian with some fixed degeneracy structure. Consider the isospectral parametrisation

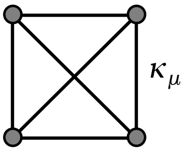

Figure 9.: A four-mode fully connected graph, where each side can experience a different coupling κ_μ.

$$H(\boldsymbol{\kappa}) = \mathcal{V}(\boldsymbol{\kappa}) H_0 \mathcal{V}^\dagger(\boldsymbol{\kappa}), \tag{3.14}$$

parameterised over points $\boldsymbol{\kappa} = (\boldsymbol{\theta}, \boldsymbol{\varphi})$ in $\mathscr{M}$. For the four-mode system, let $H_0 = \hat{n}_1 + \hat{n}_2 - \hat{n}_4$ and

$$\mathcal{V}(\boldsymbol{\theta}, \boldsymbol{\varphi}) = V_{12}(\theta_1, \varphi_1) V_{23}(\theta_2, \varphi_2) V_{34}(\theta_3, \varphi_3)$$

is our unitary of choice. The unitar operator $V_{kk+1}(\theta_k, \varphi_k)$ creates a linear mixing between the modes k and $k+1$, viz.

$$\begin{aligned} V_{kk+1} \hat{a}_k^\dagger V_{kk+1}^\dagger &= \cos\theta_k \mathrm{e}^{\mathrm{i}\varphi_k} \hat{a}_k^\dagger + \sin\theta_k \hat{a}_{k+1}^\dagger, \\ V_{kk+1} \hat{a}_{k+1}^\dagger V_{kk+1}^\dagger &= \cos\theta_k \mathrm{e}^{-\mathrm{i}\varphi_k} \hat{a}_{k+1}^\dagger - \sin\theta_k \hat{a}_k^\dagger. \end{aligned} \tag{3.15}$$

---

[8] Notice that fully-connected graphs cannot always be implemented using coupled waveguides, because evanescent hopping between waveguides is inverse proportional to their distance. Hence, couplings cannot be chosen independently of one another, rendering the implementation of some configurations of the graph impossible.

The transformation (3.15) is chosen such that the Hamiltonian $H(\boldsymbol{\kappa})$ is still bilinear in the creation and annihilation operators.

Given a single particle the system possesses one dark state

$$|d\rangle = \mathrm{e}^{\mathrm{i}\varphi_3}\cos\theta_3\big(\sin\theta_1\sin\theta_2\,|1_1\rangle + \mathrm{e}^{-\mathrm{i}\varphi_1}\cos\theta_1\sin\theta_2\,|1_2\rangle + \mathrm{e}^{-\mathrm{i}\varphi_2}\cos\theta_2\,|1_3\rangle\,\big) - \sin\theta_3\,|1_4\rangle\,.$$

A straight-forward computation of the connection reveals

$$A_{\varphi_1} = -\mathrm{i}\cos^2\theta_1\cos^2\theta_2\sin^2\theta_2,\qquad A_{\varphi_2} = -\mathrm{i}\cos^2\theta_2\cos^2\theta_3,\qquad A_{\varphi_3} = \mathrm{i}\cos^2\theta_3,$$

and $A_{\theta_k} = 0$. The curvature is readily calculated from Eq. (3.4). Its nonvanishing components are

$$\begin{aligned}
F_{\varphi_1\theta_1} &= -2\mathrm{i}\sin\theta_1\cos\theta_1\sin^2\theta_2\cos^2\theta_3, & F_{\varphi_1\theta_2} &= 2\mathrm{i}\cos^2\theta_1\sin\theta_2\cos\theta_2\cos^2\theta_3,\\
F_{\varphi_1\theta_2} &= -2\mathrm{i}\cos^2\theta_1\sin^2\theta_2\sin\theta_3\cos\theta_3, & F_{\varphi_2\theta_2} &= -2\mathrm{i}\sin\theta_2\cos\theta_2\cos^2\theta_3,\\
F_{\varphi_2\theta_3} &= -2\mathrm{i}\cos^2\theta_2\sin\theta_3\cos\theta_3, & F_{\varphi_3\theta_3} &= 2\mathrm{i}\sin\theta_3\cos\theta_3.
\end{aligned}$$

Hence, Abelian holonomies can be harnessed by adiabatically traversing loops in $\mathscr{M}$.

Next, consider the two-particle Fock layer spanned by the number states

$$\begin{aligned}
&|2_1\rangle, \quad |1_11_2\rangle, \quad |1_11_3\rangle, \quad |1_11_4\rangle, \quad |2_2\rangle,\\
&|1_21_3\rangle, \quad |1_21_4\rangle, \quad |2_3\rangle, \quad |1_31_4\rangle, \quad |2_4\rangle.
\end{aligned}$$

The matrix $H|_{\mathscr{F}_2}$ supports a three-fold degenerate dark subspace with states $|D_k\rangle$, for $k = 1, 2, 3$. Their explicit form can be found in Appendix A.2. The connection on this subspace is

$$A_{\varphi_1}\Big|^{\theta_2=0}_{\theta_1=\theta_3=\frac{\pi}{4}} = \frac{\mathrm{i}}{2}\begin{bmatrix} 0 & 0 & 0\\ 0 & 1 & \mathrm{e}^{\mathrm{i}(\varphi_1-\varphi_2)}\\ 0 & \mathrm{e}^{-\mathrm{i}(\varphi_1-\varphi_2)} & -1\end{bmatrix},\qquad A_{\varphi_2} = \mathrm{i}\cos^2\theta_2\cos^2\theta_3\begin{bmatrix} -2 & 0 & 0\\ 0 & -1 & 0\\ 0 & 0 & 1\end{bmatrix},$$

$$A_{\varphi_3} = \mathrm{i}\cos^2\theta_3\begin{bmatrix} 2 & 0 & 0\\ 0 & -1 & 0\\ 0 & 0 & 1\end{bmatrix},\qquad A_{\theta_1} = \cos\theta_2\begin{bmatrix} 0 & 0 & 0\\ 0 & 0 & -\mathrm{e}^{\mathrm{i}(\varphi_2-\varphi_1)}\\ 0 & \mathrm{e}^{\mathrm{i}(\varphi_2-\varphi_1)} & 0\end{bmatrix},$$

and $A_{\theta_2} = A_{\theta_3} = 0$. Patiently calculating the curvature

$$F_{\varphi_1\theta_1}|_{\boldsymbol{\kappa}_0} = \begin{bmatrix} -\mathrm{i} & 0 & 0\\ 0 & \frac{\mathrm{i}}{2} & -\frac{\mathrm{i}}{2\sqrt{2}}\\ 0 & -\frac{\mathrm{i}}{2\sqrt{2}} & -\frac{\mathrm{i}}{2}\end{bmatrix},\quad F_{\varphi_1\theta_2}|_{\boldsymbol{\kappa}_0} = \begin{bmatrix} \mathrm{i} & 0 & 0\\ 0 & \frac{\mathrm{i}}{2} & \frac{\mathrm{i}}{\sqrt{2}}\\ 0 & \frac{\mathrm{i}}{\sqrt{2}} & -\frac{\mathrm{i}}{2}\end{bmatrix},\quad F_{\varphi_2\theta_1}|_{\boldsymbol{\kappa}_0} = \begin{bmatrix} 0 & 0 & 0\\ 0 & 0 & \mathrm{i}\\ 0 & \mathrm{i} & 0\end{bmatrix}, \tag{3.16}$$

and its first order covariant derivative

$$\nabla_{\varphi_1} F_{\theta_1\theta_2}|_{\boldsymbol{\kappa}_0} = \begin{bmatrix} 0 & 0 & 0 \\ 0 & \mathrm{i} & -\frac{\mathrm{i}}{2\sqrt{2}} \\ 0 & -\frac{\mathrm{i}}{2\sqrt{2}} & -\mathrm{i} \end{bmatrix}, \quad \nabla_{\theta_1} F_{\varphi_2\theta_1}|_{\boldsymbol{\kappa}_0} = \begin{bmatrix} 0 & 0 & 0 \\ 0 & -\mathrm{i} & 0 \\ 0 & 0 & \mathrm{i} \end{bmatrix}, \tag{3.17}$$

highlights the non-Abelian nature of the system. For simplicity, the matrices were evaluated at the point $\boldsymbol{\kappa}_0$, with $\varphi_k = 0$ and $\theta_k = \pi/4$, and only the linear-independent contributions were shown. The matrices (3.16) and (3.17) are the infinitesimal generators of a five-dimensional matrix (Lie) group. This constitutes a lower bound to the dimension of Hol(A) [P3]. Nevertheless, the analysis illustrates that subjecting a second particle to the setup rendered the generation of more intriguing holonomies possible. More precisely, the two-particle dark states led to a non-Abelian holonomy group Hol(A) $\subset$ U(3).

The key observation is that, increasing the number of particles (from one to two) notably improved our capabilities to generate unitaries on the dark subspace (from Abelian to non-Abelian holonomies). Intuitively it is clear that the dimension of Hol(A) cannot increase continually when the particle number becomes bigger, as this would result in arbitrarily high computational power, while having only a limited supply of physical resources in $\mathscr{M}$. This leads us to an interesting question [P3]. How far can we increase the dimension of a holonomy group by subjecting an increasing number of particles to a system? A formal answer to this question will be given in the next section in terms of the *particle-number threshold* of a system.

3.2.3 Particle-number thresholds

The holonomies of a quantum system show a dependence on the particle number N. Firstly, this is due to the reason that the spectral properties (e.g., degeneracy) of a system vary when its Hamiltonian H is limited to act on different Fock layers $\mathscr{F}_N$. Secondly, it was noticed that even in the case that degeneracy increases, this does not necessarily imply a more useful (i.e., higher dimensional) holonomy group. Therefore, it is natural to ask, what is the particle number N at which one of the holonomy groups $\{\mathrm{Hol}(A_l)\}_l$, each acting on an eigenspaces $\mathscr{H}_l$ of the system, reaches its maximal dimension and is therefore most suitable for designing a useful set of unitaries. The number of particles required for this endeavour will be denoted as the particle-number threshold (PNT) N_t [P3].

Definition: *Let H be the Hamiltonian of a quantum system in second quantisation that evolves adiabatically in time. The particle-number threshold N_t denotes the minimum number of particles necessary for one of the system's holonomy groups to reach its maximum potential (maximal dimension) for the generation of holonomies.*

The above definition demands for an analysis of the holonomy groups of each eigenspace $\mathscr{H}_l$ (not just the dark subspace), in order to determine $\dim \mathrm{Hol}(A_l)$ for each l. Then, there exists a subspace with index l' such that for all other l holds

$$\dim \mathrm{Hol}(A_{l'}) \geq \dim \mathrm{Hol}(A_l).$$

In this light, the PNT N_t is the number of particles necessary to populate any state in $\mathscr{H}_{l'}$.

3.2.3.1 Properties of PNTs

The PNT N_t of a (bosonic) quantum system H is, in general, hard to calculate, as it demands for a calculation of the connection A_l for each eigenspace (there might be infinitely many). Nevertheless, some general properties can still be derived [P3]. Consider a system that consists of a collection of noninteracting subsystems, i.e., $H = \bigotimes_a H_a$. Suppose, the PNT $N_\mathrm{t}^{(a)}$ for each subsystem H_a is known and that, $\mathrm{Hol}\big(A_{l'}^{(a)}\big)$ denotes its holonomy group with maximal dimension. The composite system H then has PNT $N_\mathrm{t} = \sum_a N_\mathrm{t}^{(a)}$. This becomes evident when noting that the highest-dimensional holonomy group

$$\mathrm{Hol}(A_{l'}) = \bigotimes_a \mathrm{Hol}\big(A_{l'}^{(a)}\big)$$

is just the tensor product of the holonomy groups $\mathrm{Hol}\big(A_{l'}^{(a)}\big)$ of each individual subsystem. The holonomy group of the composite system acts on the subspace with energy $\prod_a \varepsilon_{l'}^{(a)}$, where $\varepsilon_{l'}^{(a)}$ denotes the eigenenergy of the subspace on which the group $\mathrm{Hol}\big(A_{l'}^{(a)}\big)$ acts.

Next, consider a Hamiltonian with isospectral parametrisation, that is

$$H(\boldsymbol{\kappa}) = \mathcal{V}(\boldsymbol{\kappa}) H_0 \mathcal{V}^\dagger(\boldsymbol{\kappa}), \tag{3.18}$$

with H_0 being a Hamiltonian having fixed degeneracy structure $\{d_l\}_l$ and eigenstates $\{|\psi_{l,a}\rangle\}_{l,a}$. Suppose there is a sufficiently large parameter space $\mathscr{M}$ so that $\mathcal{V}(\boldsymbol{\kappa})$ is the most general unitary operator. Adiabatic evolution in the lth eigenspace $\mathscr{H}_l = \{\mathcal{V}(\boldsymbol{\kappa})\,|\psi_{l,a}\rangle\}_{a=1}^{d_l}$ is then governed by a connection

$$(A_{l,\mu})_{ab} = \langle\psi_{l,b}|\, \mathcal{V}^\dagger \partial_\mu \mathcal{V}\, |\psi_{l,a}\rangle\,,$$

which is the most general anti-Hermitian matrix. By construction, one has $\mathrm{Hol}(A_l) = \mathrm{U}(d_l)$. For such a general parametrisation, it is indeed the eigenspace with largest degeneracy $d_{l'} \geq d_l$, that is the one most desirable for the generation of non-Abelian holonomies [P3]. Hence, N_t is the number of particles necessary to populate any state in the most degenerate eigenspace $\mathscr{H}_{l'}$.

3.2.3.2 PNT of the two-mode nonlinear Kerr-medium

In any realistic scenario, $\mathcal{V}$ will most likely not be the most general unitary operator, but will be limited to some smaller set of physically accessible operations. For concreteness, consider the two-mode Hamiltonian associated with a nonlinear Kerr medium

$$H_0 = \hat{n}_1\big(\hat{n}_1 - \mathbb{1}\big) + \hat{n}_2\big(\hat{n}_2 - \mathbb{1}\big).$$

Here, the unitary $\mathcal{V}(\alpha,\beta,\xi,\zeta)$ is a product of single and two-mode displacement

$$\begin{aligned} D_k(\alpha) &= \exp\big(\alpha\hat{a}_k^\dagger - \alpha^*\hat{a}_k\big), \\ K(\beta) &= \exp\big(\beta\hat{a}_1^\dagger\hat{a}_2 - \beta^*\hat{a}_1\hat{a}_2^\dagger\big), \end{aligned} \tag{3.19}$$

as well as single and two-mode squeezing

$$\begin{aligned} S_k(\xi) &= \exp\big(\xi(\hat{a}_k^\dagger)^2 - \xi^*\hat{a}_k^2\big), \\ M(\zeta) &= \exp\big(\zeta\hat{a}_1^\dagger\hat{a}_2^\dagger - \zeta^*\hat{a}_1\hat{a}_2\big), \end{aligned} \tag{3.20}$$

respectively [102]. By driving coherent displacement (α,β) and squeezing parameters (ξ,ζ) through a closed loop in $\mathscr{M} = \mathbb{C}^4$, holonomies on the eigenspaces of H are obtained. Pachos and Chountasis showed that this enables arbitrary U(4) transformations over the zero-eigenvalue eigenspace $\mathscr{H}_0$ [137]. At the point $(\alpha,\beta,\xi,\zeta) = \mathbf{0}$, the corresponding eigenstates reduce to

$$|0_1 0_2\rangle\,, \quad |1_1 0_2\rangle\,, \quad |0_1 1_2\rangle\,, \quad |1_1 1_2\rangle\,,$$

i.e., two photons are necessary to fully occupy the subspace.

An extended study (up to $N = 50$ photons) of the curvature F_l shows that, even though further increasing the photon number ($N > 2$) populates eigenspaces with increased degeneracy (up to $d_l = 10$ for some l), their holonomy groups do not offer a more useful holonomy group [P3]. In other words,

$$\dim \mathrm{Hol}(A_l) \leq \dim \mathrm{Hol}(A_0)$$

holds for all eigenspaces $\mathscr{H}_l$ with index $l \leq 352$ (see Tab. 1). This was done through explicit calculation of the curvature $F_{l,\mu\nu}$ and its covariant derivatives up to order three (these are to large to be displayed here). The computed dimension of the groups $\{\mathrm{Hol}(A_l)\}_l$ did not increase further after the first order derivatives, thus giving us reasonable assurance that the dimension was characterised accurately [P3].

In summary, the subspace $\mathscr{H}_0$ (containing at most two-photon states) should be preferred when the system is utilised for the generation of non-Abelian geometric phases. Therefore, the PNT of the two-mode Kerr Hamiltonian is $N_\mathrm{t} = 2$. Moreover, it was shown that restricting the parametrisation of the Hamiltonian (3.18) to unitaries $\mathcal{V}$ that can be realised by the Gaussian operations (3.19) and (3.20), led to many of the system's eigenspaces having reducible connections A_l. Hence, degeneracy became a quantity of secondary interest. In Tab. 1 the spectral properties of the two-mode Kerr Hamiltonian H are listed together with their capacity to generate holonomies on the eigenspaces $\mathscr{H}_l$ (for $l = 0,\ldots,352$). Subspaces with degeneracy $d_l \leq 4$ were excluded from Tab. 1, as their holonomy groups cannot exceed the dimension of $\mathrm{Hol}(A_0) = \mathrm{U}(4)$.

l	ε_l	d_l	$\leq N$	$\dim\{F_{l,\mu\nu}\}_{\mu\nu}$	$\dim \mathrm{Hol}(A_l)$
0	0	4	2	14	16
1	2	4	3	14	16
5	12	5	6	9	9
16	42	6	10	9	9
26	72	6	13	12	12
37	110	6	15	9	9
45	132	6	17	9	9
54	162	6	19	6	6
60	182	6	20	9	9
70	212	6	21	3	3
78	240	6	21	9	9
87	272	6	24	9	9
99	312	5	26	3	3
108	342	6	27	9	9
113	362	6	27	3	3
130	420	5	30	9	9
131	422	6	30	3	3
141	462	8	31	9	9
157	512	6	33	6	6
168	552	10	34	9	9
199	662	6	36	3	3
208	702	6	38	9	9
215	722	6	39	6	6
222	756	6	38	9	9
225	762	6	40	3	3
238	812	10	41	9	9
266	912	6	42	3	3
274	942	8	44	3	3
285	992	6	45	9	9
306	1062	8	47	3	3
320	1112	6	48	3	3
323	1122	6	48	9	9
346	1202	8	50	3	3
349	1212	6	49	3	3
352	1232	8	50	3	3

Table 1.: Holonomy groups of the two-mode nonlinear Kerr medium parameterised by the Gaussian operations (3.19) and (3.20). The table contains the degeneracy d_l of the lth eigenspace (with energy ε_l). Here, N denotes the number of particles necessary to fully occupy the corresponding eigenspace $\mathscr{H}_l$. The number of linear-independent curvature components $F_{l,\mu\nu}$ as well as the dimension of the holonomy group $\mathrm{Hol}(A_l)$. Covariant derivatives were calculated up the order of three. Taken from Ref. [P3].

3.2.3.3 PNTs of coupled harmonic oscillators

Given a collection of coupled harmonic oscillators (i.e., a linear optical system), certain specialisations arise that can simplify the calculation of a PNT notably. In these systems, population transfer between different Fock layers $\mathscr{F}_N$ does not occur, because the total number of photons is not altered throughout an evolution. From a mathematical viewpoint, this implies that the system's Hamiltonian reveals a submatrix structure, i.e.,

$$H = \bigoplus_{N \in \mathbb{N}} H|_{\mathscr{F}_N}.$$

Utilising the spectral resolution $H = \sum_l \varepsilon_l \Pi_l$ (Π_l denoting the projector onto $\mathscr{H}_l$), the eigenspaces themselves admit a similar decomposition, viz.

$$\Pi_l = \bigoplus_{N(l)} \Pi_l|_{\mathscr{F}_{N(l)}}, \tag{3.21}$$

where summation is carried out over those particle numbers $N(l)$ at which the corresponding eigenenergy ε_l occurs.

As an example, the Hamiltonian (3.11) of the three-waveguide coupler does not possess single-particle eigenstates with energy $2\sqrt{|\kappa_\mathrm{W}|^2 + |\kappa_\mathrm{E}|^2}$ (recall Sec. 3.2.1). In other words, the eigenvalue does not lie in the spectrum of $H|_{\mathscr{F}_1}$, but it is an eigenvalue of the matrix $H|_{\mathscr{F}_N}$ for $N \geq 2$. Here, the direct sum in Eq. (3.21) amounts to an infinite series starting with $N(l) = 2, 3, \ldots$.

If additionally the evolution is assumed to be adiabatic, photon transfer occurs within each eigenspace separately. Hence, the decomposition (3.21) is inherited to the time-evolution operator (quantum holonomy) [P3]

$$U_{A_l}(C) = \bigoplus_{N(l)} U_{A_l}(C)|_{\mathscr{F}_{N(l)}}. \tag{3.22}$$

Clearly, the connection will always be reducible for such a system, because it is not possible to generate transformations between different Fock layers. The best one can hope for, is to find is a highly-degenerate N-particle block in the eigenspace $\mathscr{H}_l$ such that the holonomy $U_{A_l}(C)|_{\mathscr{F}_N}$ realises any unitary transformation on the subspace $\mathscr{H}_l|_{\mathscr{F}_N}$.

Despite the quantum holonomy (3.22) potentially having an infinite-dimensional matrix representation, it might still be commuting for different loops in the parameter space $\mathscr{M}$. For instance, this is the case for the Hamiltonian (3.11) of the three-waveguide coupler. For a single photon, the matrix $H|_{\mathscr{F}_1}$ has only one dark state (see Sec. 3.2.1). Given two or three photons in the setup, $H|_{\mathscr{F}_2}$ and $H|_{\mathscr{F}_3}$ both have two dark states. Subjecting four photons to the system leads to a Hamiltonian matrix $H|_{\mathscr{F}_4}$ having three dark states. Even though degeneracy further increases, the quantum holonomy

$$U_{A_0} = \begin{bmatrix} U_{A_0}|_{\mathscr{F}_1} & & \\ & U_{A_0}|_{\mathscr{F}_2} & \\ & & \ddots \end{bmatrix}$$

will remain Abelian, because the N-particle block

$$U_{A_0}(C)|_{\mathscr{F}_N} = \mathrm{diag}\left(\mathrm{e}^{\mathrm{i}N\phi(C)}, \ldots, \mathrm{e}^{-\mathrm{i}N\phi(C)}\right),$$

is itself a diagonal matrix [see Eq. (3.13) for $N = 2$]. Here, $\phi(C)$ is the geometric phase defined in Eq. (3.12). The above analysis illustrates, that increasing the photon number in the three-waveguide coupler does not increase the holonomy group's dimension. Similar arguments hold for the other eigenspaces of the system, and thus a single photon is sufficient to generate any phase in U(1). One concludes, the PNT of the system is $N_\mathrm{t} = 1$.

3.2.3.4 PNTs of fermionic systems

Until now, all systems considered, were bosonic in nature. Nonetheless, the definition of a PNT is applicable to any quantum system given in second quantisation. Fermionic modes are associated with creation and annihilation operators fulfilling canonical anticommutation relations. Because of this, the most prominent difference to bosonic setups, is that fermions have to obey the Pauli principle, that is, two fermions cannot occupy the same mode simultaneously. This drastically reduces the number of possible states in a system and in particular, the corresponding Fock space is finite dimensional. Therefore, the computing the PNT of a fermionic system becomes much more manageable in comparison to bosonic systems.

PNTs can also be calculated for systems comprising both bosonic and fermionic modes. As a particularly simple example, consider the Jaynes-Cummings Hamiltonian describing the interaction between an incident light field and a single atomic energy level at resonance. Within the rotating wave approximation, the Hamiltonian reads [102]

$$H_\mathrm{JC} = \omega_\mathrm{A}\sigma^+\sigma^- + \omega_\mathrm{c}\hat{n} + \kappa(\hat{a}^\dagger\sigma^- + \hat{a}\sigma^+),$$

with resonance frequency ω_A of the atom, ω_c being the frequency of the incident light field, and κ describing the strength of the light-matter interaction. The atomic ladder operators $\sigma^- = |g\rangle\langle e|$ and $\sigma^+ = (\sigma^-)^\dagger$ shift an electron from the ground state $|g\rangle$ to the excited state $|e\rangle$, and vice versa. The system possesses a nondegenerate spectrum $\{\varepsilon_{n^\pm}\}_{n\in\mathbb{N}}$ with corresponding eigenstates

$$\begin{aligned} |n^+\rangle &= \sin\theta\,|g, n+1\rangle + \cos\theta\,|e, n\rangle, \\ |n^-\rangle &= \cos\theta\,|g, n+1\rangle - \sin\theta\,|e, n\rangle, \end{aligned}$$

where $\tan(2\theta) = 2\kappa\sqrt{n+1}/(\omega_\mathrm{c} - \omega_\mathrm{A})$ and n being the photon number. This (one-parameter) form of the eigenstates highlights that the underlying parameter space does not possess any curvature, i.e., $F_{n^\pm,\theta\theta} = 0$ for all photon numbers $n \in \mathbb{N}$. Hence, the system is ineligible for the generation of quantum holonomies, and this is reflected in the PNT, i.e., $N_\mathrm{t} = 0$ [P3].

3.3 Nonadiabatic Geometric Phases

The construction of adiabatic geometric phases can be generalised to the case in which the underlying subspace, on which the holonomy acts, is not an eigenspace [54]. This allows one to go beyond the adiabatic regime while keeping the evolution purely geometric. Such proposals can be advantageous as they drastically shorten the necessary evolution time or propagation length.

Let therefore $H(t)$ be the Hamiltonian of a quantum system associated with a Hilbert space $\mathscr{H}$. Consider a finite-dimensional subspace $\mathscr{H}_\psi$ spanned by a collection of orthonormal states $|\psi_a(t)\rangle$, for $a = 1, \ldots, d$. These do not need to be eigenstates. In order for the evolution to be independent of any dynamical influences, the mean energy of the Hamiltonian has to vanish on that subspace, i.e., $\langle H(t)\rangle_{\mathscr{H}_\psi} = 0$ for all t in an interval $[0, T]$. Expressing this condition in terms of the basis $\{|\psi_a\rangle\}_a$ yields

$$\langle\psi_a(t)|H(t)|\psi_b(t)\rangle = 0. \tag{3.23}$$

A state $|\eta_a(t)\rangle$ residing in the subspace $\mathscr{H}_\psi$ throughout its evolution can be expanded as $|\eta_a(t)\rangle = U(t)\,|\psi_a(t)\rangle$. Here, the unitary operator U acts solely on the subspace $\mathscr{H}_\psi$. Next, consider an orthonormal frame of evolving states, i.e., $\langle\eta_a|\eta_b\rangle = \delta_{ab}$. By linearity, one has $\langle\eta_a|\partial_t|\eta_b\rangle = 0$, due to Schrödinger's equation and condition (3.23). In compliance with these assumptions, the operator U obeys

$$(U^\dagger\partial_t U)_{ab} = (A_t)_{ba},$$

with $(A_t)_{ba} = \langle\psi_a|\partial_t|\psi_b\rangle$ being an anti-Hermitian $d \times d$ matrix. A formal solution to the above equation is given by the time-ordered matrix exponential [54]

$$U(T) = \hat{\mathbf{T}}\exp\int_0^T A_t \mathrm{d}t. \tag{3.24}$$

Suppose the evolution is such that the subspace $\mathscr{H}_\psi$ returns to its initial configuration after the time T. In other words, the evolution is cyclic, that is $|\psi_a(0)\rangle = |\psi_a(T)\rangle$ for $a = 1, \ldots, d$. Then, the operator (3.24) turns into a quantum holonomy [60], and we may well write $U(T) = U_A(C)$. Here, C denotes the loop taken by the basis $\{|\psi_a(t)\rangle\}_a$ through state space and $A = A_t\mathrm{d}t$ denotes the nonadiabatic connection [53]. The latter being a direct generalisation of the (adiabatic) Wilczek-Zee connection [52]. Unlike in the adiabatic case, here a loop C in state space does not imply a loop in the underlying parameter space $\mathscr{M}$ of the system.

Nevertheless, the nonadiabatic holonomy has similar properties as its adiabatic counterpart (see Sec. 3.1). A product of loops can be defined, i.e. $U_A(C_2 \circ C_1) = U_A(C_2)U_A(C_1)$. As one can always traverse a loop C backwards, we have $U_A(C^{-1}) = U_A^{-1}(C)$. Remaining on the same point in Hilbert space corresponds to a quantum holonomy acting as the identity, i.e., $U_A(C_0) = \mathbb{1}$ with $C_0 = \{|\psi_a\rangle\}_a$ being time independent. These properties equip the set of possible holonomies with a group structure, resulting in a holonomy group $\mathrm{Hol}(A) \subseteq \mathrm{U}(d)$. A change of the basis $|\psi_c^g\rangle = \sum_a g_{ca}\,|\psi_a\rangle$ in the subspace $\mathscr{H}_\psi$, with $g \in \mathrm{U}(d)$, preserves condition (3.23) as well as cyclicity. On the other hand, the nonadiabatic connection experiences the gauge transformation $A_t^g = gA_t g^\dagger - g\partial_t g^\dagger$.

3.3.1 Quantum photonic realisation of a U(2) holonomy

In order to harness nonadiabatic quantum holonomies from systems of coupled waveguides, the three-waveguide coupler (Fig. 10) is employed. Again, population transfer is mediated by the evanescent couplings $\kappa_\mathrm{W}(z)$ and $\kappa_\mathrm{E}(z)$ towards the central mode C only. Within an orthogonal coupled-mode theory, the Hamiltonian of the system reads

$$H(z) = \sum_{k\in\{\mathrm{W},\mathrm{E}\}} \kappa_k(z)\big(\hat{a}_k \hat{a}_\mathrm{C}^\dagger + \hat{a}_k^\dagger \hat{a}_\mathrm{C}\big). \tag{3.25}$$

As before, the propagation length z acts as the time parameter. Consider a scenario with only a single photon. Both couplings are designed to change with the same envelope $\Omega(z)$, i.e., the real-valued parametrisation $\kappa_\mathrm{W}(z) = \Omega(z)\sin(\theta/2)$ and $\kappa_\mathrm{E}(z) = \Omega(z)\cos(\theta/2)$ is employed. The states

$$\begin{aligned} |d\rangle &= \sin(\theta/2)\,|1_\mathrm{E}\rangle - \cos(\theta/2)\,|1_\mathrm{W}\rangle\,, \\ |b\rangle &= \cos(\theta/2)\,|1_\mathrm{E}\rangle + \sin(\theta/2)\,|1_\mathrm{W}\rangle\,, \end{aligned}$$

change along the propagation according to (use $H\,|d\rangle = 0$)

$$\begin{aligned} |\psi_1(z)\rangle &= U(z)\,|d\rangle = |d\rangle\,, \\ |\psi_2(z)\rangle &= \mathrm{e}^{\mathrm{i}\delta(z)} U(z)\,|b\rangle = \mathrm{e}^{\mathrm{i}\delta(z)}(\cos\delta(z)\,|b\rangle - \mathrm{i}\sin\delta(t)\,|1_\mathrm{C}\rangle), \end{aligned} \tag{3.26}$$

where $U(z) = \mathrm{e}^{-\mathrm{i}\int_{z_0}^{z} H(z')\mathrm{d}z'}$ is the time-evolution operator and $\delta(z) = \int_{z_0}^{z} \Omega(z')\mathrm{d}z'$. The reader can easily convince themselves that these states satisfy condition (3.23). Moreover, it can be readily verified that a pulse $\Omega(z)$ with $\delta(z_\mathrm{f}) = \pi$ ensures that they evolve cyclically as well. The resulting evolution is given by a quantum holonomy, which does not depend on any dynamical properties of H such as the eigenenergies or runtime. It is completely determined by the nonadiabatic connection, which has a single nonvanishing component $(A_z)_{22} = \mathrm{i}\Omega(z)$. Evaluating the matrix exponential (3.24), one is left with the holonomy $U_A(C_\theta) = \mathrm{diag}(1,-1)$ given at the base point $|\psi_1(z_0)\rangle = |d\rangle$ and $|\psi_2(z_0)\rangle = |b\rangle$. When transforming into the photon-number states $|1_\mathrm{W}\rangle$ and $|1_\mathrm{E}\rangle$ (via a change of gauge), one

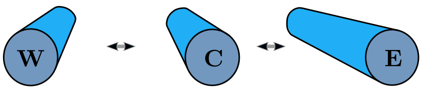

Figure 10.: Elementary architecture for the generation of nonadiabatic holonomies. The distances between the outer modes W and E, and the central one C determine the coupling.

obtains

$$U_A(C_\theta) = \begin{bmatrix} \cos\theta & -\sin\theta \\ -\sin\theta & -\cos\theta \end{bmatrix}. \tag{3.27}$$

It becomes evident that noncommuting holonomies can be engineered by traversing loops with different θ [60].

In principle, any coupling configuration $\kappa_k(z) \propto \Omega(z)$ that satisfies $\delta(z_\mathrm{f}) = \pi$ results in the same holonomy (3.27) as long as the weight θ remains fixed. For illustration, consider the one-parameter family of sine-like envelopes

$$\Omega_\omega(z) = \frac{\pi}{\Delta z} + K \sin\left(\frac{\omega z}{\Delta z}\right),$$

shown in Fig. 11. (a). Here, $\Delta z = z_\mathrm{f} - z_0 = 5\,\mathrm{cm}$ and $K = 0.15\,\mathrm{cm}^{-1}$ controls the strength of oscillation. For $\omega = m\pi$, with $m \in \mathbb{N}_0$, cyclicity is satisfied accurately, i.e., $\delta(z_\mathrm{f}) = \pi$. As ω deviates from these values, there is a mismatch at the end of the propagation, i.e., the states $|\psi_a(z)\rangle$ do not return to their initial configuration. Figure 11. (b) shows how this distortion manifest itself in a decreasing gate fidelity $\overline{F}(U_A(C_{\frac{\pi}{2}}), U_\omega)$ for a loop with $\theta = \pi/2$. Here, $U_\omega(z_\mathrm{f})$ is the time-evolution operator of the system with envelope Ω_ω. Note that large values of ω imply more rapid changes in the position of the outer waveguides W and E. Inevitably, this leads to a decrease of the fidelity. However, for $\omega \in [0, 4\pi]$ (Fig. 11) these losses are completely negligible. In Fig. 11. (b), one observes a plateau around $\omega = m\pi$. In other words slight distortions of the value of ω only alter the unitary $U_A(C)$ marginally. This is a direct manifestation of the holonomies intrinsic robustness[9] towards parametric noise.

Finally, some comparisons with the adiabatic construction from Sec. 3.1.3 might be appropriate. In both cases, a U(2) quantum holonomy was realised between the number states $|1_\mathrm{W}\rangle$ and $|1_\mathrm{E}\rangle$, but only in the nonadiabatic case is it possible to design noncommuting holonomies [compare Eqs. (3.5) and (3.27)]. The adiabatic construction relied on a loop in the parameter space of the tripod [Fig. 6. (a)], while the nonadiabatic holonomy (3.27) is the result of a loop in state space, and couplings (in principle) could even be constant $\Omega = \pi/z_\mathrm{f}$. The absence of light in the central mode is a measure of adiabaticity. Hence, the adiabatic holonomy, in good approximation, avoids population transfer to the central mode [128, P4]. In contrast, the nonadiabatic construction made use of the central waveguide as an ancilla. The ancilla is populated throughout the evolution but is not part of the final readout.

The experiments were conducted in fused-silica laser-written waveguides [P5]. A first loop $C_{\frac{\pi}{4}}$ was designed, resulitng in a unitary transformation

$$U_A(C_{\frac{\pi}{4}}) = \frac{1}{\sqrt{2}} \begin{bmatrix} 1 & -1 \\ -1 & -1 \end{bmatrix},$$

---

[9] It was shown in Ref. [63] that deviations in the fidelity are suppressed quadratically by the holonomy, i.e., $\overline{F}(U_A(C), U_\omega) \approx 1 - (\Delta\delta)^2/2$, where $\Delta\delta$ describes an imprecision in the cyclicity, that is $\delta(z_\mathrm{f}) = \pi + \Delta\delta$.

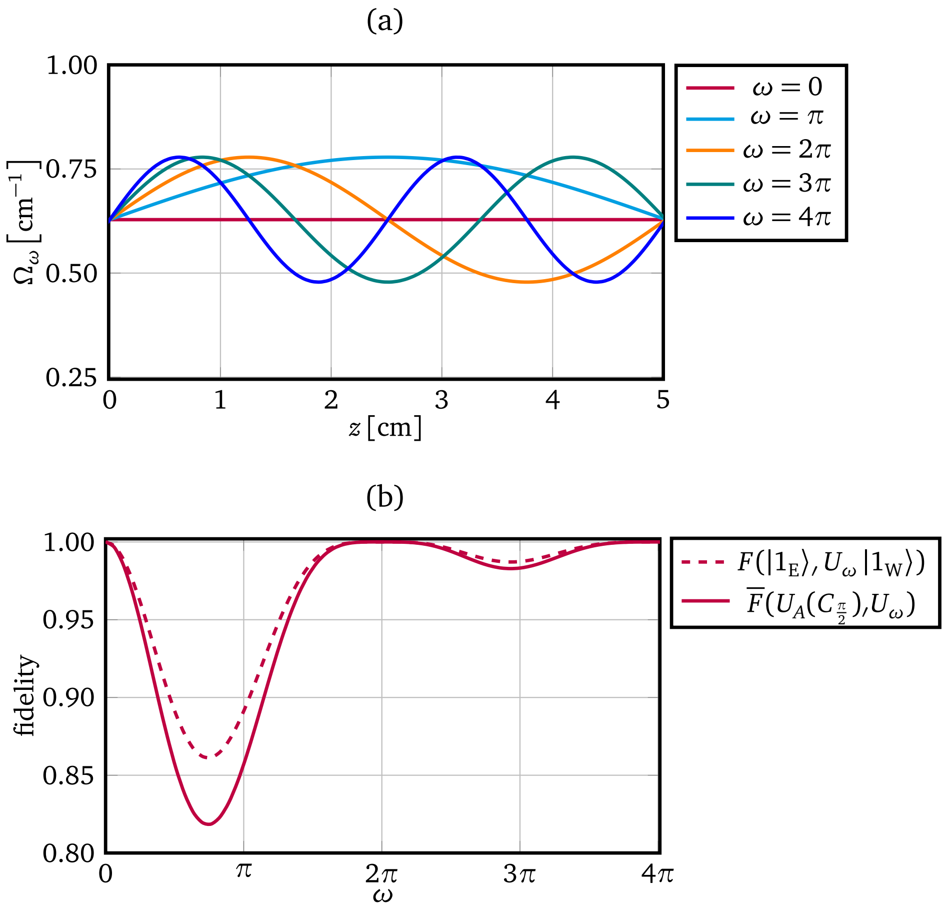

Figure 11.: (a) Coupling envelope $\Omega_\omega = \frac{\pi}{\Delta z} + K \sin\left(\frac{\omega z}{\Delta z}\right)$ with $\Delta z = 5\,\mathrm{cm}$ and $K = 0.15\,\mathrm{cm}^{-1}$, as a function of the propagation length z for various values of ω. (b) The expected fidelity between the holonomy $U_A(C_{\frac{\pi}{2}})$ and the noncyclic evolution U_ω as a function of the oscillation parameter ω. It was computed for an ensemble of input states $|1_{\mathrm{W}}\rangle$, $|1_{\mathrm{E}}\rangle$, and $|1_{\mathrm{C}}\rangle$. For the input state $|1_{\mathrm{W}}\rangle$, ideally transformed into $|1_{\mathrm{E}}\rangle$, the fidelity is shown as well (dashed line). For $\omega = 0, 2\pi, 4\pi$ cyclicity is satisfied accurately.

that creates a superposition between the outer modes. The envelope was designed using straight waveguides with a sine-like fanning at the beginning and the end of the 10 cm long glass chip, details in Ref. [P5]. Repeated single-photon measurements with input states $|1_{\mathrm{W}}\rangle$ and $|1_{\mathrm{E}}\rangle$ shows that the desired transformation is implemented with a fidelity $\overline{F} = 99.2\,\%$.

Next, the loop $C_{\frac{\pi}{2}}$ is implemented, using a similar design strategy on a 10 cm photonic chip. This results in a shift of a photon from the mode W to the mode E and vice versa, viz,

$$U_A(C_{\frac{\pi}{2}}) = \begin{bmatrix} 0 & -1 \\ -1 & 0 \end{bmatrix}.$$

The fidelity between our analytical calculation and the experimental evaluation amounts to $\overline{F} = 99.1\,\%$ In both experiments, photon loss as well as photon counts in the central mode were heralded, as these correspond to errors in the architecture which one can exclude by post processing.

3.3.2 Quantum photonic proposal for a U(5) holonomy

Utilising photonic systems for the construction of quantum holonomies has the distinct advantage that it allows, unlike atomic platforms, for multi-particle occupation of a single mode. This was already highlighted for the adiabatic case (Sec. 3.1.4). There, it resulted in a scaling of degeneracy, thus allowing for the implementation of more intriguing transformations. Here, I show how similar results hold true for nonadiabatic holonomies.

Consider a scenario in which two indistinguishable photons are subjected to the three-waveguide coupler. The Hamiltonian (3.25) has then to be evaluated on the two-photon Fock layer $\mathscr{F}_2$ spanned by the states

$$|1_\mathrm{W}1_\mathrm{C}\rangle\,,\quad |1_\mathrm{E}1_\mathrm{C}\rangle\,,\quad |2_\mathrm{W}\rangle\,,\quad |1_\mathrm{W}1_\mathrm{E}\rangle\,,\quad |2_\mathrm{E}\rangle\,,\quad |2_\mathrm{C}\rangle\,. \tag{3.28}$$

We are again seeking orthonormal states $|\psi_a(z)\rangle$ for which the condition $\langle H(z)\rangle_{\mathscr{H}_\psi} = 0$ holds. A careful analysis of the system reveals that there are five of those states. The first two states are just a copy of the single-photon states (3.26) but with an additional photon contained in the central mode, viz.

$$\begin{aligned}
|\psi_1(z)\rangle &= \hat{a}_\mathrm{C}^\dagger\,|d\rangle\,,\\
|\psi_2(z)\rangle &= \mathrm{e}^{\mathrm{i}\delta(z)}\big(\cos\delta(z)\hat{a}_\mathrm{C}^\dagger\,|b\rangle - \mathrm{i}\sqrt{2}\sin\delta(t)\,|2_\mathrm{C}\rangle\,\big).
\end{aligned}$$

The three remaining states have a more complicated form[10], that is

$$\begin{aligned}
|\psi_3(z)\rangle &= \kappa_\mathrm{W}^2\,|2_\mathrm{E}\rangle + \sqrt{2}\kappa_\mathrm{W}\kappa_\mathrm{E}\,|1_\mathrm{W}1_\mathrm{E}\rangle + \kappa_\mathrm{E}^2\,|2_\mathrm{W}\rangle\,,\\
|\psi_4(z)\rangle &= \mathrm{e}^{2\mathrm{i}\delta}\big[\cos^2\delta\big((\kappa_\mathrm{W})^2\,|2_\mathrm{W}\rangle + \sqrt{2}\kappa_\mathrm{W}\kappa_\mathrm{E}\,|1_\mathrm{W}1_\mathrm{E}\rangle + (\kappa_\mathrm{E}^*)^2\,|2_\mathrm{E}\rangle\,\big)\\
&\qquad - \sqrt{2}\mathrm{i}\sin\delta\cos\delta\big(\kappa_\mathrm{W}\,|1_\mathrm{W}1_\mathrm{C}\rangle + \kappa_\mathrm{E}\,|1_\mathrm{E}1_\mathrm{C}\rangle\,\big) - \sin^2\delta\,|2_\mathrm{C}\rangle\,\big],\\
|\psi_5(z)\rangle &= \kappa_\mathrm{W}\mathrm{e}^{\mathrm{i}\delta}\cos\delta\big(\kappa_\mathrm{W}\,|1_\mathrm{W}1_\mathrm{E}\rangle + \sqrt{2}\kappa_\mathrm{E}\,|2_\mathrm{E}\rangle\,\big) - \mathrm{i}\kappa_\mathrm{W}\mathrm{e}^{\mathrm{i}\delta}\sin\delta\,|1_\mathrm{E}1_\mathrm{C}\rangle\\
&\qquad - \kappa_\mathrm{E}\mathrm{e}^{\mathrm{i}\delta}\cos\delta\big(\kappa_\mathrm{E}\,|1_\mathrm{W}1_\mathrm{E}\rangle + \sqrt{2}\kappa_\mathrm{W}\,|2_\mathrm{W}\rangle\,\big) + \mathrm{i}\kappa_\mathrm{E}\mathrm{e}^{\mathrm{i}\delta}\sin\delta\,|1_\mathrm{W}1_\mathrm{C}\rangle\,.
\end{aligned}$$

The above states all satisfy the condition $\langle H\rangle_{\mathscr{H}_\psi} = 0$, while evolving cyclically with $\delta(z_\mathrm{f}) = \pi$ as well, thus rendering the generation of a quantum holonomy possible. It becomes a simple exercise to determine the connection. Its only nonvanishing components are $(A_z)_{22} = \mathrm{i}\Omega(z)$ and $(A_z)_{55} = \mathrm{i}\Omega(z)$. Subsequently, the quantum holonomy has a matrix representation $U_A(C_\theta) = \mathrm{diag}(1,-1,1,1,-1)$ with respect to the basis $\{|\psi_a(z_\mathrm{f})\rangle\}_a$. In order to highlight the photonic population transfer that can be achieved by the holonomy, it is useful to transform into the photon-number basis (3.28) (the state $|2_{\mathrm{C}}\rangle$ is not part of $\mathscr{H}_\psi$ at z_{f})

---

[10] In Sec. 3.5, I will provide an explicit recipe on how to construct these states. For the moment, the reader might be satisfied with the fact that these states satisfy all conditions for a holonomic evolution.

$$U_A(C_\theta) = \begin{bmatrix} -\cos\theta & \sin\theta & 0 & 0 & 0 \\ \sin\theta & \cos\theta & 0 & 0 & 0 \\ 0 & 0 & \cos^2\theta & \sin^2\theta & \frac{1}{\sqrt{2}}\sin(2\theta) \\ 0 & 0 & \sin^2\theta & \cos^2\theta & -\frac{1}{\sqrt{2}}\sin(2\theta) \\ 0 & 0 & \frac{1}{\sqrt{2}}\sin(2\theta) & -\frac{1}{\sqrt{2}}\sin(2\theta) & -\cos(2\theta) \end{bmatrix}. \tag{3.29}$$

The quantum holonomy reveals a block structure belonging to the group $\mathrm{U}(2)\oplus\mathrm{U}(3)$, which is a proper subgroup of $\mathrm{U}(5)$. While the 2×2 submatrix can create mixing between the number states $|1_{\mathrm{W}}1_{\mathrm{C}}\rangle$ and $|1_{\mathrm{E}}1_{\mathrm{C}}\rangle$, the lower block acts on the states $|2_{\mathrm{W}}\rangle$, $|1_{\mathrm{W}}1_{\mathrm{E}}\rangle$, and $|2_{\mathrm{E}}\rangle$.

3.4 Geometric Aspects of Quantum Holonomies

In quantum field theories, gauge potentials originate from internal symmetries of charge spaces as well as conservation laws [99], and at first sight it seems surprising that similar behaviour emerges from the (e.g., adiabatic) evolution of a generic quantum system.

This is due to the reason that all of physics underlies a deep geometric framework that might be divided loosely in two aspects: a local or infinitesimal aspect, and a global aspect. Much of the physicists standard lore deals with this *perturbative aspect*, for which the choice of local coordinates dismisses much of the beautiful global structure. The study of this *non-perturbative aspect* demands for a coordinate-free formulation of the laws of Nature. In this picture, all the relevant physics is encapsulated in an abstract form of *parallel transport* on a *principal fibre bundle*. Indeed, the notion of a gauge potential cannot even be made precise without referring to a *local connection one-form* on this principal fibre bundle.

3.4.1 Parallel transport in the Grassmann manifold

As a review of the full theory of fibre bundles is beyond the scope of this thesis, the general construction will be illustrated via the parallel transport of a quantum state. Consider a generic Hamiltonian $H(t)$ acting on an N-dimensional Hilbert space $\mathscr{H}$ (N might be infinite). A time evolution of a d-dimensional subspace $\mathscr{H}_\psi$ can then be associated with a curve taken by the projector $\Pi_\psi(t)$ onto $\mathscr{H}_\psi$. The mapping $\Pi_\psi \to (|\psi_a\rangle)_{a=1}^d$ onto a basis of $\mathscr{H}_\psi$, constitutes a (so-called) section of the bundle

$$\mathscr{V}_{N,d} \xrightarrow{\pi} \mathscr{G}_{N,d}.$$

This $\mathrm{U}(d)$-principal bundle consists of the base space

$$\mathscr{G}_{N,d} = \left\{\Pi_\psi : \mathscr{H} \to \mathscr{H} \,\middle|\, \Pi_\psi^2 = \Pi_\psi,\ \mathrm{Tr}\{\Pi_\psi\} = d\right\}$$

known as the Grassmann manifold $\mathscr{G}_{N,d}$, the total space

$$\mathscr{V}_{N,d} = \left\{(|\psi_a\rangle)_{a=1}^d \in \mathscr{H}_\psi \times \cdots \times \mathscr{H}_\psi \,\middle|\, \langle\psi_b|\psi_a\rangle = \delta_{ab}\right\}$$

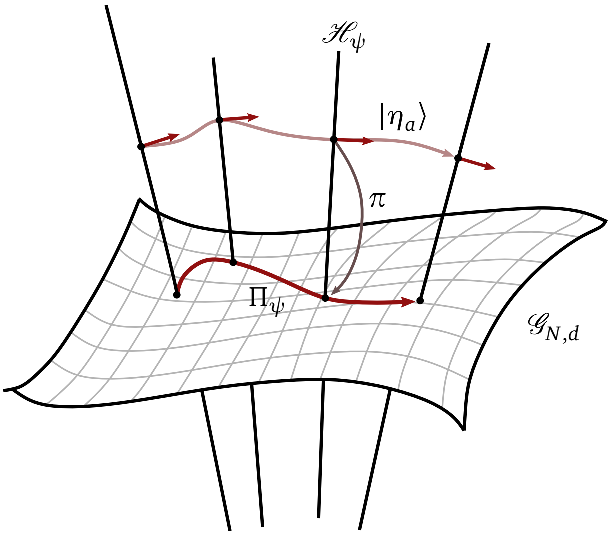

Figure 12.: Parallel transport of a state vector $|\eta_a\rangle$ in the U(d)-principal bundle $\mathscr{V}_{N,d} \to \mathscr{G}_{N,d}$. A curve Π_ψ in the Grassmann manifold is lifted horizontally into the Stiefel manifold. At every point in the base space the tangent vector of the lift is orthogonal to the fibre $\mathscr{H}_\psi$ (preimage of π).

called the Stiefel manifold $\mathscr{V}_{N,d}$, and a (surjective) bundle map $\pi : (|\psi_a\rangle)_a \mapsto \Pi_\psi$. By definition, this map is invariant under a (unitary) change of the section, i.e., both $(|\psi_a\rangle)_a$ and $(g\,|\psi_a\rangle)_a$ are projected onto the same subspace $\mathscr{H}_\psi$, for arbitrary $g \in \mathrm{U}(d)$. The set of possible orthonormal frames

$$\mathscr{H}_\psi = \left\{ (g\,|\psi_a\rangle)_{a=1}^{d} \,\middle|\, g \in \mathrm{U}(d) \right\}$$

is said to be the (typical) fibre at the point Π_ψ in $\mathscr{G}_{N,d}$. It is the preimage of the bundle map π at the point Π_ψ.

A section introduces a natural way to lift the curve $\Pi_\psi(t)$ from the base space into the total space of the bundle (Fig. 13). By definition, a curve $(|\eta_a(t)\rangle)_{a=1}^{d} \in \mathscr{V}_{N,d}$ is known as the horizontal lift of $\Pi_\psi(t) \in \mathscr{G}_{N,d}$ if its tangent vector is orthogonal to the fibre at each point. A natural way to introduce orthogonal directions in this bundle is given through the inner product[11], i.e., $\langle\psi_b|\,\nabla_t\,|\eta_a\rangle = 0$ for each $a = 1, \ldots, d$. Then the state $|\eta_a(t)\rangle$ is said to be parallely transported along the curve $\Pi_\psi(t)$. The covariant derivative acts on a quantum state according to $\nabla_t\,|\eta_a\rangle = \partial_t\,|\eta_a\rangle + A_t\,|\eta_a\rangle$, where A_t is the local connection one-form of the principal fibre bundle. Expressing the parallely transported state $|\eta_a(t)\rangle$ through the local frame $(|\psi_a(t)\rangle)_a$ yields

$$\langle\psi_b|\,\partial_t\,|\psi_a\rangle + \langle\psi_b|A_t\,|\psi_a\rangle = 0,$$

---

[11] Because each fibre $\mathscr{H}_\psi$ constitutes a vector space equipped with an inner product, the triple $\mathscr{V}_{N,d} \to \mathscr{G}_{N,d}$ is also known as a Hermitian vector bundle [121].

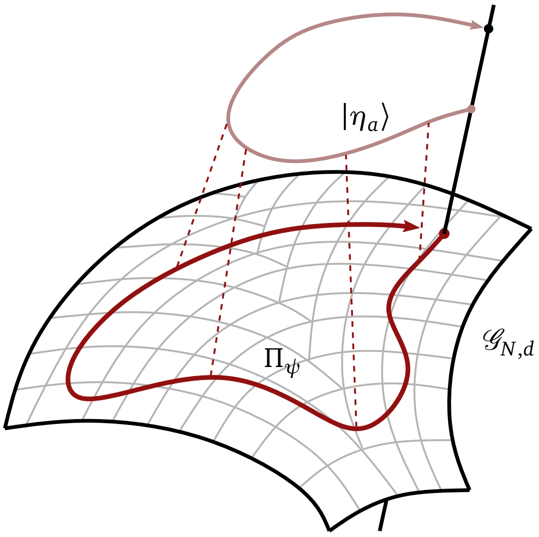

Figure 13.: Parallel transport of a state vector $|\eta_a\rangle$ along a loop Π_ψ in the Grassmann manifold $\mathscr{G}_{N,d}$. At the end of evolution, the horizontal lift $|\eta_a\rangle$ experiences a unitary shift in the fibre, that is precisely the quantum holonomy.

due to linearity. The connection $(A_t)_{ba} = -\langle\psi_b|\,\partial_t\,|\psi_a\rangle$ lies in the space of anti-Hermitian matrices. In a U(d)-principal bundle, a change of the section can always be expressed through the (unitary) action $g \in \mathrm{U}(d)$ onto the fibre $\mathscr{H}_\psi$.

A transition to the section $\Pi_\psi \mapsto (g\,|\psi_a\rangle)_a$, manifests itself in the connection as $A_t^g = gA_tg^\dagger - g\partial_t g^\dagger$. In this light, a gauge transformation is just a change of the local section. Notice that the parallel transport condition is equivalent to the disappearance of the Hamiltonian on the subspace $\mathscr{H}_\psi$, i.e., $\langle H(t)\rangle_{\mathscr{H}_\psi} = 0$. Indeed, this is nothing but the condition for a purely geometric evolution of a quantum state.

If $\Pi_\psi(t)$ forms a loop in the Grassmann manifold $\mathscr{G}_{N,d}$, i.e., $\Pi_\psi(0) = \Pi_\psi(T)$, its horizontal lift $|\eta_a(t)\rangle$ starts and ends in the same fibre (Fig. 13), but is shifted by a quantum holonomy belonging to the symmetry group U(d). If $d = 1$, we recover an Abelian (Berry or Anandan) phase as the holonomy of a U(1)-principal bundle. In this setting, the Grassmann manifold $\mathscr{G}_{N,1}$ reduces to the projective Hilbert space containing rank-one projectors [59].

Expressing the Hamiltonian H through local coordinates $\boldsymbol{\kappa} = (\kappa_\mu)_\mu$ on a smooth manifold $\mathscr{M}$, a loop in the Grassmann manifold $\mathscr{G}_{N,d}$ is mapped onto a curve in $\mathscr{M}$. Notice that if $\mathscr{H}_\psi = \mathscr{H}_0$ is the dark subspace of the Hamiltonian H, the parallel transport condition is equivalent to the adiabatic limit, and cyclicity of the dark states implies a closed loop in $\mathscr{M}$. The map $\Phi : \boldsymbol{\kappa} \mapsto \Pi_0(\boldsymbol{\kappa})$ maps points in the manifold $\mathscr{M}$ onto dark subspace projectors. A realistic quantum system is expected to have a smaller control manifold then the entire Grassmann manifold, i.e., Φ is generally not surjective. Parallel transport then has to be studied in the so-called pull-back bundle $\Phi^*\mathscr{V}_{N,d} \to \mathscr{M}$, where the total space is defined as

$$\Phi^*\mathscr{V}_{N,d} = \left\{ (|\psi_a(\boldsymbol{\kappa})\rangle)_{a=1}^d \in \mathscr{V}_{N,d} \,\middle|\, \boldsymbol{\kappa} \in \mathscr{M} \right\}.$$

For additional details, the reader might refer to Ref. [122].

3.5 Operator Formulation of Quantum Holonomies

The calculation of adiabatic and nonadiabatic quantum holonomies in systems of coupled waveguides becomes increasingly difficult when more photons participate in the propagation. This is due to the fact that the N-photon subspace of an M-mode network supports $(N+M-1)!/(N!(M-1)!)$ different Fock states. In addition, the N-photon eigenstates of a system generically take a more complicated form as N increases. The explicit form of the latter has to be known in order to calculate the holonomy on a subspace. Similar problems arise in the nonadiabatic scenario, where the identification of all multi-photon states satisfying the condition $\langle H \rangle_{\mathscr{H}_\psi} = 0$ [see Eq. (3.23)], is at first sight, a daunting task.

The problem can be overcome by referring to an operator formalism for a photon-number independent treatment of quantum holonomies in bosonic systems [P6]. The basic idea is to describe the holonomic evolution in the Heisenberg picture, instead of working in the Schrödinger picture as the literature on geometric phases suggests [138]. This leads to the technical difficulty that conditions such as adiabaticity and cyclicity, must be translated into the Heisenberg picture. The representation of (Abelian) Berry phases in an adiabatic Heisenberg picture was developed first in Ref. [139], where it was applied to the dynamics of a spin-$\frac{1}{2}$ particle in a magnetic field. The operator framework developed in Ref. [P6] can be seen as a generalisation of this approach to non-Abelian and nonadiabatic quantum holonomies. Besides offering a major computational advantage over the standard formalism, it also provides deeper insight into the emergence of geometric phases in second quantisation.

3.5.1 Holonomies in the Heisenberg picture

Consider a Hamiltonian $H(t)$ associated with a bosonic quantum system. Suppose preparation and evolution is such that a quantum state $|\Psi(t)\rangle$ resides in the subspace $\mathscr{H}_\psi$, on which the Hamiltonian's dynamics complete disappear, i.e., $\langle H \rangle_{\mathscr{H}_\psi} = 0$. This forms a valid condition for parallel transport of quantum states and in particular, describes adiabatic holonomies as a special case as well. For concreteness, if $\mathscr{H}_\psi$ is the dark subspace of a quantum system, the condition $\langle H \rangle_{\mathscr{H}_\psi} = 0$ is satisfied whenever the adiabatic limit is applicable [52]. On the other hand, if $\mathscr{H}_\psi$ is given by some time-dependent basis for which the mean energy vanishes, this describes nonadiabatic parallel transport [54].

The reader should note that the above (standard) formalism is naturally based on the Schrödinger picture, as it revolves around the time-dependent states $\{|\psi_a(t)\rangle\}_a$ spanning the subspace $\mathscr{H}_\psi$, e.g., the dark states in an adiabatic setting. While there is no natural translation of the adiabatic limit into the Heisenberg picture, in order for expectation values to coincide on the subspace $\mathscr{H}_\psi$, any mode $\hat{a}_k$ must evolve according to $\hat{a}_k \mapsto U_A^\dagger(C)\hat{a}_k U_A(C)$, where $U_A(C)$ is the (adiabatic or nonadiabatic) quantum holonomy of the loop C taken by the subspace $\mathscr{H}_\psi$ through state space the Grassmann manifold. This implies that the Heisenberg equations of motion for a purely holonomic evolution read [P6]

$$\langle \dot{\hat{a}}_k \rangle_{\mathscr{H}_\psi} = \langle [\hat{a}_k, A_t(C)] \rangle_{\mathscr{H}_\psi} + \langle \partial_t \hat{a}_k \rangle_{\mathscr{H}_\psi}, \tag{3.30}$$

which means that the generator of the evolution is now given by a connection $A_t(C) = U_A^\dagger(C) A_t U_A(C)$ instead of the Hamiltonian [P6]. Once Eq. (3.30) is solved, the parallel transport of any (analytical) function $F(\hat{a}_k, \hat{a}_k^\dagger)$ can be written down explicitly.

3.5.1.1 *Adiabatic propagation through a nonlinear Kerr medium*

As a first example, consider the adiabatic propagation through the zero-eigenvalue eigenspace $\mathscr{H}_0$ (spanned by $|0\rangle$ and $|1\rangle$) of a single-mode Kerr medium [137]

$$\mathcal{V}(\alpha, \xi) H_0 \mathcal{V}^\dagger(\alpha, \xi),$$

with $H_0 = \hat{n}(\hat{n} - 1)$ and $\mathcal{V}(\alpha, \xi) = D(\alpha) S(\xi)$ describing the combined process of coherent displacement and single-mode squeezing [cf. Eqs. (3.19) and (3.20)]. The parallel transport of $\hat{a}(t)$ is governed by the connection

$$A_t = \Pi_0 \mathcal{V}^\dagger(\alpha, \xi) \partial_t \mathcal{V}(\alpha, \xi) \Pi_0,$$

with $\Pi_0 = |0\rangle\langle 0| + |1\rangle\langle 1|$ projecting onto the subspace $\mathscr{H}_0$. An evaluation of Eq. (3.30) leads to nonlinear equations of adiabatic motion [P6]

$$\langle \dot{\hat{a}} \rangle_{\mathscr{H}_0} = (\dot{\alpha}^* \alpha - \dot{\alpha} \alpha^*) \langle \hat{a} \rangle_{\mathscr{H}_0} + \dot{\alpha}(\mu - \nu^*) \langle \hat{a}^\dagger \hat{a} \rangle_{\mathscr{H}_0} - \text{c.c.},$$

where $\mu = \cosh|\xi|$ and $\nu = \mathrm{e}^{\mathrm{i}\arg(\xi)} \sinh|\xi|$.

The emergence of nonlinear equations of motion is a generic feature of the operator description of parallel transport, both adiabatic and nonadiabatic. This is due to the connection $A = \Pi_\psi \mathrm{d}\Pi_\psi$ requiring the computation of subspace projectors Π_ψ onto $\mathscr{H}_\psi$. In the above example, we had $\Pi_\psi = \mathcal{V}\Pi_0$ and $\mathrm{d} = \partial_t(\cdot)\mathrm{d}t$. Due to the generally highly nonlinear form of these projectors in terms of bosonic modes, the computation of quantum holonomies can be an extremely challenging task in this picture [P6].

3.5.2 Linear quantum optics

The general concepts described thus far can, in principle, be applied to any bosonic system. In the following, it will be shown that in a linear optical setting, that is the Hamiltonian $H(t)$ describes a collection of harmonic oscillators [cf. Eq. (2.12)], certain symmetries arise that offer a deeper insight into the emergence of geometric phases. Consider a system of M bosonic modes that interact according to such a (bilinear) Hamiltonian. Suppose further that there is a set of orthonormal modes $\{\hat{\Psi}_k^\dagger(t)\}_{k=1,}^d$ whose excitations (action onto the vacuum state) span a subspace $\mathscr{H}_\psi = \{|\psi_a\rangle \,|\, a \in \mathbb{N}\}$ on which the mean energy of the Hamiltonian H vanishes. In Appendix A.3.1, it is show that the second-quantisation formulation of the (classical) condition $\langle H(t) \rangle_{\mathscr{H}_\psi} = 0$ is given as

$$[\hat{\Psi}_j(t), [H(t), \hat{\Psi}_k^\dagger(t)]] = 0. \tag{3.31}$$

Indeed, this implies $\langle \psi_a | H | \psi_b \rangle = 0$ for any state in $\mathscr{H}_\psi$, thus ensuring that the evolution is of purely geometric origin. Consider d orthonormal modes $\hat{\eta}_k^\dagger(t)$, which evolve in the presence of H. Hence, they must satisfy the Heisenberg equation of motion. With the ansatz $\hat{\eta}_k^\dagger(t) = \sum_j \mathcal{U}_{jk}(t)\hat{\Psi}_j^\dagger(t)$ and the condition for parallel transport (3.31), this yields

$$0 = [\hat{\eta}_j, \dot{\hat{\eta}}_k^\dagger] = \sum_{l=1}^{d} \mathcal{U}_{lj}^* \partial_t \mathcal{U}_{lk} + \sum_{l,m=1}^{d} \mathcal{U}_{lj}^* \mathcal{U}_{mk} \, (\mathcal{A}_t)_{ml}\,, \tag{3.32}$$

where $(\mathcal{A}_t)_{jk} = [\hat{\Psi}_k, \partial_t \hat{\Psi}_j^\dagger]$ denotes the operator-valued connection. If we now consider a cyclic evolution of the system, i.e., $\hat{\Psi}_k^\dagger(0) = \hat{\Psi}_k^\dagger(T)$ so that the modes undergo a loop C, the solution to Eq. (3.32) is a path-ordered integral superoperator [P6]

$$\mathcal{U}_C = \hat{\mathbf{P}} \exp \oint_C \mathcal{A}.$$

Now, the time evolution of a mode $\hat{\eta}_k^\dagger$ is given by the mapping $\hat{\eta}_k^\dagger(T) = \mathcal{U}_C[\hat{\eta}_k^\dagger(0)]$.

Strikingly, in this formulation one avoids the usage of projectors onto the relevant subspace altogether, thereby drastically simplifying the computational effort needed to determine the geometric evolution. Starting at a point where $\hat{\eta}_k^\dagger(0) = \hat{a}_k^\dagger$, it becomes evident that $\mathcal{U}_C$ can be viewed as the transfer matrix of the linear optical network being restricted to purely holonomic transfer of light between the bosonic modes. The remaining $M - d$ modes act either as ancillas for the purely geometric evolution, or create excitations in an unrelated subspace. The result can be linked to the standard formalism on geometric phases [52, 54] by noting that $\mathcal{U}_C[\hat{a}_k^\dagger] = U_A^\dagger(C)\hat{a}_k^\dagger U_A(C)$, with $U_A(C) = \hat{\mathbf{P}}\exp\oint_C A$ being the more familiar form of the holonomy. In contrast to a nonlinear optical setting, here the projection onto the relevant subspace is incorporated implicitly into the connection, thus providing an elegant photon-number independent description.

3.5.2.1 *Adiabatic propagation through the star graph*

Consider M bosonic modes being arranged as a star graph (Fig. 7), i.e. its Hamiltonian reads

$$H(z) = \sum_{k=1}^{M-1} \left(\kappa_k(z)\hat{a}_k\hat{a}_M^\dagger + \kappa_k^*(z)\hat{a}_k^\dagger\hat{a}_M \right),$$

where the couplings $\{\kappa_k\}_k$ act as local coordinates for a parameter space $\mathscr{M}$. The system has $M - 2$ (not yet orthonormal) dark modes

$$\hat{D}_j^\dagger(z) = \kappa_{j+1}(z)\hat{a}_1^\dagger - \kappa_1(z)\hat{a}_{j+1}^\dagger.$$

These operators satisfy the quantised eigenvalue problem $[H, \hat{D}_j^\dagger] = 0$. Moreover, they obey bosonic commutation relations $[\hat{D}_j, \hat{D}_k] = [\hat{D}_j^\dagger, \hat{D}_k^\dagger] = 0$ and $[\hat{D}_j, \hat{D}_k^\dagger] = \delta_{jk}$, after being orthogonalised. The above considerations make it natural to impose a second-quantisation version of the adiabatic theorem [P6], to which the proof can be found in Appendix A.3.2.

Theorem: *In the adiabatic limit, any initial preparation $\hat{\eta}_a(0)$ lying in a space spanned by a collection of (non-)degenerate eigenmodes $\{\hat{\Psi}_j(t)\}_j$ will evolve into a final operator $\hat{\eta}_a(T)$ residing in this space.*

In our case, the initial preparation $\hat{D}_j^\dagger(z_0)$ has to reside in the linear span of the modes $\{\hat{D}_j^\dagger(z)\}_{j=1}^{M-2}$ throughout the propagation. The dark modes evolve according to the holonomy $\mathcal{U}_C$ governed by the adiabatic connection

$$\left(\mathcal{A}_\mu\right)_{jk} = [\hat{D}_k, \partial_\mu \hat{D}_j^\dagger]$$

that constitutes the operator-valued counterpart of the adiabatic connection [52] (Sec. 3.1).

In Ref. [P6], it was shown that the connection $\mathcal{A}$ is irreducible[12]. Hence, $\mathrm{Hol}(\mathcal{A})$ coincides with the entire unitary group $\mathrm{U}(M-2)$. More specifically, starting the holonomy at an initial point $\boldsymbol{\kappa}_0 = (0,\dots,0,\kappa)$ shows that any transformation $\mathcal{U}_C[\hat{D}_k^\dagger(\boldsymbol{\kappa}_0)] = \mathcal{U}_C[\hat{a}_k^\dagger]$ can be implemented holonomically by designing a suitable loop in $\mathscr{M}$. This means that, due to the composition of loops $\mathcal{U}_{\prod_a C_a} = \prod_a \mathcal{U}_{C_a}$, any linear optical network can be made geometrically robust by supporting it with two auxiliary modes $\hat{a}_{M-1}$ and $\hat{a}_M$, while adiabatically traversing a closed path C in $\mathscr{M}$.

The above formulation can be linked to the standard formalism on adiabatic holonomies [P1]. Excitations of the dark modes produce dark states

$$|D_{\boldsymbol{n}}\rangle = \prod_{j=1}^{M-2} \frac{1}{\sqrt{n_j!}} \left(\hat{D}_j^\dagger\right)^{n_j} |\boldsymbol{0}\rangle$$

sharing an adiabatic subspace $\mathscr{H}_0$. However, these dark modes are not the only ones creating new dark states. Additionally, the Hamiltonian gives rise to nondegenerate bright modes

$$\hat{B}_\pm^\dagger(z) = \frac{1}{\sqrt{2}\varepsilon} \sum_{j=1}^{M-1} \kappa_j^*(z) \hat{a}_j^\dagger \pm \frac{1}{\sqrt{2}} \hat{a}_M^\dagger,$$

---

[12] The proof goes as follows. First, concentrate on loops on a submanifold of $\mathscr{M}$: $\kappa_1 = \kappa \cos\theta \sin\vartheta \mathrm{e}^{\mathrm{i}\varphi}$, $\kappa_2 = \kappa \sin\theta \sin\vartheta \mathrm{e}^{\mathrm{i}\varphi}$, $\kappa_3 = \kappa\cos\vartheta$, while $\kappa_4 = \dots = \kappa_{M-1} = 0$. Accordingly, the dark modes simplify to

$$\hat{D}_1^\dagger = \sin\theta\, \hat{a}_1^\dagger - \cos\theta\, \hat{a}_2^\dagger,\ \ \hat{D}_2^\dagger = \cos\vartheta \cos\theta\, \hat{a}_1^\dagger + \cos\vartheta \sin\theta\, \hat{a}_2^\dagger - \sin\vartheta \mathrm{e}^{\mathrm{i}\varphi}\, \hat{a}_3^\dagger,\ \ \hat{D}_3^\dagger = \hat{a}_4^\dagger,\ \ \dots\ \ \hat{D}_{M-2}^\dagger = \hat{a}_{M-1}^\dagger.$$

In this case the connection is readily calculated to

$$\mathcal{A}_\theta = \begin{bmatrix} 0 & \cos\vartheta \\ -\cos\vartheta & 0 \end{bmatrix}, \qquad \mathcal{A}_\varphi = \begin{bmatrix} 0 & 0 \\ 0 & \mathrm{i}\sin^2\vartheta \end{bmatrix}.$$

The noncommuting components of the connection allow one to generate any unitary transformation $\mathcal{U}_C$ between the modes $\hat{a}_1^\dagger$ and $\hat{a}_2^\dagger$ at the base point $(\theta,\vartheta) = (\pi/2, 0)$, see Ref. [P6] for additional details. Because the chosen submanifold was arbitrary, the argument can be repeated for any pair $\hat{a}_j$ and $\hat{a}_k$ of modes in the star graph, for $j,k \neq M-2, M-1$. It follows that any unitary $(M-2)\times(M-2)$ matrix $\mathcal{U}_{\prod_a C_a}$ can be realised by a sequence of two-mode transformations $\mathcal{U}_{C_a}$, cf. Reck *et al.* [140]. ■

where $\varepsilon = (\sum_j |\kappa_j|^2)^{1/2}$. They satisfy the (quantised) eigenvalue problem $[H, \hat{B}_\pm^\dagger] = \pm\varepsilon\hat{B}_\pm^\dagger$.

The time-evolution of the entire system is a composition of holonomies

$$\mathrm{e}^{\mathrm{i}\int_0^T \varepsilon(t)\mathrm{d}t}\,\mathcal{U}_{+,C} \oplus \mathcal{U}_{0,C} \oplus \mathrm{e}^{-\mathrm{i}\int_0^T \varepsilon(t)\mathrm{d}t}\,\mathcal{U}_{-,C},$$

where the Abelian holonomies $\mathcal{U}_{\pm,C}$ manifest themselves in the bright modes and $\mathcal{U}_{0,C}$ acts on the dark modes.

For photon numbers $N \geq 2$, there exist combinations of $\hat{B}_+^\dagger$ and $\hat{B}_-^\dagger$ that produce additional dark states. The entire dark subspace $\mathscr{H}_0$ can be generated from combined excitations of dark and bright modes. More explicitly, any function of the form

$$F(\hat{a}_k, \hat{a}_k^\dagger) = \sum_{\boldsymbol{n}\in\mathbb{N}_0^{M-1}} c_{n_1\ldots n_{M-1}} \frac{\left(\hat{D}_1^\dagger\right)^{n_1}}{\sqrt{n_1!}} \frac{\left(\hat{D}_2^\dagger\right)^{n_2}}{\sqrt{n_2!}} \cdots \frac{\left(\hat{B}_+^\dagger\hat{B}_-^\dagger\right)^{n_{M-1}}}{\sqrt{n_{M-1}!}},$$

by construction, produces an eigenstate $F(\hat{a}_k, \hat{a}_k^\dagger)\,|\boldsymbol{0}\rangle \in \mathscr{H}_0$ with energy zero.

For the sake of simplicity, consider the tripod arrangement of bosonic modes, that is the star graph for $M = 4$, into which a single photon is injected (i.e., $N = 1$). Then, one has the two dark states $|d_1\rangle = \hat{D}_1^\dagger\,|\boldsymbol{0}\rangle$ and $|d_2\rangle = \hat{D}_2^\dagger\,|\boldsymbol{0}\rangle$, whose evolution is determined by the holonomy $\mathcal{U}_{0,C}$. If one considers two photons in the setup (i.e., $N = 2$), then there are three dark states

$$|D_1\rangle = \frac{1}{\sqrt{2}}\left(\hat{D}_1^\dagger\right)^2|\boldsymbol{0}\rangle, \qquad |D_2\rangle = \hat{D}_1^\dagger\hat{D}_2^\dagger\,|\boldsymbol{0}\rangle, \qquad |D_3\rangle = \frac{1}{\sqrt{2}}\left(\hat{D}_2^\dagger\right)^2|\boldsymbol{0}\rangle.$$

Moreover, because of $[H, \hat{B}_\pm^\dagger] = \pm\varepsilon\hat{B}_\pm^\dagger$, the positive and negative eigenenergies cancel one another out in the case of simultaneous excitation of $\hat{B}_+$ and $\hat{B}_-$. Therefore, $|D_4\rangle = \hat{B}_+^\dagger\hat{B}_-^\dagger\,|\boldsymbol{0}\rangle$ is another dark state which, however, only attains a (scalar) Berry phase (due to $\mathcal{U}_{\pm,C}$) while evolving adiabatically. Thus, despite the fact that $\{|D_j\rangle\}_j$ span a common eigenspace, $|D_4\rangle$ evolves separately. This is the origin of block structure in the holonomy (3.7) in which $|D_4\rangle$ does not couple to the other eigenstates [132, P1, P6]. It can be concluded that demanding the eigenmodes (rather than the eigenstates) to evolve adiabatically explains (in contrast to the original formulation of the adiabatic theorem [115]) why there are eigenstates in $\mathscr{H}_0$ that do not couple to the other eigenstates in $\mathscr{H}_0$. This phenomenon was already observed in Refs. [132, 134] but remained unexplained until the formal treatment in Ref. [P6].

3.5.2.2 *Influence of nonorthogonal modes*

So far, our attention was restricted to benchmark systems for which transverse mode overlap could be neglected. For these linear optical networks, bosonic modes could be identified easily as the spatial modes associated with each individual waveguide. However, if these systems are studied in the strong-coupling regime, i.e., the waveguides are fairly close to each other, the orthogonality condition is no longer valid, as the overlap of transverse modes becomes relevant. A canonical quantisation of such systems is then carried out by promoting its normal modes to Hilbert-space operators, rather than the waveguide modes (see Chapter II). In general, nonorthogonality of transverse modes can be a problem, because additional contributions to the off-diagonal elements of a coupling matrix can lift degeneracy. The latter being a precondition for the generation of adiabatic holonomies.

For the sake of concreteness, the star graph arrangement of bosonic modes will serve as a sufficient benchmark. Its (classical) coupling matrix reads

$$\mathbf{K}=\begin{bmatrix} 0 & \dots & 0 & \kappa_1^* \\ \vdots & \ddots & & \vdots \\ 0 & & \ddots & \kappa_{M-1}^* \\ \kappa_1 & \dots & \kappa_{M-1} & 0 \end{bmatrix}.$$

Because the modes $\hat{\boldsymbol{a}}=(\hat{a}_k)_k$ have nonnegligible mode overlap, the operator $\hat{\boldsymbol{a}}^\dagger\mathbf{K}\hat{\boldsymbol{a}}$ is not Hermitian anymore and can therefore not act as the Hamiltonian of the system. Following Sec. 2.2, a Hamiltonian can be constructed with the help of the power matrix

$$\boldsymbol{\Sigma}=\begin{bmatrix} 1 & 0 & \dots & 0 & \sigma_1^* \\ 0 & \ddots & & & \vdots \\ \vdots & & \ddots & & \vdots \\ 0 & & & \ddots & \sigma_{M-1}^* \\ \sigma_1 & \dots & \dots & \sigma_{M-1} & 1 \end{bmatrix}.$$

A transformation between the waveguide and normal modes can be obtained from a Cholesky factorisation $\boldsymbol{\Sigma}=\left(\mathbf{Q}^{\mathrm{T}}\right)^*\mathbf{Q}$, where

$$\mathbf{Q}=\begin{bmatrix} 1 & 0 & \dots & 0 & \sigma_1 \\ 0 & \ddots & & & \vdots \\ \vdots & & \ddots & & \vdots \\ \vdots & & & 1 & \sigma_{M-1} \\ 0 & \dots & \dots & 0 & \sqrt{1-|\boldsymbol{\sigma}|^2} \end{bmatrix}.$$

Here, $\boldsymbol{\sigma}=(\sigma_j)_{j=1}^{M-1}$ was defined. From the matrix $\mathbf{Q}$ one can compute the Hermitian generator for the evolution of normal modes from Eq. (2.9). One finds

$$\mathbf{H}=\begin{bmatrix} 0 & \dots & 0 & s\kappa_1^* \\ \vdots & \ddots & & \vdots \\ 0 & & \ddots & s\kappa_{M-1}^* \\ s\kappa_1 & \dots & s\kappa_{M-1} & -2s^2\boldsymbol{\sigma}\cdot\boldsymbol{\kappa} \end{bmatrix},$$

with a scaling $s=1/\sqrt{1-|\boldsymbol{\sigma}|^2}$. The Hamiltonian governing the propagation of photons through the photonic network is given by the Hermitian operator $H=\hat{\boldsymbol{b}}^\dagger\mathbf{H}\hat{\boldsymbol{b}}$.

Remarkably, the difference between the Hamiltonian matrix $\mathbf{H}$ and the coupling matrix $\mathbf{K}$ is marginal, i.e., up to the onsite energy $(\mathbf{H})_{MM} = -2s^2\boldsymbol{\sigma}\cdot\boldsymbol{\kappa}$ the matrices only differ by the scaling s. It follows that the Hamiltonian H has the same dark modes as if the there were no transverse mode overlap. Since, the operator connection $(\mathcal{A}_\mu)_{jk} = [\hat{D}_k, \partial_\mu \hat{D}_j^\dagger]$ depends only on the structure of dark modes, it has the same form as if overlap were negligible. Hence, one can generate similar quantum holonomies despite working in the strong-coupling regime. In this light, the dark subspace can be viewed as a symmetry-protected subspace that remains unaffected by the nonorthogonality of transverse modes [P2]. This is a remarkable result as, in general, the deviations from mode-orthogonality can significantly distort the dynamics of light in a coupled-mode system [95, 96].

It should be noted that there are some limits to this form of robustness. In the above discussion, next-nearest neighbour coupling was neglected, that is coupling between the outer modes of the star graph. However, in the regime where transverse mode overlap becomes relevant, this next-nearest coupling will be become eventually nonnegligible as propagation times increase. In this case, $\mathbf{H}$ would be close to a fully occupied matrix and degeneracy of the dark subspace would be lifted. Nevertheless, the above result is still useful. It tells us that we can bring individual waveguides really close to the central mode M when traversing a parameter loop, because transverse mode overlap does not harm the geometric phase. However, it should be avoided doing this simultaneously with multiple outer waveguides, as this would incline next-nearest neighbour coupling beyond the central mode.

3.5.2.3 Nonadiabatic propagation through the star graph

The construction of adiabatic holonomies can be formulated analogously for the case where the cyclic evolution is not restricted to just the eigenmodes but to a more general collection of modes for which dynamical contributions from the Hamiltonian completely disappear. We return to the linear optical setting, where M bosonic modes are arranged as a star graph. If it is assumed that all couplings evolve with the same envelope, i.e., $\kappa_k(z) \propto \Omega(z)$, the dark modes become z-independent, viz. $\hat{\Psi}_j(z) = \hat{D}_j(z) = \hat{D}_j(z_0)$ for $j = 1,\dots,M-2$. Moreover, under these assumptions it is always possible to find another operator $\hat{B}^\dagger = \Omega^{-1}\sum_j \kappa_j^* \hat{a}_j^\dagger$ (that is not an eigenmode) such that $[\hat{D}_j, \hat{B}^\dagger] = [\hat{a}_M, \hat{B}^\dagger] = 0$. The propagation of the operator $\hat{B}^\dagger$ along z is computed in the Heisenberg picture, i.e., $\hat{\Psi}_{M-1}^\dagger(z) = \mathrm{e}^{\mathrm{i}\delta(z)} U^\dagger(z)\hat{B}^\dagger U(z)$. This can be given an explicit expression using a series expansion in powers of $H(z) = \Omega(z)h$, with h being the z-independent part of the star graph Hamiltonian. One finds

$$U^\dagger \hat{B}^\dagger U = \hat{B}^\dagger + \sum_{n=1}^{\infty} \frac{(-\mathrm{i}\delta)^n}{n!} \underbrace{[h,[h,\dots[h,\hat{B}^\dagger]]]}_{n-\text{times}} = \hat{B}^\dagger - \mathrm{i}\delta[h,\hat{B}^\dagger] + \frac{(-\mathrm{i}\delta)^2}{2}[h,[h,\hat{B}^\dagger]] \mp \dots,$$

with $\delta(z) = \int_{z_0}^{z} \Omega(z')\mathrm{d}z'$, as a formal solution to the Heisenberg equation of motion. Utilising $[h, \hat{B}^\dagger] = \hat{a}_M^\dagger$ and $[h, \hat{a}_M^\dagger] = \hat{B}^\dagger$ result in a compact expression for the evolution, that is [P6]

$$\hat{\Psi}_{M-1}^\dagger(z) = \mathrm{e}^{\mathrm{i}\delta(z)}\big(\cos\delta(z)\hat{B}^\dagger - \mathrm{i}\sin\delta(z)\hat{a}_M^\dagger\big). \tag{3.33}$$

One can check that $[\hat{\Psi}_j, \hat{\Psi}_k] = [\hat{\Psi}_j^\dagger, \hat{\Psi}_k^\dagger] = 0$ and $[\hat{\Psi}_j, \hat{\Psi}_k^\dagger] = \delta_{jk}$. The excitations of the modes $\{\hat{\Psi}_j^\dagger(z)\}_j$ define a subspace $\mathscr{H}_\psi$. Next, demand $\delta(z_\mathrm{f}) = \pi$ to ensure cyclicity, i.e., $\hat{\Psi}_j(z_\mathrm{f}) = \hat{\Psi}_j(z_0)$ for $j = 1, \ldots, M-1$. After verifying that

$$[\hat{\Psi}_j, [H, \hat{\Psi}_k^\dagger]] = 0,$$

one can check that all conditions for a holonomic evolution are satisfied. The only nonvanishing component of the connection is $(\mathcal{A}_z)_{M-1,M-1} = \mathrm{i}\Omega(z)$. Hence, the nonadiabatic quantum holonomy reads

$$\mathcal{U}_C = \mathrm{diag}(1, \ldots, -1) \in \mathrm{U}(M-1).$$

When replacing the generating operators by the original bosonic modes via a change of gauge $\hat{\Psi}_k^\dagger(z_\mathrm{f}) = \sum_j g_{jk} \hat{a}_j^\dagger(z_\mathrm{f})$, the holonomy transforms according to $\mathcal{U}_C^g = g\,\mathcal{U}_C g^\dagger$. The unitary $\mathcal{U}_C^g \in \mathrm{U}(M-1)$ gives rise to noncommutative quantum holonomies. By traversing a sequence of loops in state space any element in the group $\mathrm{U}(M-1)$ can be realised via a quantum holonomy, i.e., the connection $\mathcal{A}_z$ is irreducible[13].

Similar to the adiabatic scenario, the holonomy $\mathcal{U}_C^g$ can be viewed as a transfer matrix describing the unitary mixing of bosonic modes $\hat{a}_k^\dagger$ or, equivalently, the superoperator $\mathcal{U}_C^g[\hat{a}_k^\dagger] = U_A^\dagger(C)\hat{a}_k^\dagger U_A(C)$. It follows that, in principle, any linear optical network can be implemented by means of nonadiabatic holonomies.

For concreteness, return to the three-waveguide coupler (star graph with $M = 3$) with coupling $\kappa_k(z) \propto \Omega(z)$ for $k = \mathrm{W}, \mathrm{E}$. While the dark mode $\hat{D}^\dagger = \kappa_\mathrm{E}\hat{a}_\mathrm{W}^\dagger - \kappa_\mathrm{W}\hat{a}_\mathrm{E}^\dagger$ evolves trivially along z, i.e., $\hat{\Psi}_1^\dagger(z) = \hat{D}^\dagger$, due to $[H, \hat{D}^\dagger] = 0$, the mode $\hat{B}^\dagger = \Omega^{-1}\big(\kappa_\mathrm{W}^*\hat{a}_\mathrm{W}^\dagger + \kappa_\mathrm{E}^*\hat{a}_\mathrm{E}^\dagger\big)$ evolves into $\hat{\Psi}_2^\dagger(z)$ given by Eq. (3.33). These modes satisfy the condition for a holonomic propagation, i.e., the mixing of modes $\hat{a}_\mathrm{W}^\dagger$ and $\hat{a}_\mathrm{E}^\dagger$ is given by a quantum holonomy. When

---

[13] The proof goes as follows. Restrict attention to loops with $\kappa_1 = \Omega\sin(\theta/2)\mathrm{e}^{-\mathrm{i}\varphi}$, $\kappa_2 = -\Omega\cos(\theta/2)$, $\kappa_3 = 0, \ldots, \kappa_{M-1} = 0$, where (θ, φ) are constant parameter angles determining the unitary of choice. In this case, the relevant operators are

$$\hat{\Psi}_1^\dagger = \sin(\theta/2)\mathrm{e}^{-\mathrm{i}\varphi}\hat{a}_2^\dagger + \cos(\theta/2)\hat{a}_1^\dagger, \quad \hat{\Psi}_2^\dagger = \hat{a}_3^\dagger, \quad \ldots \quad \hat{\Psi}_{M-2}^\dagger = \hat{a}_{M-2}^\dagger, \quad \hat{\Psi}_{M-1}^\dagger = \mathrm{e}^{\mathrm{i}\delta}\big(\cos\delta\hat{B}^\dagger - \mathrm{i}\sin\delta\hat{a}_M^\dagger\big),$$

where $\hat{B}^\dagger = \sin(\theta/2)\mathrm{e}^{\mathrm{i}\varphi}\hat{a}_1^\dagger - \cos(\theta/2)\hat{a}_2^\dagger$, for the given configuration. Under cyclic evolution $\delta(z_\mathrm{f}) = \pi$ the (operator-valued) holonomy becomes

$$\mathcal{U}_C = \begin{bmatrix} \cos\theta & \mathrm{e}^{\mathrm{i}\varphi}\sin\theta \\ \mathrm{e}^{-\mathrm{i}\varphi}\sin\theta & -\cos\theta \end{bmatrix}.$$

As was noted in Ref. [60], two consecutive loops allow for the construction of any unitary 2 × 2 matrix. The holonomy group $\mathrm{Hol}(\mathcal{A})$ is independent of the chosen submanifold in the coupling space $\mathscr{M}$. Hence, the U(2) transformations can be applied to any pair of modes $(\hat{a}_j, \hat{a}_k)_{j\neq k}$ for all $j, k = 1, \ldots M-1$. The fact that we can construct any element of $\mathrm{U}(M-1)$ in a fully holonomic fashion is now a direct consequence of the argument by Reck *et al.* [140]. ■

two photons are injected into the optical setup, there are three different states

$$\frac{1}{\sqrt{2}}\big(\hat{\Psi}_1^\dagger\big)^2 |\mathbf{0}\rangle\,, \qquad \hat{\Psi}_1^\dagger\hat{\Psi}_2^\dagger |\mathbf{0}\rangle\,, \qquad \frac{1}{\sqrt{2}}\big(\hat{\Psi}_2^\dagger\big)^2 |\mathbf{0}\rangle$$

spanning a subspace $\mathscr{H}_\psi$ on which a U(3) holonomy can be realised. Interestingly, the central mode $\hat{a}_\mathrm{C}$ of the system itself satisfies $[\hat{a}_\mathrm{C}, [H, \hat{a}_\mathrm{C}^\dagger]] = 0$ and evolves according to an Abelian holonomy $\hat{a}_\mathrm{C}^\dagger(z_\mathrm{f}) = \mathrm{e}^{\mathrm{i}\pi}\hat{a}_\mathrm{C}^\dagger(z_0)$. Hence, the states $\hat{a}_\mathrm{C}^\dagger\hat{\Psi}_1^\dagger |\mathbf{0}\rangle$ and $\hat{a}_\mathrm{C}^\dagger\hat{\Psi}_2^\dagger |\mathbf{0}\rangle$ span another subspace $\mathscr{H}_{\psi'}$ on which U(2) transformations can be generated. This is a general feature of this operator formulation. If there are several modes evolving according to a quantum holonomy, products of those will generate a product of holonomies. This operator point of view illuminates the origin of the block structure of the nonadiabatic holonomy (3.29).

IV | Holonomic Quantum Computation with Photons

Carefully controlled quantum systems show exotic and counter intuitive behaviour. Based on this, a novel form of information processing can be conducted. In standard proposals for quantum computation (QC) the manipulation of qubits is often realised by fast-switching dynamical interactions governed by external fields. In this picture, the experimentalist controls a set of on-off Hamiltonians to implement a quantum-gate logic, thus solving a computational task for which no efficient classical algorithm is known.

An alternative viewpoint to this so-called circuit model is given by geometric and topological QC [40, 141]. In these nondynamical models information processing can be based on adiabatic [1], and nonadiabatic quantum holonomies [60] (see Chapter III), or unusual quantum statistics (e.g., anyonic) [41] emerging from the exotic properties of topological quantum field theories [142]. These approaches to QC come along with some unique and surprising fault-tolerance features. In particular, quantum information processing (QIP) can be conducted on a subspace on which the Hamiltonian vanishes completely, thus making the output independent of timing errors or fluctuations in the spectrum. In other words, in these models the computation is completely determined by some geometric or topological feature of the theory, such as areas and volumes in state space [59], or Chern numbers [143]. This in turn leads to an intrinsic robustness of the computation towards local perturbations [144]. Other approaches do not aim at protecting the individual system, but use sophisticated many-particle interactions to establish an error-resilient macroscopic structure that resembles the topology of, e.g., a torus [44].

This chapter is mainly concerned with the paradigm of holonomic QC, in which the manipulation of quantum information is achieved through a sequence of holonomies. The inherent robustness of a holonomic QC can be combined with most error-correcting codes including stabiliser [145], concatenated [146], and surface codes [147, 148]. In Sec. 4.1, well established concepts from quantum information theory will be reviewed. Section 4.2 investigates integrated photonic structures, on which QC can be performed using dual-rail encoded qubits. I show that the developed architectures allow for the construction of any linear optical transformation in a geometrically protected way. After these foundations are established, Sections 4.3 and 4.4 are concerned with more specialised topics, namely holonomic and measurement-based QC, respectively. When provided with a graph state, universal holonomic QC can be conducted in a hybrid approach using techniques from measurement-based QC.

4.1 Elements of Quantum Information Theory

A computation is a process which solves complex tasks by carrying out a large number of simple mathematical operations. The solution strategy for a given task is known as an algorithm. An algorithm is said to be efficient if the number of operations only scales polynomial with the size of the computational problem. As classical systems cannot efficiently simulate large quantum systems — a widely believed but unproven conjecture[1] — quantum systems themselves might act as the carrier of information, thus enabling algorithmic shortcuts based on entanglement and coherent superpositions. In the following, I present the foundations of quantum information theory to the degree as it is relevant to the thesis.

4.1.1 Qubits and their manipulation

Unlike classical information, quantum information can not only be in the computational basis $|0\rangle_\ell$ and $|1\rangle_\ell$, but in any superposition

$$|\psi\rangle = \alpha_0 \, |0\rangle_\ell + \alpha_1 \, |1\rangle_\ell \, .$$

The normalisation $|\alpha_0|^2 + |\alpha_1|^2 = 1$ ensures a probabilistic interpretation of the measurement output. The state $|\psi\rangle$ is said to be a single-qubit state. Extending this notion to a composition of n quantum systems, each encoding a single qubit, leads to the definition of an n-qubit state

$$|\psi\rangle = \sum_{i_1, i_2 \ldots i_n \in \{0,1\}} \alpha_{i_1 i_2 \ldots i_n} \, |i_1 i_2 \ldots i_n\rangle_\ell \, ,$$

where $|i_1 i_2 \ldots i_n\rangle_\ell = |i_1\rangle_\ell \otimes |i_2\rangle_\ell \otimes \cdots \otimes |i_n\rangle_\ell$ is the usual abbreviation for the tensor product of binary states. In an information-theoretical language, the state $|\psi\rangle$ is called the (quantum) code word and the space containing all such code words is said to be the (quantum) code, which will be denoted as $\mathscr{C}$. An important difference between the 2^n-dimensional Hilbert space $\mathscr{C}$ and a classical code (containing bit strings of length n) is the possibility for multipartite entangled states [4], i.e., the code word $|\psi\rangle$ cannot be written as an n-fold tensor product of single-qubit states. Together with the superposition principle, this potentially leads to algorithmic speed-ups in comparison to classical information processing [151].

4.1.1.1 Quantum gates

In order to perform QC, an initially prepared state must be manipulated in such a way that the output resembles the solution of a difficult computational task. The most common way to do this is by applying (unitary) quantum gates onto the code. Prominent examples include the single-qubit Pauli gates, which with respect to the canonical basis

---

[1] For example, Ref. [149] reported a quantum advantage achieved on Google's superconducting quantum computer. Only recently, an efficient classical algorithm to complete the same task was constructed [150].

$$|0\rangle_\ell = \begin{bmatrix} 1 \\ 0 \end{bmatrix}, \qquad |1\rangle_\ell = \begin{bmatrix} 0 \\ 1 \end{bmatrix},$$

take the matrix representation

$$X = \begin{bmatrix} 0 & 1 \\ 1 & 0 \end{bmatrix}, \qquad Y = \begin{bmatrix} 0 & -\mathrm{i} \\ \mathrm{i} & 0 \end{bmatrix}, \qquad Z = \begin{bmatrix} 1 & 0 \\ 0 & -1 \end{bmatrix}.$$

Certainly, X corresponds to a bit-flip operation, similar to the classical NOT operation, while Y and Z are without any classical counterpart. Other heavily used single-qubit gates are the Hadamard transformation and $\pi/4$-phase rotation

$$W = \frac{1}{\sqrt{2}} \begin{bmatrix} 1 & 1 \\ 1 & -1 \end{bmatrix}, \qquad S = \begin{bmatrix} 1 & 0 \\ 0 & \mathrm{i} \end{bmatrix}.$$

Note that the Hadamard transformation W maps the computational states $|0\rangle_\ell$ and $|1\rangle_\ell$ into the superpositions $|\pm\rangle = (|0\rangle_\ell \pm |1\rangle_\ell)/\sqrt{2}$. In general, a single qubit gate U belongs to the unitary group U(2).

Tensor products of single-qubit gates are also known as local operations and by themselves these cannot create entanglement [151]. More intriguing multi-qubit operations are necessary for such an endeavour [152, 153]. For instance, two-qubit controlled gates

$$\mathrm{C}U = |0\rangle_\ell \langle 0|_\ell \otimes \mathbb{1} + |1\rangle_\ell \langle 1|_\ell \otimes U, \tag{4.1}$$

where U is a single-qubit gate, involve nonlocal interactions. Here, the second (target) qubit is left unchanged when the first (control) qubit is in the state $|0\rangle_\ell$. Conversely, if the first qubit is in the state $|1\rangle_\ell$, the local operation U is applied to the target. These gates belong to the group U(4) and have a 4×4 matrix representation with respect to the two-qubit basis $|00\rangle_\ell$, $|01\rangle_\ell$, $|10\rangle_\ell$, and $|11\rangle_\ell$. In general, an n-qubit gate is a member of the unitary group U(2^n). These might also include controlled operations with more than one target or controller. A quantum algorithm on n qubits then consists of a sequence of such gates. Typically, when we say that we can realise a specific set of gates, it is assumed that we are able to apply each of them to any qubits we want.

4.1.1.2 Measurement formalism

Quantum mechanical measurements are not only relevant for the final readout of a QC, but allow for the manipulation of qubits (beyond unitaries) as well. For our purposes it suffices to restrict attention to projective measurements. These are defined by a set of Hermitian positive operators $\{\Pi_i\}_i$ that square to themselves, i.e., $\Pi_i^2 = \Pi_i$, and are orthogonal, that is $\Pi_i \Pi_j = 0$, for $i \neq j$. The operators project a quantum state ϱ onto $\Pi_i \varrho \Pi_i$. The state after the measurement thus, depends on the measurement result i that is obtained with probability $p_i = \mathrm{Tr}\{\Pi_i \varrho\}$.

The most basic example of such a measurement distinguishes between the computational states, i.e., $\Pi_0 = |0\rangle_\ell \langle 0|_\ell$ and $\Pi_1 = |1\rangle_\ell \langle 1|_\ell$. The probability of the state $|\psi\rangle = \alpha_0 |0\rangle_\ell + \alpha_1 |1\rangle_\ell$ to collapse into $|0\rangle_\ell$ or $|1\rangle_\ell$ after measurement, is readily obtained to be $|\alpha_0|^2$ and $|\alpha_1|^2$, respectively. Moreover, the computational states are eigenstates of the Pauli-Z matrix. One has the spectral resolution $Z = \Pi_0 - \Pi_1$, and the above prescription is said to be a measurement of the observable Z. Analogously, one can perform a measurement of the Pauli-X operator. The corresponding projectors are $\Pi_+ = |+\rangle \langle +|$ and $\Pi_- = |-\rangle \langle -|$. Measurements involving only a single qubit are also known as local measurements and from an engineering viewpoint, these are easy to implement.

4.1.2 Circuit model

We are now equipped with the tools to introduce a mathematical model of QC. A quantum computer consists of a Hilbert space $\mathscr{C}$ containing the quantum information, a fundamental gate set $\{U_k\}_k$ comprising the physical architecture from which more intriguing operations have to be designed, and a final readout in terms of measurement operators $\{\Pi_j\}_j$ [154]. A graphical way of illustrating this procedure can be introduced via circuit diagrams [151], e.g.,

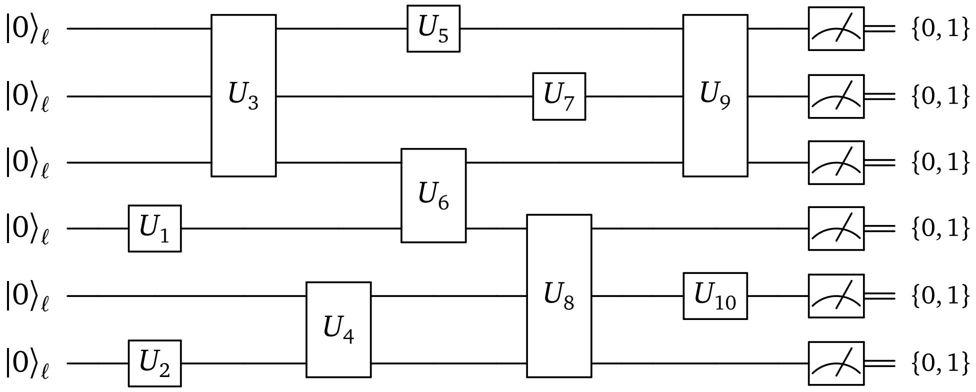

In such a diagram time flows from left to right and each wire represent a qubit, while blocks ranging over multiple wires denote the action of multi-qubit gates. The overall unitary operator transforming input state, here $|00\ldots 0\rangle_\ell$, constitutes the quantum algorithm. Finally, the output state is measured leading to a register of classical bits.

4.1.2.1 Computational universality

When only a rather limited gate set is at ones disposal, it will (supposedly) not be possible to realise arbitrary quantum algorithms. Given an n-qubit code, ideally one would like to have a complete set of elementary gates such that any element of the group $\mathrm{U}(2^n)$ can be designed as a sequence of those. If this is possible the gate set is said to be universal for QC [133]. Universality is an important property that needs to be satisfied in order to build a useful quantum computer[2].

---

[2] Nevertheless, there are some computational problems for which QC offers advantageous solutions without having a universal gate set. Prominent examples are boson sampling [155] and quantum annealing [156].

Several universal sets of quantum gates are known [151]. The simplest one comprises rotations $R_x(\varphi) = \mathrm{e}^{-\mathrm{i}\frac{\varphi}{2}X}$ and $R_z(\varphi) = \mathrm{e}^{-\mathrm{i}\frac{\varphi}{2}Z}$ around the x and z-axis of the Bloch sphere, and a maximally entangling two-qubit gate, like the controlled-NOT operation $\mathrm{C}X$. In contrast, the Pauli gates by themselves are not universal, but only generate the n-qubit Pauli group $\mathscr{P}_n$ consisting of tensor products of Pauli operators. In particular, they cannot create entanglement as they belong to the class of local operations. Remarkably, even the gate set $\{\mathrm{C}Z, W, S\}$, containing the nontrivial two-qubit gate $\mathrm{C}Z$, fails to be universal. Instead, these gates generate the so-called n-qubit Clifford group $\mathscr{N}(\mathscr{P}_n)$, which is formally defined as the normaliser of the Pauli group, i.e.,

$$\forall\, V \in \mathscr{N}(\mathscr{P}_n): \quad V P V^{\dagger} \in \mathscr{P}_n$$

for any operator $P \in \mathscr{P}_n$. Quite clearly, $\mathscr{N}(\mathscr{P}_n)$ is a proper subgroup of $\mathrm{U}(2^n)$, e.g., the single-qubit unitary $\sqrt{S}$ does not lie in the Clifford group. Nevertheless, when the Clifford group is augmented by the gate $\sqrt{S}$, then a complete set of gates is at hand, that enables universal QC. Strikingly, the quantum dynamics described by the Clifford group $\mathscr{N}(\mathscr{P}_n)$, despite containing entangling gates, can be simulated efficiently on a classical computer, a result known as the Gottesman-Knill theorem [157].

Even though the notion of computational universality is intuitive enough, some formalisation of the concept might be appropriate to address potential caveats. Given a set of gates $\{U_k\}_k$ belonging to the group $\mathrm{U}(d)$, the set $\{U_k\}_k$ lies dense in $\mathrm{U}(d)$ if any unitary $d \times d$ matrix U can be approximated to arbitrary precision by a (classically computable) finite sequence, viz.

$$\forall\, U \in \mathrm{U}(d): \quad \Big\| U - \prod\nolimits_{k=1}^{K} U_k \Big\| \leq \epsilon \tag{4.2}$$

for arbitrarily small $\epsilon > 0$. A particular computation U is deemed efficiently implementable when the length of the sequence $K(\epsilon)$ has a mild (poly-logarithmic) dependence on ϵ [158]. The notion of universality in terms of dense gate sets is, in a sense, topological in its own, as one does not need to specify the operator norm in the above definition.

4.2 Linear Optical Quantum Computation

There exist a variety of different physical architectures on which QC can be based. Which of these platforms will turn out to be the most suitable (i.e., reliable and scalable) for the design of useful quantum technologies is up to current scientific debate. Whatever the final implementation might look like, most certainly, the photon will play a key role in its working mechanism — might it be as a mediator of interaction, a hybrid devise, or even an all-out optical quantum processor. Therefore, the following pages are dedicated to linear optical QC [159]. As its name suggests, here unitary quantum gates are implemented using linear optical elements, such as beam splitters, fibre couplers, photonic waveguides, etc.

A natural starting point for our discussion is the definition of a photonic qubit. This can be done by using a single photon in a setup with two spatial modes W and E. This is known as a dual-rail logic, viz.

$$|0\rangle_\ell = \hat{a}_{\mathrm{W}}^\dagger |\mathbf{0}\rangle\,, \qquad |1\rangle_\ell = \hat{a}_{\mathrm{E}}^\dagger |\mathbf{0}\rangle\,,$$

with $|\mathbf{0}\rangle = |0_{\mathrm{W}} 0_{\mathrm{E}}\rangle$ being the two-mode vacuum state. In the spirit of this thesis, we might think of these modes as being implemented in terms of two (fused-silica laser-written) waveguides. In this situation, the dual rail logic is sometimes referred to as a path encoding [160], as well. There are of course other forms of encoding, such as photon-number encoding or continuous-variable QC [161]. The advantage of the dual-rail logic is that, it is easy to herald for photon loss with this convention, because an ideal (i.e., lossless) propagation would conserve the overall photon number [162].

The evanescent coupling $\kappa = \text{const.}$ between the two modes applies a linear transformation to the bosonic operators. After the propagation length $\Delta z = z_{\mathrm{f}} - z_0$, the latter are transformed into [102]

$$\begin{bmatrix} \hat{a}_{\mathrm{W}}^\dagger(z_{\mathrm{f}}) \\ \hat{a}_{\mathrm{E}}^\dagger(z_{\mathrm{f}}) \end{bmatrix} = \begin{bmatrix} \tau & \rho \\ \rho^* & -\tau \end{bmatrix} \begin{bmatrix} \hat{a}_{\mathrm{W}}^\dagger(z_0) \\ \hat{a}_{\mathrm{E}}^\dagger(z_0) \end{bmatrix}, \tag{4.3}$$

where $\tau = \cos(|\kappa|\Delta z)$ and $\rho = \mathrm{e}^{\mathrm{i}\arg(\kappa)}\sin(|\kappa|\Delta z)$. The unitary in Eq. (4.3) is the transfer matrix of the two-mode coupler.

Given a collection of M bosonic modes $\hat{\boldsymbol{a}} = (\hat{a}_k)_k$, any $M \times M$ transfer matrix $\mathcal{U}$ can be implemented as a sequence of two-mode transformations between pairs of modes. This argument goes back to Reck *et al.* [140], and is based on a decomposition of $\mathcal{U}$ into a product of unitary 2×2 matrices. I wish to emphasise that this does not imply (quantum) computational universality of linear optical networks, as nonlinear optical effects are necessary to realise controlled unitaries (on the level of qubits). The latter are necessary as linear optical transformations cannot create an entangled state with respect to the multipartite structure defined by the dual-rail encoding[3]. Nevertheless, linear optical QC is still believed to outperform classical computation in some tasks, for instance, in the generation of random numbers [163].

In order to construct a universal paradigm, nonlinear transformations on the modes have to be added. Harnessing Kerr nonlinearities could, in principle, induce controlled-phase gates, but third order optical nonlinearities are notoriously small for a field with such a low intensity as a single photon [164]. However, experimental advances may eventually overcome this. Alternatively, this can also be done, for instance, via click-counting detectors, measuring the impinging of a single photon. Unfortunately, these measurement-induced nonlinearities [28, 29], generally, have a low success rate and scalability of quantum algorithms, thus becomes quickly unfeasible. In principle, the success rate can be boosted substantially by teleportation protocols [165], requiring a large number of Bell pairs which makes the proposal difficult to implement by current technological means. It is due to these difficulties that most modern proposals for linear optical QC are based on the a-priori (measurement-induced) preparation of a highly-entangled resource state. Once such a resource state, e.g., a graph state, is prepared, universal (measurement-based) QC [166] can be realised in terms of linear optical elements and single-photon detectors only (details in Sec. 4.4). The shift of the main computational expense towards initial state preparation can, in principle, be dealt with using modern multiplexing methods [167], thus boosting the maximal number of photons that can be manipulated simultaneously.

---

[3] Nonetheless, the transformation (4.3) can generate entanglement between the spatial modes, e.g., $|1_{\mathrm{W}} 1_{\mathrm{E}}\rangle \mapsto \big(|2_{\mathrm{W}}\rangle - |2_{\mathrm{E}}\rangle\big)/\sqrt{2}$ via a Hong-Ou-Mandel interferometer ($\tau = \rho = 1/2$) [102, 164].

4.2.1 Holonomic optics

While integrated photonic waveguides proved to be a reliable tool in the implementation of linear optical networks, there are still parametric fluctuations as well as dynamical influences that can harm the interferometric stability of these networks. Moreover, the transfer matrix in Eq. (4.3) is determined by just one evanescent coupling κ as well as the overall propagation length Δz, thus leaving the experimentalist with a rather narrow design strategy for a specific transformation.

In order to establish more versatile design strategies, it might be advantageous to incorporate the techniques from Chapter III. A design strategy has to be established relying solely on holonomies. As linear optical transformations are in general noncommuting, these phases must be of non-Abelian type. While the standard formalism on quantum holonomies [58, 60] does not provide any immediate resolution of the issue, the operator formalism developed in Sec. 3.5 allows for an elegant photon-number independent description of quantum holonomies [P6]. Attention lies on nonadiabatic holonomies, as these have path-shortening (diabatic) implementations, thus enabling miniaturisation of the optical setup to some degree.

Recall the form of the tight-binding Hamiltonian for the three-waveguide coupler

$$H(z) = \sum_{k\in\{\mathrm{W},\mathrm{E}\}} \big(\kappa_k(z)\hat{a}_k\hat{a}_{\mathrm{C}}^\dagger + \kappa_k^*(z)\hat{a}_k^\dagger\hat{a}_{\mathrm{C}}\big).$$

Let $\kappa_{\mathrm{W}}(z) = \Omega(z)\sin(\theta/2)\,\mathrm{e}^{-\mathrm{i}\varphi}$ and $\kappa_{\mathrm{E}}(z) = -\Omega(z)\cos(\theta/2)$, where (θ,φ) are constant parameter angles. In this configuration, the relevant operators are

$$\begin{aligned}\hat{\Psi}_1^\dagger(t) &= \sin(\theta/2)\mathrm{e}^{-\mathrm{i}\varphi}\hat{a}_{\mathrm{E}}^\dagger + \cos(\theta/2)\hat{a}_{\mathrm{W}}^\dagger,\\ \hat{\Psi}_2^\dagger(t) &= \mathrm{e}^{\mathrm{i}\delta(z)}\big(\cos\delta(z)\hat{B}^\dagger - \mathrm{i}\sin\delta(z)\hat{a}_{\mathrm{C}}^\dagger\big),\end{aligned}$$

where

$$\hat{B}^\dagger = \sin(\theta/2)\mathrm{e}^{\mathrm{i}\varphi}\hat{a}_{\mathrm{W}}^\dagger - \cos(\theta/2)\hat{a}_{\mathrm{E}}^\dagger,$$

for the given configuration. The corresponding connection is simply $(\mathcal{A}_z)_{22} = \mathrm{i}\Omega(z)$. Under cyclic evolution $\delta(z_{\mathrm{f}}) = \pi$ the (operator-valued) holonomy becomes

$$\mathcal{U}_C = \begin{bmatrix}\cos\theta & \mathrm{e}^{\mathrm{i}\varphi}\sin\theta\\ \mathrm{e}^{-\mathrm{i}\varphi}\sin\theta & -\cos\theta\end{bmatrix}. \tag{4.4}$$

Two subsequent applications of the above transfer matrix allow for the implementation of any U(2) transformations between the outer modes $\hat{a}_{\mathrm{W}}$ and $\hat{a}_{\mathrm{E}}$ of the system.

Given a collection of M modes the transfer holonomy $\mathcal{U}_C$ can be applied to any pair of modes $(\hat{a}_i, \hat{a}_j)_{j \neq k}$ for all $j, k = 1, \ldots M$, provided a sufficient number of (central) ancilla modes is at hand, such that population transfer between the modes j and k can be mediated in a fully geometric fashion. The fact that we can construct any unitary transformation (on the modes) is now a direct consequence of the argument by Reck *et al.* [140]. Figure 14 illustrates the mapping from a directional coupler to the three-waveguide coupler, that replaces the (standard) transfer matrix in Eq. (4.3) (depending on $\kappa \Delta z$) with the holonomic transfer matrix from (4.4) (depending on $\delta(z_{\mathrm{f}}) = \pi$). Applying this replacement onto an entire multi-mode network as sketched in Fig. 14 (b), results in a linear optical network, that depends only on the path C taken by the bosonic operators, i.e., $\hat{\boldsymbol{a}}(z_{\mathrm{f}}) = \hat{\boldsymbol{a}}(C)$.

4.3 Holonomic Quantum Computation

The circuit model of QC offers a straight-forward way to realise QIP in terms of switching on and off local Hamiltonians in an appropriate manner. However, other computational models exist. These models can differ from the circuit model not only in their theoretical make-up, but in terms of the necessary resources as well. In this section, the paradigm of holonomic QC [1, 60] is presented. In their seminal paper [1], Zanardi and Rasetti proposed this novel scheme for the manipulation of quantum information, in which the entire quantum-gate logic is built from holonomies.

4.3.1 Adiabatic holonomic gates

Given a quantum system H with d-fold degenerate eigenspace $\mathscr{C} = \{|\psi_a\rangle\}_{a=1}^{d}$, a holonomic gate $U_A(C) = \hat{\mathbf{P}} \exp \oint_C A$ is realised by designing an adiabatic loop C in a parameter space $\mathscr{M}$. Here, the adiabatic connection $(A_\mu)_{ab} = \langle \psi_b | \partial_\mu | \psi_a \rangle$ is computed from the eigenstates $|\psi_a\rangle$. Overall dynamical phases can be neglected, because these are irrelevant to any computational task. A quantum algorithm $\prod_i U_A(C_i)$ on this subspace can be implemented by composing a sequence of loops $\prod_i C_i$. In this context, irreducibility of the connection A

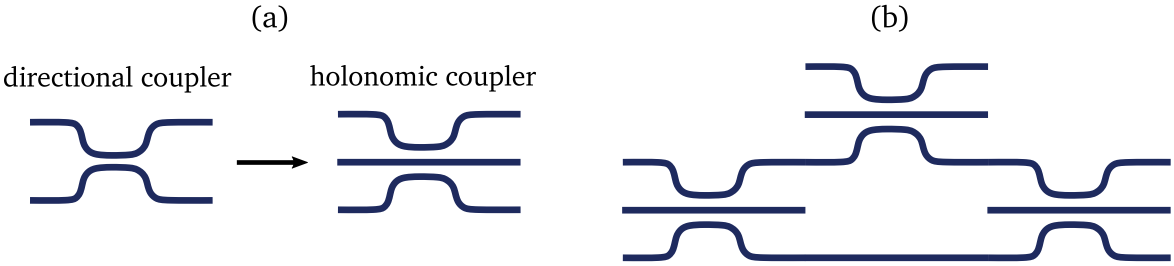

Figure 14.: (a) Any linear optical two-mode transformation can be realised holonomically by replacing the directional coupler with a three-waveguide coupler in cyclic configuration. (b) Construction of a multi-mode network solely based on holonomies.

is intrinsically linked to the notion of computational universality. Precisely speaking, if the considered eigenspace has an underlying (physical) multi-partite structure, i.e., $\mathscr{C} = \left(\mathbb{C}^2\right)^{\otimes n}$, then $\mathscr{C}$ might be viewed as an n-qubit quantum code with $d = 2^n$. In this case, having an irreducible connection allows for the realisation of any quantum algorithm by adiabatic holonomies [1]. More formally, the holonomy group $\mathrm{Hol}(A)$ lies dense in $\mathrm{U}(2^n)$.

Single-qubit holonomic gates can be realised using the tripod formation of bosonic modes [Fig. 6. (a)]. Considering only a single photon in the propagation, the Hamiltonian of the system reads

$$H = \sum_{k\in\{\mathrm{W},\mathrm{E},\mathrm{A}\}} \left(\kappa_k \left|1_\mathrm{C}\right\rangle \left\langle 1_k\right| + \kappa_k^* \left|1_k\right\rangle \left\langle 1_\mathrm{C}\right|\right),$$

where summation runs over the outer modes. At the initial configuration $\boldsymbol{\kappa}_0 = (0, 0, \kappa)$ the two dark states of the system take a particular simple form, that is $|D_1(\boldsymbol{\kappa}_0)\rangle = |1_\mathrm{W}\rangle$, $|D_2(\boldsymbol{\kappa}_0)\rangle = |1_\mathrm{E}\rangle$. These define the computational states $|0\rangle_\ell$ and $|1\rangle_\ell$, respectively. Here, any loop C starts and ends at the base point $\boldsymbol{\kappa}_0$. While the holonomy group $\mathrm{Hol}(A)$ is independent of the chosen base point [59], a clever choice of the initial configuration $\boldsymbol{\kappa}_0$ simplifies state preparation to some extend.

With the purpose of constructing specific gates, consider the parametrisation $\kappa_\mathrm{W} = \kappa \cos\theta \sin\vartheta \mathrm{e}^{\mathrm{i}\varphi}$, $\kappa_\mathrm{E} = \kappa \sin\theta \sin\vartheta \mathrm{e}^{\mathrm{i}\varphi}$, and $\kappa_\mathrm{A} = \kappa \cos\vartheta$, where $\theta \in [0, \pi]$ and $\vartheta, \varphi \in [0, 2\pi)$. The components of the connection are computed to ($A_\vartheta = 0$)

$$A_\theta = \begin{bmatrix} 0 & \cos\vartheta \\ -\cos\vartheta & 0 \end{bmatrix}, \qquad A_\varphi = \begin{bmatrix} 0 & 0 \\ 0 & \mathrm{i}\sin^2\vartheta \end{bmatrix}.$$

Due to the complex coupling strength κ_W, we have a non-Abelian gauge potential at our disposal, i.e., $[A_\theta, A_\varphi] \neq 0$. Path ordering can be satisfied by traversing a plaquette $\square$ along the coordinate lines. For concreteness, let

$$\begin{aligned}\square : (\theta_0, \vartheta_0, \varphi_0) &\rightarrow (\theta_1, \vartheta_0, \varphi_0) \rightarrow (\theta_1, \vartheta_0, \varphi_1) \rightarrow (\theta_1, \vartheta_1, \varphi_1) \\ &\rightarrow (\theta_0, \vartheta_1, \varphi_1) \rightarrow (\theta_0, \vartheta_1, \varphi_0) \rightarrow (\theta_0, \vartheta_0, \varphi_0).\end{aligned}$$

A direct integration along the Wilson lines of $\square$ yields the holonomy as a path-ordered product

$$\begin{aligned} U_A(\square) &= \exp\left(\int_{\varphi_1}^{\varphi_0} A_\varphi\big|_{\vartheta_1} \mathrm{d}\varphi\right) \exp\left(\int_{\theta_1}^{\theta_0} A_\theta\big|_{\vartheta_1} \mathrm{d}\theta\right) \exp\left(\int_{\varphi_0}^{\varphi_1} A_\varphi\big|_{\vartheta_0} \mathrm{d}\varphi\right) \exp\left(\int_{\theta_0}^{\theta_1} A_\theta\big|_{\vartheta_0} \mathrm{d}\theta\right), \\ &= \begin{bmatrix} 1 & 0 \\ 0 & \mathrm{e}^{-\mathrm{i}\sin^2\vartheta_1 \Delta\varphi} \end{bmatrix} \begin{bmatrix} \cos\phi_1 & -\sin\phi_1 \\ \sin\phi_1 & \cos\phi_1 \end{bmatrix} \begin{bmatrix} 1 & 0 \\ 0 & \mathrm{e}^{\mathrm{i}\sin^2\vartheta_0 \Delta\varphi} \end{bmatrix} \begin{bmatrix} \cos\phi_0 & \sin\phi_0 \\ -\sin\phi_0 & \cos\phi_0 \end{bmatrix}, \end{aligned}$$

where the second equality can be verified by inserting the definitions $\Delta\varphi = \varphi_1 - \varphi_0$ and $\phi_i = \cos\vartheta_i(\theta_1 - \theta_0)$ for $i = 0, 1$. The holonomic gate $U_A(\square)$ yields the resolution of a unitary 2×2 matrix. Hence, any element in the group $\mathrm{U}(2)$ can be implemented by traversing a suitable plaquette.

4.3.1.1 Adiabatic holonomic QC on subsystems

So far, the encoded information was to be prepared in only one of the system's eigenspaces. In the discussion of the tripod structure, the dark subspace was the eigenspace of choice, while our study of PNTs suggests to chose the subspace which possesses the highest-dimensional holonomy group. In any case, the chosen eigenspace ideally possesses a natural multi-partite structure, so that a quantum code can be defined. Since there is no guarantee that one can decompose an eigenspace $\mathscr{H}_l$ into a product of single-qubit Hilbert spaces in any physically relevant way [169], one has to come up with a consistent labeling of logical qubits. This problem, sometimes referred to as the *complexity issue* [58, 59], must be addressed in order to enable efficient holonomic QC.

One possible remedy to this predicament might be to use the natural multi-partite structure induced by the Hamiltonian, i.e., labelling qubits with respect to the spatial modes of a system. As obvious this solution might seem at first sight, it leads to a rather subtle issue, namely the generated holonomies may not act as a proper quantum gate solely within one of the eigenspaces, but rather on a logical quantum code $\mathscr{C} \subset \mathscr{H}$. A series of holonomies in different eigenspaces might then be needed to produce the desired transformation on the level of qubits. Nevertheless, because one can (hopefully) generate any transformation on each of the respective eigenspaces, it may be well possible, if the eigenspaces are large enough, to generate any linear optical computation within the code [P1].

Let us clarify the above statements using a generic example. In the following, I will show how the tripod arrangement, given two indistinguishable photons, serves as a sufficient setup for the implementation of two-qubit states. For that, recall the form of the first-order bright states $|B_{\pm,1}\rangle, |B_{\pm,2}\rangle \in \mathscr{H}_\pm$ given in the parametrisation (3.8). At the point $\boldsymbol{\kappa} = (0,0,\kappa)$, these simplify to

$$|B_{\pm,1}(\boldsymbol{\kappa}_0)\rangle = \frac{1}{\sqrt{2}}(|1_\mathrm{W}1_\mathrm{A}\rangle \pm |1_\mathrm{W}1_\mathrm{C}\rangle), \qquad |B_{\pm,2}(\boldsymbol{\kappa}_0)\rangle = \frac{1}{\sqrt{2}}(|1_\mathrm{E}1_\mathrm{A}\rangle \pm |1_\mathrm{E}1_\mathrm{C}\rangle).$$

Logical qubits are then defined with respect to the spatial mode structure of the waveguide network, using a dual rail encoding

$$|00\rangle_\ell = |1_\mathrm{W}1_\mathrm{A}\rangle\,, \quad |01\rangle_\ell = |1_\mathrm{W}1_\mathrm{C}\rangle\,, \quad |10\rangle_\ell = |1_\mathrm{E}1_\mathrm{A}\rangle\,, \quad |11\rangle_\ell = |1_\mathrm{E}1_\mathrm{C}\rangle\,. \tag{4.5}$$

With this definition at hand, any two-qubit state $|\psi\rangle$ lies completely in the code $\mathscr{C} = \mathscr{H}_+ \oplus \mathscr{H}_-$. The composite holonomy acting on the code reads

$$U(\phi_C, \omega) = \mathrm{e}^{\mathrm{i}\omega} U_{A_+}(C) \oplus \mathrm{e}^{-\mathrm{i}\omega} U_{A_-}(C).$$

Because the code $\mathscr{C}$ extends over more than one eigenspace, dynamical phases $\omega(z_\mathrm{f}) = \int_{z_0}^{z_\mathrm{f}} \varepsilon(z)\mathrm{d}z$ can no longer be removed. Furthermore,

$$U_{A_\pm}(C) = \begin{bmatrix} \cos\phi_C & -\sin\phi_C \\ \sin\phi_C & \cos\phi_C \end{bmatrix}$$

are the holonomies acting on the product states $|B_{\pm,1}(\boldsymbol{\kappa}_0)\rangle = |0\rangle_\ell \otimes |\pm\rangle$ and $|B_{\pm,2}(\boldsymbol{\kappa}_0)\rangle = |1\rangle_\ell \otimes |\pm\rangle$, respectively. Here, $\phi_C = \oint_C \sin\vartheta \mathrm{d}\vartheta$ is a purely geometric phase. In the computational basis (4.5), the composite holonomy can be written as a tensor product

$$U(\phi_C, \omega) = W(\phi_C) \otimes V(\omega),$$

of the single-qubit gates

$$W(\phi_C) = \begin{bmatrix} \cos\phi_C & -\sin\phi_C \\ \sin\phi_C & \cos\phi_C \end{bmatrix}, \qquad V(\omega) = \begin{bmatrix} \cos\omega & -\mathrm{i}\sin\omega \\ -\mathrm{i}\sin\omega & \cos\omega \end{bmatrix}.$$

In circuit notation, the tripod realises the architecture

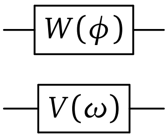

on the code. Indeed, any gate in the group U(2) ⊗ U(2) can be designed in this way. As the tripod formation corresponds to a linear optical network, it could have been anticipated that no entangling operations are encountered. Note that the computation is not entirely geometric in nature, because the dynamical phase ω contributes to the composite holonomy. At least on the formal level, these can be shifted onto a separate qubit, while the remaining qubit is transformed by a holonomic gate [170].

4.3.2 Nonadiabatic gates

A networking of adiabatic holonomies demands exceedingly large photonic chips, because adiabaticity has to be ensured for each gate in the network. An alternative, path-shortening, paradigm relies on a quantum-gate logic built from nonadiabatic quantum holonomies [60]. Elementary gates are designed in terms of holonomies $U_A(C) = \hat{\mathbf{T}} \exp \int_0^T A_t \mathrm{d}t$, with the nonadiabatic connection $(A_t)_{ba} = \langle \psi_a | \partial_t | \psi_b \rangle$ governing the evolution. Recall that the states $|\psi_a(t)\rangle$ are independent of the Hamiltonian's dynamics, i.e., $\langle \psi_a | H | \psi_b \rangle = 0$. The code $\mathscr{C}$ is spanned by these states at their initial configuration, i.e., $\mathscr{C} = \{|\psi_a(0)\rangle\}_a$. In order to ensure a proper read-out of qubits at the end of the computation, the states have to evolve cyclically, i.e., $|\psi_a(0)\rangle = |\psi_a(T)\rangle$ for $a = 1, \ldots d$. Moreover, it is desirable for $\mathscr{C}$ to possess a multi-partite structure that allows for the interpretation of $U_A(C)$ as a multi-qubit gate, thus rendering efficient QIP possible.

The construction of single-qubit holonomic gates is possible utilising the three-waveguide coupler. When only a single photon is subjected to the optical setup, the Hamiltonian takes the form

$$H = \sum_{k \in \{\mathrm{W},\mathrm{E}\}} \left(\kappa_k |1_\mathrm{C}\rangle \langle 1_k| + \kappa_k^* |1_k\rangle \langle 1_\mathrm{C}| \right), \tag{4.6}$$

where complex couplings $\kappa_{\mathrm{E}}(z) = \Omega(z)\sin(\theta/2)\mathrm{e}^{-\mathrm{i}\varphi}$ and $\kappa_{\mathrm{W}}(z) = -\Omega(z)\cos(\theta/2)$ induce population transfer from the outer modes to the central one and vice versa. This is similar to the construction in Sec. 4.2.1. The nonadiabatic quantum holonomy reads

$$U_A(C_{\theta,\varphi}) = \begin{bmatrix} \cos\theta & \mathrm{e}^{\mathrm{i}\varphi}\sin\theta \\ \mathrm{e}^{-\mathrm{i}\varphi}\sin\theta & -\cos\theta \end{bmatrix}. \tag{4.7}$$

Defining the computational basis $|0\rangle_\ell = |1_{\mathrm{W}}\rangle$ and $|1\rangle_\ell = |1_{\mathrm{E}}\rangle$, the unitary matrix $U_A(C_{\theta,\varphi})$ acts as a single-qubit gate. The implementation of two subsequent loops allows one to construct any single-qubit gate by holonomic means [60]. The state $|1_{\mathrm{C}}\rangle$ participates in the evolution as an ancilla but is not part of the read-out. Due to cyclicity $\delta(z_{\mathrm{f}}) = \pi$, the code $\mathscr{C} = \{|0\rangle_\ell, |1\rangle_\ell\}$ is mapped onto itself and a proper read-out of logical states is possible in terms of single-photon detectors at the end facet of the waveguides E and W.

There are some important differences between the adiabatic construction from the previous section and the nonadiabatic realisation presented here. The obvious first, nonadiabatic holonomic QC is not restricted to an adiabatic subspace, therefore diabatic contributions do not harm the quantum gate to be implemented. Secondly, in the adiabatic scenario the cyclic evolution of the dark states can be mapped onto a parameter loop in $\mathscr{M}$. This correspondence breaks down in the nonadiabatic case, where, the couplings $\{\kappa_k\}_k$ play a more passive role and can even be constant, e.g., $\Omega = \pi/z_{\mathrm{f}}$.

The fact that any coupling scheme with $\delta(z_{\mathrm{f}}) = \pi$ realises the same holonomic gate gives the experimentalist a useful design freedom for the optical network. The resilience of nonadiabatic holonomic gates towards different sources of parametric noise was studied in Ref. [63] in the context of an atomic three-level system. An improved super-robust version was proposed and analysed in Ref. [171]. Due to the mathematical equivalence with the coupled-mode Hamiltonian (4.6), most of their findings are applicable to the photonic setup as well. In the following, an error analysis for sequences of holonomic gates is given based on the results from Ref. [P7].

4.3.2.1 *Transition errors*

A loop C has to be designed by corresponding coupling pulses $\kappa_{\mathrm{W}}(z)$ and $\kappa_{\mathrm{E}}(z)$. The choice of (parameter) angles θ and φ in Eq. (4.7) fixes the gate, while any envelope $\Omega(z)$ with $\delta(z_{\mathrm{f}}) = \pi$ ensures cyclicity. However, even though the gate (4.7) is purely geometric in its make up, a sequence of those does not need to be. This has its origin in the transition error between two subsequent gates. In order to illustrate this point, suppose one first designs the loop $C_{\frac{5\pi}{2},\pi}$ resulting in a bit flip $U(C_{\frac{5\pi}{2},\pi}) = -X$. Then, a second loop $C_{\pi,0}$ is engineered, applying the phase shift $U(C_{\pi,0}) = -Z$. There is still a freedom of choice in the coupling configuration, namely the envelope $\Omega(z)$. Fig. 15 shows two different types of coupling that would ideally realise a bit flip X followed by a Z gate. However, in Fig. 15. (a) the constant coupling configuration demands for a smooth (e.g. sine-like) transition between the two gates. This transition is not geometrically robust and distorts cyclicity of the overall evolution, i.e., the photonic wave function leaks out of the computational subspace $\mathscr{C}$. In contrast, Fig. 15. (b) overcomes this issue using Gaussian pulses for each segment. Hence, the transition error can be avoided nearly perfectly, by

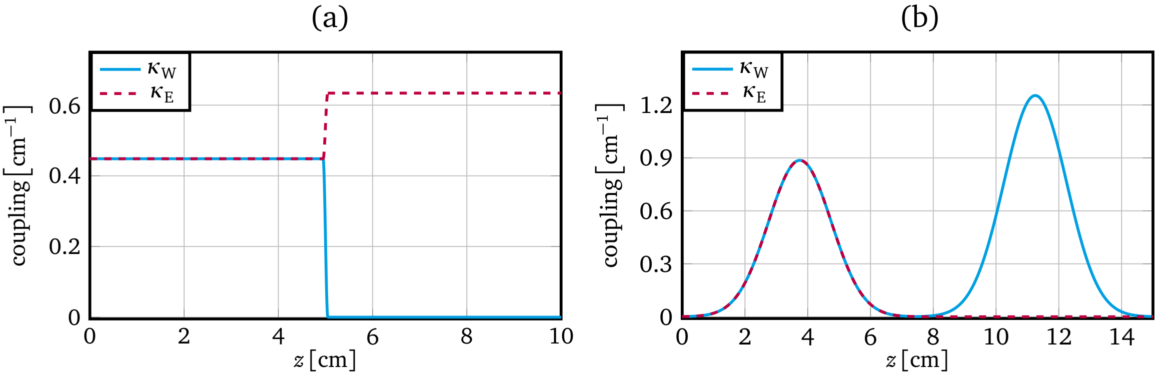

Figure 15.: Couplings κ_{W} and κ_{E} for the sequential implementation of the gate ZX as a function of the propagation length z. Each envelope function is designed to satisfy $\int_0^{z_g} \Omega(z)\mathrm{d}z \approx \pi$ per gate. (a) Constant coupling segments for the implementation of each gate with $\Omega = \pi/z_g$ and $z_g = 4.95\,\mathrm{cm}$. There is a transition length $\Delta z = 0.1\,\mathrm{cm}$ after the first gate has been applied, leading to a mismatch with the computational subspace $\mathscr{C}$. The transition is designed smoothly in terms of a sine-like geometry. (b) Gaussian-shaped coupling pulses $\Omega_X(z) = \sqrt{\pi/2}\exp[-(z-z_g/2)^2/2]$, with $z_g = 7.5\,\mathrm{cm}$, and $\Omega_Z = \Omega_X(z-z_g)$, ensuring a smooth transition between the two parameter variations. Adapted from Ref. [P6].

ensuring a smooth transition. However, the mitigation of transition errors between the gates came at a cost [P7]. Due to the Gaussian transition between the loops $C_{\frac{5\pi}{2},\pi}$ and $C_{\pi,0}$, one is forced to increase the coupling strengths and extend the propagation length for each gate substantially, because one still needs to pick up $\delta(z_{\mathrm{f}}) = \pi$ per gate. This might lead into a strong coupling regime or demand for a magnification of the experimental setup. This in turn limits miniaturisation or increases the time the qubits will be subjected to a decohering environment, thus introducing new errors. Ideally, one would like to use particular simple and resource-saving coupling schemes while avoiding transition errors as well. A remedy to this predicament will be given in Sec. 4.4.1, where holonomic computations are supported with a highly-entangled resource state, thus realising operations in parallel, instead of applying them in sequence [P7].

4.3.2.2 Errors due to bending losses

Gate errors manifesting in the propagated output state $\varrho(z)$ may not only originate from deviations in cyclicity as well as photon loss into the environment due to the bending of waveguides (see Chapter II). Our measure of quality will be the fidelity

$$F(|\psi\rangle, \varrho) = \langle\psi(z_{\mathrm{f}})|\varrho(z_{\mathrm{f}})|\psi(z_{\mathrm{f}})\rangle$$

between the ideal output state $|\psi(z_{\mathrm{f}})\rangle = ZX\,|\psi(z_0)\rangle$ and the propagated state $\varrho(z_{\mathrm{f}}) = \mathcal{N}(|\psi(z_0)\rangle\langle\psi(z_0)|)$ obtained from a noisy evolution $\mathcal{N}$ of the input state $|\psi(z_0)\rangle$. The photon loss in the kth waveguide will be modelled in terms of a loss rate $\gamma_k(z)$ [109].

(a) **Propagation with constant coupling**

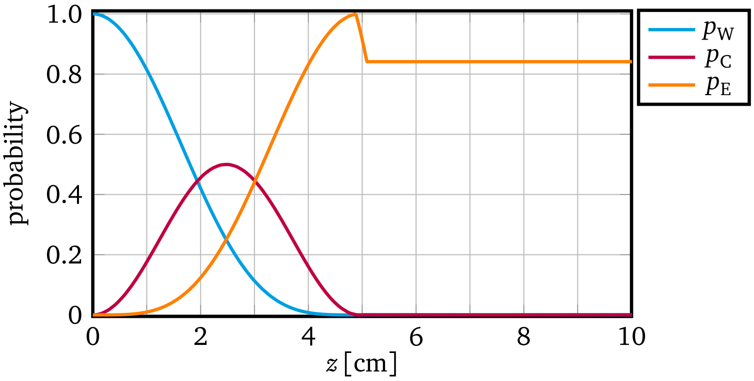

(b) **Propagation with Gaussian coupling**

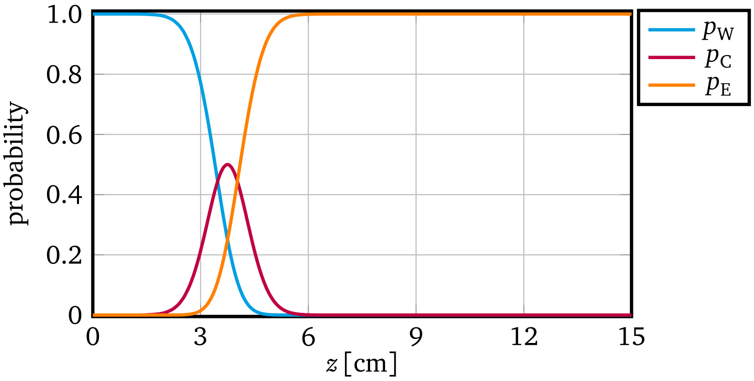

Figure 16.: Propagation of the state $|0\rangle_\ell = |1_W\rangle$ through the lossy architecture given in terms of the probability distribution $p_k(z)$ for the photon being in the kth site ($k = W, C, E$) as a function of the propagation length z. (a) Probability distribution for constant coupling segments, connected by a sine-like step [Fig. 15. (a)]. (b) Probability distribution for Gaussian coupling pulses [Fig. 15. (b)]. The plots are obtained from a numerical solution of Eq. (2.15) for the parameters $K_1 = 0.5\,\mathrm{cm}^{-1}$, $K_2 = 0.042\,\mathrm{cm}^{-1}$, $K_3 = 23.9\,\mathrm{cm}^{-1}$, and $K_4 = 0.1\,\mu\mathrm{m}^{-1}$.

Figure 16 shows the probability distribution obtained from a noisy propagation of the input state $|\psi(z_0)\rangle = |0\rangle_\ell$, for the coupling configurations from Fig. 15. (a) and (b), obtained from a numerical solution of the Master equation (2.15) (see Chapter II). Both coupling configurations (ideally) realise the gates $U_A(C_{\frac{5\pi}{2},\pi}) = -X$ and $U_A(C_{\pi,0}) = -Z$ sequentially. Ideally, the input $|0\rangle_\ell$ would evolve into $-|1\rangle_\ell$ after traversing one of the optical networks (a) or (b). Figure 16. (a) shows the two-loop implementation of the holonomic transformation $U = U_A(C_{\pi,0})U_A(C_{\frac{5\pi}{2},\pi})$ using straight waveguides for each gate that are connected via a sine-like transition segment leading to a mismatch with the computational subspace as well as introducing strong scattering into the surrounding medium. The average gate fidelity

$$\overline{F}(U,\mathcal{N}) = \frac{1}{3}\sum_k F(U\,|\psi_k\rangle\,,\varrho_k), \qquad \varrho_k = \mathcal{N}(|\psi_k\rangle\,\langle\psi_k|),$$

for an ensemble of input states $|\psi_k\rangle \in \{|0\rangle_\ell\,,|1\rangle_\ell\,,|1_\mathrm{C}\rangle\}$ is $\overline{F}_{(\mathrm{a})} = 93.11\,\%$. Next, Fig. 16. (b) shows the propagation with Gaussian-shaped coupling pulses. Due to the increased propagation length, the transition between the two gates is smooth and does not require an additional transition segment. Hence, photon loss is only due to the bending of waveguides. This amounts to a gate fidelity of $\overline{F}_{(\mathrm{b})} = 99.69\,\%$.

4.3.2.3 Holonomic coin-flip game

In order to further address the networking of holonomic gates, a simple quantum algorithm is considered in the following, that is the quantum coin-flip game [172]. Starting point of the game is a single qubit (quantum coin) prepared in the state $|0\rangle_\ell$ (e.g., head). Now both participants — Alice and Bob — secretly write down their respective operations to be applied to the qubit before measurement. Alice wins the game if the qubit remains in the state $|0\rangle_\ell$ after all operations were carried out. Bob achieves victory if the output is in the state $|1\rangle_\ell$. The game proceeds as follows: Alice will perform a first operation, then Bob applies his operation (without any knowledge of Alice's gate), finally Alice applies a third operation (without any knowledge of Bob's gate).

If Alice and Bob are both restricted to using classical operations, i.e., the identity $\mathbb{1}$ and the NOT-operation X, none of them can get an advantage over the other. Making the correct decision in such a scenario, thus amounts to guessing which of the two operations the adversary applied, i.e., there is a 50 % chance of guessing correctly. However, if Alice is equipped with the power of quantum mechanics, that is any element of U(2) is at her disposal, then she can employ a game-theory optimal strategy guaranteeing her a win. She does so by choosing her first operation to be the Hadamard transform W. In the game, this results in the state $(|0\rangle_\ell + |1\rangle_\ell)/\sqrt{2}$. This is an eigenstate of Bob's classical gate set $\{\mathbb{1}, X\}$, and thus he cannot alter the state. Independent of what Bob's choice was, Alice will apply the Hadamard gate W again. The quantum coin returns to the state $|0\rangle_\ell$, thus winning Alice the game.

A photonic realisation of the above algorithm relies on the manipulation of a dual-rail encoded qubit $|0\rangle_\ell = |1_\mathrm{W}\rangle$ and $|1\rangle_\ell = |1_\mathrm{E}\rangle$ resembling the quantum coin. Now there are two possible scenarios in the game; Bob either applies the identity $\mathbb{1}$ or he flips the qubit via X. The corresponding circuit diagrams are

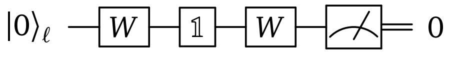

and

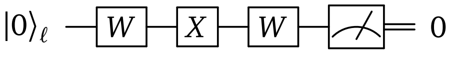

respectively. The holonomic implementation of the coin-flip game is based on the three-waveguide coupler. The corresponding loops that have to be designed for the two scenarios are

$$U_A(C_{\frac{\pi}{4},0})\mathbb{1}U_A(C_{\frac{\pi}{4},0}) = W\mathbb{1}W$$

and

$$U_A(C_{\frac{\pi}{4},0})U_A(C_{\frac{\pi}{2},0})U_A(C_{\frac{\pi}{4},0}) = WXW,$$

respectively. Experimental realisation of both scenarios was done in terms of fused-silica waveguides on a chip of length 10 cm. Repeated iteration of the game revealed that Alice's chance of winning was measured to be above 99 % in both cases.

Coupling configurations for the different loops were chosen such that transition errors became manageable. Absorption and bending losses can be handled by means of heralded single-photon measurements. Main obstacle to longer game sequences are inhomogeneities in the material limiting scalability of the individual gate. Additional details on the experiments will be published in Ref. [P5].

Concluding the analysis of experimental data, I come to the conclusion that nonadiabatic holonomies appear to be the more promising platform for the design of future quantum technologies. Even though gate fidelities were not too different compared to an adiabatic implementation, the path-shortening realisation is crucial for a potential networking of holonomic transformations. While adiabatic gates are limited to a regime where diabetic effects become imperceptible, for nonadiabatic holonomic gates designed via a constant envelope function Ω, one has $\delta(z_f) = \Omega z_f$. This means, in the nonadiabatic case, miniaturisation is only limited by the implementable coupling strength that can be realised.

4.4 Measurement-Based Quantum Computation

In this section, we look at another alternative model for QC. Around the turn of the millennium Briegel and Raussendorf developed a framework for the manipulation of quantum information that is not based on a networking of quantum gates [173, 174]. Instead, encoded information is transformed by a sequence of local measurements. These, generally, non-reversible transformations must be chosen in a sensible way so that the output state can be viewed as the result of a unitary evolution. This approach to the processing of qubits is known as measurement-based QC [166]. The starting point and initial resource of measurement-based QC is a highly-entangled state, dubbed the graph state [175].

To be more precise, consider a graph G with qubits at its vertices that are prepared either as encoded information $|\psi\rangle = \alpha_0 |0\rangle_\ell + \alpha_1 |1\rangle_\ell$ or in the state $|+\rangle$. The edges of the graph correspond to connecting the two qubits via a controlled-Z operation,

$$|\Psi_G\rangle = \prod_{(i,j)} \mathrm{CZ}_{ij}\Big(\bigotimes_k |\psi\rangle_k \bigotimes_k |+\rangle_k\Big)$$

with indices (i, j) running over the set of edges of the graph G. In Fig. 17 the construction is illustrated. Specifically, if the underlying graph has the structure of a lattice as in Fig. 17. (a), the state $|\Psi_G\rangle$ is known as a cluster state [173]. After performing a sequence

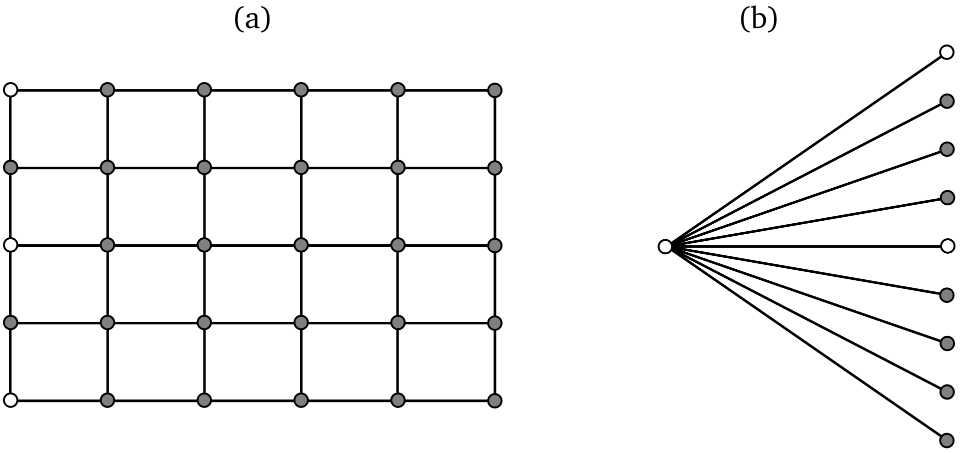

Figure 17.: Examples of graph states $|\Psi_G\rangle$ associated with a graph G. Vertices of the graph denote prepared qubits. A hollow vertex indicates a qubit that is part of the encoded information. Edges connecting the vertices refer to a controlled-Z operation between the respective qubits. (a) A specific type of graph state known as a cluster state, in which qubits are arranged in a lattice. (b) A more general type of graph state.

of local measurements on $|\Psi_G\rangle$, the remainder of the graph state can be viewed as the final output of a QC.

The most simple example that demonstrates the principles of measurement-based QC consists of two qubits $|\psi\rangle$ and $|+\rangle$ being connected by a single controlled-Z gate. For nonvanishing amplitudes α_0 and α_1 this provides an entangled state

$$|\Psi_{\circ\!-\!\bullet}\rangle = \alpha_0 \, |0\rangle_\ell \otimes |+\rangle + \alpha_1 \, |1\rangle_\ell \otimes |-\rangle \,.$$

Performing a projective measurement on the first qubit in the basis $|\pm_\varphi\rangle = (|0\rangle_\ell \pm \mathrm{e}^{\mathrm{i}\varphi} \, |1\rangle_\ell)/\sqrt{2}$, results in the second qubit being transformed into

$$|\psi^{(m)}_{\text{out}}\rangle = X^m W R_z(\varphi) \, |\psi\rangle \,.$$

Notice that the output state depends explicitly on the obtained measurement outcome $m \in \{0, 1\}$, that is if the first qubit was in the state $|0\rangle_\ell$ or $|1\rangle_\ell$. We thus identify X^m as a by-product operator of the (probabilistic) computation. As the measurement outcome m is known, its action onto the state can be removed after the computation by classical post processing, i.e., a relabelling of the logical states $|0\rangle_\ell$ into $|1\rangle_\ell$ and vice versa. For practical purposes, it is often convenient to interpret the adaptive measurement as being implemented by a single-qubit gate $U(\varphi) = \mathrm{e}^{\mathrm{i}\varphi/2} R_z(\varphi) W$ acting on the graph state, followed by a Pauli-Z measurement. The corresponding circuit reads

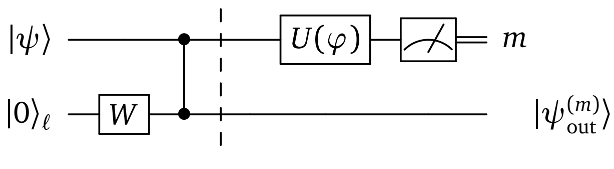

with the dashed vertical line separating the graph state preparation from the local measurements.

The previous example can be readily extended so that it allows for the simulation of any single-qubit gate. Therefore, a chain of four qubits has to be prepared

$$|\Psi_{\circ-\bullet-\bullet-\bullet}\rangle = \mathrm{C}Z_{12}\mathrm{C}Z_{23}\mathrm{C}Z_{34}\big(\,|\psi\rangle \otimes |+\rangle^{\otimes 3}\,\big).$$

Here, the first qubit is considered as an encoded input $|\psi\rangle$. Performing a sequence of measurements $\{|\pm_{\varphi_i}\rangle\,\langle\pm_{\varphi_i}|\}_i$ on the first three qubits, $i = 1, 2, 3$, results in the fourth qubit being teleported onto the state

$$\begin{aligned} |\psi^{(m)}_{\mathrm{out}}\rangle &= X^{m_3} W R_z(\varphi_3) X^{m_2} W R_z(\varphi_2) X^{m_1} W R_z(\varphi_1)\,|\psi\rangle\,, \\ &= X^{m_3} Z^{m_2} X^{m_1} W R_z\big((-1)^{m_2}\varphi_3\big) R_x\big((-1)^{m_1}\varphi_2\big) R_z(\varphi_1)\,|\psi\rangle\,, \end{aligned} \tag{4.8}$$

where the commutation relations

$$R_z(\varphi_i)X = XR_z(-\varphi_i), \quad R_x(\varphi_i)Z = ZR_x(-\varphi_i),$$

and $WX = ZW$ were used. We observe that, a conditioning of the parameter angles $\varphi_2' = (-1)^{m_1}\varphi_2$ and $\varphi_3' = (-1)^{m_2}\varphi_3$ is necessary to obtain the desired output state deterministically. The quantum circuit diagram of this procedure is just a concatenation of the previous diagram

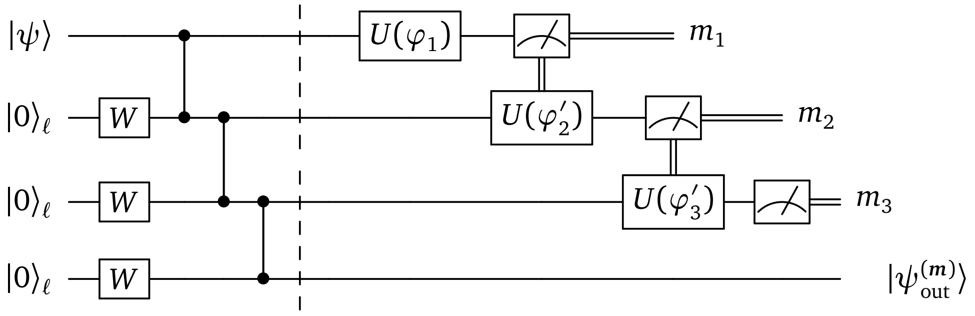

including a (classical) conditioning of the gates that act on qubit two and three. By adjusting the measurement angles φ_i any desired single-qubit operation can be applied to the input $|\psi\rangle$. The by-product operator in Eq. (4.8) can be removed via post processing.

It remains to show that the measurement-based approach allows for the construction of entangling two-qubit operations, necessary for universality. Starting from the four-qubit graph state

$$|\Psi_{\circ-\bullet-\bullet-\circ}\rangle = \mathrm{C}Z_{12}\mathrm{C}Z_{23}\mathrm{C}Z_{34}\big(\,|\psi\rangle \otimes |+\rangle^{\otimes 2} \otimes |\psi\rangle\,\big),$$

we obtain the output state

$$|\psi^{(m)}_{\mathrm{out}}\rangle = Z^{m_2} \otimes Z^{m_1}\mathrm{C}Z\big(\,|\psi\rangle \otimes |\psi\rangle\,\big)$$

via a Pauli-X measurement of qubit two and three. The corresponding circuit reads

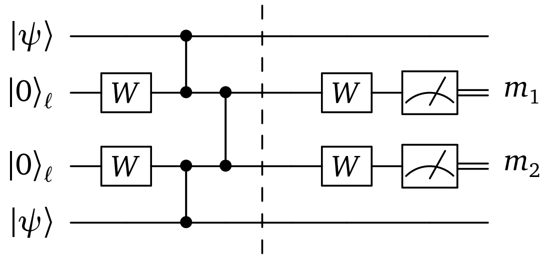

The above examples demonstrate that it is generally possible to perform universal QC by connecting individual qubits using entangling gates followed by local measurements. A two-dimensional graph state is necessary for this endeavour, because one needs to support the construction for the CZ operation with single-qubit operations [175]. Measurement-based QC is desirable over a circuit architecture whenever the preparation of a graph state and single-qubit measurements are physically easier to implement than the successive realisation and application of fragile entangling quantum gates. Originally, measurement-based QC was envisaged to be implemented in terms of optical lattices consisting of ultra-cold atoms [176, 177]. Within this setting, preparation of the graph state is carried out by turning on (two-local) Ising interactions that connect neighbouring qubits. Nevertheless, quantum optics has excelled to become the primary contestant for measurement-based QC [178, 179], and a measurement-based Deutsch algorithm has already been realised in experiment [180]. One of the reasons for this development is that after the laborious preparation of the graph state, one is rewarded with a particular simple realisation of local measurements solely in terms of linear optical elements.

4.4.1 Concatenation of gate simulations

The occurrence of random by-product operators is an ever present feature of measurement-based QC. In the following, the treatment of these will be formalised [173, 175]. Given a graph state $|\Psi_G\rangle$ on which local measurements have been performed, the output state of the computation can be written as $|\psi_{\text{out}}\rangle = \prod_k U_{\Sigma_k} U_k |\psi\rangle$. Here, U_k are individual unitary operations induced by each measurement and U_{Σ_k} are their respective by-product operators originating from the random measurement outcome. Commuting the by-product operators to the left, so that they can be dealt with at the end of the computation, results in $|\psi_{\text{out}}\rangle = U_\Sigma \prod_k U'_k |\psi\rangle$. The modified unitaries U'_k can depend on the measurement results associated with previous operations, and U_Σ is the total by-product operator lying in the Pauli group $\mathscr{P}_n$. The latter can be dealt with by means of classical post-processing [173]. Note that if U_k lies in the Clifford group $\mathscr{N}(\mathscr{P}_n)$, then we have $U'_k = U_k$. In order to deterministically use non-Clifford operations, one has to condition the adaptive measurement on previous outcomes, within runtime of the algorithm, thus introducing a notion of temporal complexity into measurement-based QC [173]. As an example, recall Eq. (4.8) in which the individual by-product operators $U_{\Sigma_k} = X^{m_k}$ were commuted to the left, resulting in the overall by-product operator $U_\Sigma = X^{m_3} Z^{m_2} X^{m_1}$. Generally, the unitary operations $U_k = R_k(\varphi_k)$ do not lie in the Clifford group, and thus had to be adapted on previous measurements, i.e., $\varphi'_k = (-1)^{m_{k-1}} \varphi_k$ for $k = 2, 3$.

4.4.2 Holonomic manipulation of graph states

Besides each coming along with a number of desirable fault-tolerance features, practical implementations of holonomic QC and measurement-based QC will still suffer from errors. For instance, an approach based on a networking of nonadiabatic holonomies suffers from transition errors between subsequent loops (cf. Sec. 4.3.2.1), thus implementing a slightly distorted gate. Moreover, long propagation times will inevitably increase decoherence (e.g., photon loss) until interaction with the environment becomes dominant. On the other hand, in a measurement-based QC operations can be applied in parallel, but the computation is harmed by imprecisions in the measurement setup, thus projecting on a slightly erroneous output state.

In the following, I will devise a hybrid approach between holonomic QC and measurement-based QC [P7]. The key idea is to perform the adaptive measurements in a rotated basis that is obtained by means of a nonadiabatic holonomy. Due to the entanglement of the underlying graph state, gate operations in holonomic QC can be carried out in parallel. One therefore does not need to design holonomic gates sequentially avoiding transition errors all together.

In this combined model, individual qubits in a graph state $|\Psi_G\rangle$ undergo simultaneous loops C_k, for $k = 1, \ldots, K$. Thus, the graph state is manipulated by a sequence of local (single-qubit) unitaries resulting in the state

$$\prod_{k=1}^{K} U_A(C_k)\,|\Psi_G\rangle\,,$$

In the final step of the model, local measurements in the computational (Pauli-Z) basis are performed on the qubits $k = 1, \ldots, K$. Each measurement leads to the remainder of the graph state accumulating a by-product operator U_{Σ_k}. The circuit diagram of the hybrid approach reads

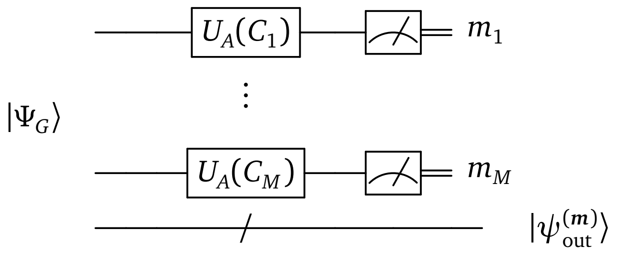

Clearly, this is a form of measurement-based QC, in which the projective measurements

$$U_A(C_k)\,|m\rangle_\ell\,\langle m|_\ell\,U_A^\dagger(C_k)$$

with $m \in \{0, 1\}$, were obtained from holonomies $U_A(C_k)$ acting on the kth qubit. Under the assumption of noiseless Pauli-Z measurements and an accurately prepared graph state $|\Psi_G\rangle$, the final output is completely determined by the loops $C_1, \ldots, C_K$. Therefore, this specific graph state computation inherits the fault-tolerance features and intrinsic robustness of holonomic QC. The circuit diagram depicts a situation in which all operations are applied simultaneously. Similar to the standard formalism on measurement-based QC, holonomic non-Clifford operations $U_A(C_k)$ demand for a conditioning on previous measurements in order to make the entire paradigm deterministic. In this picture, the temporal complexity, i.e., the number of non-Clifford operations to be utilised in a computation, might be interpreted as a minimal path length of the loops $C_1, \dots, C_K$, in order to allow conditioning on previous measurements.

For completeness, even though quantum holonomies are a rather special type of unitaries, the above paradigm still allows for universal measurement-based QC. This can be seen most easily, by considering the holonomic gates (4.7), harnessed from the three-waveguide coupler. Consider four such couplers, in each of which, a single photon is injected. The four photons shall be entangled to each other such that they are described by the graph state $|\Psi_{\circ\!-\!\bullet\!-\!\bullet\!-\!\bullet}\rangle$, where qubits are defined through a path encoding, i.e., $|0\rangle_\ell = |1_\mathrm{W}\rangle$ and $|1\rangle_\ell = |1_\mathrm{E}\rangle$. If an individual qubit in the graph state traverses a loop $C_{\frac{\pi}{4},\varphi_k} = C_{\varphi_k}$ with $\theta = \pi/4$ before being measured in the computational basis, this corresponds to a measurement in the rotated basis $|+_{-\varphi_k}\rangle = U_A(C_{\varphi_k})\,|0\rangle_\ell$ and $|-_{\varphi_k}\rangle = -U_A(C_{\varphi_k})\,|1\rangle_\ell$, where

$$U_A(C_{\varphi_k}) = \frac{1}{\sqrt{2}} \begin{bmatrix} 1 & \mathrm{e}^{\mathrm{i}\varphi_k} \\ \mathrm{e}^{-\mathrm{i}\varphi_k} & -1 \end{bmatrix}.$$

Any single-qubit unitary can be applied to the encoded state $|\psi\rangle$ by adaptive measurements on the first three qubits

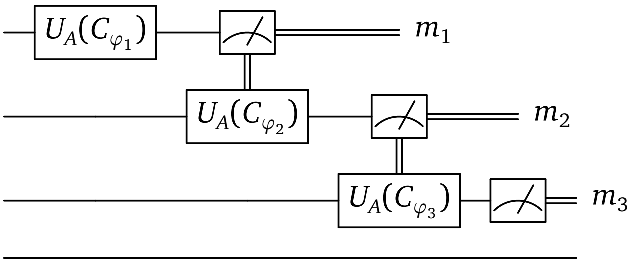

Note that the conditioning of later measurements on previous ones can, in principle, always be accounted for by adjusting the envelope $\Omega_k(z)$ for the holonomy $U_A(C_{\varphi_k})$. A nontrivial two-qubit gate CZ can be implemented by first preparing the graph state $|\Psi_{\circ\!-\!\bullet\!-\!\bullet\!-\!\circ}\rangle$, and then measuring qubits two and three in the Pauli-X basis (similar to Sec. 4.4). The corresponding circuit reads

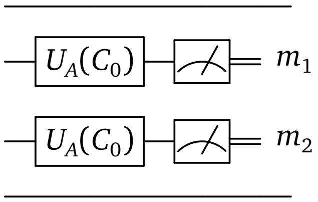

In summary, standard results on measurement-based QC were utilised to conclude that universal photonic QC is possible, when an array of multiple three-waveguide couplers is provided with a highly entangled resource state. This can be done, using nonadiabatic holonomies, by employing a dual-rail encoding for pairs of modes into which a single photon is injected.

4.4.2.1 Parallelisation vs. composition

In order to point out advantages of performing QC in this hybrid model, a comparison to the standard circuit implementation — based on a sequence of holonomies — will be conducted [P7].

If one follows the hybrid approach, single-qubit holonomic gates X and Z can be applied in parallel using a chain of three qubits. The graph state for this case reads

$$|\Psi_{\circ\!-\!\bullet\!-\!\bullet}\rangle = \mathrm{C}Z_{12}\mathrm{C}Z_{23}\big(|\psi\rangle \otimes |+\rangle^{\otimes 2}\big)$$

Performing simultaneous measurements on the first two qubits with angles $\varphi_1 = \varphi_2 = \pi$, the third qubit transforms to $U_\Sigma ZX\,|\psi\rangle$ with $U_\Sigma = (-1)^{m_1} X^{m_2} Z^{m_1}$ being the associated by-product operator. The circuit diagram associated with this measurement scheme reads

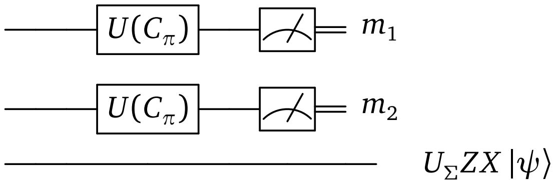

This corresponds to a total of 9 waveguides, as for every (dual-rail encoded) qubit there is a central ancilla mode mediating the coupling. In the above computation, conditioning on previous measurements is obsolete, because the gate ZX to be realised, lies in the Clifford group.

The local unitaries that manipulated the qubits before measurement are designed again by nonadiabatic holonomies with constant $\Omega = \pi/z_\mathrm{f}$. Due to the straight waveguide design, bending losses do not occur, unlike in the two-loop scenario discussed in Sec. 4.3.2.2. Furthermore, because gate operations are applied in parallel, transition segments between the gates that would distort cyclicity (see Sec. 4.3.2.1) are obsolete. Hence, the gate fidelity in this case amounts to $\overline{F} = 100\,\%$. This shows clearly that nonadiabatic holonomic QC can profit from the parallelisation of gate operations, making it robust towards transition errors and bending losses, while keeping the optical network scalable. Conversely, nonadiabatic holonomic QC is known to be robust towards parametric and timing errors [63]. Moreover, the holonomic implementation gives the experimentalist a freedom of design for the photonic network that might be helpful in achieving an effective conditioning of non-Clifford operations. Therefore, I forecast a *fruitful symbiosis* between measurement-based QC and holonomic QC that could potentially lead to more reliable quantum information processors [P7].

V | Braids and the Jones Polynomial

Topology is the study of the spatial properties of objects that are preserved under continuous deformations. In physical systems such invariants manifest themselves in global degrees of freedom. For instance, the statistics of non-Abelian anyons in effectively (2+1)-dimensional models only depend on the number and order of braids the quasi-particles underwent before their fusion [168, 181]. This braiding is often expressible as the holonomy of a suitable (anyonic) connection [58]. Therefore one can think about the braiding of anyons as a specific realisation of a geometric phase that possesses maximal topological content. This further hints at the existence of a continuous route from holonomic to topological QC [57]. Signatures of quantised phases have already been measured in superconductors [182, 183] originating from the fractional quantum Hall effect. A braiding of (Ising) anyons has been realised experimentally in integrated photonic waveguides [129, 184, 185], but these implementations fail to be universal [186]. Design strategies are often based on the preparation of pairs of so-called Majorana fermions [187, 188]. It turns out that, beyond their desirable fault-tolerance features, anyonic statistics can be linked to new quantum algorithms that differ substantially from the more familiar search algorithms [6] and cryptographic protocols [10].

Knot theory, a subarea of topology, is concerned with the topological equivalence of knots [189]. Quantities that characterise knots (modulo continuous deformations), such as the seminal Jones polynomial [190], are known as knot invariants. These polynomials are of interest whenever strand-like structures emerge. For instance, Jones polynomials were first connected to topological quantum field theories by Witten [42]. Since then, they have been linked to various areas of research, such as the study of DNA ring molecules [191], topological entanglement [192], and statistical physics [193]. However, distinguishing knots in terms of the Jones polynomial demands for a diagrammatic unravelling of the strands. This becomes quickly unfeasible when the number of crossings in a knot increases. Because the evolution of anyons depends only on the braiding of their world lines, the final measurement statistic behaves similar to a knot invariant. Determining Jones polynomials is a BQP-complete problem [194], and doing so through anyonic evolutions outperforms any known classical algorithm [195].

The chapter contains an introduction to Jones polynomials in Sec. 5.1. Particular emphasis is given on the representation of knots in terms of (unitary) braids. In Sec. 5.2, the role of Jones polynomials in topological quantum field theories is briefly elucidated. In Sec. 5.3, I devise a measurement-based version of the Hadamard test suitable for an all-out photonic estimation of Jones polynomials. In the spirit of this thesis, nonadiabatic holonomies will be employed to carry out the algorithm in a fully geometric fashion.

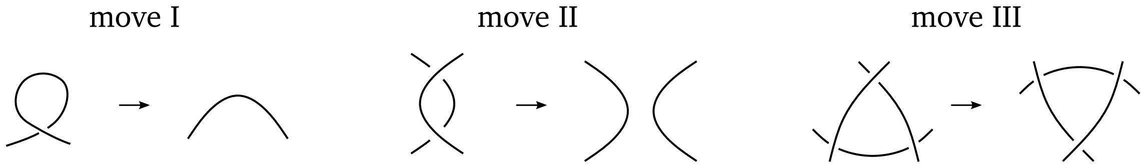

Figure 18.: Continuous deformations of strands expressed by the three Reidemeister moves. Move I removes twisting of a strand. Move II separates strands that lie on top of each other. Move III shifts a strand under a crossing.

5.1 The Jones Polynomial Algorithm

Knot theory is a subject concerned with the equivalence of knots up to smooth deformations, such as shifting, bending, or twisting of their strands [189]. A quantity that distinguishes knots that differ beyond these so-called *ambient isotopies* is known as a knot invariant. To be more precise, given an image (embedding into the plane) of a knot, a knot invariant does not change under the three Reidemeister moves shown in Fig. 18, as these do not cut into the knot.

A first step towards the construction of a knot invariant is the translation of images of knots into a mathematical quantity that is consistent with the Reidemeister moves. A first candidate to achieve this is the Kauffman bracket $\langle K \rangle$ of a knot K. Under the Kauffman bracket crossings in the knot are evaluated according to the Skein relations introduced in Fig. 19. This introduces avoided crossings finally resulting in a weighted sum of multiple unknots. Additionally, let $\langle \bigcirc \rangle = 1$ for the bracket of the unknot $\bigcirc$, as well as $\langle \bigcirc \sqcup K \rangle = d \langle K \rangle$ for any disjoint union with a knot K. Here, d is a complex number yet to be determined. Therefore, let $\bigcirc\!\!\!\bigcirc$ be two overlapping strands. The second Reidemeister move implies that these can be separated, i.e., $\langle \bigcirc\bigcirc \rangle = \langle \bigcirc\!\!\!\bigcirc \rangle$. Moreover, $\langle \bigcirc\bigcirc \rangle = d \langle \bigcirc \rangle$. Applying the Skein relations to $\langle \bigcirc\!\!\!\bigcirc \rangle$, demands that

$$\langle \bigcirc\bigcirc \rangle - \langle \bigcirc\!\!\!\bigcirc \rangle = d + A^2 + A^{-2} = 0.$$

Hence, $d = -A^2 - A^{-2}$. With the above set of rules at hand, any knot can be unraveled into a series of unknots with different coefficients, thus resulting in a polynomial in $A \in \mathbb{C}$.

As an elementary example, consider the twisted representations of the unknot $\bigcirc$ shown in Fig. 20. While the Kauffman bracket of the second knot coincides with the one of the

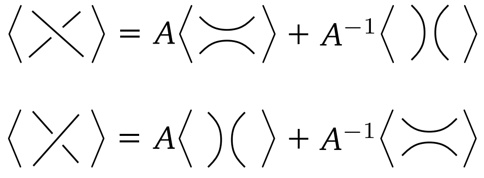

Figure 19.: Skein relations to resolve crossings in a knot. The knots build from the avoided crossings are weighted with complex numbers A and A^{-1}, respectively.

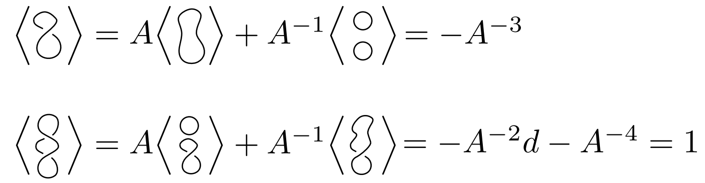

Figure 20.: Kauffman brackets of braided representations of the unknot ◯. The upper and lower knot can be deformed into ◯ by applying the Reidemeister move I and II, respectively.

unknot, i.e., $\langle$◯$\rangle = 1$ (as one would like from a proper knot invariant), the one of the first knot does not. Hence, the Kauffman bracket fails to be a knot invariant. This could have been expected as it is only invariant under the Reidemeister moves II and III but not move I. This can be directly observed by applying the Skein relations to move I. Specifically, resolving the crossing in move I gives an additional factor of $(-A)^3$ for which a proper knot invariant has to compensate.

In order to construct a polynomial that is invariant under all three Reidemeister moves, a correction to the Kauffman bracket in terms of the writhe $w(K)$ is necessary. As illustrated in Fig. 21. (a), the writhe gives an orientation to the strands of a knot, and according to this orientation every crossing contributes with positive or negative sign. For example, the Hopf link K_{HL} shown in Fig. 21. (b) is equipped with a positive orientation, thus having a writhe of $w(K_{\mathrm{HL}}) = 2$. Finally, the Jones polynomial of a knot K can be defined [190]

$$V_K(A) = (-A^3)^{-w(K)} \langle K \rangle \,. \tag{5.1}$$

If two knots K and K' are topologically equivalent, then their corresponding Jones polynomials coincide, i.e., $V_K(A) = V_{K'}(A)$. In contrast, if $V_K(A) \neq V_{K'}(A)$, then one has the case of two knots that differ beyond ambient isotopies, i.e., it follows $K \neq K'$. It should be emphasised that this construction does not give a one-to-one correspondence between knots and polynomial, as for instance, two nonequivalent knots can have the same Jones polynomial. A knot invariant that gives distinct values for each knot is said to be a complete knot invariant [189]. While Jones polynomials are not complete, complete knot invariants

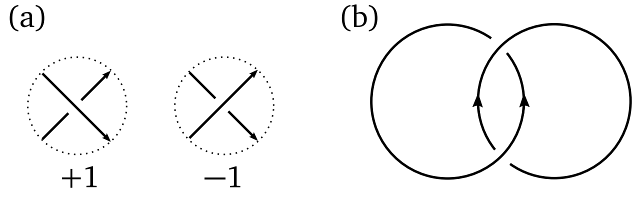

Figure 21.: (a) Convention for the contribution to the writhe from each crossing. (b) Knot diagram of the Hopf link with positive orientation.

exist such as the *knot complement*. Table 2 summarises the relation between knots and their Jones polynomials [40].

Knots		Jones polynomial
$K = K'$	$\Rightarrow$	$V_A(K) = V_A(K')$
$K \neq K'$	$\Leftarrow$	$V_A(K) \neq V_A(K')$

Table 2.: Relation between knots and their Jones polynomials. Inspired by Ref. [40].

The writhe is simple to calculate, scaling only linear with the number of crossings n. As such, the complexity of computing the Jones polynomial is mainly due to the Kauffman bracket. The recursive relationship dictated by the Skein relations demands for the evaluation of 2^n diagrams giving rise to an exponential increase in computational expense.

5.1.1 Knots from braids

In order to give more structure to a knot it is natural to view the latter as being generated from a sequence of elementary braids b_i, for $i = 1, \ldots, s-1$, that are then glued together. Here, s is the number of strands from which the knot is constructed. These braids, together with their inverses, form a group known as the s-strand Artin braid group $\mathscr{B}_s$ [196]. The action of b_i and b_i^{-1} onto the strands is illustrated in Fig. 22. Due to their diagrammatic origin, these elementary braids satisfy the Yang-Baxter equations [40]

$$\text{for} \quad i \neq j \pm 1: \quad b_i b_j = b_j b_i, \qquad b_i b_{i+1} b_i = b_{i+1} b_i b_{i+1}, \qquad b_i b_i^{-1} = b_i^{-1} b_i = e. \tag{5.2}$$

In the third equation, e denotes the identity element in $\mathscr{B}_s$ that is associated with leaving the strands unbraided. Figure 23 illustrates the above relations through their diagrammatic form.

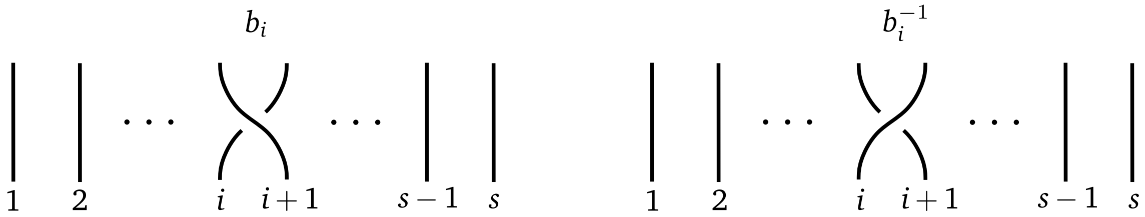

Figure 22.: Diagrammatic representation of the elementary braid b_i and its inverse b_i^{-1} acting on a collection of s strands.

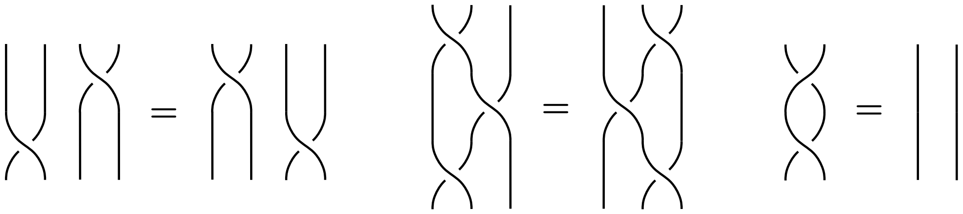

Figure 23.: Diagrammatic relations corresponding to the Yang-Baxter equations (5.2), satisfied by all b_i in the s-strand braid group $\mathscr{B}_s$.

The loose ends of a braid word b in $\mathscr{B}_s$ can be connected to each other in a variety of ways, thus resulting in a knot. Given a braid word

$$b = \prod_l b_{i_l}^{k_l}, \qquad i_l \in \{1, \ldots, s-1\}, \qquad k_l \in \{-1, 1\},$$

the corresponding braid closure is denoted as $\overline{b}$. In this picture, the writhe of a knot is just $w(\overline{b}) = \sum_l k_l$. Figures 24. (a) and (b) depict the trace and plat closure of a knot, respectively. Notice that any knot can be constructed (always in multiple ways) from the closure of a product of elementary braids, a result known as Alexander's theorem [197].

5.1.2 The Temperley-Lieb algebra

For many practical calculations it is advantageous to have a matrix representation ρ of the s-strand braid group $\mathscr{B}_s$. The matrices $\rho(b_i)$ then conserve the Yang-Baxter equations (5.2), thus handing us an algebraic description of a knot. A particular useful representation maps elements in $\mathscr{B}_s$ onto complex matrices with the help of the Temperley-Lieb algebra TL_s [40]. The latter is generated from elements E_i with $i = 1, \ldots, s-1$, that satisfy

$$\text{for} \quad i \neq j \pm 1: \quad E_i E_j = E_j E_i, \qquad E_i E_{i+1} E_i = E_i, \qquad E_i^2 = d E_i. \tag{5.3}$$

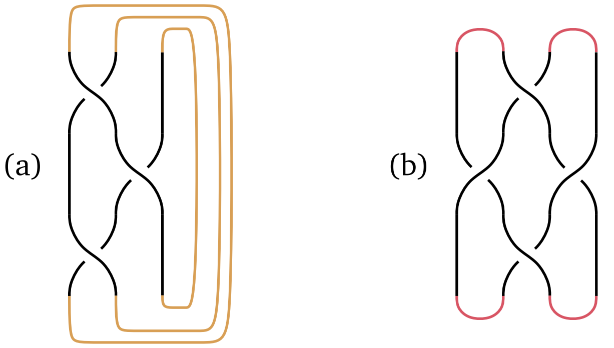

Figure 24.: Diagrammatic representation of braid closures. (a) Trace closure of the braid word $b_1 b_2 b_1$. (b) Plat closure of the braid word $b_2 b_1^{-1} b_3^{-1} b_2$. Adapted from Ref. [P7].

With these generators at our disposal, the matrix representation of an elementary braid b_i is defined as

$$\rho(b_i) = A\mathbb{1} + A^{-1}E_i, \qquad \rho(b_i^{-1}) = A^{-1}\mathbb{1} + AE_i. \tag{5.4}$$

The reader can readily convince themselves, using the relations (5.3), that the matrices $\rho(b_i)$ satisfy the Yang-Baxter equations (5.2), thus revealing the necessity of the Temperley-Lieb algebra to be established first. The representation of a more general braid word $b = \prod_l b_{i_l}^{k_l}$ is then just given by the matrix product $\rho(b) = \prod_l \rho(b_{i_l}^{k_l})$.

5.1.3 Algebraic calculation of the Jones polynomial

Given a representation ρ of the s-strand braid group $\mathscr{B}_s$, the Jones polynomial $V_K(A)$ of a knot $K = \overline{b}$ can be obtained from an evaluation of the matrix trace $\mathrm{Tr}\{\rho(b)\}$ [40, 181]. The explicit relation between these two quantities depends on the specific form of the representation ρ as well as the closure. While there are, in principle, many such representations, in this work I will only be concerned with those that are unitary, i.e., $\rho^\dagger(b_i)\rho(b_i) = \mathbb{1}$ for all $i = 1, \ldots, s-1$. This implies that E_i is a Hermitian matrix and $|A| = 1$, as can be verified from Eq. (5.4). For example, a unitary representation for the three-strand braid group ($s = 3$) was derived in Ref. [198]. There, the generators of the Temperley-Lieb algebra were given as

$$E_1 = \begin{bmatrix} d & 0 \\ 0 & 0 \end{bmatrix}, \qquad E_2 = \begin{bmatrix} d^{-1} & \sqrt{1-d^{-2}} \\ \sqrt{1-d^{-2}} & d - d^{-1} \end{bmatrix}.$$

For $A = \mathrm{e}^{\mathrm{i}\theta}$ with

$$\theta \in [0, \pi/6] \sqcup [\pi/3, 2\pi/3] \sqcup [5\pi/6, 7\pi/6] \sqcup [4\pi/3, 5\pi/3] \sqcup [11\pi/6, 2\pi]$$

the matrices

$$\rho(b_1) = \begin{bmatrix} -A^{-3} & 0 \\ 0 & A \end{bmatrix}, \qquad \rho(b_2) = \begin{bmatrix} A + A^{-1}d^{-1} & A^{-1}\sqrt{1-d^{-2}} \\ A^{-1}\sqrt{1-d^{-2}} & A + A^{-1}\left(d - d^{-1}\right) \end{bmatrix}, \tag{5.5}$$

are the generators of a unitary representation of the group $\mathscr{B}_3$. For the given representation, the Kauffman bracket of a trace closure $\overline{b}$ can be calculated in terms of a matrix trace [198, 199]

$$\langle \overline{b} \rangle = \mathrm{Tr}\{\rho(b)\} + A^{w(b)}(d^2 - 2), \tag{5.6}$$

In particular, the identity element $\rho(e) = \mathbb{1}$ leads to $\langle \overline{e} \rangle = d^2$, which is consistent with a diagrammatic calculation of $\langle \bigcirc \bigcirc \bigcirc \rangle$.

Unitary representations of the s-strand braid group $\mathscr{B}_s$ for $s \geq 3$, can be obtained explicitly by means of the AJL (Aharonov-Jones-Landau) algorithm [181, 200] but (in its original formulation) only allows for an evaluation of the Jones polynomial for isolated

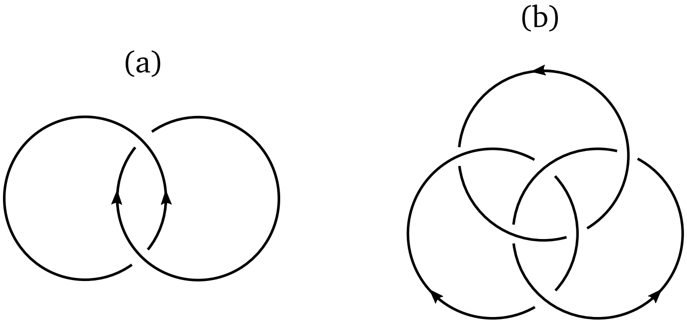

Figure 25.: Diagrammatic representation of knots. Arrows indicate orientation of each strand. (a) Knot diagram of the Hopf link generated from the braid word $b_1 b_1$. (b) Knot diagram of the Borromean rings being the trace closure of the braid word $b_1 b_2^{-1} b_1 b_2^{-1} b_1 b_2^{-1}$.

values of θ. An extension of this algorithm to continuous values of θ was presented by Kauffman and Lomonaco in Ref. [201]. For the interested reader, I outline their procedure and give a representation of the four-strand braid group $\mathscr{B}_4$ in Appendix A.4.

5.1.4 Jones polynomials of knots on three strands

For the purpose of illustration, I demonstrate the algebraic calculation of the Jones polynomial on two benchmark examples, the Hopf link and the Borromean rings shown in Fig. 25. (a) and (b), respectively.

The Hopf link K_{HL} resembles two interlocked rings and can be constructed on two strands only, via a closure of the braid word $b = b_1 b_1$. Its unitary representation evaluates to $\mathrm{Tr}\{\rho(b)\} = A^2 + A^{-6}$. The Kauffman bracket (5.6) evaluates to

$$\langle \overline{b} \rangle = d^{-1}\left(A^2 + A^{-2} + A^6 + A^{-6}\right) = -A^4 - A^{-4}.$$

where $w(\overline{b}) = 2$ was used. The additional factor d^{-1} occurs, due to an additional strand in $\mathscr{B}_3$ that is not part of the Hopf link and therefore has to be removed. This yields the Jones polynomial of the Hopf link

$$V_{K_{\text{HL}}}(A) = -A^{-2} - A^{-10}.$$

This result is in agreement with a diagrammatic calculation of the Jones polynomial using the Skein relations.

As a second example, consider a knot that can be constructed on three strands. The so-called Borromean rings K_{BR} are obtained from a (trace) closure of the braid word

$b = b_1 b_2^{-1} b_1 b_2^{-1} b_1 b_2^{-1}$. Its matrix representation (5.4) is computed to

$$\rho(b) = \begin{bmatrix} \dfrac{2A^4 - A^8 + 2A^{12} - A^{16} + A^{20} - 1}{A^{12} + A^{16}} & -\dfrac{(A^4-1)^2(A^8+1)\sqrt{1+A^4+A^8}}{A^{10}+A^{14}} \\ \dfrac{(A^4-1)^2(A^8+1)\sqrt{1+A^4+A^8}}{A^6+A^{10}} & \dfrac{1 - A^4 + 2A^8 - A^{12} + 2A^{16} - A^{20}}{A^4+A^8} \end{bmatrix}. \tag{5.7}$$

Inserting the result into Eq. (5.6), while noting that $w(\overline{b}) = 0$ gives the corresponding Jones polynomial

$$V_{K_{\text{BR}}}(A) = -A^{12} - A^{-12} + 3A^8 + 3A^{-8} - 2A^4 - 2A^{-4} + 4.$$

This is in agreement with the results of a graphical calculation in terms of the Skein relations. The latter would demand for an evaluation of $2^6 = 64$ diagrams.

5.2 Jones Polynomials in Topological Quantum Field Theory

Up to this date, quantum field theory is still the most renowned tool to describe elementary particle and high-energy physics. It is the backbone of the Standard Model which successfully explains the electromagnetic, the weak, and the strong interaction [114]. Experimental testing verifies its predictions to a high degree of accuracy [202]. As these are all gauge theories, their equations of motion are derived from an action principle of the form $\delta S[A] = 0$. Variational calculus is carried out with respect to the gauge potential $A(x^\mu)$ that depends on the coordinates $x^\mu = (t, x, y, z)$ on the spacetime $\mathscr{M}$. Here, the action

$$S[A] = \int_{\mathscr{M}} L(A_\mu, \partial_\nu A_\mu) \mathrm{d}x^\mu$$

is expressed through a suitable Lagrangian L, determining the forces at work. This construction ensures that the corresponding Euler-Lagrange equations are invariant under a change of gauge. For instance, the Lagrangian of the electromagnetic field $L_{\text{EM}} = \frac{1}{2}(\varepsilon_0 |\boldsymbol{E}|^2 - \mu_0^{-1} |\boldsymbol{B}|^2)$ leads to Maxwell's equations in vacuum. Here, the fields can be expressed using the vector potential $\boldsymbol{A}$, viz. $\boldsymbol{E} = -\partial_t \boldsymbol{A}$ and $\boldsymbol{B} = \boldsymbol{\nabla} \times \boldsymbol{A}$. It turns out that the requirement of gauge invariance strongly limits the possible Lagrangian, describing a physical theory in a $(3+1)$-dimensional spacetime.

Strikingly, if one considers a $(2+1)$-dimensional spacetime, there are novel Lagrangians that describe a physical theory, due to the simplified setting. Witten pointed out that the Lagrangian [142]

$$L_{\text{CS}}(A_\mu, \partial_\nu A_\mu) = \frac{m}{2} \varepsilon^{\mu\nu\sigma} A_\mu \partial_\nu A_\sigma, \tag{5.8}$$

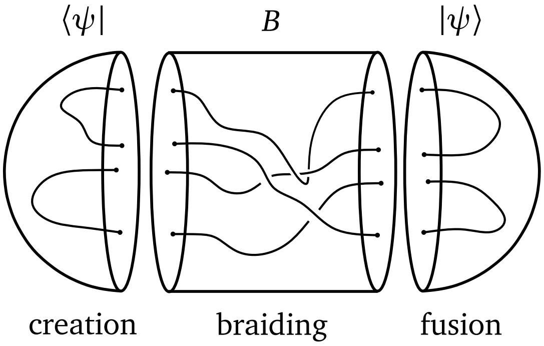

Figure 26.: Anyonic evolution of a state $|\psi\rangle$ in a (2+1)-dimensional spacetime. Time flows from the left to the right. Initially, pairs of anyons are created from the vacuum. As time goes by, these undergo an exchange interaction due to a braiding B of their world lines. Fusion of the anyons results in a knot being formed.

with $\varepsilon^{\mu\nu\sigma}$ being the (totally anti-symmetric) Levi-Civita symbol, leads to the Chern-Simons action $S_{\mathrm{CS}}[A]$, which is invariant under a change of gauge[1] $A_\mu^\omega = A_\mu + \partial_\mu \omega$. Here, $\omega(x^\mu)$ is a smooth function of the spacetime coordinates $x^\mu = (t, x, y)$. In Eq. (5.8), the constant m is given in units of mass. Hence, the equations of motion induced by L_{CS} give rise to *massive* electromagnetic fields (or massive photons) [203].

It should be emphasised that the theory described by the Lagrangian L_{CS} is fundamentally different from the physics encountered in a $(3+1)$-dimensional spacetime. Specifically, L_{CS} does not depend on the local geometry of the underlying spacetime[2]. In other words, the interaction between particles (e.g., the charges) does not depend on their relative position. Remarkably, such exotic behaviour can be realised in experiment by designing quantum mechanical systems whose configuration is confined to a quasi $(2+1)$-dimensional structure. For example, measuring the Hall effect using strong magnetic fields at low temperatures, the Brownian motion of electrons becomes negligible compared to the incident Lorentz force. Thus, the system behaves according to its dynamics confined to a two-dimensional space. As a result, the measured Hall resistivity becomes a topological invariant given by the winding number of the electric current, see e.g., [40]. Another implementation uses non-Abelian braiding of light, rendered possible by injecting coherent states into *topologically guided modes* in specially fabricated photonic waveguide arrays [184, 185]. Roughly speaking, the paraxial propagation of light effectively eliminates one spatial dimension from the analysis via the relation $z = ct$. This makes integrated photonic waveguides a promising platform for the simulation of anyons [204].

The aforementioned (Abelian) Chern-Simons theory is a special case of a topological quantum field theory [142]. The latter describes processes in which the amplitude of a wave function only depends on the topology of a particle's world line. The situation is analysed in Fig. 26, where pairs of anyons are created from the vacuum, then (potentially) non-Abelian braiding of their world lines results in a unitary transformation B on the state, final fusion of the anyons concludes the evolution. Due, to the topological nature of the process, the expectation value $\langle \psi | B | \psi \rangle$ only depends on the sequence of elementary braids, contained in the unitary operator B. It is therefore related to the Wilson loop $W_{\prod_i C_i}$, with C_i being a spacetime loop formed by a pair of anyons (from vacuum excitation to final fusion) [40]. The holonomy associated with the Wilson loop is of rather special type as it is determined by the anyons statistic, thus depending only on the topology of the loops $\{C_i\}_i$ instead of continuous quantities, such as the enclosed area.

---

[1] This can be shown explicitly using integration by parts for the action $S_{\mathrm{CS}}[A^\omega]$, where the functions $A_\mu(x^\mu)$ and $\omega(x^\mu)$ vanish at the boundary of the spacetime [40].

[2] In contrast, the Lagrangian of the electromagnetic interaction in 3+1 dimensions involves inner products, e.g., $|\boldsymbol{E}|^2 = g_{\mu\nu}E^\mu E^\nu$, thus depending on the metric tensor $g_{\mu\nu}$ of the spacetime.

By construction, expectation values must be unaffected by smooth deformations of the anyon's world line. It follows that $\langle \psi | B | \psi \rangle$ is invariant under the three Reidemeister moves (Fig. 18), thus carrying information about the knot K formed by the fusion of anyons. The latter amounts to a plat closure of the braid word B. Remarkably, having an anyonic system at our disposal, the Jones polynomial can be extracted from [200]

$$V_K(A) = (-A^3)^{-w(\overline{B})} d^{s-1} \langle \psi | B | \psi \rangle \, .$$

From the above equation it is immediately clear, that if the anyons are not braided, but only change their relative position to each other, one has $B = \mathbb{1}$, resulting in $V_{\bigcirc \cdots \bigcirc} = d^{s-1}$. This is indeed the Jones polynomial one would obtain from a diagrammatic calculation $\langle \bigcirc \cdots \bigcirc \rangle = d^{s-1}$ for a collection of s unknots.

In conclusion, anyons can be used to compute the Jones polynomial of a knot. The complexity of implementing the braid word B is linear in the number of crossings, thus outperforming a graphical calculation of the associated Jones polynomial (Sec. 5.1), which had an exponential scaling. Conversely, knowing the Jones polynomial of a knot is equivalent to the prediction of amplitudes in a topological quantum field theory. In the following, an alternative quantum algorithm is provided that relies on the preparation of unitary gates satisfying the Yang-Baxter equations. Even though these systems are not anyonic in nature, they still incorporate the algebraic relations (5.2) of the braid group.

5.3 Quantum Calculation of Knot Invariants

Previously, it was noticed that the computational expense of determining the Jones polynomial (5.1) rises exponentially with the number of crossings when evaluating diagrams in the Kauffman bracket of a knot (Fig. 27, right). This makes it simply unfeasible to unravel large knots on a classical computer. As an example, the Gordian knot (Fig. 27, left) contains 65 crossings, which would result in the conversion of 2^{65} diagrams into a polynomial. On the other hand, we already saw in the last section that a computation of the Jones polynomial is equivalent (up to linear expense) to the evaluation of a unitary transformation. A quantum algorithm that estimates the trace of a (unitary) $D \times D$ matrix $\rho(b)$ is the Hadamard test [200, 199].

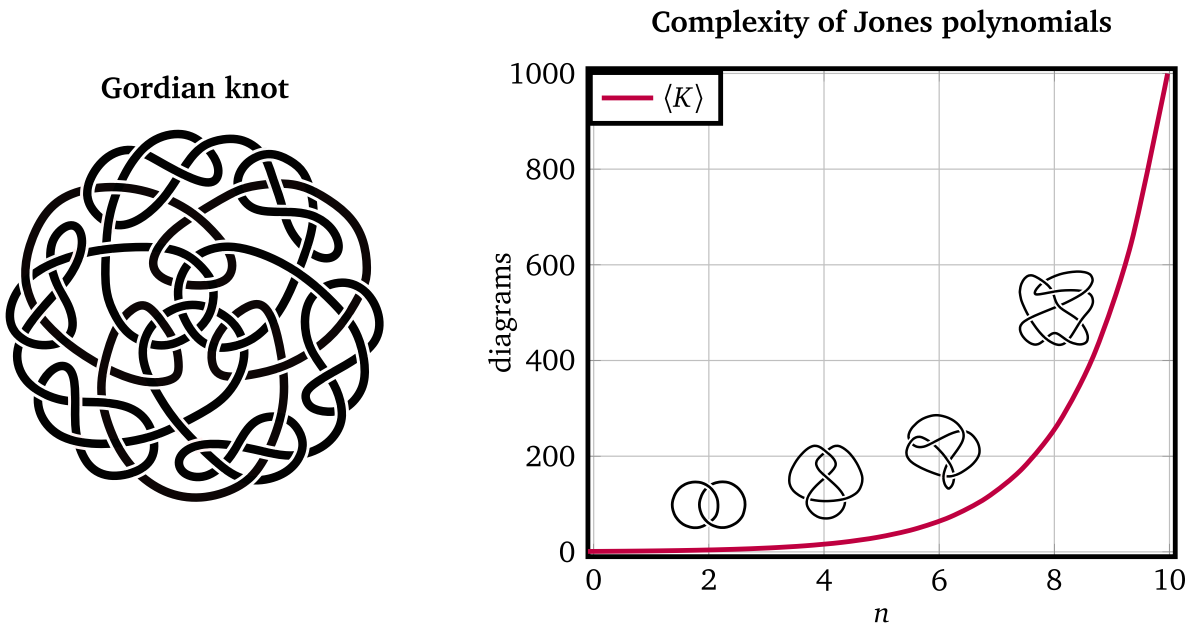

Figure 27.: (Left) Diagrammatic representation of the Gordian knot containing 65 crossings. (Right) Number of diagrams in the evaluation of the Kauffman bracket $\langle K \rangle$ of a knot K as a function of its crossings n.

5.3.1 Hadamard test

One first prepares a work qubit in the state $|0\rangle_\ell$ while the remaining n qubits (for $D = 2^n$) are initialised in some state $|\Phi_j\rangle$. The set $\{|\Phi_j\rangle\}_{j=1}^{D}$ shall form an orthonormal basis for the D-dimensional subspace on which the gate $\rho(b)$ acts, so it can be used to evaluate a matrix trace. Second, the input state $|0\rangle_\ell \otimes |\Phi_j\rangle$ is send into the quantum circuit

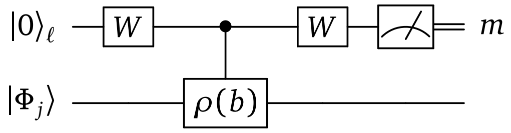

where the controlled braiding $C\rho(b)$ is managed by the work qubit, which in turn is finally measured in the computational basis. Repeating the Hadamard test until a sufficient statistic of measurement outcomes $m \in \{0, 1\}$ is obtained, then provides $\mathrm{Re}\,\langle\Phi_j|\,\rho(b)\,|\Phi_j\rangle$, to satisfactory precision. Analogously, $\mathrm{Im}\,\langle\Phi_j|\,\rho(b)\,|\Phi_j\rangle$ can be obtained from a difference of probability distributions, utilising the circuit

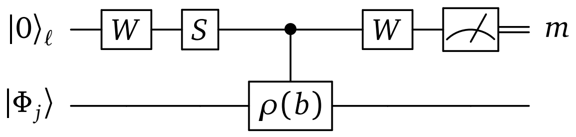

to be implemented. When the computational procedure is reiterated for all states $|\Phi_j\rangle$, the quantity $\mathrm{Tr}\{\rho(b)\}$ can be determined to arbitrary precision. In conclusion, the presented circuits give rise to an efficient way to compute the Jones polynomial, because the number of qubits $\log D$ depends only on the dimension of ρ and is independent of the number of crossings [40]. Taking into account that, in most practical situations, the controlled braiding will be engineered as a sequence $\mathrm{C}\rho(b) = \prod_l \mathrm{C}\rho\big(b_{i_l}^{k_l}\big)$, the number of gate operations still scales linearly with the number of crossings.

5.3.1.1 Hadamard test for the three-strand representation

For the moment, concentrate on three-stranded knots. Recalling the unitary representation (5.5), one observes that the Hadamard test reduces to a circuit involving two qubits. In Ref. [205], this representation was put to use in an NMR quantum calculation of several Jones polynomials. For our purposes, it is more advantageous to resolve the controlled-unitary $\mathrm{C}\rho(b)$ via the circuit identity [151]

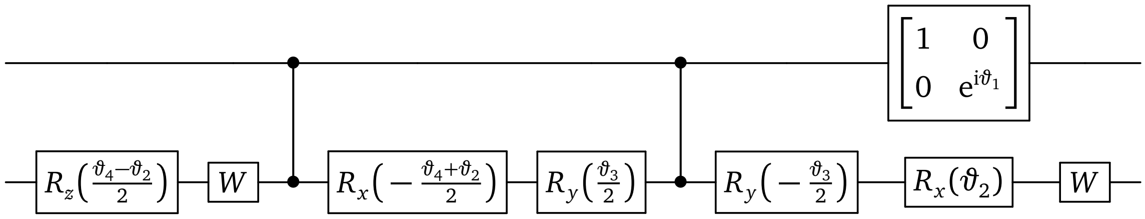
$\begin{bmatrix}1 & 0\\ 0 & e^{i\vartheta_1}\end{bmatrix}$
$R_z\left(\frac{\vartheta_4-\vartheta_2}{2}\right)$
W
$R_x\left(-\frac{\vartheta_4+\vartheta_2}{2}\right)$
$R_y\left(\frac{\vartheta_3}{2}\right)$
$R_y\left(-\frac{\vartheta_3}{2}\right)$
$R_x(\vartheta_2)$
W

where

$$\rho(b) = e^{i\vartheta_1} R_z(\vartheta_2) R_y(\vartheta_3) R_z(\vartheta_4) \tag{5.9}$$

can be composed into a general single-qubit gate. Appendix A.5.1 contains a proof of this circuit identity. The angles $\{\vartheta_j\}_j$ will depend on the given braid word b.

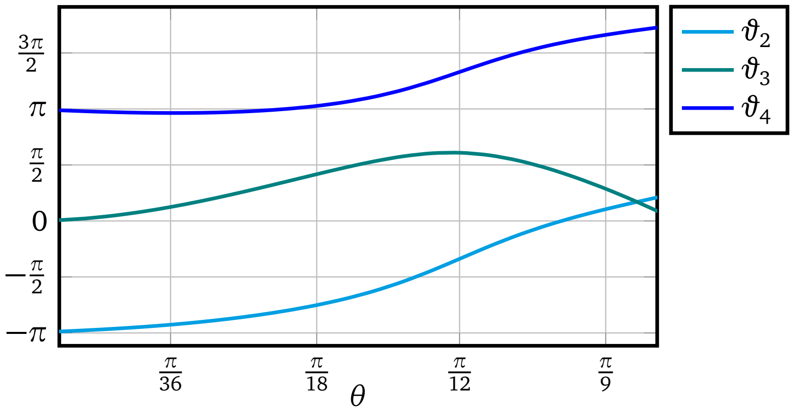

Figure 28.: Bloch sphere angles ϑ_j with $j = 2, 3, 4$ for the controlled braiding with $\rho(b)$ of the Borromean rings. The graphic was obtained by solving Eq. (5.9) for 22 equidistant values of θ in the interval $[0, \pi/6]$.

For example, the decomposition for the Hopf link is (recall $A = \mathrm{e}^{\mathrm{i}\theta}$)

$$\rho(b_1)\rho(b_1) = \mathrm{e}^{-2\mathrm{i}\theta} R_z(0) R_y(0) R_z(8\theta).$$

Moreover, the matrix representation of the Borromean rings, given in Eq. (5.7), belongs to the special unitary group SU(2). Hence, $\vartheta_1 = 0$, while Fig. 28 shows how the resolution (5.9), determined by the remaining parameters ϑ_2, ϑ_3, and ϑ_4, changes as a function of the parameter θ. This in turn fixes the quantum circuit for the Hadamard test.

5.3.2 Measurement-based Hadamard test

When seeking a physical implementation of the Hadamard test, the main computational expense lies in the realisation of the controlled braiding operation $\mathrm{C}\rho(b)$. This becomes particularly problematic when devising an implementation relying solely on photons. Entangling photonic qubits during propagation is exceedingly difficult when the controlled braiding is comprised of many such operations. In Sec. 4.4, measurement-based QC was introduced as an alternative paradigm evading such technological hurdles.

Here, I present a measurement-based version of the Hadamard test for knots formed on three strands. The above circuit decomposition is particularly useful in adjusting the measurement pattern once the decomposition (5.9) of a braid word is known. Figure 29 shows the measurement-based realisation of the Hadamard test for knots on three strands starting from a 4 × 13 lattice of qubits. In Appendix A.5.2, it is shown that the graph state computation in Fig. 29. (b) coincides with the conventional Hadamard test. In Appendix A.5.3, the overall by-product operators for the Hadamard test is derived as well. Note that the graph state shown in Fig. 29. (b) is not the simplest one possible, but can be viewed as being obtained from the cluster state, shown in Fig. 29. (a). The redundant qubits are removed from the cluster by Pauli-Z measurements such that the above circuit is directly written into the cluster [176]. The given measurement pattern, even though being not the most resource-efficient (qubit-saving), has the advantage of being easily translated into the desired Hadamard test, once the decomposition (5.9) is known. It is therefore more flexible and can be readily adjusted if the Jones polynomial of a different knot becomes of interest.

In the spirit of this thesis, the graph state computation in Fig. 29 is envisaged to be carried out by applying quantum holonomies to the individual qubits in the graph, followed by a measurement in the computational basis. The photonic realisation of this setup would be conducted as follows. First, 52 indistinguishable photons are entangled into a 4×13 cluster state $|\Psi_G\rangle$ by means of some highly nonlinear process. Next, each photon is sent into a three-waveguide coupler, e.g., by using fibre beam splitters. Unnecessary qubits are removed via single-photon detectors (Pauli-Z measurements). The remaining 26 correlated photons have to undergo measurement in a rotated basis. Therefore, the couplings $\kappa_{\mathrm{W}}(z), \kappa_{\mathrm{E}}(z) \propto \Omega(z)$ are chosen such that each qubit in $|\Psi_G\rangle$ undergoes a holonomic single-qubit transformation $U_A(C_\varphi)$, i.e., $\int_{z_0}^{z_{\mathrm{f}}} \Omega(z)\mathrm{d}z = \pi$. The loop C_φ followed by a Pauli-Z measurement in terms of single-photon detectors then realises a measurement in the basis $U_A(C_\varphi)\,|0\rangle_\ell$ and $U_A(C_\varphi)\,|1\rangle_\ell$. The parameter φ in each gate, has to be adjusted according to the specific braiding.

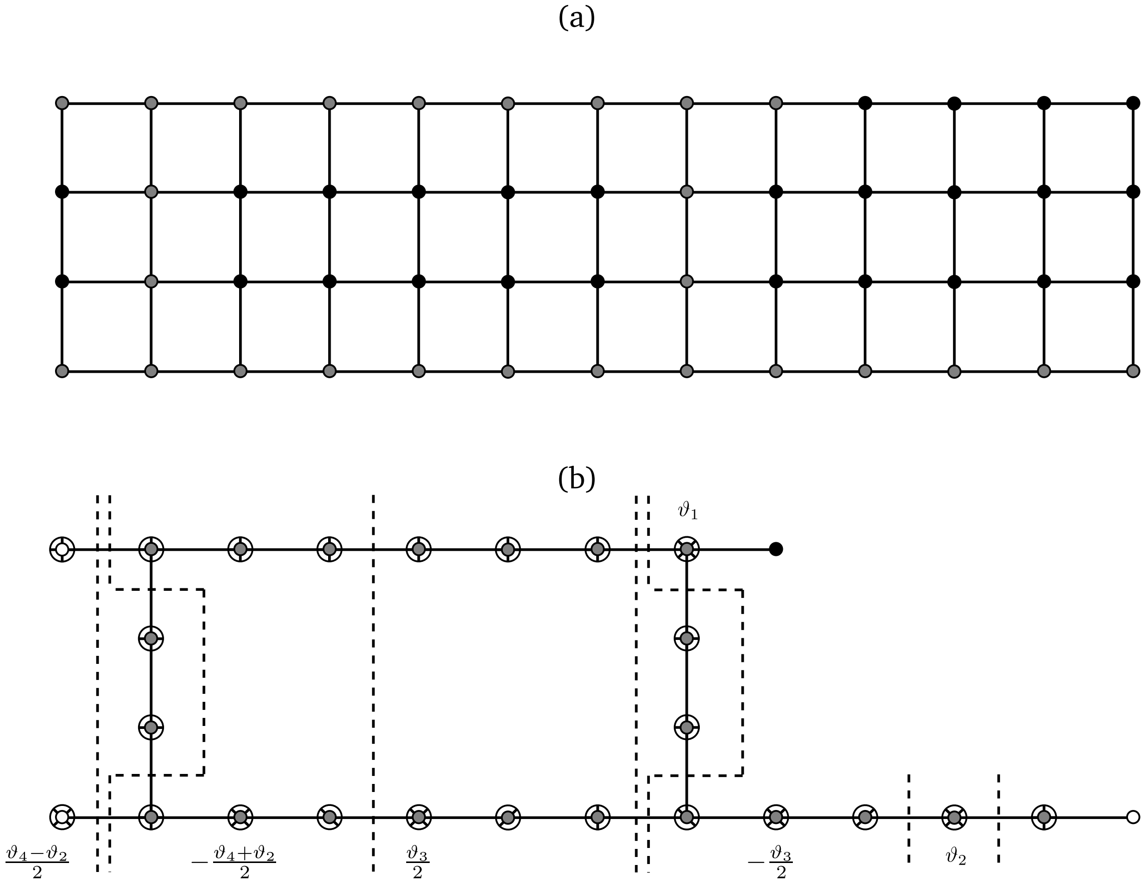
(a)
(b)
ϑ_1
$\frac{\vartheta_4-\vartheta_2}{2}$
$-\frac{\vartheta_4+\vartheta_2}{2}$
$\frac{\vartheta_3}{2}$
$-\frac{\vartheta_3}{2}$
ϑ_2

Figure 29.: Measurement-based execution of the Hadamard test with controlled braiding $C\rho(b)$ (a) Preparation of a cluster state consisting of 4×13 qubits. Redundant qubits are removed from the cluster via a Pauli-Z measurement denoted with the symbol $\bullet$. (b) Rotations into the suitable bases are carried out by single-loop holonomies $U_A(C_{\varphi_k})$. The symbol $\oplus$ denotes a measurement in the Pauli-X basis. Qubits labelled with $\oslash$ or $\circledbslash$ are measured in the $\varphi = \pm\pi/2$ basis, respectively. Finally, qubits marked with $\otimes$ are measured in one of the Bloch sphere angles (5.9). The graph state computation estimates the real part of $\mathrm{Tr}\{\rho(b)\}$ from the measurement statistic of the work qubit. Vertical dashed lines separate the graph state into a sequence of simulated single-qubit and two-qubit operations (see Appendix A.5.2).

VI | Summary and Conclusion

This thesis revolves around the realisation of quantum holonomies by means of integrated photonic waveguides. Based on a quantisation of the electromagnetic field in an array of coupled waveguides, a tight-binding theory for the paraxial propagation of light was devised (Chapter II). Propagation of light in strongly coupled waveguides was described within a nonorthogonal coupled-mode theory. It was shown how specific arrangements of the bosonic modes, such as the star graph, allowed for the generation of, both adiabatic and nonadiabatic, holonomies (Chapter III). The results of an experimental collaboration were briefly discussed. This included the first quantum photonic realisation of a U(3) holonomy, by utilising two-photon interference in an adiabatic propagation [P4], as well as an all-out holonomic implementation of the quantum-optical coin-flip game using nonadiabatic holonomic gates [P5]. I came to the conclusion that an implementation in terms of nonadiabatic holonomies is more promising. The reasons for this are the following: Firstly, nonadiabatic holonomies provide a path-shortening realisation and can be implemented in a planar array of waveguides. Secondly, in an all-out photonic setting there is no ground state protection against loss that would incline us to prefer an adiabatic implementation. Such a protection against decay is more relevant to atomic and trapped-ion platforms. Moreover, relations between quantum holonomies and several contributing factors were highlighted, including degeneracy of subspaces and the number of photons involved in the propagation. We witnessed that an increase in degeneracy, due to more photons being involved [P1], does not necessarily result in a more versatile (i.e., higher-dimensional) holonomy group. The particle-number threshold (PNT) of a quantum system was introduced to assess this observation. The PNT gives the number of photons necessary to fully harness the holonomy group of highest dimension [P3]. In addition, a unified operator framework for quantum holonomies was devised [P6]. Within this framework, it was shown that the propagation of light in the star graph (i.e., the tripod) arrangement remains unaffected by distortions from transverse mode overlaps [P2], thus providing an additional symmetry-based protection. Furthermore, the formalism allowed me to prove that any linear optical transformation can be implemented using holonomies only. These findings were put to use in a novel form of measurement-based QC that solely relied on holonomic gates to transform parts of the graph state before measurements are applied (Chapter IV). Utilising holonomic operations in a measurement-based setting led to a fruitful symbiosis between the two paradigms, i.e., gate operations can be applied in parallel (avoiding transition and bending errors) and local measurements are designed in an error-resilient style [P7]. It turned out that, performing measurement-based QC by purely geometric means is no restriction at all, as it enabled an efficient estimation of the Jones polynomials of elementary knots (Chapter V).

6.1 Outlook

The proposals devised in this thesis enable a novel form of photonic QIP. Hopefully, the design freedom and robustness, inherent in a holonomic implementation of photonic waveguides, can be utilised in improved design strategies for reliable quantum technologies. What *reliable* means might depend crucially on the given physical context, the commercial demand, the time at our disposal, and the computational problem which is to be solved. An informal definition of what constitutes reliable and scalable QIP might be inherited from classical computer science and engineering [206].

Computer engineering is the art and science of translating user requirements we do not fully understand; into hardware and software we cannot precisely analyze; to operate in environments we cannot accurately predict; all in such a way that the society at large is given no reason to suspect the extent of our ignorance.

> Adapted from Ralph Caplan's *By Design: Why there are no locks on the bathroom doors in the Hotel Louis XIV and other object lessons* (Fairchild Books, New York, 2004).

Certainly, QIP is far from reaching this goal and has to be considered in its early technological stages, striving for proof-of-principle demonstrations [149, 207] that verify a possible quantum advantage [208, 209]. Nevertheless, a good amount of enthusiasm surrounds current research on QIP and QC, based mainly on two factors. Firstly, quantum-error correction is, in principle, possible. And secondly, the existence of a threshold theorem for QC. The latter states that, if error rates are low enough, and sufficient overhead in qubits can be provided, arbitrarily long QC can be achieved [206]. The route towards fault-tolerant large-scale QC has to be paved by either increasing the error threshold (by developing improved codes) or designing highly reliable architectures for QIP.

The thesis at hand, hopes to reinforce the optimism surrounding the field of QC by devising novel schemes for a more adaptable manipulation of photonic qubits and showing how these can be utilised for the implementation of holonomic quantum algorithms. In the following, I present a number of unexplored issues that are close to the subject at hand but have not been addressed so far.

Scalability of holonomic networks — In photonic waveguides, quantum holonomies offer only a protection against parametric noise. However, primary sources of errors are inhomogeneities in the material and photon loss, thus limiting scalability of the architecture. The antidote to this issue is the usage of path-shortening realisations of holonomic gates. Exploring alternative platforms, such as lithium-niobate or silicon-on insulator waveguides, might be crucial for the fabrication of miniaturised holonomic chips, because fused-silica waveguides lack the sufficient scalability due to their weak-refractive index contrast. On the theoretical side, studying more general cyclicity conditions for the three-waveguide coupler [210] as well as ultra-fast holonomies [211] might be a fruitful endeavour. This should not be to difficult, as proposals for atomic systems usually can be directly translated into a tight-binding Hamiltonian.

Nonadiabatic topological phases — Another aspect of photonic holonomies that might be worth investigating, is the transition to topological QC. While this is well understood in an adiabatic setting [129, 184, 212], there are no comparative references on nonadiabatic holonomic gates of topological origin, i.e., the holonomy depends only on a topological invariant of the system. A promising starting point of such an investigation is the three-waveguide coupler. Its geometric phase might become topological given additional constraints on its configurations or by providing ancilla modes that allow to discretise steps in the holonomic evolution.

SU(d,d)-valued operator holonomy — Section 3.5 contained the derivation of a holonomic Heisenberg picture. For a collection of coupled oscillators, this led to a holonomic version of the transfer matrix in linear optics. The operator holonomy $\mathcal{U}_C$ realised a U(d) transformation between the spatial modes of a network. An ambitious student of mathematical physics might try to extend this notion to include nonlinear optical effects, e.g., Bogoljubov transformations $\hat{\boldsymbol{a}}^\dagger \mapsto \mathcal{W}[\hat{\boldsymbol{a}}] + \mathcal{U}[\hat{\boldsymbol{a}}^\dagger]$, where the pair $(\mathcal{W}, \mathcal{U})$ belongs to the symmetry group SU(d,d). An intuitive starting point for such an endeavour is the parallel transport condition $[\hat{\eta}_a, \dot{\hat{\eta}}_b^\dagger] = 0$ for an evolving mode $\hat{\eta}_b^\dagger = \sum_a \left(\mathcal{W}_{ba} \hat{\Psi}_a + \mathcal{U}_{ba} \hat{\Psi}_a^\dagger \right)$.

Particle-number thresholds — In Sec. 3.2, I introduced the concept of a particle-number threshold (PNT), which is the minimal number of particles necessary to harness the highest-dimensional holonomy group of a quantum system. PNTs give rise to a number of theoretical questions that might be explored in future works. For instance: Are there quantum systems not possessing a PNT? That would imply the dimension of a holonomy group increases further and further upon subjecting more particles to the system. I expect such peculiar behaviour only in the case of infinitely many modes coupling to one another, as a finite-dimensional parameter space should never enable infinite computational resources. A more rigorous argument might be pursued in a future work. There is also a lack of analytical tools to compute PNTs. While this is a manageable task for fermionic systems (where Fock spaces are finite-dimensional), it becomes a challenging issue for bosonic systems, where there is no bound on the particle number.

A | Supplementary Results

This part of the appendix contains various theorems and calculations that support the results presented in the thesis.

A.1 Coupling and Overlap between Cylindrical Waveguides

In the following, the coupling strength, the mode overlap, and the self-coupling between two adjacent waveguides are computed. These quantities were plotted as a function of their spatial separation in Fig. 3. (a) (see Chapter II). For simplicity, focus lies on cylindrical step-index waveguides of radius R with a weak refractive-index contrast Δn_j compared to the host material n_0.

Consider a scenario in which each waveguide is assumed to be identical and supports only its first transverse mode $w_j(\boldsymbol{r}_\perp)$. Furthermore, recall that a transverse mode $w_j(\boldsymbol{r}_\perp)$ of a single waveguide satisfies its own Helmholtz equation

$$\left(\boldsymbol{\nabla}_\perp^2 + \frac{\omega^2}{c^2}\left[n_0 + \Delta n_j(\boldsymbol{r})\right]^2 - \beta^2\right) w_j(\boldsymbol{r}_\perp) = 0, \tag{A.1}$$

where $\Delta n_j(\boldsymbol{r})$ equals $n_\mathrm{I} \ll 1$ inside the waveguide, that is $|\boldsymbol{r}_\perp| \leq R$, and 0 outside the waveguide, that is $|\boldsymbol{r}_\perp| > R$. When switching to cylindrical coordinates (r, φ, z), with origin at the waveguide core, it becomes evident that a solution to Eq. (A.1) must be 2π-periodic with respect to φ. Hence, $w_j(\boldsymbol{r}_\perp) = w_j(r)\mathrm{e}^{-\mathrm{i}m\varphi}$ with m accounting for higher order modes. As we are only interested in the fundamental mode we set $m = 0$. Subsequently Eq. (A.1) becomes

$$\begin{aligned} \partial_r^2 w_j(r) + \frac{1}{r}\partial_r w_j(r) + k_\mathrm{t}^2 w_j(r) &= 0, \quad \text{for} \quad r \leq R, \\ \partial_r^2 w_j(r) + \frac{1}{r}\partial_r w_j(r) - \gamma^2 w_j(r) &= 0, \quad \text{for} \quad r > R, \end{aligned} \tag{A.2}$$

with $r = |\boldsymbol{r}_\perp|$. In Eq. (A.2), I introduced the parameters

$$\begin{aligned} k_\mathrm{t}^2 &= (n_0 + n_\mathrm{I})^2/\lambda\!\!\!^{-2} - \beta^2, \\ \gamma^2 &= \beta^2 - n_0^2/\lambda\!\!\!^{-2}. \end{aligned}$$

The exact solution to Eq. (A.2) has the compact form [93]

$$w_j(\boldsymbol{r}_\perp) = \begin{cases} J_0(k_\mathrm{t} r)/J_0(k_\mathrm{t} R), & \text{if } r \le R \text{ (core)}, \\ K_0(\gamma r)/K_0(\gamma R), & \text{if } r > R \text{ (bulk)}, \end{cases}$$

where J_0 is the zeroth order Bessel function of first kind and K_0 is the zeroth order, modified Bessel function of second kind. The normalisation of Bessel functions ensures continuity at the boundary of the waveguide. A suitable choice of k_t and γ further ensures differentiability of w_j at $r = R$. Without going into further detail the latter one can be determined graphically from the boundary condition

$$k_\mathrm{t} R \frac{\partial_{k_\mathrm{t} R} J_0(k_\mathrm{t} R)}{J_0(k_\mathrm{t} R)} = \gamma R \frac{\partial_{\gamma R} K_0(\gamma R)}{K_0(\gamma R)},$$

by searching for intersections between the left- and right-hand side of the above equations. For details the reader might refer to Ref. [93].

Once the fundamental mode is explicitly known, one can calculate the coupling and overlap between adjacent waveguides. Assuming an identical fabrication process for each waveguide, the transverse mode of an adjacent waveguide is simply

$$w_{j+1}(x, y) = w_j(x + \delta, y) \tag{A.3}$$

where I chose a Cartesian frame with the jth waveguide being at the origin. In Eq. (A.3), it was assumed, without the loss of generality, that the position of each waveguide differs by a displacement δ in x-direction. Utilising Eq. (A.3) the coupling and mode overlaps (2.7) between two waveguides becomes

$$\begin{aligned} \kappa_{jj+1}(\delta) &= \frac{1}{\lambda} \int_{S_{\Delta n_j}} n_\mathrm{I} w_j^*(x, y) w_j(x + \delta, y) \mathrm{d}x \mathrm{d}y, \\ \sigma_{jj+1}(\delta) &= \int_{S_\infty} w_j^*(x, y) w_j(x + \delta, y) \mathrm{d}x \mathrm{d}y, \\ \nu_j(\delta) &= \frac{1}{\lambda} \int_{S_{\Delta n_{j+1}(\delta)}} n_\mathrm{I} |w_j(x, y)|^2 \mathrm{d}x \mathrm{d}y, \end{aligned}$$

with $S_{\Delta n_j}$ being the part of transverse plane on which Δn_j is nonvanishing. For two properly normalised modes, i.e., $\sigma_{jj} = 1$, the coupling, self-coupling and overlap of transverse modes could be obtained as an interpolating function (shown in Fig. 3). In Fig. 30, the transverse mode fields of two waveguides are plotted in the (x, y)-plane. One can clearly observe an overlap, thus verifying the nonorthogonal nature of these fields.

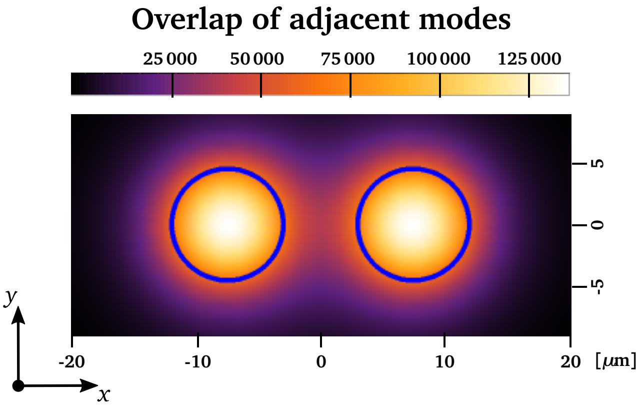

Figure 30.: Density plot of fundamental mode fields of two adjacent waveguides (blue circles) of radius $R = 4.8\,\mu\text{m}$ with a bulk index $n_0 = 1.452$ and a weak contrast $n_\mathrm{I} = 6.53 \cdot 10^{-4}$ for each waveguide. The wavelength of the injected light beam considered, is $\lambda = 633\,\text{nm}$. The separation between the waveguides (measured from the center) is $\delta = 16\,\mu\text{m}$. The overall field is given in relative units such that each mode is normalised.

A.2 Dark States of the Four-Mode Fully-Connected Graph

In this appendix, the two-particle dark states of the four-mode fully-connected graph (3.14) are listed. These are the zero-eigenvalue eigenstates of the Hamiltonian matrix $H|_{\mathscr{F}_2}$. Their explicit form is [P3]

$$
\begin{aligned}
|D_1\rangle &= \frac{1}{\sqrt{2}}\big(\mathrm{e}^{\mathrm{i}\varphi_3}\sin\theta_1\sin\theta_2\cos\theta_3\hat{a}_1^\dagger + \mathrm{e}^{\mathrm{i}(\varphi_3-\varphi_1)}\cos\theta_1\sin\theta_2\cos\theta_3\hat{a}_2^\dagger \\
&\quad + \mathrm{e}^{\mathrm{i}(\varphi_3-\varphi_2)}\cos\theta_2\cos\theta_3\hat{a}_3^\dagger - \sin\theta_3\hat{a}_4^\dagger\big)^2\,|\mathbf{0}\rangle\,, \\
|D_2\rangle &= \big(\sin\theta_1\sin\theta_2\sin\theta_3\hat{a}_1^\dagger + \mathrm{e}^{-\mathrm{i}\varphi_1}\cos\theta_1\sin\theta_2\sin\theta_3\hat{a}_2^\dagger + \mathrm{e}^{-\mathrm{i}\varphi_2}\cos\theta_2\sin\theta_3\hat{a}_3^\dagger + \mathrm{e}^{-\mathrm{i}\varphi_3}\cos\theta_3\hat{a}_4^\dagger\big) \\
&\quad \times \big(\mathrm{e}^{\mathrm{i}\varphi_1}\cos\theta_1\hat{a}_1^\dagger - \sin\theta_1\hat{a}_2^\dagger\big)\,|\mathbf{0}\rangle\,, \\
|D_3\rangle &= \big(\sin\theta_1\sin\theta_2\sin\theta_3\hat{a}_1^\dagger + \mathrm{e}^{-\mathrm{i}\varphi_1}\cos\theta_1\sin\theta_2\sin\theta_3\hat{a}_2^\dagger + \mathrm{e}^{-\mathrm{i}\varphi_2}\cos\theta_2\sin\theta_3\hat{a}_3^\dagger + \mathrm{e}^{-\mathrm{i}\varphi_3}\cos\theta_3\hat{a}_4^\dagger\big) \\
&\quad \times \big(\mathrm{e}^{\mathrm{i}\varphi_1}\sin\theta_1\cos\theta_2\hat{a}_1^\dagger + \mathrm{e}^{\mathrm{i}(\varphi_2-\varphi_1)}\cos\theta_1\cos\theta_2\hat{a}_2^\dagger\big)\,|\mathbf{0}\rangle\,,
\end{aligned}
$$

where the parameter angles (θ_k, φ_k) are defined in Eq. (3.15). In Sec. 3.2, these were used to calculate the local curvature of the system and its first-order derivative [see Eq. (3.16)].

A.3 Details on the Operator Formulation of Quantum Holonomies

In the following, a parallel transport condition for bosonic modes is derived that applies to any collection of coupled harmonic oscillators (i.e., linear optical networks). Furthermore, I provide a proof of the strong adiabatic theorem.

A.3.1 Mode quantisation under geometric constraints

The following quantisation procedure is similar to the one in Ref. [P6]. Given a collection of M classical modes that interact according to a linear optical network. The vector of amplitudes $\boldsymbol{\alpha}$ transforms according to $\boldsymbol{\alpha}(T) = \boldsymbol{U}\boldsymbol{\alpha}(0)$, where T is the propagation time. As the transformation of modes must be unitary, the transfer matrix can be written as

$$\boldsymbol{U}(T) = \hat{\mathbf{T}}\mathrm{e}^{\mathrm{i}\int_0^T \mathbf{K}(t)\mathrm{d}t},$$

where $\mathbf{K}$ is a Hermitian $M \times M$ matrix. Its components can be written as $(\mathbf{K})_{jk} = \kappa_{jk} + \beta_k \delta_{jk}$, where $\kappa_{jk} = \kappa_{kj}^*$ and $\beta_k \in \mathbb{R}$. By construction, $\boldsymbol{\alpha}(t)$ is a solution to $\partial_t \boldsymbol{\alpha} = \mathrm{i}\mathbf{K}\boldsymbol{\alpha}$. Hence, κ_{jk} can be interpreted as a coupling between the modes j and k. Furthermore, β_k might be viewed as a propagation constant.

Suppose one has a system with $d < M$ orthonormal modes $\boldsymbol{\Psi}_j(t) = \big(c_{jk}(t)\big)_k$ satisfying the condition for a holonomic evolution, i.e., the relation [54, P6]

$$(\boldsymbol{\Psi}_j^*)^{\mathrm{T}}\mathbf{K}\boldsymbol{\Psi}_k = \sum_{l,m=1}^{M} c_{jl}^* c_{km} (\mathbf{K})_{lm} = 0 \tag{A.4}$$

holds for all $j, k = 1, \ldots, d$.

A (field) quantisation is carried out by promoting the amplitudes to Hilbert space operators $\hat{a}_k^\dagger$, viz. $\boldsymbol{\Psi}_k \mapsto \hat{\Psi}_k^\dagger = \sum_j c_{jk} \hat{a}_k^\dagger$. The Hamiltonian H of the theory is obtained via a comparison between the Heisenberg equation of motion $\partial_t \hat{a}_k^\dagger = \mathrm{i}[H, \hat{a}_k^\dagger]$ and $\partial_t \hat{\boldsymbol{a}}^\dagger = \mathrm{i}\mathbf{K}\hat{\boldsymbol{a}}^\dagger$. This leads to

$$H(t) = \sum_{j<k}^{M} \kappa_{jk}(t) \hat{a}_j \hat{a}_k^\dagger + \kappa_{jk}^*(t) \hat{a}_j^\dagger \hat{a}_k + \sum_{j=1}^{M} \beta_j(t) \hat{a}_j^\dagger \hat{a}_j.$$

On the level of bosonic modes, Eq. (A.4) is equivalent to the parallel transport condition $[\hat{\Psi}_j, [H, \hat{\Psi}_k^\dagger]] = 0$. Using bosonic commutation relations, one arrives at

$$\begin{aligned}
[\hat{\Psi}_j, [H, \hat{\Psi}_k^\dagger]] &= \sum_{l,m} c_{jl}^* c_{km} \Big(\sum_{n<p} \big(\kappa_{np} [\hat{a}_l, [\hat{a}_n \hat{a}_p^\dagger, \hat{a}_m^\dagger]] + \kappa_{np}^* [\hat{a}_l, [\hat{a}_n^\dagger \hat{a}_p, \hat{a}_m^\dagger]] \big) + \sum_n \beta_n [\hat{a}_l [\hat{a}_n^\dagger \hat{a}_n, \hat{a}_m^\dagger]] \Big), \\
&= \sum_{l,m} c_{jl}^* c_{km} \Big(\sum_{n<p} \big(\kappa_{np} \delta_{lp} \delta_{nm} + \kappa_{np}^* \delta_{ln} \delta_{pm} \big) + \beta_l \delta_{lm} \Big), \\
&= \sum_{l,m} c_{jl}^* c_{km} \big(\kappa_{lm} + \beta_l \delta_{lm} \big),
\end{aligned} \tag{A.5}$$

thus verifying the assertion.

In order to show that the quantisation leaves us with photon-number states that evolve in a purely holonomic fashion, one expects that any state $|\psi_{\boldsymbol{n}}\rangle$ lying in the subspace

$$\mathscr{H}_\psi = \left\{ \prod_{j=1}^{d} \sqrt{n_j!}^{\,-1} \big(\hat{\Psi}_j^\dagger\big)^{n_j} |\mathbf{0}\rangle \,\middle|\, \boldsymbol{n} \in \mathbb{N}_0^d \right\}$$

satisfies the condition $\langle \psi_{\boldsymbol{n}} | H | \psi_{\boldsymbol{m}} \rangle = 0$ for all $\boldsymbol{n}, \boldsymbol{m} \in \mathbb{N}_0^d$. This can be shown as follows. First, note that if both sequences differ in their total photon number, $\sum_j (\boldsymbol{n})_j \neq \sum_j (\boldsymbol{m})_j$, then $\langle \psi_{\boldsymbol{n}} | H | \psi_{\boldsymbol{m}} \rangle = 0$ follows immediately, because the photon number in a linear optical network is not altered throughout the evolution. Second, the claim can be readily verified for the case of a single photon

$$\langle \psi_{\boldsymbol{n}} | H | \psi_{\boldsymbol{m}} \rangle = \langle \mathbf{0} | \hat{\Psi}_k H \hat{\Psi}_j^\dagger | \mathbf{0} \rangle = \langle \mathbf{0} | [\hat{\Psi}_k, [H, \hat{\Psi}_j^\dagger]] | \mathbf{0} \rangle = 0,$$

where $H|\mathbf{0}\rangle = 0$ was utilised. This is nothing but the initially assumed condition for parallel transport. Moving to a scenario involving two photons, one notes that

$$\langle \mathbf{0} | \hat{\Psi}_j \hat{\Psi}_k H \hat{\Psi}_l^\dagger \hat{\Psi}_m^\dagger | \mathbf{0} \rangle = \langle \mathbf{0} | [\hat{\Psi}_j \hat{\Psi}_k, [H, \hat{\Psi}_l^\dagger \hat{\Psi}_m^\dagger]] | \mathbf{0} \rangle .$$

Moreover, a direct computation reveals that

$$\begin{aligned} \langle \mathbf{0} | [\hat{\Psi}_j \hat{\Psi}_k, [H, \hat{\Psi}_l^\dagger \hat{\Psi}_m^\dagger]] | \mathbf{0} \rangle &= \langle \mathbf{0} | \hat{\Psi}_j \big[\hat{\Psi}_k, [H, \hat{\Psi}_l^\dagger] \hat{\Psi}_m^\dagger + \hat{\Psi}_l^\dagger [H, \hat{\Psi}_m^\dagger] \big] | \mathbf{0} \rangle , \\ &= \delta_{km} \langle \mathbf{0} | \hat{\Psi}_j H \hat{\Psi}_l^\dagger | \mathbf{0} \rangle + \delta_{kl} \langle \mathbf{0} | \hat{\Psi}_j H \hat{\Psi}_m^\dagger | \mathbf{0} \rangle = 0. \end{aligned}$$

Here, I made use of the bosonic commutation relations $[\hat{\Psi}_j, \hat{\Psi}_k^\dagger] = \delta_{jk}$, while remembering that $\langle \mathbf{0} | \hat{\Psi}_k H \hat{\Psi}_j^\dagger | \mathbf{0} \rangle = 0$ for all $j, k = 1, \ldots, d$. The argument can be continued for higher photon numbers, i.e., the remainder of the proof follows by induction [213].

A.3.2 Proof of the strong adiabatic theorem

Even though the adiabatic propagation of photon-number states, subject to a bilinear Hamiltonian $H(t)$, does not violate the original formulation of the adiabatic theorem [115], it has become clear that a stronger version can be formulated [P6], that is

Theorem: *In the adiabatic limit, any initial preparation $\hat{\eta}(0)$ lying in a space spanned by a collection of (non-)degenerate eigenmodes $\{\hat{\Psi}_{mk}(t)\}_k$ will evolve into a final operator $\hat{\eta}(T)$ residing in this space.*

The proof follows Ref. [P6]. Consider $H(t)$ to be the quantum system of interest, giving rise to (possibly) degenerate eigenmodes $\hat{\Psi}_{nj}(t)$ with eigenvalue $\varepsilon_n(t)$, i.e., $[H, \hat{\Psi}_{nj}^\dagger] = \varepsilon_n \hat{\Psi}_{nj}^\dagger$ at every instant. I make the ansatz

$$\hat{\eta}^\dagger(t) = \sum_{n,j} c_{nj}(t) \hat{\Psi}_{nj}^\dagger(t), \tag{A.6}$$

for the most general bosonic mode of the time-dependent system. When comparing the explicit time-derivative of Eq. (A.6) with the Heisenberg equation of motion $\dot{\hat{\eta}}^\dagger = \mathrm{i}[H, \hat{\eta}^\dagger] = \mathrm{i}\sum_{n,j} \varepsilon_n \hat{\Psi}^\dagger_{nj}$, one arrives at

$$\sum_{n,j} \big(\dot{c}_{nj}(t)\hat{\Psi}^\dagger_{nj}(t) + c_{nj}(t)\partial_t \hat{\Psi}^\dagger_{nj}(t)\big) = 0, \tag{A.7}$$

where I made use of the Heisenberg equation for the eigenmodes $\dot{\hat{\Psi}}^\dagger_{nj} = \mathrm{i}\varepsilon_n \hat{\Psi}^\dagger_{nj} + \partial_t \hat{\Psi}^\dagger_{nj}$. Concentrate on the the mth eigenenergy with d-fold degenerate eigenmodes $\{\hat{\Psi}_{mk}(t)\}_{k=1}^{d}$, and act onto Eq. (A.7) with $[\hat{\Psi}_{mk}, \cdot\,]$. Using the commutation relations $[\hat{\Psi}_{mk}, \hat{\Psi}^\dagger_{nj}] = \delta_{mn}\delta_{kj}$ yields

$$\dot{c}_{mk} = -\sum_{n,j} c_{nj}[\hat{\Psi}_{mk}, \partial_t \hat{\Psi}^\dagger_{nj}]. \tag{A.8}$$

Next, we apply ∂_t to the quantised eigenvalue problem which yields

$$[\dot{H}, \hat{\Psi}^\dagger_{nj}] + [H, \partial_t \hat{\Psi}^\dagger_{nj}] = \dot{\varepsilon}_n \hat{\Psi}^\dagger_{nj} + \varepsilon_n \partial_t \hat{\Psi}^\dagger_{nj},$$

where it was noticed that $\partial_t H = \dot{H}$. Contracting this result with $\hat{\Psi}_{mk}$ for $m \neq n$ leaves one with

$$\varepsilon_n[\hat{\Psi}_{mk}, \partial_t \hat{\Psi}^\dagger_{nj}] = [\hat{\Psi}_{mk}, [\dot{H}, \hat{\Psi}^\dagger_{nj}]] + [\hat{\Psi}_{mk}, [H, \partial_t \hat{\Psi}^\dagger_{nj}]]. \tag{A.9}$$

Using the Jacobi identity one can show that $[\hat{\Psi}_{mk}, [H, \partial_t \hat{\Psi}^\dagger_{nj}]] = \varepsilon_m [\hat{\Psi}_{mk}, \partial_t \hat{\Psi}^\dagger_{nj}]$. It follows that Eq. (A.9) can be given in the compact form

$$[\hat{\Psi}_{mk}, \partial_t \hat{\Psi}^\dagger_{nj}] = \frac{[\hat{\Psi}_{mk}, [\dot{H}, \hat{\Psi}^\dagger_{nj}]]}{\varepsilon_n - \varepsilon_m}.$$

Inserting the above result into Eq. (A.8) one obtains

$$\dot{c}_{mk} = -\sum_j c_{mj}\big(\mathcal{A}^{(m)}_t\big)_{jk} - \sum_{n\neq m}\sum_j c_{nj} \frac{[\hat{\Psi}_{mk}, [\dot{H}, \hat{\Psi}^\dagger_{nj}]]}{\varepsilon_n - \varepsilon_m}, \tag{A.10}$$

with the $d \times d$ matrix $\mathcal{A}^{(m)}$ being the local connection one-form for adiabatic parallel transport. Its components were defined as $\big(\mathcal{A}^{(m)}_t\big)_{jk} = [\hat{\Psi}_{mk}, \partial_t \hat{\Psi}^\dagger_{mj}]$.

An evolution is said to be adiabatic if the Hamiltonian H changes slowly enough over time $t \in [0, T]$, such that its explicit time-dependence can be neglected in the evolution governed by Eq. (A.10). This is clearly the case when

$$\max_{0\leq t\leq T} \big\|[\hat{\Psi}_{mk}, [\dot{H}, \hat{\Psi}^\dagger_{nj}]]\big\| \ll \min_{0\leq t\leq T} \big|\varepsilon_n - \varepsilon_m\big| \tag{A.11}$$

giving a validity condition for the adiabatic propagation. On the left-hand side of Eq. (A.11), we maximise with respect to the induced operator norm. We further observe that in this adiabatic limit the evolution of the components $c_{mk}(t)$ is governed by the system of first-order differential equations $\dot{\boldsymbol{c}} = \mathcal{A}_t \boldsymbol{c}$, with $\boldsymbol{c} = (c_{mk})_{k=1}^{d}$. In this limit, it becomes evident that the dynamical equations for c_{mk} and c_{nk} decouple for $m \neq n$. This means that any initial mode $\hat{\eta}^{\dagger}(0)$ will evolve according to $\hat{\eta}^{\dagger}(T) = \hat{\mathbf{T}} \mathrm{e}^{\int_0^T \mathcal{A}_t \mathrm{d}t} \hat{\eta}^{\dagger}(0)$, lying in the span of eigenmodes $\{\hat{\Psi}_{mk}(T)\}_k$. ■

Figure 31.: Depiction of the graph G_r consisting of $r-1$ nodes and $r-2$ edges.

A.4 Unitary Representation of the Four-Strand Braid Group

Here, I review the improved version of the AJL-algorithm from Ref. [201]. This allows for the evaluation of Jones polynomials $V_K(A)$ for continuous values of A. Moreover, the algorithm enables the construction of matrix representations of the Artin braid group $\mathscr{B}_s$ for $s \geq 3$.

Let G_r be a chain consisting of $r-1$ nodes and $r-2$ edges. The graph is depicted in Fig. 31. A path p consisting of $s = r-2$ steps (more generally, $r \geq s+2$) on the graph can be expressed as a bit string of length s, with 0 denoting a step to the left and 1 a step to the right. These paths can be used to label an orthonormal basis $\{|p\rangle\}_p$. The generators E_j of the Temperley-Lieb algebra TL_s can be calculated from their action onto these vectors, viz.

$$E_j\,|p\rangle = \begin{cases} 0, & \text{for } p^{\lfloor j,j+1\rfloor} = 00, \\ \frac{\lambda_{l-1}}{\lambda_l}\,|p\rangle + \frac{\sqrt{\lambda_{l-1}\lambda_{l+1}}}{\lambda_l}\,|p^{\cdots j-1\rfloor}10p^{\lfloor j+2\ldots}\rangle, & \text{for } p^{\lfloor j,j+1\rfloor} = 01, \\ \frac{\lambda_{l+1}}{\lambda_l}\,|p\rangle + \frac{\sqrt{\lambda_{l-1}\lambda_{l+1}}}{\lambda_l}\,|p^{\cdots j-1\rfloor}01p^{\lfloor j+2\ldots}\rangle, & \text{for } p^{\lfloor j,j+1\rfloor} = 10, \\ 0, & \text{for } p^{\lfloor j,j+1\rfloor} = 11. \end{cases} \tag{A.12}$$

Here, $p^{\cdots j-1\rfloor}$ denotes the first $j-1$ entries of the bit string p. Likewise, $p^{\lfloor j+2\ldots}$ denotes the subpath from $j+2$ to s and $p^{\lfloor j,j+1\rfloor}$ denotes the two bits at position j and $j+1$. Moreover, $\lambda_{l(p)} = \sin(l(p)\theta)$ with $l(p)$ being the endpoint of the subpath $p^{\cdots j-1\rfloor}$ in G_r. Once these generators are known, the elementary braids in $\mathscr{B}_s$ can be written as [recall Eq. (5.4)]

$$\rho(b_j) = A\mathbb{1} + A^{-1}E_j. \tag{A.13}$$

A braid word $b \in \mathscr{B}_s$ that consists of sequences of these elementary braids then amounts to a matrix product.

In order to evaluate the Jones polynomial of a Knot formed under a trace closure of the braid word b, the Markov trace [181]

$$\mathrm{Tr}_{\mathrm{M}}\{\rho(b)\} = \frac{1}{N}\sum_p \lambda_{l(p)}\,\langle p|\rho(b)|p\rangle$$

has to be employed. Here, $N = \sum_p \lambda_{l(p)}$. Once the Markov trace is known, the Jones polynomial can be obtained from [181]

$$V_K(A) = (-A^3)^{-w(\overline{b})}d^{s-1}\mathrm{Tr}_{\mathrm{M}}\{\rho(b)\}.$$

For the purpose of illustration, suppose we want to calculate the Jones polynomial of the Stevedore knot K_S shown in Fig. 32. The Stevedore knot can be constructed on four strands. It is the closure of the braid word $b = b_1^{-1} b_2 b_1^{-1} b_3 b_2^{-1} b_3 b_2$. An algebraic calculation of $V_{K_\mathrm{S}}(A)$ demands for a unitary representation of $\mathscr{B}_4$. Therefore, let $s = 4$ and $r = 6$. One can easily write down the possible paths on G_6, these are shown in Fig. 32 (from top to bottom) and read

$$|1010\rangle, \quad |1100\rangle, \quad |1011\rangle, \quad |1101\rangle, \quad |1110\rangle, \quad |1111\rangle.$$

Making use of Eq. (A.12), the generators of TL_4 can be given explicitly, viz.

$$E_1 = \begin{bmatrix} d & 0 & 0 & 0 & 0 & 0 \\ 0 & 0 & 0 & 0 & 0 & 0 \\ 0 & 0 & d & 0 & 0 & 0 \\ 0 & 0 & 0 & 0 & 0 & 0 \\ 0 & 0 & 0 & 0 & 0 & 0 \\ 0 & 0 & 0 & 0 & 0 & 0 \end{bmatrix}, \qquad E_2 = \begin{bmatrix} d^{-1} & \frac{\sqrt{d^2-1}}{d} & 0 & 0 & 0 & 0 \\ \frac{\sqrt{d^2-1}}{d} & \frac{d^2-1}{d} & 0 & 0 & 0 & 0 \\ 0 & 0 & d^{-1} & \frac{\sqrt{d^2-1}}{d} & 0 & 0 \\ 0 & 0 & \frac{\sqrt{d^2-1}}{d} & \frac{d^2-1}{d} & 0 & 0 \\ 0 & 0 & 0 & 0 & 0 & 0 \\ 0 & 0 & 0 & 0 & 0 & 0 \end{bmatrix},$$

and

$$E_3 = \begin{bmatrix} d & 0 & 0 & 0 & 0 & 0 \\ 0 & 0 & 0 & 0 & 0 & 0 \\ 0 & 0 & 0 & 0 & 0 & 0 \\ 0 & 0 & 0 & \frac{d}{d^2-1} & \frac{d\sqrt{d^2-2}}{d^2-1} & 0 \\ 0 & 0 & 0 & \frac{d\sqrt{d^2-2}}{d^2-1} & \frac{d(d^2-2)}{d^2-1} & 0 \\ 0 & 0 & 0 & 0 & 0 & 0 \end{bmatrix},$$

where $d = -A^2 - A^{-2}$ as usual. With these generators at hand, one can compute the matrix representation of the Stevedore knot. In contrast to the algorithm by Kauffman and Lomanco [199] [where we had $A = \exp(\mathrm{i}\theta)$], Eq. (A.13) gives a unitary representation for $A = \mathrm{i}e^{\mathrm{i}\theta}$, with $\theta \in [0, \pi/r]$. Evaluation of the Markov trace $\mathrm{Tr}_\mathrm{M}\{\rho(b)\}$ for the Stevedore knot leads to the Jones polynomial

$$V_{K_\mathrm{S}}(A) = A^{-16} - A^{-12} + A^8 + A^{-8} - A^4 - 2A^{-4} + 2.$$

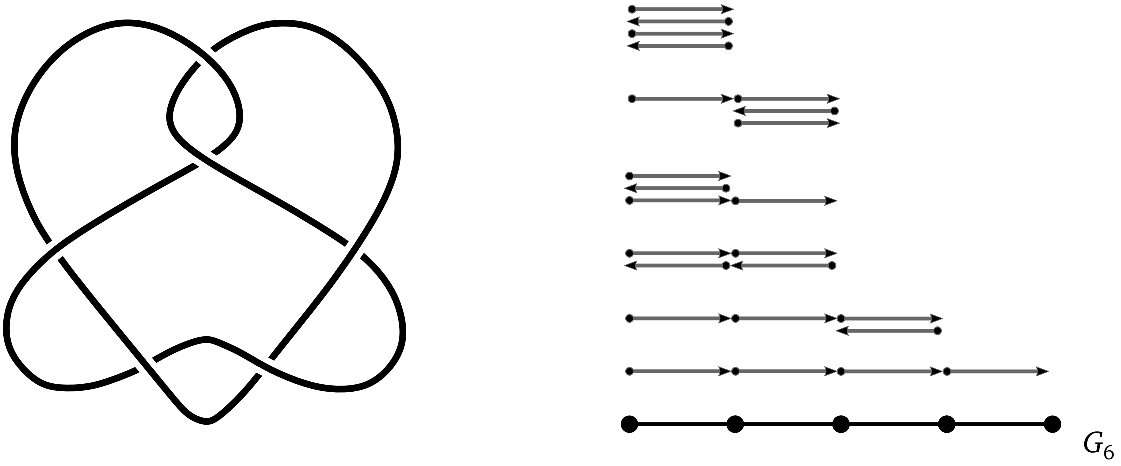

Figure 32.: (Left) Diagrammatic representation of the Stevedore knot. The knot is constructed on four strands as the (trace) closure of the braid word $b_1^{-1} b_2 b_1^{-1} b_3 b_2^{-1} b_3 b_2$. (Right) Possible paths p on the graph G_6.

A.5 Details on the Holonomic Manipulation of Graph States

This part of the appendix contains supplementary material supporting the results of Chapter V. First, I provide a circuit decomposition for arbitrary two-qubit controlled operations. Secondly, the working mechanism of the measurement-based Hadamard test is verified. Thirdly, the overall by-product operator for the (measurement-based) Hadamard test is derived.

A.5.1 Circuit identity for controlled unitaries

Consider the controlled operation $|0\rangle_\ell \langle 0|_\ell \otimes \mathbb{1} + |1\rangle_\ell \langle 1|_\ell \otimes \rho(b)$, with an arbitrary single-qubit gate

$$\rho(b) = \mathrm{e}^{\mathrm{i}\vartheta_1} R_z(\vartheta_2) R_y(\vartheta_3) R_z(\vartheta_4).$$

Its quantum circuit reads

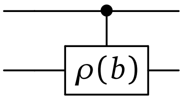

Here, I show that the above circuit can be decomposed into

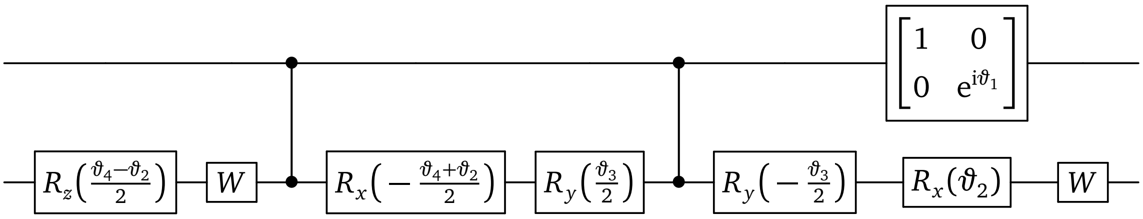
$R_z\left(\frac{\vartheta_4-\vartheta_2}{2}\right)$
W
$R_x\left(-\frac{\vartheta_4+\vartheta_2}{2}\right)$
$R_y\left(\frac{\vartheta_3}{2}\right)$
$R_y\left(-\frac{\vartheta_3}{2}\right)$
$\begin{bmatrix}1 & 0\\ 0 & \mathrm{e}^{\mathrm{i}\vartheta_1}\end{bmatrix}$
$R_x(\vartheta_2)$
W

The proof goes as follows. If the control qubit is in the state $|0\rangle_\ell$ the circuit transforms the target qubit according to

$$\begin{aligned}
&W R_x(\vartheta_2) R_y\left(\frac{\vartheta_3}{2}-\frac{\vartheta_3}{2}\right) R_x\left(-\frac{\vartheta_4+\vartheta_2}{2}\right) W R_z\left(\frac{\vartheta_4-\vartheta_2}{2}\right)\\
&= W R_x\left(\frac{\vartheta_2-\vartheta_4}{2}\right) W R_z\left(\frac{\vartheta_4-\vartheta_2}{2}\right) = \mathbb{1},
\end{aligned}$$

where I made use of $R_k(\vartheta+\vartheta') = R_k(\vartheta)R_k(\vartheta')$ for $k = x, y, z$, as well as $R_z(\vartheta) = W R_x(\vartheta) W$. In contrast, if the control qubit is in the state $|1\rangle_\ell$ the target qubit will experience two additional Z gates throughout the circuit, viz.

$$\begin{aligned}
&W R_x(\vartheta_2) R_y\left(-\frac{\vartheta_3}{2}\right) Z R_y\left(\frac{\vartheta_3}{2}\right) R_x\left(-\frac{\vartheta_4+\vartheta_2}{2}\right) Z W R_z\left(\frac{\vartheta_4-\vartheta_2}{2}\right)\\
&= R_z(\vartheta_2) W R_y(-\vartheta_3) R_x\left(\frac{\vartheta_4+\vartheta_2}{2}\right) W R_z\left(\frac{\vartheta_4-\vartheta_2}{2}\right) = R_z(\vartheta_2) R_y(\vartheta_3) R_z(\vartheta_4).
\end{aligned}$$

In the above equation, the relations $R_y(\vartheta) = WR_y(-\vartheta)W = ZR_y(-\vartheta)Z$ and $ZR_x(\vartheta) = R_x(-\vartheta)Z$ were utilised. Summarising the calculation and recalling that the control qubit experiences a phase gate shows that the circuit implements the controlled unitary

$$\begin{aligned}|0\rangle_\ell \langle 0|_\ell \otimes \mathbb{1} + |1\rangle_\ell \langle 1|_\ell \otimes \rho(b) = &\left[e^{i\frac{\vartheta_1}{2}} R_z(\vartheta_1) \otimes WR_x(\vartheta_2) R_y\left(-\frac{\vartheta_3}{2}\right)\right] \mathrm{C}Z \\ &\times \left[\mathbb{1} \otimes R_y\left(\frac{\vartheta_3}{2}\right) R_x\left(-\frac{\vartheta_4+\vartheta_2}{2}\right)\right] \mathrm{C}Z \left[\mathbb{1} \otimes WR_z\left(\frac{\vartheta_4-\vartheta_2}{2}\right)\right]\end{aligned} \tag{A.14}$$

thus proving the assertion. The circuit decomposition was utilised in Sec. 5.3.1 to allow for an efficient implementation of the Hadamard test. ■

A.5.2 Measurement pattern for the Hadamard test

Next, we show that the Hadamard test is equivalently realised by the measurement pattern from Fig. 29. Attention is restricted to the estimation of $\mathrm{Re}\,\langle \Phi_j | \rho(b) | \Phi_j \rangle$. The imaginary part can be obtained similarly. The measurements are applied in accordance with the simulated gate time, i.e. following Fig. 29 from the left to the right. In order to ensure clarity, I proceed in steps each discussing the simulation of an elementary gate (dashed lines in Fig. 29), while keeping track of the respective by-product operators. The unitary sequence realised by the setup is (ignoring an overall phase $e^{i\vartheta_1/2}$)

$$\begin{aligned}&U_{\Sigma_8} (\mathbb{1} \otimes W) U_{\Sigma_7} [\mathbb{1} \otimes WR_z(\vartheta_2)] U_{\Sigma_6} \left[WR_z(\vartheta_1) \otimes WR_z\left(\frac{\pi}{2}\right) R_x\left((-1)^{n_{10}+1}\frac{\vartheta_3}{2}\right) R_z\left(-\frac{\pi}{2}\right)\right] \\ &\times U_{\Sigma_5} \mathrm{C}Z U_{\Sigma_4} \left[W \otimes WR_x\left(\frac{\pi}{2}\right) R_z\left(\frac{\vartheta_3}{2}\right)\right] U_{\Sigma_3} \left[W \otimes WR_z\left(-\frac{\pi}{2}\right) R_x\left((-1)^{n_3+1}\frac{\vartheta_4+\vartheta_2}{2}\right)\right] \\ &\times U_{\Sigma_2} \mathrm{C}Z U_{\Sigma_1} \left[W \otimes WR_z\left(\frac{\vartheta_4-\vartheta_2}{2}\right)\right],\end{aligned} \tag{A.15}$$

where computational segments are separated by the respective by-product operators

$$\begin{aligned} U_{\Sigma_1} &= X^{m_1} \otimes X^{n_1}, & U_{\Sigma_3} &= X^{m_5} Z^{m_4} X^{m_3} \otimes X^{n_5} Y^{n_4} X^{n_3}, \\ U_{\Sigma_2} &= Z^{m_2} \otimes Z^{n_2}, & U_{\Sigma_4} &= X^{m_8} Z^{m_7} X^{m_6} \otimes X^{n_8} Z^{n_7} Y^{n_6}, \\ U_{\Sigma_5} &= Z^{m_9} \otimes Z^{n_9}, & U_{\Sigma_6} &= X^{m_{10}} \otimes X^{n_{12}} Z^{n_{11}} X^{n_{10}}, \\ U_{\Sigma_7} &= \mathbb{1} \otimes X^{n_{13}}, & U_{\Sigma_8} &= \mathbb{1} \otimes X^{n_{14}}. \end{aligned}$$

In the above, Y gates emerged due to the commutation relations $R_z(\pm\pi/2)X = \pm YR_z(\pm\pi/2)$ and $R_x(\pm\pi/2)Z = \mp YR_x(\pm\pi/2)$. Let us assume for the moment that after a computation all 24 measurement outcomes were ideal, i.e. $m_j = 0$ and $n_k = 0$ for all j, k. The conditioning of non-Clifford operations in Eq. (A.15) then becomes obsolete and the above by-product operators reduce to the identity. What remains is a matter of straight-forward algebra to verify that Eq. (A.15) can be summarised to

$$(W \otimes \mathbb{1})\big[\,|0\rangle_\ell \langle 0|_\ell \otimes \mathbb{1} + |1\rangle_\ell \langle 1|_\ell \otimes \rho(b)\big](W \otimes \mathbb{1}). \tag{A.16}$$

When provided with the input state $|0\rangle_\ell \otimes |\Phi_j\rangle$ and a subsequent (Pauli-Z) measurement of the control qubit, the entire computation (A.16) coincides with the Hadamard test.

A.5.3 Post-processing for the Hadamard test

In this part of the appendix, I compute the overall by-product operator of the measurement-based QC (A.15). The propagation relations

$$\begin{aligned} \mathrm{C}Z(\mathbb{1} \otimes X) &= (Z \otimes X)\mathrm{C}Z, & \mathrm{C}Z(X \otimes \mathbb{1}) &= (X \otimes Z)\mathrm{C}Z, \\ \mathrm{C}Z(\mathbb{1} \otimes Z) &= (\mathbb{1} \otimes Z)\mathrm{C}Z, & \mathrm{C}Z(Z \otimes \mathbb{1}) &= (Z \otimes \mathbb{1})\mathrm{C}Z, \end{aligned} \tag{A.17}$$

are particularly useful to carry through with the calculation.

This is done segment by segment (according to the dashed lines in Fig. 29) to make the calculation more traceable. Starting with the first by-product operator U_{Σ_1}, we obtain the forward propagated unitary $\tilde{U}_{\Sigma_1} = X^{m_1} Z^{n_1} \otimes Z^{m_1} X^{n_1}$ from the relation $\mathrm{C}Z U_{\Sigma_1} = \tilde{U}_{\Sigma_1} \mathrm{C}Z$. Next, the new by-product $U_{\Sigma_2}\tilde{U}_{\Sigma_1} = X^{m_1} Z^{n_1+m_2} \otimes X^{n_1} Z^{m_1+n_2}$ (we neglect overall phases ±1, ±i) must be propagated through the second segment. This yields

$$\begin{aligned} &W \otimes W R_z\left(-\frac{\pi}{2}\right) R_x\left((-1)^{n_3+1}\frac{\vartheta_4+\vartheta_2}{2}\right) U_{\Sigma_2}\tilde{U}_{\Sigma_1} \\ &= \tilde{U}_{\Sigma_2} W \otimes W R_z\left(-\frac{\pi}{2}\right) R_x\left((-1)^{n_3+1+m_1+n_2}\frac{\vartheta_4+\vartheta_2}{2}\right), \end{aligned}$$

where $\tilde{U}_{\Sigma_2} = X^{n_1+m_2} Z^{m_1} \otimes X^{m_1+n_2} Y^{n_1}$. Propagating the operator

$$U_{\Sigma_3}\tilde{U}_{\Sigma_2} = X^{n_1+m_2+m_3+m_5} Z^{m_1+m_4} \otimes X^{m_1+n_2+n_3+n_5} Y^{n_1+n_4}$$

through the third segment

$$W \otimes W R_x\left(\frac{\pi}{2}\right) R_z\left(\frac{\vartheta_3}{2}\right) U_{\Sigma_3}\tilde{U}_{\Sigma_2} = \tilde{U}_{\Sigma_3} W \otimes W R_x\left(\frac{\pi}{2}\right) R_z\left((-1)^{b_2}\frac{\vartheta}{2}\right)$$

gives the intermediate result $\tilde{U}_{\Sigma_3} = X^{m_1+m_4} Z^{a_2} \otimes X^{n_1+n_4} Z^{b_2+n_1+n_4}$. Here, I introduced the shorthand $a_2 = n_1 + m_2 + m_3 + m_5$ and $b_2 = m_1 + n_1 + n_2 + n_3 + n_4 + n_5$. In the above calculation we made already use of the fact that $Y \propto XZ \propto ZX$ when ignoring overall phase factors of ±1, ±i. Furthermore, we notice that the occurrence of powers of $2n_j$ or $2m_k$ can always be set to zero, because the Pauli operators square to the identity. Next, one propagates

$$U_{\Sigma_4}\tilde{U}_{\Sigma_3} = X^{c_2} Z^{a_3} \otimes X^{d_2} Z^{b_3}$$

through the two-qubit operation, which results in

$$CZ\,U_{\Sigma_4}\tilde{U}_{\Sigma_3} = X^{c_2}Z^{d_2+a_3}\otimes X^{d_2}Z^{c_2+b_3}CZ = \tilde{U}_{\Sigma_4}CZ.$$

In the above, I defined

$$\begin{aligned}
c_2 &= m_1+m_4+m_6+m_8,\\
d_2 &= n_1+n_4+n_6+n_8,\\
a_3 &= n_1+m_2+m_3+m_5+m_7,\\
b_3 &= m_1+n_2+n_3+m_5.
\end{aligned}$$

Together with the by-product from the fifth segment we find that

$$U_{\Sigma_5}\tilde{U}_{\Sigma_4} = X^{c_2}Z^{f_1}\otimes X^{d_2}Z^{f_2}$$

has to be commuted past

$$\begin{aligned}
WR_z(\vartheta_1)\otimes WR_z\left(\frac{\pi}{2}\right)R_x\left((-1)^{n_{10}+1}\frac{\vartheta_3}{2}\right)R_z\left(-\frac{\pi}{2}\right)U_{\Sigma_5}\tilde{U}_{\Sigma_4}&\\
= \tilde{U}_{\Sigma_5}WR_z\big((-1)^{c_2}\vartheta_1\big)\otimes WR_z\left(\frac{\pi}{2}\right)R_x\left((-1)^{n_{10}+d_2+f_2+1}\frac{\vartheta_3}{2}\right)R_z\left(-\frac{\pi}{2}\right)&,
\end{aligned}$$

with the forward-propagated operator

$$\tilde{U}_{\Sigma_5} = X^{f_1}Z^{c_2}\otimes X^{d_2+f_2}Y^{d_2}\sim X^{f_1}Z^{c_2}\otimes X^{f_2}Z^{d_2}.$$

Commuting $U_{\Sigma_6}\tilde{U}_{\Sigma_5} = X^{f_1+m_{10}}Z^{c_2}\otimes X^{f_2+n_{10}+n_{12}}Z^{d_2+n_{11}}$ through the sixth segment leads to

$$\begin{aligned}
\mathbb{1}\otimes WR_z(\vartheta_2)U_{\Sigma_6}\tilde{U}_{\Sigma_5} &= X^{f_1+m_{10}}Z^{c_2}\otimes Z^{f_2+n_{10}+n_{12}}X^{d_2+n_{11}}WR_z\big((-1)^{f_2+n_{10}+n_{12}}\vartheta_2\big),\\
&= \tilde{U}_{\Sigma_6}\mathbb{1}\otimes WR_z\big((-1)^{f_2+n_{10}+n_{12}}\vartheta_2\big).
\end{aligned}$$

Finally, propagating the by-product operator

$$U_{\Sigma_7}\tilde{U}_{\Sigma_6} = X^{g_1}Z^{c_2}\otimes X^{g_2}Z^{g_3}$$

with

$$\begin{aligned}
g_1 &= f_1+m_{10} = m_2+m_3+m_5+m_7+m_9+m_{10}+n_4+n_6+n_8,\\
g_2 &= d_2+n_{11}+n_{13} = n_1+n_4+n_6+n_8+n_{11}+n_{13},\\
g_3 &= f_2+n_{10}+n_{12} = n_2+n_3+n_9+n_{10}+n_{12}+m_4+m_5+m_6+m_8,
\end{aligned}$$

past the last segment yields

$$U_\Sigma = U_{\Sigma_8}X^{g_1}Z^{c_2}\otimes X^{g_3}Z^{g_2} = X^{g_1}Z^{c_2}\otimes X^{g_3+n_{14}}Z^{g_2}$$

which is total by-product operator of the Hadamard test. The measurement angles in Eq. (A.15) have to be conditioned on previous measurements according to the following replacements

$$\begin{aligned}
\vartheta_1 &\to (-1)^{c_2}\vartheta_1,\\
\vartheta_2 &\to (-1)^{f_2+n_{10}+n_{12}}\vartheta_2,\\
\vartheta_3 &\to (-1)^{b_2}\vartheta_3,\\
(-1)^{n_{10}+1}\vartheta_3 &\to (-1)^{n_{10}+d_2+f_2+1}\vartheta_3,\\
(-1)^{n_3+1}(\vartheta_2+\vartheta_4) &\to (-1)^{n_3+1+b_1}(\vartheta_2+\vartheta_4).
\end{aligned}$$

B | Unpublished Manuscript

This appendix contains the unpublished manuscript [P7]. Its key results were presented in the Chapters IV and V of the thesis.

Combining measurement-based quantum computation with nonadiabatic holonomic quantum computation

Julien Pinske, Kilian Abraham, and Stefan Scheel*
Institut für Physik, Universität Rostock, Albert-Einstein–Straße 23-24, D-18059 Rostock, Germany

(Dated: December 15, 2022)

We combine measurement-based quantum computation (MBQC) with nonadiabatic holonomic quantum computation (HQC). The key idea is to perform the adaptive measurements in a rotated basis that is obtained by means of a non-Abelian geometric phase. Due to the entanglement of the underlying graph state, gate operations in HQC can be carried out in parallel. One therefore does not need to design holonomic gates sequentially which would introduce longer evolution times as well as transition errors. We benchmark the superiority and robustness of this hybrid approach by comparing it with the sequential implementation of holonomic gates within an integrated quantum optical setting. Finally, our findings are utilised for a quantum calculation of the Jones polynomial. Our results indicate that MBQC and HQC can profit from one another in terms of their error resilience, thus improving scalability of the underlying architecture.

I. INTRODUCTION

Quantum information processing relies on devices that can exploit the laws of quantum theory to a high degree of accuracy. Computers that utilise these principles are generally believed to outperform classical computers [1–3]. There are several different models on which quantum computation (QC) can be based. The most common of these is the circuit model [4]. Analogously to the circuit model of classical information processing, here the manipulation of an initial input state is done in terms of a sequence of (unitary) gates. An alternative model is measurement-based QC (MBQC) [5–7] in which a highly entangled quantum state (a graph state) has to be prepared as an initial resource. Then the computation is carried out by projective measurements that remove part of the graph. The remainder of the graph state is the answer to the computational problem. Physical implementations of MBQC are already possible using superconducting qubits [8], and might soon be realised in optical lattices as well [9, 10]. However, the primary contestant for MBQC is linear optics supported by nondeterministic gates [11–13] or nonlinearities [14, 15]. A third model on which QC can be implemented is holonomic QC (HQC9, both adiabatic [16] and nonadiabatic [17]. In this model, the computation is carried out through the cyclic [18–20], or noncyclic [21], evolution of a subspace in which the encoded information resides. Currently, platforms for the experimental realisation of nonadiabatic HQC range from superconducting qubits [22, 23], liquid NMR [24], and trapped ions [25].

Even though the listed models are all computationally equivalent, i.e. they all allow for universal QC and can be translated into one another, they generally each come with different technological demands for implementation and have distinct fault-tolerance features. For example, MBQC can be topologically protected by designing a three-dimensional cluster state [26, 27] (i.e. a graph state that corresponds to a lattice of qubits). Removing some regions of the cluster by Pauli-Z measurements gives the remaining cluster a nontrivial topology that can deal with probabilistic gate errors and imperfect preparation of the cluster state [28]. Moreover, in such measurement-based schemes, classical registers, necessary for read-out, can also be assumed to be completely noiseless [29]. In contrast, HQC only depends on the geometry of the path the encoded subspace takes through Hilbert space giving HQC paradigms an inherent robustness towards local perturbations as well as being agnostic towards dynamical contributions from the underlying physical architecture, e.g. eigenenergies or runtime [30, 31]. Computational models might even be compatible. For instance, in Refs. [32, 33] cluster state computations were considered where the adaptive measurement pattern was replaced by adiabatic deformations of a Hamiltonian who has the cluster state as its ground state. This combination of MBQC and adiabatic HQC can be helpful in increasing the feasibility of adiabatic schemes and can even be made fully topological [34]. More generally, combining computational paradigms with the goal of harvesting their error-resilience properties is a promising, and maybe even necessary, endeavour as the current limitations on QC are set by the threshold theorem [35, 36]. Even with quantum error-correcting codes, it is still necessary to boost gate fidelities by a substantial margin. Hence, passive error correction schemes of combined computational models might be the firm footing on which a large-scale quantum computer can be build.

In the present work, we show how MBQC can be combined with nonadiabatic HQC. We do so by performing the adaptive measurements in a rotated basis which is obtained by means of a non-Abelian geometric phase (quantum holonomies). It turns out that due to the entanglement of the graph state, the gate operations in HQC can be parallelised so that the necessary resources differ notably from a standard HQC proposal. Moreover, due to this parallelisation, paths in Hilbert space do not need to be traversed sequentially, thus improving scalability

---

* stefan.scheel@uni-rostock.de

of HQC as well as avoiding transition errors that stem from connection segments between subsequent gates. After showing universality of the combined approach, we study these beneficial effects on the example of a three-level Hamiltonian.

We illustrate our findings on the example of integrated photonic waveguides [37, 38]. A substantial boost in gate fidelity, due to the combination of MBQC and nonadiabatic HQC, is reported. More precisely, the linear optical structures under investigation avoid bending of waveguides which would lead to photon scattering into the environment. Recently, Refs. [39–41] reported on the experimental realisations of similar architectures in terms of fused-silica laser-written waveguides from which (adiabatic) holonomic gates were constructed.

In order to illustrate that this joint approach is practical for the implementation of quantum algorithms, we present an explicit construction for the quantum calculation of the Jones polynomial [42] which is an important quantity in topology characterising a knot up to smooth deformations, e.g. bending, twisting, and shifting. It plays an important role in anyonic quantum information [43] and topological quantum field theories [44]. Knowing the Jones polynomial can be useful in various areas of statistical physics, applied technologies and medicine, where complex strand-like structures emerge [45, 46]. From the point of view of classical computation, the Jones polynomial, as well as most knot invariants, have an exponential rise in computational expense when the number of crossings in a knot increases [47, 48]. However, the quantum algorithm presented in Ref. [49] estimates the Jones polynomial with polynomial expense. In Ref. [50] experimental NMR quantum calculations of the Jones polynomial were presented. In contrast, this article contains the first quantum optical setup that allows for an equivalent quantum simulation in terms of currently existing technologies.

The structure of the article is as follows. Section II is dedicated to a review of models of QC. In particular, we present the fundamentals of MBQC and nonadiabatic HQC to the extent as it is relevant to this work. In Sec. III we combine these models and construct a universal gate set that only depends on the geometry of loops associated with any HQC proposal. We also use this section to investigate its error-resilience properties in terms of a benchmark Hamiltonian relevant to integrated quantum optics. The combined model is then put to test in Sec. IV on the example of a quantum algorithm that estimates the Jones polynomial. Finally, Sec. V contains a summary of our results as well as some concluding remarks. In Appendix A we provide additional details on the open-system dynamics of integrated photonic waveguides, in particular with regards to bending losses. Appendix B derives the measurement-based realisation of the Hadamard test as well as the explicit form of the relevant by-product operators.

II. MODELS OF QUANTUM COMPUTATION

In the standard picture of quantum information processing, an initially prepared quantum state consisting of multiple qubits, is transformed by a cascade of fast switching on-and-off interactions or driving external fields. The set of unitary operators $\{U_k\}_k$ induced by such manipulations acts on the input state $|\psi\rangle$ in sequential order realising the quantum algorithm. Therefore, each U_k can be viewed as a gate acting on a few or many qubits of the entire system. Prominent examples for these basic building blocks are the Pauli gates $X = \sigma^x$, $Y = \sigma^y$, and $Z = \sigma^z$ acting on a single qubit. Universal quantum computation can be achieved by supporting arbitrary single-qubit operations with a nontrivial two-qubit operation, e.g. a controlled-Z gate CZ. In general, the final output state $\prod_k U_k |\psi\rangle$ is then subject to a quantum mechanical measurement performing the read-out. Throughout the article, we shall only be concerned with projective measurements.

In the following we will investigate two alternative models of QC, namely MBQC [6, 7] and nonadiabatic HQC [17]. Both of these models, in principle, allow for universal quantum computation and are therefore computationally equivalent to the circuit model.

A. Measurement-based quantum computation

MBQC [5, 28] is a model for quantum information processing in which a highly entangled graph state $|\Psi_G\rangle$ is prepared as an initial resource for the algorithm. To be more precise, consider a graph G with qubits at its vertices that are prepared either as encoded information $|\psi\rangle = \alpha_0 |0\rangle + \alpha_1 |1\rangle$ ($\alpha_j \in \mathbb{C}$) or in the state $|+\rangle = (|0\rangle + |1\rangle)/\sqrt{2}$. The edges of the graph correspond to connecting the two qubits via a controlled-Z operation, $|\Psi_G\rangle = \prod_{(i,j)} CZ_{ij}(\bigotimes_k |\psi\rangle_k \bigotimes_k |+\rangle_k)$, with indices (i, j) running over the set of edges of the graph G. After performing a sequence of single-qubit measurements on $|\Psi_G\rangle$, the remainder $|\psi_{\text{out}}\rangle = \prod_k U_{\Sigma_k} U_k |\psi\rangle$ of the graph state can be viewed as the final output of the quantum computation. Commuting the by-product operators so that they can be dealt with at the end of the computation results in $|\psi_{\text{out}}\rangle = U_\Sigma \prod_k U'_k |\psi\rangle$. Here, we introduced modified unitaries U'_k that depend on the measurement results of previously implemented operations, and U_Σ is the total by-product operator lying in the Pauli group, and thus can be dealt with by means of classical post-processing. Note that, if U_k lies in the Clifford group, then we have $U'_k = U_k$. In order to deterministically use non-Clifford operations, we have to condition the adaptive measurement on previous outcomes, within runtime of the algorithm, thus introducing a notion of temporal complexity into MBQC [7].

B. Nonadiabatic holonomic quantum computation

We now turn to another approach to QC. This time the computation will neither be implemented by measurement (as in the cluster state model) nor by any dynamical interaction (as in the circuit model). HQC is an all-out geometric approach to QC in which a geometric quantity, the holonomy, plays the role of the unitary gate [16, 17]. It is computationally equivalent to the circuit model, but comes along with some desirable fault-tolerance features.

The starting point of this computational paradigm is a time-dependent Hamiltonian $H(t)$. Consider a collection of states $\{|\zeta_k(t)\rangle\}_k$ that span an N-dimensional subspace $\mathscr{C}(t)$ of the Hilbert space $\mathscr{H}(t)$ of the entire system. The evolution of these states shall be of purely geometric nature in the sense that, at every instance in time,

$$\langle\zeta_j(t)|H(t)|\zeta_k(t)\rangle = 0 \tag{1}$$

holds for all $j, k = 1, \ldots, N$. Under this constraint, the time-evolution operator becomes (we set $\hbar = 1$) [17, 20]

$$U(T) = \mathcal{T}\mathrm{e}^{\int_0^T A_t \mathrm{d}t}, \tag{2}$$

where $\big(A_t\big)_{kj} = \langle\zeta_j|\partial_t|\zeta_k\rangle$ is known as the nonadiabatic connection [20] and $\mathcal{T}$ denotes time ordering. The connection A_t mediates parallel transport of an initial state $|\psi(0)\rangle \in \mathscr{C}(0)$ along a path C through the Hilbert space $\mathscr{H}$ taken by the states $\{|\zeta_k(t)\rangle\}_k$. If we further assume C to be a loop, i.e. each state $|\zeta_k(t)\rangle$ evolves cyclically, then $\mathscr{C}(0) = \mathscr{C}(T)$ defines a computational subspace on which the unitary (2) acts as a gate. In particular, if there is an underlying multi-partite structure with $N = 2^n$, then $\mathscr{C}(0)$ might be viewed as an n-qubit quantum code to which we return at the end of the loop $C(t)$. After traversing the loop, the final state $|\psi(T)\rangle = U(T)\,|\psi(0)\rangle$ differs from the input by the unitary (2) known as a quantum holonomy. Indeed, U is a quantity of the given loop, agnostic towards parametric and timing errors [30], and we may as well write $U = U(C)$. It was shown in Ref. [17] that, in general, two noncommuting loops are necessary to perform universal quantum computation on the relevant subspace.

For the purpose of illustration, consider the following benchmark Hamiltonian of a three-level system

$$H(t) = \sum_{i=0,1} \kappa_i(t)\,|a\rangle\,\langle i| + \kappa_i^*(t)\,|i\rangle\,\langle a|\,, \tag{3}$$

where κ_i (for $i = 0, 1$) denotes the time-varying coupling strength between the logical state $|i\rangle$ and an auxiliary state $|a\rangle$. We consider a scenario in which both couplings change with the same envelope, here $\kappa_0(t) = \Omega(t)\sin(\theta/2)\mathrm{e}^{-\mathrm{i}\varphi}$ and $\kappa_1(t) = -\Omega(t)\cos(\theta/2)$. The time evolution of the states $|d\rangle = \kappa_0\,|1\rangle - \kappa_1\,|0\rangle$ and $|b\rangle = \kappa_0^*\,|0\rangle + \kappa_1^*\,|1\rangle$ reads

$$\begin{aligned}
|\zeta_1(t)\rangle &= U(t)\,|d\rangle = |d\rangle\,,\\
|\zeta_2(t)\rangle &= \mathrm{e}^{\mathrm{i}\delta(t)}U(t)\,|b\rangle = \mathrm{e}^{\mathrm{i}\delta(t)}\big(\cos\delta(t)\,|b\rangle - \mathrm{i}\sin\delta(t)\,|a\rangle\,\big),
\end{aligned} \tag{4}$$

where $U(t) = \mathrm{e}^{-\mathrm{i}\int_0^t H(\tau)\mathrm{d}\tau}$ is the time-evolution operator and $\delta(t) = \int_0^t \Omega(\tau)\mathrm{d}\tau$. The states (4) span a subspace $\mathscr{C}$ on which dynamical effects do not contribute, i.e. condition (1) is satisfied at every instance in time. Hence, the overall evolution on this subspace does not depend on any dynamical properties of H such as eigenenergies or runtime. If we choose a pulse $\Omega(t)$ such that $\delta(T) = \pi$, the states (4) evolve cyclically. Then $\mathscr{C}(0) = \mathscr{C}(T)$ forms a single-qubit space spanned by the logical states $|0\rangle$ and $|1\rangle$. The purely geometric gates that can be designed in this way, are determined from the nonadiabatic connection, with the single nonvanishing component $(A_t)_{22} = \mathrm{i}\Omega(t)$. The cyclic evolution of the system implements the time-ordered unitary $U(C) = \mathrm{diag}(1, -1)$ according to Eq. (2). When transforming into the computational basis, we obtain

$$U(C) = \begin{bmatrix} \cos\theta & \mathrm{e}^{\mathrm{i}\varphi}\sin\theta \\ \mathrm{e}^{-\mathrm{i}\varphi}\sin\theta & -\cos\theta \end{bmatrix}, \tag{5}$$

which is a universal single-qubit gate, i.e. any element in the unitary group U(2) can be written as $U(C_2)U(C_1)$, where a sequence of two loops C_1 and C_2 has to be engineered [17].

1. *Transition errors*

A loop C in Hilbert space has to be designed by corresponding coupling pulses $\kappa_0(t)$ and $\kappa_1(t)$. The choice of (parameter) angles θ and φ in Eq. (5) fixes the gate, while any envelope $\Omega(t)$ with $\delta(T) = \pi$ will ensure cyclicity. The geometric robustness of such a gate towards different sources of errors was studied in Ref. [30], while an improved super-robust version was proposed and analysed in Ref. [31]. However, even though these investigations show that the gate (5) is geometrically protected, a sequence of those need not to be. This has its origin in the transition error between two subsequent gates $U(C_1)$ and $U(C_2)$. In order to illustrate this point, suppose C_1 is a loop with $(\theta_1, \varphi_1) = (5\pi/2, \pi)$ so that $U(C_1) = -X$ realises a bit flip and a second noncommuting loop C_2 has $(\theta_2, \varphi_2) = (\pi, 0)$ yielding the phase shift $U(C_2) = -Z$. There is still a freedom of choice in the coupling configuration, namely the envelope $\Omega(t)$. Figure 1 shows two different types of coupling that would ideally realise a bit flip X followed by a Z gate. However, in Fig. 1. (a) the constant coupling configuration demands for a smooth (e.g. sine-like) transition between the two gates. This transition is not geometrically robust and distorts cyclicity of the overall evolution, i.e. the evolution leaves the computational subspace $\mathscr{C}(T)$. In contrast, Fig. 1. (b) overcomes this issue using Gaussian pulses for each segment. Hence, the transition error can be avoided nearly perfectly, while also ensuring a smooth transition. A similar configuration was used, for instance, in Ref. [22] for the experimental realisation of two subsequent nonadiabatic gates for the manipulation of superconducting qubits. On the other hand, we observe that the mitigation of transition and parameter errors between the gates came at a cost. Due to the Gaussian transition between the loops C_1 and C_2, one is forced to increase the coupling strengths as well as to extend the evolution time for each gate substantially, because we still need to pick up $\delta(T_{\rm g}) = \pi$ as the area under the integral. In some physical setups, this might lead into a strong coupling regime or demand for a magnification of the experimental setups. This might in turn limit miniaturisation or increase the time the system will be subjected to the environment, thus introducing new errors. Ideally, one would like to have the best of both worlds, i.e. using particularly simple and resource-saving coupling schemes while avoiding transition errors as well.

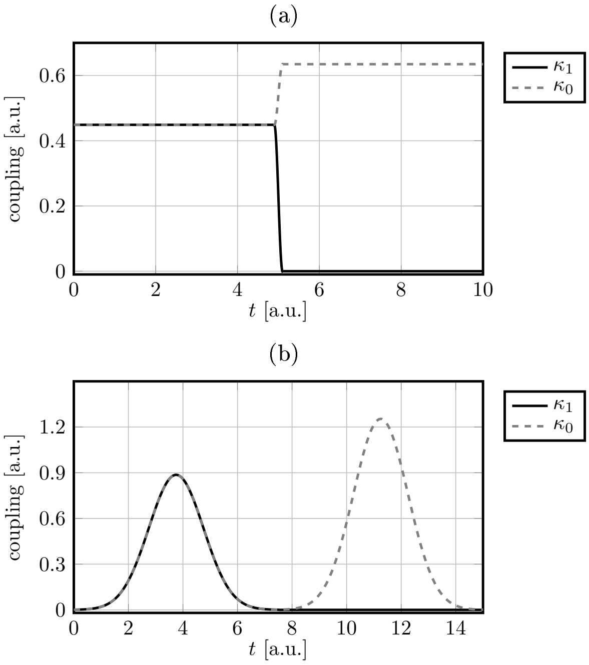

FIG. 1. Coupling parameters κ_0 (black, solid plot) and κ_1 (gray, dashed plot) for the sequential implementation of the gate ZX as a function of dimensionless time t. Each envelope function is designed to satisfy $\int_0^{T_{\rm g}} \Omega(t) \mathrm{d}t \approx \pi$ per gate, thus corresponding to a cyclic evolution of $\mathscr{C}(t)$. (a) Constant coupling segments for the implementation of each gate with $\Omega = \pi/T_{\rm g}$ and $T_{\rm g} = 4.95$. There is a transition time of $\Delta t = 0.1$ after the first gate has been applied, leading to a mismatch with the computational subspace $\mathscr{C}(T_{\rm g})$. The transition is designed smoothly in terms of a sine-like function. (b) Gaussian-shaped coupling pulses $\Omega_X(t) = \sqrt{\pi/2}\exp[-(t - T_{\rm g}/2)^2/2]$, with $T_{\rm g} = 7.5$, and $\Omega_Z = \Omega_X(t - T_{\rm g})$, ensuring a smooth transition (without an additional segment) between the two parameter variations.

III. COMBINING MBQC AND NONADIABATIC HQC

In this section, we present a combined approach to QC utilising ingredients of MBQC and HQC paradigms, as well as analysing its advantages over existing schemes. In our combined model, parts of an initially prepared $(n + M)$-qubit graph state $|\Psi_G\rangle$ undergo simultaneous loops C_k, for $k = 1, \ldots, M$ in the Hilbert space $\mathscr{H}$ of the entire system. After traversing these loops, the graph state is manipulated by a sequence of local (single-qubit) unitaries resulting in the state $\prod_k U_{\sigma(k)}(C_k) |\Psi_G\rangle$, where $\sigma(k)$ picks out the qubit on which the corresponding operation $U_{\sigma(k)}$ acts. Because of the composability of loops, $C = C_1 \circ \cdots \circ C_M$ is associated with a single loop realising the entire transformation. In the final step of the model, single-qubit measurements in the computational (Pauli-Z) basis are performed on the qubits $\sigma(k)$, for $k = 1, \ldots, M$, leading to some overall by-product operator U_Σ. The remaining n-qubit state is associated with the output of the computational paradigm. The corresponding circuit reads

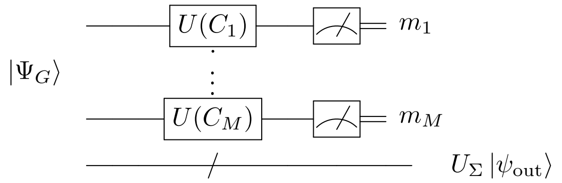

One can clearly observe that this is a form of MBQC, in which the projective measurements

$$\{U(C_k) |i\rangle_{\sigma(k)} \langle i|_{\sigma(k)} U(C_k)^\dagger\}_{i=0,1}$$

were obtained from local holonomies $U(C_k)$. Under the assumption of noiseless Pauli-Z measurements and an accurately prepared graph state $|\Psi_G\rangle$, the final output is completely determined by the composite loop C. Therefore, this specific graph state computation inherits the fault-tolerance features and intrinsic robustness of HQC. So far, we discussed the situation in which all operations are applied simultaneously. Similar to the standard formalism on MBQC, non-Clifford operations demand for a conditioning of holonomic operations in order to make the entire paradigm deterministic. In this picture, the temporal complexity, i.e. the number of non-Clifford operations to be utilised in a computation, might be interpreted as a minimal path length of the composite loop $C = C_1 \circ \cdots \circ C_M$ in order to allow conditioning on previous measurements.

In order to prove that this combined model is still universal, we make use of the benchmark system (3) studied in the previous section. The system Hamiltonian provides us with a universal set of holonomic single-qubit gates obtained from (5) and can therefore be used to perform local rotations on qubits that allow for the measurement in an arbitrary basis. This suffices to enable universal quantum computation on any number of qubits when provided with a graph state. In this way, MBQC can profit from a holonomic implementation leading to increased fidelity of local unitaries due to parametric robustness. Interestingly, also the converse is true. HQC can benefit from a measurement-based implementation of a quantum algorithm as well. This is due to the fact, that in the measurement-based model the computation can be parallelised by performing measurements on a collection of qubits of the graph state.

Let us clarify the issue for the case of single-qubit gates. First of all, it is possible to transform from the computational basis $|0\rangle$ and $|1\rangle$ into the states

$$\frac{1}{\sqrt{2}}\big(\,|0\rangle + \mathrm{e}^{\mathrm{i}\varphi}\,|1\rangle\,\big), \qquad \frac{1}{\sqrt{2}}\big(\,|0\rangle - \mathrm{e}^{\mathrm{i}\varphi}\,|1\rangle\,\big),$$

respectively, by means of the holonomy (5). This is achieved by traversing a loop $C_{\frac{\pi}{2}}$ with $\theta = \pi/2$, so that the gate $U(C_{\frac{\pi}{2}})$ is applied before the qubit reaches the measurement in the computational basis. It is then possible to construct any single qubit gate on a chain of four qubits

$$|\Psi_G\rangle = \mathrm{C}Z_{12}\mathrm{C}Z_{23}\mathrm{C}Z_{34}\big(\,|\psi\rangle \otimes |+\rangle^{\otimes 3}\,\big),$$

by performing three such measurements on the first three qubits. The input state $|\psi\rangle$ is then teleported to the fourth one being accompanied by the unitary

$$\begin{aligned} &X^{m_3}WR_z(\varphi_3)X^{m_2}WR_z(\varphi_2)X^{m_1}WR_z(\varphi_1) \\ &= U_\Sigma WR_z((-1)^{m_2}\varphi_3)R_x((-1)^{m_1}\varphi_2)R_z(\varphi_1), \end{aligned} \tag{6}$$

where $U_\Sigma = X^{m_3}Z^{m_2}X^{m_1}$ is the total by-product operator and $R_k(\varphi) = \mathrm{e}^{-\mathrm{i}\varphi/2\sigma^k}$ denotes rotation around the kth axis of the Bloch sphere with $k \in \{x, y, z\}$. The computation can be made completely deterministic by performing the measurements conditionally, i.e. $\varphi_2 \to (-1)^{m_1}\varphi_2$, and $\varphi_3 \to (-1)^{m_2}\varphi_3$. In any practical situation the conditioning can be achieved by choosing the function $\Omega(t)$ for each holonomy in an appropriate manner. Remarkably, it is not necessary to implement gates sequentially, but rather in parallel, due to the entanglement which was provided as a resource for the computation by the graph state. It follows that transition errors between subsequent loops do not enter the quantum computation in this combined approach. Notably, in the combined approach, we do need to design the three noncommuting loops $\{C_k\}_k$ to construct arbitrary single-qubit rotations, instead of the usual two noncommuting loops demanded in a standard HQC proposal [16, 17].

For completeness, note that, the holonomy (5) allows to design nontrivial two-qubit operations as well, when provided with the graph state

$$|\Psi_G\rangle = \mathrm{C}Z_{12}\mathrm{C}Z_{23}\mathrm{C}Z_{34}\big(\,|\psi\rangle \otimes |+\rangle^{\otimes 2} \otimes |\psi\rangle\,\big).$$

For instance, if the second and third qubit prepared in the state $|+\rangle$ both undergo the loop $C_{\frac{\pi}{4}}$ restricted to $(\theta, \varphi) = (\pi/4, 0)$, resulting in the holonomic rotation $U(C_{\frac{\pi}{4}}) = W$, and followed by a subsequent measurement in the computational basis, this will perform a CZ operation (up to by-product operators) leaving us with the output state $Z^{m_2} \otimes Z^{m_1}\mathrm{C}Z\,|\psi\rangle \otimes |\psi\rangle$. In summary, we have shown that universal holonomic quantum computation can be performed by exclusively referring to single-qubit measurements when provided with a highly entangled resource state. The problem of transition errors between sequentially occurring gates is removed due to the parallelisation of the computation by means of entanglement.

A. Integrated quantum optics

In order to quantify the advantages of our combined approach over standard implementations of MBQC, we will compare the single-loop realisation utilising the graph state, with a standard two-loop scheme found in the circuit model. For concreteness, we will study the realisation within a linear optical setting. The elementary architecture consists of two spatial modes, which couple solely via a third central mode. The tight-binding Hamiltonian of the system reads

$$H = \sum_{i=0,1} \kappa_i a_i a^\dagger_{\mathrm{aux}} + \kappa_i^* a_i^\dagger a_{\mathrm{aux}}, \tag{7}$$

where $a_k^\dagger$ and a_k are the bosonic creation and annihilation operators for the kth mode, respectively ($k = 0, 1, \mathrm{aux}$). There are many optical devices that might allow for the implementation of such a system, e.g. beam splitters and phase shifters [51, 52] or integrated photonic waveguides [53, 54]. In this work, interest lies on the latter implementation. Figure 2 shows the particular example of fused-silica laser-written waveguides that resemble the spatial modes. In such a setting, the propagation length $z = ct$ (c being the vacuum speed of light) plays a similar role as the time parameter, due to the paraxial nature of the problem. When a single photon is injected into one of the outer modes one can label a computational basis in a dual-rail encoding that is, a photon in mode 0 corresponds to the logical state $|0\rangle = a_0^\dagger\,|\mathbf{0}\rangle$ while a photon in mode 1 is interpreted as $|1\rangle = a_1^\dagger\,|\mathbf{0}\rangle$, with $|\mathbf{0}\rangle$ denoting the three-mode vacuum. This labelling of logical states is nothing other than the dual-rail encoding. Defining $|a\rangle = a^\dagger_{\mathrm{aux}}\,|\mathbf{0}\rangle$, the quantum optical Hamiltonian (7) coincides with the three-level system (3). Note that the ancilla mode a_{aux} is only excited while traversing the loop in Hilbert space that gives the final holonomy. Due to cyclicity, the code is mapped onto itself, and a proper read-out of logical states is possible in terms of single-photon detectors.

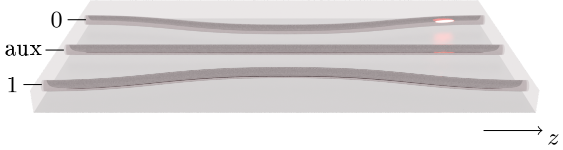

FIG. 2. Elementary architecture for the generation of nonadiabatic holonomic single-qubit gates. The varying distances between the outer modes a_0 and a_1 to the central one a_{aux} depend on the coupling configuration $\kappa_0(z)$ and $\kappa_1(z)$ that implement the desired gate.

In order to illustrate the realisation of holonomic gates, we consider the bit-flip operation $-X$ followed by a phase flip $-Z$. In the setting under investigation, gate errors manifesting in the propagated output state Λ (density operator) may originate from deviations in cyclicity as well as photon loss into the environment due to the bending of waveguides [55, 56]. Our measure of quality will be the (expected) fidelity $F(U\left|\psi\right\rangle, \Lambda) = \langle\psi|U^\dagger \Lambda U|\psi\rangle$ between the ideal output state $U\left|\psi\right\rangle = ZX\left|\psi\right\rangle$ and the propagated state $\Lambda = \mathcal{N}(\left|\psi\right\rangle\left\langle\psi\right|)$ obtained from a noisy evolution $\mathcal{N}$ of the input state $\left|\psi\right\rangle$. The photon loss in the kth waveguide will be modelled in terms of a Markovian dissipator $\gamma_k(z)$ [57]. Details on the validity of this approach and the evaluation of bending losses can be found in Appendix. A.

Figure 3 shows the probability distribution obtained from a noisy propagation of the input state $\left|0\right\rangle$, where we utilised the sequential coupling configurations from Fig. 1 (a) and (b). Ideally, the input $\left|0\right\rangle$ would evolve into $-\left|1\right\rangle$ after traversing one of the optical networks (a) or (b). Figure 3 (a) shows the two-loop implementation of the holonomic gate U using straight waveguides for each gate that are connected via a sine-like transition segment leading to a mismatch with the computational subspace as well as introducing strong scattering into the surrounding medium. The average gate fidelity $\overline{F}(U, \mathcal{N}) = \sum_k w_k F(U\left|\psi_k\right\rangle, \Lambda_k)$ for an equal distribution $(w_k = 1/3)$ of the states $\left|0\right\rangle$, $\left|1\right\rangle$ and $\left|\mathrm{a}\right\rangle$ is found to be $\overline{F}_{(\mathrm{a})} = 93.11\,\%$. Next, Fig. 3. (b) shows the propagation with Gaussian-shaped coupling pulses. Due to the increased propagation length, the transition between the two gates is smooth and does not require an additional transition segment. Hence, scattering is only due to the bending of waveguides. This amounts to a gate fidelity of $\overline{F}_{(\mathrm{b})} = 99.69\,\%$. In contrast, if one follows the combined approach put forward in Sec. III, the two holonomic gates can be parallelised using a chain of three qubits as an initial graph state, i.e. $\left|\Psi_G\right\rangle = \mathrm{C}Z_{12}\mathrm{C}Z_{23}\left|\psi\right\rangle\left|+\right\rangle\left|+\right\rangle$. Performing simultaneous measurements on the first two qubits with angles $\varphi_1 = \varphi_2 = \pi$, the third qubit transforms to $U_\Sigma ZX\left|\psi\right\rangle$ with $U_\Sigma = (-1)^{m_1} X^{m_2} Z^{m_1}$ being the associated by-product operator. The circuit diagram associated with this measurement scheme reads

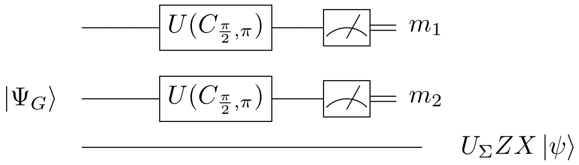
$\left|\Psi_G\right\rangle$
$U(C_{\frac{\pi}{2},\pi})$
$U(C_{\frac{\pi}{2},\pi})$
m_1
m_2
$U_\Sigma ZX\left|\psi\right\rangle$

This corresponds to a total of 9 waveguides as for every qubit there is a central ancilla mode mediating the coupling. The fact that no conditioning of the computation is needed stems from the fact that the benchmark example $U = ZX$ lies in the Clifford group.

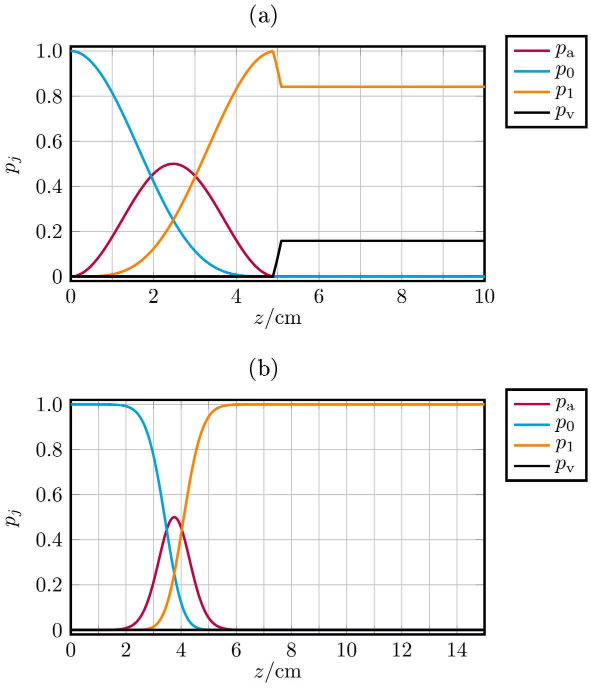

FIG. 3. Propagation of the state $\left|\psi(0)\right\rangle = \left|0\right\rangle$ through the lossy architecture given in terms of the probability distribution $p_k(z)$ for the photon being in the kth site $(k = 0, 1, \mathrm{aux})$ or being lossed p_{vac} as a function of the propagation length z. (a) Probability distribution for constant coupling segments, connected by a sine-like step [Fig. 1. (a)]. (b) Probability distribution for Gaussian coupling pulses [Fig. 1. (b)].

The local unitaries that manipulate the qubits to be measured are designed again by nonadiabatic holonomies with constant $\Omega = \pi/T_{\mathrm{g}}$. Due to the straight waveguide design, no scattering losses occur in contrast to the two-loop scenario in Fig. 3 (b). Furthermore, because gate operations are parallelised, there are no transition segments needed that would distort cyclicity as in Fig. 3 (a). Hence, the expected gate fidelity in this case amounts to $\overline{F} = 100\,\%$. This shows clearly that nonadiabatic HQC can profit from the parallelisation of gate operations, making it robust towards transition errors and bending losses, while keeping the optical network scalable. Conversely, nonadiabatic HQC is known to be robust towards parametric and timing errors, see e.g. [30]. We therefore propose a fruitful symbiosis between MBQC and HQC that could potentially lead to more reliable quantum information processors due to improved gate fidelities.

IV. QUANTUM COMPUTATION OF THE JONES POLYNOMIAL

Knot theory, a subarea of topology, is a subject concerned with the equivalence of knots up to smooth deformations, such as shifting, bending, or twisting of their strands, also known as the Reidemeister moves [58]. A quantity that distinguishes knots that differ beyond these ambient isotopies is known as a knot invariant.

The first step towards a knot invariant is the Kauffman bracket $\langle K\rangle$ of a knot K. Under the Kauffman bracket, crossings in the knot are evaluated according to the Skein relations shown in Fig. 4. Moreover, we set $\langle \bigcirc \rangle = 1$ with $\bigcirc$ being the unknot and $\langle \bigcirc \sqcup K\rangle = d\,\langle K\rangle$, where $d = -A^2 - A^{-2}$. With these set of rules at hand any knot can be unravelled into a series of unknots with different coefficients, thus resulting in a polynomial in $A \in \mathbb{C}$.

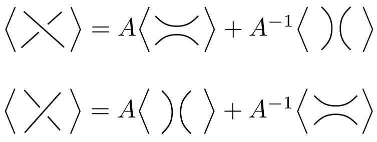

FIG. 4. Skein relations to resolve crossings in a knot. The knots build from the avoided crossings are weighted with complex numbers A and A^{-1}, respectively.

In order to construct a polynomial that is invariant under smooth deformations, a correction to the Kauffman bracket in terms of the writhe $w(K)$ is necessary [58], which gives an orientation to the strands of a knot, and accordingly every crossing contributes with positive or negative sign. Finally, one can introduce the Jones polynomial [42] of a knot K as

$$V_K(A) = (-A^3)^{-w(K)}\,\langle K\rangle\,. \tag{8}$$

If two knots K and K' are equal, then their corresponding Jones polynomials are equivalent, i.e. $V_K(A) = V_{K'}(A)$. In contrast, if $V_K(A) \neq V_{K'}(A)$, then the two knots differ beyond ambient isotopies, i.e. it follows $K \neq K'$. Finally, note that the Jones polynomial does not constitute a bijection, as two nonequivalent knots can have the same Jones polynomial. The writhe is simple to calculate, scaling only linear with the number of crossings N. As such, the complexity of computing the Jones polynomial is mainly due to the Kauffman bracket polynomial. The recursive relationship dictated by the Skein relations (Fig. 4) demands for the evaluation of 2^N diagrams giving rise to an exponential increase in computational effort.

A. Knots from braids

In order to structure the set of all knots, it is natural to view the latter as being generated from a sequence of elementary braids b_i, for $i = 1, \dots, s-1$, that are glued together. Here, s is the number of strands from which the knot is constructed. These braids, together with their inverses, form the s-strand braid group $\mathcal{B}_s$ [59]. The action of b_i onto the strands is illustrated in Fig. 5. If the braided strands are closed, the result is a knot. Indeed, any knot can be constructed (in multiple ways) from a sequence of elementary braids [60]. Moreover, these elementary braids satisfy the Yang-Baxter equations [61, 62]

$$\begin{aligned} b_i b_j &= b_j b_i, \quad \text{for} \quad i \neq j \pm 1, \\ b_i b_{i+1} b_i &= b_{i+1} b_i b_{i+1}, \\ b_i b_i^{-1} &= b_i^{-1} b_i = e, \end{aligned} \tag{9}$$

with e being the identity element in $\mathcal{B}_s$ that is associated with not braiding the strands at all. Any knot K can be constructed from a general braid word $b = \prod_l b_{i_l}^{k_l}$ with $i_l \in \{1, \dots, s-1\}$ and $k_l \in \{-1, 1\}$. By that we mean that under a closure $\bar{b}$ of the braid b we obtain the desired knot up to ambient isotopies. From this point of view, the writhe of the knot is just $w(\bar{b}) = \sum_l k_l$.

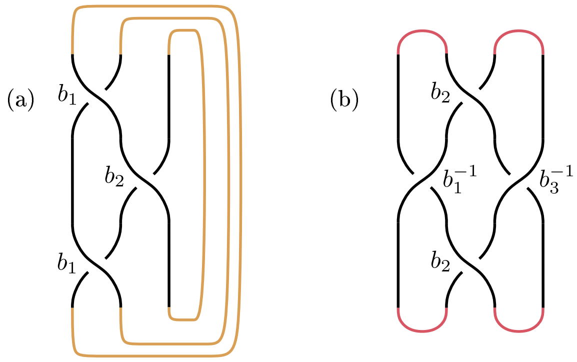

FIG. 5. Diagrammatic representation of elementary braiding. The braid b_i introduces a crossing between strands i and $i+1$. (a) Trace closure of the braid word $b_1 b_2 b_1$. (b) Plat closure of the braid word $b_2 b_1^{-1} b_3^{-1} b_2$.

B. Unitary representation of the braid group

A particularly useful representation ρ maps elements in $\mathcal{B}_s$ onto complex $D \times D$-matrices with the help of the Temperley-Lieb algebra TL$_s$ [63]. The latter is generated from elements E_i with $i = 1, \dots, s-1$ that satisfy

$$\begin{aligned} E_i E_j &= E_j E_i, \quad \text{for} \quad i \neq j \pm 1, \\ E_i E_{i\pm 1} E_i &= E_i, \\ E_i^2 &= d E_i. \end{aligned}$$

With these generators, the matrix representation of an elementary braid b_i is given as

$$\begin{aligned} \rho(b_i) &= AI + A^{-1}E_i, \\ \rho(b_i^{-1}) &= A^{-1}I + AE_i. \end{aligned} \tag{10}$$

The representation of a more general braid word $b = \prod_l b_{i_l}^{k_l}$ is then the product $\rho(b) = \prod_l \rho(b_{i_l}^{k_l})$. Once such a representation is known, the Jones polynomial $V_K(A)$ of a knot $K = \bar{b}$ can be obtained from an evaluation of the matrix trace $\mathrm{Tr}\{\rho(b)\}$ [43, 63]. The explicit connection between these two quantities depends on the chosen ρ. While there are, in principle, many such representations, in this work we are only concerned with those that are unitary, i.e. $\rho^\dagger(b_i)\rho(b_i) = I$ for all $i = 1, \dots, s-1$. In this case, we have $|A| = 1$ and E_i being Hermitian, as can be seen from Eqs. (10). For example, a unitary representation for the three-strand braid group ($s = 3$), that was derived in Ref. [65], is

$$E_1 = \begin{bmatrix} d & 0 \\ 0 & 0 \end{bmatrix}, \quad E_2 = \begin{bmatrix} d^{-1} & \sqrt{1-d^{-2}} \\ \sqrt{1-d^{-2}} & d - d^{-1} \end{bmatrix}. \tag{11}$$

Indeed, for $A = \mathrm{e}^{\mathrm{i}\theta}$ with

$$\begin{aligned} \theta \in &[0, \pi/6] \sqcup [\pi/3, 2\pi/3] \sqcup [5\pi/6, 7\pi/6] \\ &\sqcup [4\pi/3, 5\pi/3] \sqcup [11\pi/6, 2\pi] \end{aligned}$$

the matrices (10) form a unitary representation of $\mathcal{B}_3$. For the given representation the Kauffman bracket can then be calculated in terms of a matrix trace [65]

$$\langle \bar{b} \rangle = \mathrm{Tr}\{\rho(b)\} + A^{w(b)}(d^2 - 2). \tag{12}$$

Unitary representations of the general s-strand braid group $\mathcal{B}_s$ can be obtained explicitly by means of the AJL (Aharonov-Jones-Landau) algorithm [49, 64] but which (in its original formulation) only allows for an evaluation of the Jones polynomial for isolated values of A. An extension of this algorithm to continuous values of A was presented by Kauffman and Lomonaco in Ref. [66].

C. A Quantum algorithm for the Jones polynomial on three-strand braids

The computational effort of determining the Jones polynomial (8) rises exponentially with the number of crossings when evaluating diagrams in the Kauffman bracket of a knot. This makes it unfeasible to unravel large knots on a classical computer. On the other hand, we already noted that a computation of the Jones polynomial is equivalent (up to linear expense) to the evaluation of the matrix trace with respect to some representation ρ. A quantum algorithm that estimates the trace of a (unitary) $D \times D$-matrix $\rho(b)$ is the so-called Hadamard test [49]. First, one prepares a work qubit in the state $|0\rangle$ while the remaining n qubits (for $D = 2^n$) are initialised in some state $|\Phi_j\rangle$. The set $\{|\Phi_j\rangle\}_{j=1}^D$ shall form an orthonormal basis for the D-dimensional subspace on which the gate $\rho(b)$ acts, so it can be used to evaluate a matrix trace. Second, the input state $|0\rangle \otimes |\Phi_j\rangle$ is fed into the quantum circuit

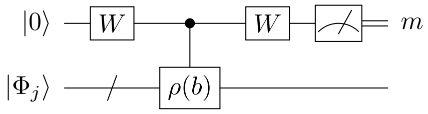

where the work qubit acts as the control for the two-qubit gate $|0\rangle\langle 0| \otimes I + |1\rangle\langle 1| \otimes \rho(b)$. Repeating the Hadamard test until a sufficient statistics of measurement outcomes $m \in \{0, 1\}$ of the work qubit is obtained, then provides $\mathrm{Re}\,\langle \Phi_j|\,\rho(b)\,|\Phi_j\rangle$. Analogously, we obtain $\mathrm{Im}\,\langle \Phi_j|\,\rho(b)\,|\Phi_j\rangle$ from the difference of probability distributions, which requires the circuit

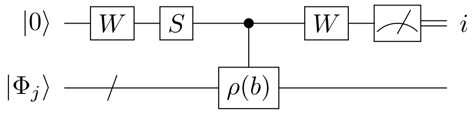

to be implemented. Here, a phase gate $S = |0\rangle\langle 0| - \mathrm{i}\,|1\rangle\langle 1|$ was inserted to obtain the imaginary part of the trace. When the computational procedure is reiterated for all states $|\Phi_j\rangle$, the quantity $\mathrm{Tr}\{\rho(b)\}$ can be determined. In conclusion, the presented circuits give rise to an efficient way to compute the Jones polynomial (8), because the number of qubits $\log D$ depends only on the dimension of ρ and is independent of the number of crossings [63].

1. *Holonomic measurement pattern*

We are left with the task of implementing the Hadamard test in terms of a graph state computation that only utilises single-loop holonomies. For simplicity, we will only be concerned with closures of three-strand braids. Recalling the unitary representation (10) with generators (11), we observe that the Hadamard test reduces to a circuit involving two qubits. It is then advantageous to resolve the controlled-unitary $|0\rangle\langle 0| \otimes I + |1\rangle\langle 1| \otimes \rho(b)$ via the circuit identity

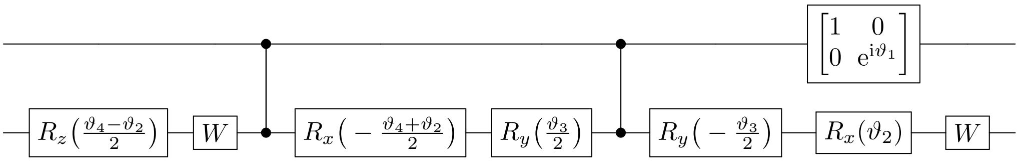
$\begin{bmatrix}1 & 0\\ 0 & e^{i\vartheta_1}\end{bmatrix}$
$R_z\left(\frac{\vartheta_4-\vartheta_2}{2}\right)$
W
$R_x\left(-\frac{\vartheta_4+\vartheta_2}{2}\right)$
$R_y\left(\frac{\vartheta_3}{2}\right)$
$R_y\left(-\frac{\vartheta_3}{2}\right)$
$R_x(\vartheta_2)$
W

(13)

where

$$\rho(b) = e^{i\vartheta_1} R_z(\vartheta_2) R_y(\vartheta_3) R_z(\vartheta_4) \tag{14}$$

must be satisfied. Appendix B contains a proof of this equivalence. The angles $\{\vartheta_j\}_j$ will depend on the given braid word b. Using the above resolution of the controlled braiding, the measurement pattern implementing the entire Hadamard test is given in Fig. 6. In Appendix B we provide a step-by-step calculation verifying this result as well as deriving the forward-propagated by-product operators for the algorithm under study. Note that the shown graph state for this computation is not the simplest one possible, but can be viewed as being obtained from the cluster state of a 4×13 lattice of qubits. The redundant qubits are removed from the cluster by Pauli-Z measurements such that the above circuit is directly written into the cluster [5]. The given measurement pattern, even though being not the most resource-efficient (qubit-saving), has the advantage of being easily translated into the desired Hadamard test, once the decomposition (14) is known. It is therefore more flexible and can be readily adjusted if the Jones polynomial of a different knot becomes of interest.

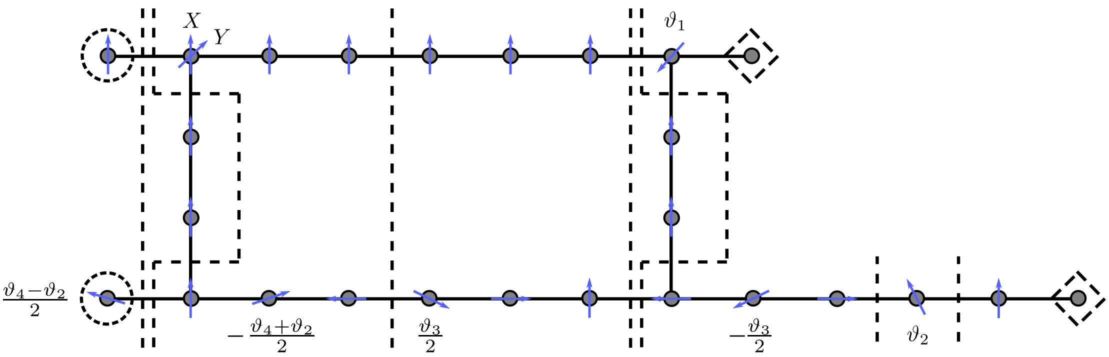
X
Y
ϑ_1
$\frac{\vartheta_4-\vartheta_2}{2}$
$-\frac{\vartheta_4+\vartheta_2}{2}$
$\frac{\vartheta_3}{2}$
$-\frac{\vartheta_3}{2}$
ϑ_2

FIG. 6. Holonomic measurement-based realisation of the Hadamard test with controlled braiding $|0\rangle\langle 0| \otimes I + |1\rangle\langle 1| \otimes \rho(b)$. Rotations into the suitable bases are carried out by single-loop holonomies. The diamond-shaped boxes denote the output. Upwards arrows denote measurements in the Pauli-X basis. The horizontal arrows → and ← correspond to measurements with $\varphi = \pi/2$ and $\varphi = -\pi/2$, respectively. The remaining arrows are related to measurements associated with non-Clifford operations determined by the parameters $\{\vartheta_j\}_j$ for $j = 1, 2, 3, 4$. The second qubit in the upper graph is measured in Pauli-X (Pauli-Y) basis in order to estimate the real (imaginary) part of $\mathrm{Tr}\{\rho(b)\}$ from the measurement statistic of the work qubit, i.e. the upper output qubit is measured in the Pauli-Z basis. Vertical dashed lines separate the graph state into a sequence of simulated single-qubit and two-qubit operations.

2. *Hopf link*

As a first example, we selected the Hopf link shown in Fig. 7. This knot can be constructed on two strands by a closure of the braid word $b = b_1 b_1$. Its unitary representation evaluates to $\mathrm{Tr}\{\rho(b)\} = A^2 + A^{-6}$. We choose a convention such that $w(\bar{b}) = 2$ (Fig. 7) for this knot. Inserting this into Eq. (12) yields the Jones polynomial of the Hopf link

$$V_{\mathrm{HL}}(A) = -A^{-2} - A^{-10}.$$

The trace of $\rho(b) = e^{-2i\theta} R_z(0) R_y(0) R_z(8\theta)$ can be obtained similarly from the holonomic graph state computation in Fig. 6 by adjusting the angles $\{\vartheta_j\}_j$ in the measurement scheme.

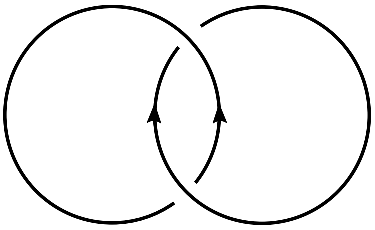

FIG. 7. Knot diagram of the Hopf link generated from the braid word $b_1 b_1$. Arrows indicate orientation of each strand.

3. The Borromean rings

As our second example, we choose a knot constructed on three strands. The so-called Borromean rings are depicted in Fig. 8, and its generating braid word reads $b = b_1 b_2^{-1} b_1 b_2^{-1} b_1 b_2^{-1}$. An explicit calculation of the corresponding matrix representation (10) leads us to the unitary matrix

$$\rho(b) = \begin{bmatrix} \frac{2A^4 - A^8 + 2A^{12} - A^{16} + A^{20} - 1}{A^{12} + A^{16}} & -\frac{(A^4-1)^2(A^8+1)\sqrt{1+A^4+A^8}}{A^{10}+A^{14}} \\ \frac{(A^4-1)^2(A^8+1)\sqrt{1+A^4+A^8}}{A^6+A^{10}} & \frac{1-A^4+2A^8-A^{12}+2A^{16}-A^{20}}{A^4+A^8} \end{bmatrix} .$$

Inserting the result into Eq. (12), while noting that $w(b) = 0$, gives the corresponding Jones polynomial (8)

$$V_{\mathrm{BR}}(A) = -A^{12} - A^{-12} + 3A^8 + 3A^{-8} - 2A^4 - 2A^{-4} + 4.$$

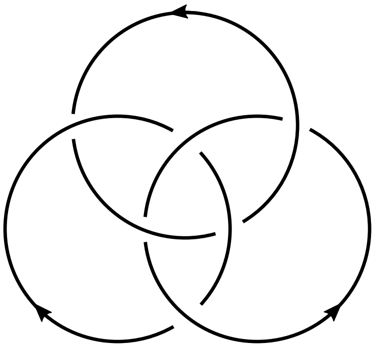

FIG. 8. Knot diagram of the Borromean rings generated from the braid word $b_1 b_2^{-1} b_1 b_2^{-1} b_1 b_2^{-1}$. Arrows indicate orientation of each strand.

While a graphical calculation in terms of the Skein relations (Fig. 4) would demand for an evaluation of $2^6 = 64$ diagrams, the Hadamard test in Fig. 6 is independent of the number of crossings in a knot. We only have to adjust the measurement pattern according to the braid word b associated with the Borromean rings. Because $\det(\rho(b_1)) = -A^{-2}$ and $\det(\rho(b_2^{-1})) = -A^2$ it follows that $\det(\rho(b)) = 1$, and hence $\vartheta_1 = 0$ in the decomposition (14), i.e. $\rho(b) \in \mathrm{SU}(2)$. Figure 9 shows how the resolution (14), determined by the remaining parameters ϑ_2, ϑ_3, and ϑ_4, depends on the angle θ. This in turn fixes the measurement basis in Fig. 6.

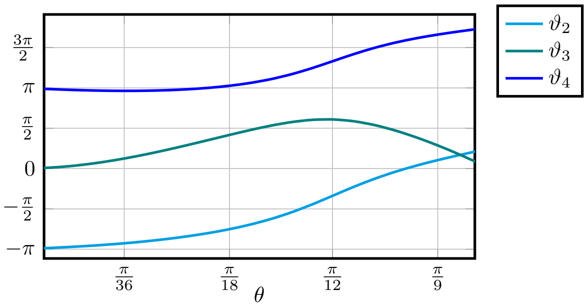

FIG. 9. Measurement angles for the graph state computation in Fig. 6 simulating the Hadamard test with controlled braiding $\rho(b)$ for the Borromean rings. The graphic was obtained by solving Eq. (14) for 22 equidistant values of θ in the interval $[0, \pi/6]$.

V. CONCLUSIONS

In this article we combined measurement-bases quantum computation (MBQC) and nonadiabatic holonomic quantum computation (HQC) to obtain an improved, error resilient, model of quantum computation (QC). We have shown how both approaches profit from each other in a symbiotic way. On the one hand, the stability of a graph state computation is improved due to performing measurements in a rotated basis that were obtained by using geometric phases (holonomies). On the other hand, HQC profits from the fact that the entanglement of the graph state allows to parallelise holonomic gates instead of executing them sequentially. This realisation of QC avoids transition errors between holonomic gates and allows for a resource-efficient way of performing QC. We investigated the joint approach on an explicit benchmark Hamiltonian and its implementation via tools from integrated quantum optics. Our study revealed an increased gate fidelity when compared with the standard formulation of nonadiabatic HQC, thus verifying that the combined model has richer fault-tolerance features. Finally, we illustrated that in our geometric formulation of the theory, that MBQC does not lose any of its practicality, by studying a quantum algorithm that estimates the Jones polynomial in a computationally efficient manner. We believe that current implementations of MBQC, in particular those that rely on linear optics, can benefit from our proposal, possibly moving one step closer to the desired notion of scalable quantum computation.

ACKNOWLEDGMENTS

Financial support by the Deutsche Forschungsgemeinschaft (DFG SCHE 612/6-1) is gratefully acknowledged.

Appendix A: Propagation through lossy optics

When a quantum state of light $|\psi(z)\rangle$ is injected into the three-waveguide coupler discussed in Sec. III A, its propagation is not only subject to the coupled-mode Hamiltonian (7), but also experiences Markovian loss γ_k in the kth mode ($k = 0, 1, \mathrm{aux}$). Here, we are interested in the loss of a single photon, e.g. due to scattering into the environment or absorption. Hence, we can safely employ the Born approximating, that is the state of the environment (ambient medium) is not altered throughout the evolution. In addition we assume that the scattered photons are irrevocably lost, which allows us to treat γ_k as Markovian dissipators. Under these assumption the propagated state $\Lambda(z)$ evolves according to the Markovian Master equation [57]

$$\partial_z\Lambda = \mathrm{i}[\Lambda, H] + \sum_k \gamma_k\big(2a_k\Lambda a_k^\dagger - a_k^\dagger a_k\Lambda - \Lambda a_k^\dagger a_k\big). \quad \text{(A1)}$$

Here, we are mainly interested in photon loss due to a bending of waveguides. Following the heuristic approach from Ref. [67], this type of loss depends on the Gaussian radius of curvature

$$r_k(z) = \frac{\Big(1 + \big[\partial_z \Delta x_k(z)\big]^2\Big)^{\frac{2}{3}}}{|\partial_z^2 \Delta x_k(z)|},$$

where $\Delta x_k(z)$ is the position of the kth waveguide (measured from the center). The loss rate is then [55]

$$\gamma_k(z) = K_1 \mathrm{e}^{-K_2 r_k(z)},$$

with material parameters $K_1 = 0.5\,\mathrm{cm}^{-1}$ and $K_2 = 0.042\,\mathrm{cm}^{-1}$. The propagated state $\Lambda(z)$ was obtained by numerical solution of the system of first-order differential equations

$$\begin{aligned}
\partial_z\Lambda_{\mathrm{vv}} &= 2\gamma_0\Lambda_{00} + 2\gamma_1\Lambda_{11},\\
\partial_z\Lambda_{00} &= -2\,\mathrm{Im}\big(\kappa_0\Lambda_{0\mathrm{a}}\big) - 2\gamma_0\Lambda_{00},\\
\partial_z\Lambda_{10} &= \mathrm{i}\big(\kappa_0\Lambda_{1\mathrm{a}} - \kappa_1\Lambda_{0\mathrm{a}}^*\big) - (\gamma_0 + \gamma_1)\Lambda_{10},\\
\partial_z\Lambda_{11} &= -2\,\mathrm{Im}\big(\kappa_1\Lambda_{1\mathrm{a}}\big) - 2\gamma_1\Lambda_{11}, \qquad \text{(A2)}\\
\partial_z\Lambda_{0\mathrm{a}} &= \mathrm{i}\big(\kappa_0(\Lambda_{00} - \Lambda_{\mathrm{aa}}) + \kappa_1\Lambda_{10}^*\big) - \gamma_0\Lambda_{0\mathrm{a}},\\
\partial_z\Lambda_{1\mathrm{a}} &= \mathrm{i}\big(\kappa_1(\Lambda_{11} - \Lambda_{\mathrm{aa}}) + \kappa_0\Lambda_{10}\big) - \gamma_1\Lambda_{1\mathrm{a}},\\
\partial_z\Lambda_{\mathrm{aa}} &= 2\,\mathrm{Im}\big(\kappa_0\Lambda_{0\mathrm{a}} + \kappa_1\Lambda_{1\mathrm{a}}\big),
\end{aligned}$$

which is the matrix representation of Eq. (A1) with respect to the Fock basis

$$|\mathbf{0}\rangle, \quad a_0^\dagger|\mathbf{0}\rangle, \quad a_1^\dagger|\mathbf{0}\rangle, \quad \text{and} \quad a_{\mathrm{aux}}^\dagger|\mathbf{0}\rangle.$$

Note that the central waveguide is lossless as the position of the central mode is not altered throughout the propagation, i.e. $\gamma_{\mathrm{aux}}(z) = 0$. The system of equations (A2) was solved for the two coupling configurations shown in Fig. 1. In order to translate the couplings $\kappa_k(z)$ into the distances $\Delta x_k(z)$ we made use of an exponential curve $\kappa_k(z) = K_3\mathrm{e}^{-K_4\Delta x_k(z)}$ with material parameters set to $K_3 = 23.9\,\mathrm{cm}^{-1}$ and $K_4 = 0.1\,\mu\mathrm{m}^{-1}$. Finally, the propagated state $\Lambda(z)$ was used to calculate the fidelities given in Sec. III A.

Appendix B: Measurement-based realisation of the Hadamard test

Here we provide details on the realisation of the Hadamard test by means of a graph state computation. First, we show that the controlled unitary $|0\rangle\langle 0| \otimes I + |1\rangle\langle 1| \otimes U$, with an arbitrary single-qubit gate $U = \mathrm{e}^{\mathrm{i}\vartheta_1}R_z(\vartheta_2)R_y(\vartheta_3)R_z(\vartheta_4)$, is implemented exactly by the circuit (13) introduced in subsection IV C. There, $U = \rho(b)$ with b being the braid word generating a knot (under braid closure) whose Jones polynomial is to be estimated. If the control qubit is in the state $|0\rangle$ the circuit transforms the target qubit according to

$$\begin{aligned}
&WR_x(\vartheta_2)R_y\Big(\frac{\vartheta_3}{2} - \frac{\vartheta_3}{2}\Big)R_x\Big(-\frac{\vartheta_4 + \vartheta_2}{2}\Big)WR_z\Big(\frac{\vartheta_4 - \vartheta_2}{2}\Big)\\
&= WR_x\Big(\frac{\vartheta_2 - \vartheta_4}{2}\Big)WR_z\Big(\frac{\vartheta_4 - \vartheta_2}{2}\Big) = I,
\end{aligned}$$

where we made use of $R_k(\vartheta + \vartheta') = R_k(\vartheta)R_k(\vartheta')$ for $k = x, y, z$, as well as $R_z(\vartheta) = WR_x(\vartheta)W$ to arrive at the last equality. In contrast, if the control qubit is in the state $|1\rangle$ the target qubit will experience two additional Z gates throughout the circuit, viz.

$$\begin{aligned}
&WR_x(\vartheta_2)R_y\Big(-\frac{\vartheta_3}{2}\Big)ZR_y\Big(\frac{\vartheta_3}{2}\Big)\\
&\times R_x\Big(-\frac{\vartheta_4 + \vartheta_2}{2}\Big)ZWR_z\Big(\frac{\vartheta_4 - \vartheta_2}{2}\Big)\\
&= R_z(\vartheta_2)WR_y(-\vartheta_3)R_x\Big(\frac{\vartheta_4 + \vartheta_2}{2}\Big)WR_z\Big(\frac{\vartheta_4 - \vartheta_2}{2}\Big),\\
&= R_z(\vartheta_2)R_y(\vartheta_3)R_z(\vartheta_4).
\end{aligned}$$

In the above equation we utilised $R_y(\vartheta) = WR_y(-\vartheta)W = ZR_y(-\vartheta)Z$ and $ZR_k(\vartheta) = R_k(\vartheta)Z$ for $k = x, y$. Summarising the calculation and recalling that the control qubit experiences a phase gate shows that the circuit implements the controlled unitary

$$\begin{aligned}
&|0\rangle\langle 0| \otimes I + |1\rangle\langle 1| \otimes U =\\
&\Big[\mathrm{e}^{\mathrm{i}\frac{\vartheta_1}{2}}R_z(\vartheta_1) \otimes WR_x(\vartheta_2)R_y\Big(-\frac{\vartheta_3}{2}\Big)\Big]\mathrm{C}Z\times\\
&\Big[I \otimes R_y\Big(\frac{\vartheta_3}{2}\Big)R_x\Big(-\frac{\vartheta_4 + \vartheta_2}{2}\Big)\Big]\mathrm{C}Z\Big[I \otimes WR_z\Big(\frac{\vartheta_4 - \vartheta_2}{2}\Big)\Big]
\end{aligned} \quad \text{(B1)}$$

thus proving the assertion.

Next, we show that the Hadamard test is equivalently realised by the measurement pattern from Fig. 6. We apply the measurements in accordance with the simulated gate time, i.e. following Fig. 6 from the left to the right. In order to ensure clarity, we proceed in steps each discussing the simulation of an elementary gate (dashed lines in Fig. 6), while keeping track of the respective by-product operators. The unitary sequence realised by the setup is (ignoring the phase $\mathrm{e}^{\mathrm{i}\frac{\vartheta_1}{2}}$)

$$\begin{aligned} &U_{\Sigma_8} I \otimes W U_{\Sigma_7} I \otimes W R_z(\vartheta_2) U_{\Sigma_6} W R_z(\vartheta_1) \otimes W R_z\Big(\frac{\pi}{2}\Big) R_x\Big((-1)^{n_{10}+1}\frac{\vartheta_3}{2}\Big) R_z\Big(-\frac{\pi}{2}\Big) U_{\Sigma_5} \mathrm{C}Z \\ &\times U_{\Sigma_4} W \otimes W R_x\Big(\frac{\pi}{2}\Big) R_z\Big(\frac{\vartheta_3}{2}\Big) U_{\Sigma_3} W \otimes W R_z\Big(-\frac{\pi}{2}\Big) R_x\Big((-1)^{n_3+1}\frac{\vartheta_4+\vartheta_2}{2}\Big) U_{\Sigma_2} \mathrm{C}Z U_{\Sigma_1} W \otimes W R_z\Big(\frac{\vartheta_4-\vartheta_2}{2}\Big), \end{aligned} \tag{B2}$$

where computational segments are separated by the respective by-product operators

$$\begin{aligned} U_{\Sigma_1} &= X^{m_1} \otimes X^{n_1}, \\ U_{\Sigma_2} &= Z^{m_2} \otimes Z^{n_2}, \\ U_{\Sigma_3} &= X^{m_5} Z^{m_4} X^{m_3} \otimes X^{n_5} Y^{n_4} X^{n_3}, \\ U_{\Sigma_4} &= X^{m_8} Z^{m_7} X^{m_6} \otimes X^{n_8} Z^{n_7} Y^{n_6}, \\ U_{\Sigma_5} &= Z^{m_9} \otimes Z^{n_9}, \\ U_{\Sigma_6} &= X^{m_{10}} \otimes X^{n_{12}} Z^{n_{11}} X^{n_{10}}, \\ U_{\Sigma_7} &= I \otimes X^{n_{13}}, \\ U_{\Sigma_8} &= I \otimes X^{n_{14}}. \end{aligned}$$

In the above, Y gates emerged due to the commutation relations $R_z(\pm\pi/2)X = \pm Y R_z(\pm\pi/2)$ and $R_x(\pm\pi/2)Z = \mp Y R_x(\pm\pi/2)$. Let us assume for the moment that after a computation all 24 measurement outcomes were ideal, i.e. $m_j = 0$ and $n_k = 0$ for all j, k. The conditioning of non-Clifford operations in Eq. (B2) then becomes obsolete and the above by-product operators reduce to the identity. What remains is a matter of straight-forward algebra to verify that (B2) can be summarised to

$$(W \otimes I)(|0\rangle\langle 0| \otimes I + |1\rangle\langle 1| \otimes U)(W \otimes I). \tag{B3}$$

When the two-qubit unitary (B3) induced by the graph state computation acts on the state $|0\rangle \otimes |\Phi_j\rangle$ and a subsequent (Pauli-Z) measurement on the work qubit is performed, the entire paradigm coincides with the circuit diagram of the Hadamard test.

1. Post-processing

In order to ensure a deterministic execution of the Hadamard test, we have to bring the expression (B2) into a form, where all by-product operators were commuted to the left (propagated forward). The total by-product operator U_Σ will still be a tensor product of spurious Pauli operators that can be dealt with after the computation. As the overall unitary contains Bloch-sphere rotations around some general angle ϑ_k, not all operations in (B2) belong to the Clifford group. Hence, propagating the U_{Σ_i} through the implemented unitaries results in an unavoidable conditioning of later measurements on the previous ones. We do so segment by segment to make the calculation more traceable. Starting with the first by-product operator U_{Σ_1}, we obtain the forward propagated unitary $\tilde{U}_{\Sigma_1} = X^{m_1} Z^{n_1} \otimes Z^{m_1} X^{n_1}$ from the relation $\mathrm{C}Z U_{\Sigma_1} = \tilde{U}_{\Sigma_1} \mathrm{C}Z$ using

$$\mathrm{C}Z(I \otimes X) = (Z \otimes X)\mathrm{C}Z, \quad \mathrm{C}Z(X \otimes I) = (X \otimes Z)\mathrm{C}Z.$$

In the next step, the operator

$$U_{\Sigma_2} \tilde{U}_{\Sigma_1} = X^{m_1} Z^{n_1+m_2} \otimes X^{n_1} Z^{m_1+n_2} \tag{B4}$$

must be propagated through the third segment (ending at U_{Σ_3}). Using standard commutation relations we find

$$\tilde{U}_{\Sigma_2} = X^{n_1+m_2} Z^{m_1} \otimes X^{m_1+n_1+n_2} Z^{n_1}$$

(up to a global phase ±1 or ±i). Note that, commuting $Z^{m_1+n_2}$ from Eq. (B4) past the x-rotation led to a conditioning on the measurement outcome $m_1 + n_2$, viz.

$$(-1)^{n_3+1}\frac{\vartheta_4+\vartheta_2}{2} \rightarrow (-1)^{m_1+n_2+n_3+1}\frac{\vartheta_4+\vartheta_2}{2}.$$

Next, one propagates the operator

$$U_{\Sigma_3} \tilde{U}_{\Sigma_2} = X^{n_1+m_2+m_3+m_5} Z^{m_1+m_4} \otimes X^{m_1+\sum_{i=1}^{5} n_i} Z^{n_1+n_4}$$

past the fourth segment (ending at U_{Σ_4}). This procedures carries on until all operators are on the most left-hand side of (B2). Finally we arrive at

$$U_\Sigma = X^{\gamma_4} Z^{\gamma_3} \otimes X^{\gamma_2} Z^{\gamma_1} \tag{B5}$$

for the overall by-product operator associated with the entire Hadamard test. The measurements amount to a syndrome

$$\begin{aligned} \gamma_1 &= n_1 + n_4 + n_6 + n_8 + n_{11} + n_{13}, \\ \gamma_2 &= n_2 + n_3 + n_9 + n_{10} + n_{12} + n_{14} + m_4 + m_5 + m_6 + m_8, \\ \gamma_3 &= m_1 + m_4 + m_6 + m_8, \\ \gamma_4 &= n_4 + n_6 + n_8 + m_2 + m_3 + m_5 + m_7 + m_9 + m_{10}. \end{aligned}$$

While we carried through with this calculation, the non-Clifford operations obtained a conditioning on some of the previous measurement outcomes, and thus the measurement pattern in Fig. 6 must be adjusted according to the following replacements in Eq. (B2)

$$\begin{aligned} \vartheta_1 &\rightarrow (-1)^{\gamma_3}\vartheta_1, \\ \vartheta_2 &\rightarrow (-1)^{\gamma_2}\vartheta_2, \\ \vartheta_3 &\rightarrow (-1)^{m_1+\sum_{i=1}^{5} n_i}\vartheta_3, \\ (-1)^{n_{10}+1}\vartheta_3 &\rightarrow (-1)^{\gamma_5+n_{10}+1}\vartheta_3, \end{aligned}$$

where $\gamma_5 = n_1 + n_2 + n_3 + n_4 + n_6 + n_8 + n_9 + m_4 + m_5 + m_6 + m_8$. This mapping conditions the relevant measurements in order to perform the Hadamard test in a fully deterministic fashion. A classical post-processing will correct the action of the operator (B5).

[1] D. Deutsch and R. Jozsa, Rapid solution of problems by quantum computation, Proc. R. Soc. Lond. A **439**, 553 (1992).

[2] J. Preskill, Quantum Computing in the NISQ era and beyond, Quantum **2**, 79 (2018).

[3] F. Arute, K. Arya, R. Babbush, D. Bacon, J. C. Bardin, R. Barends, R. Biswas, S. Boixo, F. G. S. L. Brandao, D. A. Buell et al., Quantum supremacy using a programmable superconducting processor, Nature (London) **574**, 505 (2019).

[4] M. A. Nielsen and I. L. Chuang, *Quantum Computation and Quantum Information* (Cambridge University Press, New York, 2010).

[5] R. Raussendorf and H. J. Briegel, A One-Way Quantum Computer, Phys. Rev. Lett. **86**, 5188 (2001).

[6] R. Raussendorf, D. E. Browne, and H. J. Briegel, The one-way quantum computer - a non-network model of quantum computation, J. Mod. Opt. **49**, 1299 (2002).

[7] R. Raussendorf, D. E. Browne, and H. J. Briegel, Measurement-based quantum computation on cluster states, Phys. Rev. A **68**, 022312 (2003).

[8] R. Sk, Alakesh Baishya, B. K. Beheral, and P. K. Panigrahi, Experimental realization of quantum teleportation of an arbitrary two-qubit state using a four-qubit cluster state, Quantum Inf. Process **19**, 87 (2020).

[9] K. Inaba, Y. Tokunaga, K. Tamaki, K. Igeta, and M. Yamashita, High-Fidelity Cluster State Generation for Ultracold Atoms in an Optical Lattice, Phys. Rev. Lett. **112**, 110501 (2014).

[10] F. Schäfer, T. Fukuhara, S. Sugawa, Y. Takasu, and Y. Takahashi, Tools for quantum simulation with ultracold atoms in optical lattices. Nat. Rev. Phys. **2**, 411(2020).

[11] E. Knill, R. Laflamme, and G. Milburn, A scheme for efficient quantum computation with linear optics, Nature (London) **409**, 46 (2001).

[12] M. A. Nielsen, Optical Quantum Computation Using Cluster States, Phys. Rev. Lett. **93**, 040503 (2004).

[13] S. Scheel, K. Nemoto, W. J. Munro, and P. L. Knight, Measurement-induced nonlinearity in linear optics, Phys. Rev. A **68**, 032310 (2003).

[14] P. Walther, K. Resch, T. Rudolph, E. Schenck, H. Weinfurter, V. Vedrall, M. Aspelmeyerl, and A. Zeilinger, Experimental one-way quantum computing, Nature **434**, 169-176 (2005).

[15] M. V. Larsen, X. Guo, C. R. Breum, J. S. Neergaard-Nielsen, and U. L. Andersen, Deterministic generation of a two-dimensional cluster state, Science **369**, 366-372 (2019).

[16] P. Zanardi and M. Rasetti, Holonomic Quantum Computation, Phys. Lett. A **264**, 94 (1999).

[17] E. Sjöqvist, D. M. Tong, L. M. Andersson, B. Hessmo, M. Johansson, and K. Singh, Non-adiabatic holonomic quantum computation, New J. Phys. **14**, 103035 (2012).

[18] M. V. Berry, Quantal Phase Factors Accompanying Adiabatic Changes, Proc. R. Soc. London, Ser. A **392**, 45 (1984).

[19] F. Wilczek and A. Zee, Appearance of Gauge Structure in Simple Dynamical Systems, Phys. Rev. Lett. **52**, 2111 (1984).

[20] J. Anandan, Non-adiabatic non-abelian geometric phase, Phys. Lett. A **133**, 171 (1988).

[21] D. Kult, J. Åberg, and E. Sjöqvist, Noncyclic geometric changes of quantum states, Phys. Rev. A **74**, 022106 (2006).

[22] A. A. Abdumalikov, Jr., J. M. Fink, K. Juliusson, M. Pechal, S. Berger, A. Wallraff, and S. Filipp, Experimental realization of non-Abelian non-adiabatic geometric gates, Nature (London) **496**, 482 (2013).

[23] K. Xu, W. Ning, X.-J. Huang, P.-R. Han, H. Li, Z.-B. Yang, D. Zheng, H. Fan, and S.-B. Zheng, Demonstration of a non-Abelian geometric controlled-NOT gate in a superconducting circuit, Optica **8**, 972 (2021).

[24] G. Feng, G. Xu, and G. Long, Experimental Realization of Nonadiabatic Holonomic Quantum Computation, Phys. Rev. Lett. **110**, 190501 (2013).

[25] M.-Z. Ai, S. L., Z. Hou, R. He, Z.-H. Qian, Z.-Y. Xue, J.-M. Cui, Y.-F. Huang, C.-F. Li, and G.-C. Guo, Experimental Realization of Nonadiabatic Holonomic Single-Qubit Quantum Gates with Optimal Control in a Trapped Ion, Phys. Rev. Applied **14**, 054062 (2020).

[26] R. Raussendorf, J. Harrington, and K. Goyal, Topological fault-tolerance in cluster state quantum computation, New J. Phys. **9**, 199 (2007).

[27] A. G. Fowler and K. Goyal, Topological cluster state quantum computing, Quant. Inf. Comput. **9**, 721 (2001).

[28] H. J. Briegel, D. E. Browne, W. Dür, R. Raussendorf, and M. Van den Nest, Measurement-based quantum computation, Nature Phys. **5**, 19 (2009).

[29] D. A. Lidar and T. A. Brun, *Quantum Error Correction* (Cambridge University Press, Cambridge, UK, 2013).

[30] M. Johansson, E. Sjöqvist, L. M. Andersson, M. Ericsson, B. Hessmo, K. Singh, and D. M. Tong, Robustness of nonadiabatic holonomic gates, Phys. Rev. A **86**, 062322 (2012).

[31] B.-J. Liu, Y.-S. Wang, and M.-H. Yung, Super-robust nonadiabatic geometric quantum control, Phys. Rev. Research **3**, L032066 (2021).

[32] D. Bacon and S. T. Flammia, Adiabatic cluster-state quantum computing, Phys. Rev. A **82**, 030303(R) (2010).

[33] B. Antonio, D. Markham, and J. Anders, Adiabatic graph-state quantum computation, New J. Phys. **16**, 113070 (2014).

[34] C. Cesare, A. J. Landahl, D. Bacon, S. T. Flammia, and A. Neels, Adiabatic topological quantum computing, Phys. Rev. A **92**, 012336 (2015).

[35] P. Aliferis, D. Gottesman, and J. Preskill, Quantum accuracy threshold for concatenated distance-3 codes, Quant. Inf. Comput. **6**, 97 (2006).

[36] E. T. Campbell, B. M. Terhal, and C. Vuillot, Roads towards fault-tolerant universal quantum computation, Nature (London) **549**, 172 (2017).

[37] A. Szameit and S. Nolte, Discrete optics in femtosecond-laser- written photonic structures, J. Phys. B **43**, 163001 (2010).

[38] J. M. Arrazola, V. Bergholm, K. Bradler, T. R. Bromley, M. J. Collins, I. Dhand, A. Fumagalli, T. Gerrits, et al., Quantum circuits with many photons on a programmable nanophotonic chip, Nature (London) **591**, 54 (2021).

[39] F. Yu, X.-L. Zhang, Z.-G. Chen, Z.-N. Tian, Q.-D. Chen, H.-B. Sun, G. Ma, Non-Abelian braiding on photonic chips, Nat. Photon. **16**, 390 (2022).

[40] S. Scheel, A. Szameit, A braid for light, Nat. Photon. **16**, 344 (2022).

[41] V. Neef, J. Pinske, F. Klauck, et al., Three-dimensional non-Abelian quantum holonomy, Nat. Phys. (2022).

[42] V. F. R. Jones, A polynomial invariant for knots via von Neumann algebras, Bull. Am. Math. Soc. **12**, 103 (1985).

[43] B. Field and T. Simula, Introduction to topological quantum computation with non-Abelian anyons, Quantum Sci. Technol. **3**. 045004 (2018).

[44] E. Witten, Quantum Field Theory and the Jones Polynomial, Commun. Math. Phys. **121**, 351 (1989).

[45] J. R. Goldman and L. H. Kauffman, Rational Tangles, Adv. Applied Math. **18**, 300 (1997).

[46] S. A. Wilkinson, Modelling supercoiled DNA knots and catenanes by means of a new regular isotopy invariant, Acta Applicandae Mathematica **25**, 1 (1991).

[47] F. Jaeger, D. L. Vertigan, and D. J. A. Welsh, On the computational complexity of the Jones and Tutte polynomials, Math. Proc. Camb. Phil. Soc. **108**, 35 (1990).

[48] D. Aharonov and I. Arad, The BQP-hardness of approximating the Jones polynomial, New J. Phys. **13**, 035019 (2011).

[49] D. Aharonov, V. F. R. Jones, Z. Landau, A polynomial quantum algorithm for approximating the Jones polynomial, Algorithmica, **55**, 395 (2009).

[50] R. Marx et al., Nuclear-magnetic-resonance quantum calculations of the Jones polynomial, Phys. Rev. A **81**, 032319 (2010).

[51] M. Reck, A. Zeilinger, H. J. Bernstein, and P. Bertani, Experimental realization of any discrete unitary operator, Phys. Rev. Lett. **73**, 58 (1994).

[52] J. C. Garcia-Escartin, V. Gimeno, and J. J. Moyano-Fernández, Multiple photon effective Hamiltonians in linear quantum optical networks, Opt. Commun.**430**, 434 (2019).

[53] J. Liñares, M. C. Nistal, D. Barral, V. Moreno, and C. Montero, Quantization of coupled waveguided modes progression in integrated photonic devices, Proc. of SPIE **6996**, 69961R-1 (2008).

[54] R. Keil, B. Pressl, R. Heilmann, M. Gräfe, G. Weihs, and A. Szameit, Direct measurement of second-order coupling in a waveguide lattice, Appl. Phys. Lett. **107**, 241104 (2015).

[55] D. Marcuse, Bending losses of the asymmetric slab waveguide, Bell Syst. Tech. J. **50**, 2551 (1971).

[56] T. Eichelkraut, S. Weimann, S. Stützer, S. Nolte, and A. Szameit, Radiation-loss management in modulated waveguides, J. Opt. Lett. **39**, 6831 (2014).

[57] L. Teuber and S. Scheel, Solving the quantum master equation of coupled harmonic oscillators with Lie-algebra methods, Phys. Rev. A **101**, 042124 (2020).

[58] P. R. Cromwell, *Knots and Links* (Cambridge University Press, Cambridge, 2004).

[59] E. Artin, Theory of braids, Ann. Math. **48**, 101 (1947).

[60] J. W. Alexander, A lemma on systems of knotted curves, Proc. Nat. Acad. Sci. USA **9**, 93 (1923).

[61] C. N. Yang, Some Exact Results for the Many-Body Problem in one Dimension with Repulsive Delta-Function Interaction, Phys. Rev. Lett. **19**, 1312 (1967).

[62] R. J. Baxter, *Exactly Solved Models in Statistical Mechanics* (Academic Press, London, 1982).

[63] J. K. Pachos, *Introduction to Topological Quantum Computation*, (Cambridge University Press, New York, 2012).

[64] L. Kauffman and S. Lomonaco, Topological quantum computing and the Jones polynomial, Proc. of SPIE **6244**, 62440Z-16 (2006).

[65] L. Kauffman and S. Lomonaco, A 3-stranded quantum algorithm for the Jones Polynomial, Proc. of SPIE **6573**, 65730T-1 (2007).

[66] L. Kauffman and S. Lomonaco, Quantum algorithms for the Jones polynomial, Proc. of SPIE **7702**, 770203-1 (2010).

[67] K. Becker, Minimizing Bending Losses in Photonic Waveguides for Quantum Optical Applications, Master thesis, University of Rostock, 2018.

Bibliography

List of Publications

[P1] J. Pinske, L. Teuber, and S. Scheel, Highly degenerate photonic waveguide structures for holonomic computation, Phys. Rev. A **101**, 062314 (2020).

[P2] J. Pinske and S. Scheel, Symmetry-protected non-Abelian geometric phases in optical waveguides with nonorthogonal modes, Phys. Rev. A **105**, 013507 (2022).

[P3] J. Pinske, V. Burgtorf, and S. Scheel, Particle-number threshold for non-Abelian geometric phases, preprint, arXiv:2301.11999v1 (2022).

[P4] V. Neef, J. Pinske, F. Klauck, *et al.*, Three-dimensional non-Abelian quantum holonomy, Nature Phys. **19**, 30 (2023).

[P5] V. Neef, J. Pinske, M. Heinrich, *et al.*, Non-adiabatic holonomies for photonic quantum computing, *in preparation*.

[P6] J. Pinske and S. Scheel, Geometrically robust linear optics from non-Abelian geometric phases, Phys. Rev. Research **4**, 0023086 (2022).

[P7] J. Pinske, K. Abraham, and S. Scheel, Combining measurement-based quantum computation with nonadiabatic holonomic quantum computation, unpublished manuscript (Appendix B).

References

[1] P. Zanardi and M. Rasetti, Holonomic quantum computation, Phys. Lett. A **264**, 94 (1999).

[2] T. Ladd, F. Jelezko, R. Laflamme, *et al.*, Quantum computers, Nature (London) **464**, 45 (2010).

[3] J. Preskill, Quantum Computing in the NISQ era and beyond, Quantum **2**, 79 (2018).

[4] R. Horodecki, P. Horodecki, M. Horodecki, and K. Horodecki, Quantum entanglement, Rev. Mod. Phys. **81**, 865 (2009).

[5] D. Deutsch and R. Jozsa, Rapid Solution of Problems by Quantum Computation, Proc. R. Soc. Lond. A **439**, 553 (1992).

[6] L. K. Grover, A fast quantum mechanical algorithm for database search, Proceedings, 28th Annual ACM Symposium on the Theory of Computing (STOC), 212 (1996).

[7] P. Shor, Polynomial-Time Algorithms for Prime Factorization and Discrete Logarithms on a Quantum Computer, Siam. J. Comput. **26**, 1484 (1997).

[8] R. P. Feynman, Simulating physics with computers, Int. J. Theor. Phys., **21**, 467 (1982).

[9] S. Lloyd, Universal quantum simulators, Science **273**, 1073 (1996).

[10] C. H. Bennett and G. Brassard, Quantum cryptography: Public key distribution and coin tossing, In Proceedings of IEEE International Conference on Computers, Systems and Signal Processing, **175**, 8 (1984).

[11] M.-H. Hsieh and M. M. Wilde, Entanglement-Assisted Communication of Classical and Quantum Information, IEEE Trans. Inf. Theory **56**, 4682 (2010).

[12] J. Biamonte, P. Wittek, N. Pancotti, *et al.*, Quantum machine learning, Nature (London) **549**, 195 (2017).

[13] B. Heim, M. Soeken, S. Marshall, *et al.*, Quantum programming languages, Nat. Rev. Phys. **2**, 709 (2020).

[14] M. Cusumano, The Business of Quantum Computing, Communications of the ACM 61.10 (2018).

[15] M. Kjaergaard, M. E. Schwartz, J. Braumüller, *et al.*, Superconducting Qubits: Current State of Play, Annu. Rev. Condens. Matter Phys. **11**, 369 (2020).

[16] J. I. Cirac and P. Zoller, Quantum Computations with Cold Trapped Ions, Phys. Rev. Lett. **74**, 4091 (1995).

[17] L. Vandersypen and M. Eriksson, Quantum computing with semiconductor spins, Phys. Today **72**, 38 (2019).

[18] B. Yang, H. Sun, C.-J. Huang, *et al.*, Cooling and entangling ultracold atoms in optical lattices, Science **369**, 550 (2020).

[19] P. M. Platzman, Quantum Computing with Electrons Floating on Liquid Helium, Science. **284**, 1967 (1999).

[20] H. Walther, B. T. H. Varcoe, B.-G. Englert, and T. Becker, Cavity quantum electrodynamics, Rep. Prog. Phys. **69**, 1325 (2006).

[21] L. M. K. Vandersypen and I. L. Chuang, NMR techniques for quantum control and computation, Rev. Mod. Phys. **76**, 1037 (2005).

[22] S. Slussarenko and G. J. Pryde, Photonic quantum information processing: A concise review, Appl. Phys. Rev. **6**, 041303 (2019).

[23] L. Thylen and L. Wosinski, Integrated photonics in the 21st century, Photonics Res. **2**, 75 (2014).

[24] G. B. Xavier, G. Lima, Quantum information processing with space-division multiplexing optical fibres, Commun. Phys. **3**, 9 (2020).

[25] A. Politi, M. J. Cryan, J. G. Rarity, *et al.*, Silica-on-silicon waveguide quantum circuits, Science **320**, 646 (2008).

[26] A. Szameit and S. Nolte, Discrete optics in femtosecond-laser-written photonic structures, J. Phys. B **43**, 163001 (2010).

[27] J. Carolan, J. D. A. Meinecke, P. J. Shadbolt, *et al.*, On the experimental verification of quantum complexity in linear optics. Nat. Photon. **8**, 621 (2014).

[28] E. Knill, R. Laflamme, and G. Milburn, A scheme for efficient quantum computation with linear optics, Nature (London) **409**, 46 (2001).

[29] S. Scheel, K. Nemoto, W. J. Munro, and P. L. Knight, Measurement-induced nonlinearity in linear optics, Phys. Rev. A **68**, 032310 (2003).

[30] K.-H. Luo, V. Ansari, M. Massaro, *et al.*, Counter-propagating photon pair generation in a nonlinear waveguide, Opt. Express **28**, 3215 (2020).

[31] E. Campbell, B. Terhal, and C. Vuillot, Roads towards fault-tolerant universal quantum computation, Nature (London) **549**, 172 (2017).

[32] J. P. Gaebler, T. R. Tan, Y. Lin, *et al.*, High-Fidelity Universal Gate Set for $^9\mathrm{Be}^+$ Ion Qubits, Phys. Rev. Lett. **117**, 060505 (2016).

[33] D. A. Lidar, I. L. Chuang, and K. B. Whaley, Decoherence-Free Subspaces for Quantum Computation, Phys. Rev. Lett. **81**, 2594 (1998).

[34] L. Viola and S. Lloyd, Dynamical suppression of decoherence in two-state quantum systems, Phys. Rev. A. **58**, 2733 (1998).

[35] E. Knill, R. Laflamme, and L. Viola, Theory of Quantum Error Correction for General Noise, Phys. Rev. Lett. **84**, 2525 (2000).

[36] E. Farhi, J. Goldstone, S. Gutmann, *et al.*, A Quantum Adiabatic Evolution Algorithm Applied to Random Instances of an NP-Complete Problem, Science **292**, 472 (2001).

[37] D. Gottesman, Class of quantum error-correcting codes saturating the quantum Hamming bound, Phys. Rev. A **54**, 1862 (1996).

[38] M. Grassl, P. Shor, G. Smith, J. Smolin, and B. Zeng, Generalized concatenated quantum codes, Phys. Rev. A **79**, 050306(R) (2009).

[39] M. H. Freedman, A. Kitaev, M. J. Larsen, and Z. Wang, Topological Quantum Computation, Bull. New Ser. Am. Math. Soc. **40**, 31 (2002).

[40] J. K. Pachos, *Introduction to Topological Quantum Computation* (Cambridge University Press, New York, 2012).

[41] A. Kitaev, Anyons in an exactly solved model and beyond, Ann. Phys. **321**, 2 (2006).

[42] E. Witten, Quantum field theory and the Jones polynomial, Commun. Math. Phys. **121**, 351 (1989).

[43] C. Nash, *Differential Topology and Quantum Field Theory* (Academic Press, San Diego, 1991).

[44] A. Yu. Kitaev, Fault-tolerant quantum computation by anyons, Ann. Phys. **303**, 2 (2003).

[45] A. G. Fowler, M. Mariantoni, J. M. Martinis, and A. N. Cleland, Surface codes: Towards practical large-scale quantum computation Phys. Rev. A **86**, 032324 (2012).

[46] H. Bombin and M. A. Martin-Delgado, Topological Computation without Braiding, Phys. Rev. Lett. **98**, 160502 (2007).

[47] M. V. Berry, Quantal phase factors accompanying adiabatic changes, Proc. Math. Phys. Eng. Sci. **392**, 45 (1984).

[48] Y. Aharonov and D. Bohm, Significance of Electromagnetic Potentials in the Quantum Theory, Phys. Rev. **115**, 485 (1959).

[49] A. Tonomura, N. Osakabe, T. Matsuda, *et al.*, Evidence for Aharonov-Bohm effect with magnetic field completely shielded from electron wave, Phys. Rev. Lett. **56**, 792 (1986).

[50] S. Pancharatnam, Generalized Theory of Interference, and Its Applications, Proc. Indian Acad. Sci. A. **44**, 247 (1956).

[51] B. Simon, Holonomy, the Quantum Adiabatic Theorem, and Berry's Phase, Phys. Rev. Lett. **51**, 2167 (1983).

[52] F. Wilczek and A. Zee, Appearance of Gauge Structure in Simple Dynamical Systems, Phys. Rev. Lett. **52**, 2111 (1984).

[53] Y. Aharonov and J. Anandan, Phase change during a cyclic quantum evolution, Phys. Rev. Lett. **58**, 1593 (1987).

[54] J. Anandan, Non-adiabatic non-Abelian geometric phase, Phys. Lett. A **133**, 171 (1988).

[55] E. Cartan, Sur une classe remarquable d'espaces de Riemann, Bull. de la Soc. Math. de France **54**, 214 (1926).

[56] E. Cartan, Sur une classe remarquable d'espaces de Riemann. II, Bull. de la Soc. Math. de France **55**, 114 (1927).

[57] P. Zanardi and S. Lloyd, Topological Protection and Quantum Noiseless Subsystems Phys. Rev. Lett. **90**, 067902 (2003).

[58] J. K. Pachos, P. Zanardi, and M. Rasetti, Non-Abelian Berry connections for quantum computation, Phys. Rev. A **61**, 010305(R) (1999).

[59] J. K. Pachos and P. Zanardi, Quantum Holonomies for Quantum Computing, Int. J. Mod. Phys. B **15**, 1257 (2001).

[60] E. Sjöqvist, D. M. Tong, L. M. Andersson, B. Hessmo, M. Johansson, and K. Singh, Non-adiabatic holonomic quantum computation, New J. Phys. **14**, 103035 (2012).

[61] D. Parodi, M. Sassetti, P. Solinas *et al.*, Fidelity optimization for holonomic quantum gates in dissipative environments, Phys. Rev. A **73**, 052304 (2006).

[62] P. Solinas, P. Zanardi, and N. Zanghi, Robustness of non-Abelian holonomic quantum gates against parametric noise, Phys. Rev. A **70**, 042316 (2004).

[63] M. Johansson, E. Sjöqvist, L. M. Andersson, *et al.*, Robustness of nonadiabatic holonomic gates, Phys. Rev, A **86**, 062322 (2012).

[64] L. M. Duan, J. Cirac, and P. Zoller, Geometric Manipulation of Trapped Ions for Quantum Computation, Science **292**, 1695 (2001).

[65] M.-Z. Ai, S. Li, Z. Hou, R. He, *et al.*, Experimental Realization of Nonadiabatic Holonomic Single-Qubit Quantum Gates with Optimal Control in a Trapped Ion, Phys. Rev. Applied **14**, 054062 (2020).

[66] A. A. Abdumalikov Jr., J. M. Fink, K. Juliusson, *et al.*, Experimental realization of non-Abelian non-adiabatic geometric gates, Nature (London) **496**, 482 (2013).

[67] Y. Xu, Z. Hua, T. Chen, *et al.*, Experimental Implementation of Universal Nonadiabatic Geometric Quantum Gates in a Superconducting Circuit Phys. Rev. Lett. **124**, 230503 (2020).

[68] Y. Dong, S.-C. Zhang, Y. Zheng, *et al.*, Experimental Implementation of Universal Holonomic Quantum Computation on Solid-State Spins with Optimal Control, Phys. Rev. Applied **16**, 024060 (2021).

[69] G. Feng, G. Xu, and G. Long, Experimental Realization of Nonadiabatic Holonomic Quantum Computation, Phys. Rev. Lett. **110**, 190501 (2013).

[70] K. G. Wilson, Confinement of quarks, Phys. Rev. D **10**, 2445 (1974).

[71] M. C. Bañuls and K. Cichy, Review on novel methods for lattice gauge theories, Rep. Prog. Phys. **83**, 024401 (2020).

[72] C. Rovelli, Loop Quantum Gravity, Living Rev. Relativ. **1**, 1 (1998).

[73] A. Einstein, Über einen die Erzeugung und Verwandlung des Lichts betreffenden heuristischen Gesichtspunkt, Ann. Phys. **17**, 132 (1905).

[74] M. Planck, Zur Theorie des Gesetzes der Energieverteilung im Normalspectrum, Verh. Dtsch. Phys. Ges. **17**, 237 (1900).

[75] D. M. Greenberger, M.A. Horne, A. Shimony and A. Zeilinger, Bell's theorem without inequalities, Am. J. Phys. **58**, 1131 (1990).

[76] C. Reimer, M. Kues, P. Roztocki, *et al.*, Generation of multiphoton entangled quantum states by means of integrated frequency combs, Science **351**, 1176 (2016).

[77] W. Rosenfeld, D. Burchardt, Ro. Garthoff, *et al.*, Event-Ready Bell Test Using Entangled Atoms Simultaneously Closing Detection and Locality Loopholes, Phys. Rev. Lett. **119**, 010402 (2017).

[78] M. Tillmann, S.-H. Tan, S. E. Stoeckl, *et al.*, Generalized Multiphoton Quantum Interference, Phys. Rev. X **5**, 041015 (2015).

[79] M. Rezai, J. Sperling, and I. Gerhardt, What can single photons do what lasers cannot do? Quantum Sci. Technol. **4**, 045008 (2019).

[80] E. A. J. Marcatili, Dielectric rectangular waveguide and directional coupler for integrated optics, Bell Syst. Tech. J. **48**, 2071 (1969).

[81] L. Sansoni, F. Sciarrino, G. Vallone, *et al.*, Polarization entangled state measurement on a chip, Phys. Rev. Lett. **105**, 200503 (2010).

[82] J. R. Pierce, Coupling of modes of propagation, J. Appl. Phys. **25**, 179 (1954).

[83] S. A. Schelkunoff, Conversion of Maxwell's equations into generalized Telegraphist's equations, Bell Syst. Tech. J. **34**, 995 (1955).

[84] H. A. Haus, W. P. Huang, S. Kawakami, and N. A. Whitaker, Coupled-mode theory of optical waveguides, J. Lightw. Technol. **5**, 16 (1987).

[85] H. A. Haus and W. Huang, Coupled-mode theory, Proc. IEEE **79**, 1505 (1991).

[86] S. Nolte, M. Will, J. Burghoff, and A. Tünnermann, Femtosecond waveguide writing: a new avenue to three-dimensional integrated optics, Appl. Phys. A **77**, 109 (2003).

[87] K. Itoh, W. Watanabe, S. Nolte, and C. B. Schaffer, Ultrafast processes for bulk modification of transparent materials, MRS Bull. **31**, 620 (2006).

[88] A. Szameit, F. Dreisow, T. Pertsch, *et al.*, Control of directional evanescent coupling in fs laser written waveguides, Opt. Express **15**, 1579 (2007).

[89] O. Alibart, V. D'Auria, M. Micheli, *et al.*, Quantum photonics at telecom wavelengths based on lithium niobate waveguides, J. Opt. **18**, 104001 (2016).

[90] D. Gloge, Weakly guiding fibers, Appl. Opt. **10**, 2252 (1971).

[91] G. Bellanca, P. Orlandi, and P. Bassi, Assessment of the orthogonal and non-orthogonal coupled-mode theory for parallel optical waveguide couplers, J. Opt. Soc. Am. A **35**, 577 (2018).

[92] L. Teuber, Non-Hermitian dynamics in lossy photonic waveguide systems, Ph.D. thesis, University of Rostock (2018).

[93] B. E. A. Saleh and M. C. Teich, *Fundamentals of Photonics* (Wiley, New York, 2007).

[94] W. Streifer, M. Osinski, A. Hardy, Reformulation of the coupled-mode theory of multiwaveguide systems, J. Lightwave Tech. **5**, 1 (1987).

[95] S. Weimann, Complex lattice modes in waveguide networks and photonic solids, Ph.D. thesis, University of Rostock (2018).

[96] J. Bentzien, Experimental demonstration of photonic evanescent hopping beyond the tight-binding approximation, Bachelor thesis, University of Rostock (2021).

[97] C. M. Bender and S. Boettcher, Real Spectra in Non-Hermitian Hamiltonians Having $\mathcal{PT}$ Symmetry, Phys. Rev. Lett. **80**, 5243 (1998).

[98] R. El-Ganainy, K. Makris, M. Khajavikhan, *et al.*, Non-Hermitian physics and PT symmetry, Nature Phys. **14**, 11 (2018).

[99] M. Peskin and D. Schroeder, An Introduction to Quantum Field Theory (Westview Press, Chicago, 1995).

[100] J. Liñares and M. C. Nistal, Quantization of coupled modes propagation in integrated optical waveguides, J. Mod. Opt. **50**, 781 (2003).

[101] D. Barral and J. Liñares, Spatial propagation of quantum light states in longitudinally inhomogeneous waveguides, J. Opt. Soc. Am. B **32**, 1993 (2015).

[102] W. Vogel and D.-G. Welsch, *Quantum Optics* (Wiley-VCH, Weinheim, 2006).

[103] W. J. Westerveld, P. Urbach, *Silicon Photonics - Electromagnetic theory* (Bristol, IOP, 2017).

[104] J. Liñares, M. C. Nistal, D. Barral, *et al.*, Quantization of coupled waveguided modes progression in integrated photonic devices, Proc. of SPIE **6996**, 69961R-1 (2008).

[105] J. C. Garcia-Escartin, V. Gimeno, and J. J. Moyano-Fernández, Multiple photon effective Hamiltonians in linear quantum optical networks, Optics Communications **430**, 434 (2019).

[106] L. Knoll, S. Scheel, D.-G. Welsch QED in dispersing and absorbing media, preprint, arXiv:quant-ph/0006121v5 (2003).

[107] T. C. Guo and W. W. Guo, A potential scattering formulation for mode couplings of electromagnetic waves in waveguides, J. Appl. Phys. **52**, 635 (1981).

[108] H.-P. Breuer and F. Petruccione, *The Theory of Open Quantum Systems* (Oxford University Press, Oxford, 2006).

[109] L. Teuber and S. Scheel, Solving the quantum master equation of coupled harmonic oscillators with Lie-algebra methods, Phys. Rev. A **101**, 042124 (2020).

[110] A. Shabani and D. A. Lidar, Completely positive post-Markovian master equation via a measurement approach, Phys. Rev. A **71**, 020101(R) (2005).

[111] H.-P. Breuer, Genuine quantum trajectories for non-Markovian processes, Phys. Rev. A **70**, 012106 (2004).

[112] D. Marcuse, Bending losses of the asymmetric slab waveguide, Bell Syst. Tech. J. **50**, 2551 (1971).

[113] K. Becker, Minimizing Bending Losses in Photonic Waveguides for Quantum Optical Applications, Master thesis, University of Rostock (2021).

[114] T. P. Cheng and L. F. Li, *Gauge theory of elementary particle physics* (Oxford University Press, Oxford, 1984).

[115] M. Born and V. A. Fock, Beweis des Adiabatensatzes, Z. Phys. **51**, 165 (1928).

[116] L. Hardy, Quantum Theory From Five Reasonable Axioms, preprint, arXiv:quant-ph/0101012v4 (2001).

[117] A. Recati, T. Calarco, P. Zanardi, J. I. Cirac, and P. Zoller, Holonomic quantum computation with neutral atoms, Phys. Rev. A **66**, 032309 (2002).

[118] J. Dalibard, F. Gerbier, G. Juzeliūnas, and P. Öhberg, Colloquium: Artificial gauge potentials for neutral atoms, Rev. Mod. Phys. **83**, 1523 (2011).

[119] R. L. Karp, F. Mansouri, and J. S. Rno, Product integral formalism and non-Abelian Stokes theorem, J. Math. Phys. **40**, 6033 (1999).

[120] N. Goldman, G. Juzeliūnas, P. Öhberg, and I. B. Spielman, Light-induced gauge fields for ultracold atoms, Rep. Prog. Phys. **77**, 126401 (2014).

[121] M. cihara, *Geometry, Topology and Physics* (Taylor & Francis Group, New York, USA, 2013).

[122] K. Fujii, Note on coherent states and adiabatic connections, curvatures, J. Math. Phys. **41**, 4406 (2000).

[123] W. Ambrose and I. M. Singer, A theorem on holonomy, Trans. AMS **75**, 428 (1953).

[124] D. Lucarelli, Chow's theorem and universal holonomic quantum computation, J. Phys. A: Math. Gen. **35**, 5107 (2002).

[125] D. Lucarelli, Control aspects of holonomic quantum computation, J. Math. Phys. **46**, 052103 (2005).

[126] R. Montgomery, *A Tour of Subriemannian Geometries, Their Geodesics, and Applications* (American Mathematical Society, Providence, 2002).

[127] B.-L. Weng, D.-M. Lai, and X.-D. Zhang, Non-Abelian geometric phase in four waveguide arrays, Phys. Rev. A **85**, 053801 (2012).

[128] M. Kremer, L. Teuber, A. Szameit, and S. Scheel, Optimal design strategy for non-Abelian geometric phases using Abelian gauge fields based on quantum metric, Phys. Rev. Research **1**, 033117 (2019).

[129] F. Yu, X.-L. Zhang, Z.-G. Chen, *et al.*, Non-Abelian braiding on photonic chips, Nat. Photon. **16**, 390 (2022).

[130] M. Wilde, Quantum Information Theory, (Cambridge University Press, Cambridge, 2013).

[131] R. G. Unanyan, B. W. Shore, and K. Bergmann, Laser-driven population transfer in four-level atoms: Consequences of non-Abelian geometrical adiabatic phase factors, Phys. Rev. A **59**, 2910 (1999).

[132] A. P. Hope, T. G. Nguyen, A. Mitchell, and A. D. Greentree, Adiabatic two-photon quantum gate operations using a long-range photonic bus, J. Phys. B-At. Mol. Opt. **48**, 055503 (2015).

[133] S. Lloyd, Almost Any Quantum Logic Gate is Universal, Phys. Rev. Lett. **75**, 346 (1995).

[134] C. J. Bradly, M. Rab, A. D. Greentree, and A. M. Martin, Coherent tunneling via adiabatic passage in a three-well Bose-Hubbard system, Phys. Rev. A **85**, 053609 (2012).

[135] H. Oukraou, L. Vittadello, V. Coda, *et al.*, Control of adiabatic light transfer in coupled waveguides with longitudinally varying detuning, Phys. Rev. A **95**, 023811 (2017).

[136] S. Mukherjee, M. DiLiberto, P. Öhberg, *et al.*, Experimental Observation of Aharonov-Bohm Cages in Photonic Lattices, Phys. Rev. Lett. **121**, 075502 (2018).

[137] J. Pachos and S. Chountasis, Optical holonomic quantum computer, Phys. Rev. A **62**, 052318 (2000).

[138] A. Bohm, A. Mostafazadeh, H. Koizumi, *et al. The Geometric Phase in Quantum Systems* (Springer, Berlin, 2003).

[139] Y. Brihaye and P. Kosifiski, Adiabatic approximation and Berry's phase in the Heisenberg picture, Phys. Lett. A **195**, 296 (1994).

[140] M. Reck, A. Zeilinger, H. J. Bernstein, and P. Bertani, Experimental realization of any discrete unitary operator, Phys. Rev. Lett. **73**, 58 (1994).

[141] J.Zhang, T. H. Kyaw, S. Filipp, *et al.*, Geometric and holonomic quantum computation, preprint, arXiv:2110.03602v2 (2021).

[142] E. Witten, Topological Quantum Field Theory, Commun. Math. Phys. **117**, 353 (1988).

[143] E. Prodana, H. Schulz-Baldes, Non-commutative odd Chern numbers and topological phases of disordered chiral systems, J. Funct. Analys. **271**, 1150 (2016).

[144] P. Solinas, P. Zanardi, and N. Zanghi, Robustness of non-Abelian holonomic quantum gates against parametric noise, Phys. Rev. A **70**, 042316 (2004).

[145] O. Oreshkov, T. A. Brun, and D. A. Lidar, Scheme for fault-tolerant holonomic computation on stabilizer codes, Phys. Rev. A **80**, 022325 (2009).

[146] O. Oreshkov, T. A. Brun, and D. A. Lidar, Fault-Tolerant Holonomic Quantum Computation, Phys. Rev. Lett. **102**, 070502 (2009).

[147] Y.-C. Zheng and T. A. Brun, Fault-tolerant holonomic quantum computation in surface codes, Phys. Rev. A **91**, 022302 (2015).

[148] C. Wu, Y. Wang, X.-L. Feng, and J.-L. Chen, Holonomic Quantum Computation in Surface Codes, Phys. Rev. Applied **13**, 014055 (2020).

[149] F. Arute, K. Arya, R. Babbush, *et al.*, Quantum supremacy using a programmable superconducting processor, Nature (London) **574**, 505 (2019).

[150] F. Pan, K. Chen, and P. Zhang, Solving the Sampling Problem of the Sycamore Quantum Circuits, Phys. Rev. Lett. **129**, 090502 (2022).

[151] M. A. Nielsen and I. L. Chuang, *Quantum Computation and Quantum Information* (Cambridge University Press , New York, 2010).

[152] A. Barenco, A universal two-bit gate for quantum computation, Proc. R. Soc. Lond. A **449**, 679 (1995).

[153] D. P. DiVincenzo, Two-bit gates are universal for quantum computation, Phys. Rev. A **51**, 1015 (1995).

[154] D. P. DiVincenzo, The Physical Implementation of Quantum Computation, Fortschritte der Phys. **48**, 9 (2000).

[155] S. Aaronson and A. Arkhipov, The computational complexity of linear optics, Theory Comput. **9**, 143 (2013).

[156] P. Hauke, H. G. Katzgraber, W. Lechner, *et al.*, Perspectives of quantum annealing: methods and implementations, Rep. Prog. Phys. **83**, 054401 (2020).

[157] S. Aaronson and D. Gottesman, Improved simulation of stabilizer circuits, Phys. Rev. A. **70**, 052328 (2004).

[158] P. Zanardi, Holonomic quantum computation, in *Quantum Error Correction* ed. by D. A. Lidar and T. A. Brun (Cambridge University Press, Cambridge, 2013).

[159] J. L. O'Brien, Optical quantum computing, Science **318**, 1567 (2007).

[160] S. Bartolucci, P. Birchall, H. Bombin *et al.*, Fusion-based quantum computation, preprint, arXiv:2101.09310v1 (2021).

[161] C. Weedbrook, S. Pirandola, R. G.-Patrón, *et al.*, Gaussian quantum information, Rev. Mod. Phys. **84**, 621 (2012).

[162] D. E. Browne and T. Rudolph, Resource-efficient linear optical quantum computation, Phys. Rev. Lett. **95**, 010501 (2005).

[163] O. Kwon, Y.-W. Cho, and Y.-H. Kim, Quantum random number generator using photon-number path entanglement, Appl. Opt. **48**, 1774 (2009).

[164] D. F. Walls, G. J. Milburn, Quantum Optics, (Springer, Berlin Heidelberg, 2008).

[165] D. Gottesman and I. L. Chuang, Demonstrating the viability of universal quantum computation using teleportation and single-qubit operations, Nature (London) **402**, 390 (1999).

[166] H. J. Briegel, D. E. Browne, W. Dür, *et al.*, Measurement-based quantum computation, Nat. Phys. **5**, 19 (2009).

[167] E. Meyer-Scott, N. Prasannan, I. Dhand, *et al.*, Scalable Generation of Multiphoton Entangled States by Active Feed-Forward and Multiplexing, Phys. Rev. Lett. **129**, 150501 (2022).

[168] C. Nayak, S. H. Simon, A. Stern, M. Freedman, and S. D. Sarma, Non-Abelian anyons and topological quantum computation, Rev. Mod. Phys. **80**, 1083 (2008).

[169] P. Zanardi, D. A. Lidar, and S. Lloyd, Quantum Tensor Product Structures are Observable Induced, Phys. Rev. Lett. **92**, 060402 (2004).

[170] O. Oreshkov. Holonomic Quantum Computation in Subsystems, Phys. Rev. Lett. **103**, 090502 (2009).

[171] B.-J. Liu, Y.-S. Wang, and M.-H. Yung, Super-robust nonadiabatic geometric quantum control, Phys. Rev. Research **3**, L032066 (2021).

[172] R. Müller and F. Greinert, Playing with a Quantum Computer, preprint, arXiv:2108.06271v1 (2021).

[173] R. Raussendorf and H. J. Briegel, A One-Way Quantum Computer, Phys. Rev. Lett. **86**, 5188 (2001).

[174] R. Raussendorf, D. E. Browne, and H. J. Briegel, The one-way quantum computer — a non-network model of quantum computation, J. Mod. Opt. **49**, 1299 (2002).

[175] R. Raussendorf, D. E. Browne, and H. J. Briegel, Measurement-based quantum computation on cluster states, Phys. Rev. A **68**, 022312 (2003).

[176] H. J. Briegel and R. Raussendorf, Persistent entanglement in arrays of interacting particles, Phys. Rev. Lett. **86**, 910 (2001).

[177] I. Bloch, Ultracold quantum gases in optical lattices, Nature Phys. **1**, 23 (2005).

[178] C. Y. Lu., X.-Q. Zhou, O. Gühne, *et al.*, Experimental entanglement of six photons in graph states, Nature Phys. **3**, 91 (2007).

[179] B. J. Brown and S. Roberts, Universal fault-tolerant measurement-based quantum computation, Phys. Rev. Research **2**, 033305 (2020).

[180] M. S. Tame, R. Prevedel, M. Paternostro, *et al.*, Experimental Realization of Deutsch's Algorithm in a One-Way Quantum Computer, Phys. Rev. Lett. **98**, 140501 (2007).

[181] B. Field and T. Simula, Introduction to topological quantum computation with non-Abelian anyons, Quantum Sci. Technol. **3**, 045004 (2018).

[182] K. v. Klitzing, G. Dorda, and M. Pepper, New Method for High-Accuracy Determination of the Fine-Structure Constant Based on Quantized Hall Resistance, Phys. Rev. Lett. **45**, 494 (1980).

[183] A. Tsukazaki, A. Ohtomo, T. Kita, *et al.*, Quantum Hall effect in polar oxide heterostructures, Science *315*, 1388 (2007).

[184] T. Iadecola, T. Schuster, and C. Chamon, Non-Abelian Braiding of Light, Phy. Rev. Lett. **117**, 073901 (2016).

[185] A. J. Menssen, J. Guan, D. Felce, M. J. Booth, and I. A. Walmsley, Photonic Topological Mode Bound to a Vortex, Phys. Rev. Lett. **125**, 117401 (2020).

[186] S. Bravyi, Universal quantum computation with the $\nu = 5/2$ fractional quantum Hall state, Phys. Rev. A **73**, 042313 (2006).

[187] J. K. Pachos, The wavefunction of an anyon, Ann. Phys. **322**, 1254 (2007).

[188] J.-S. Xu, K. Sun, J. K. Pachos, *et al.*, Photonic implementation of Majorana-based Berry phases, Sci. Adv. **4**, eaat6533 (2018).

[189] K. Murasugi, *Knot Theory and Its Applications* (Springer Verlag, Heidelberg, 1996).

[190] V. F. R. Jones, A polynomial invariant for knots via von Neumann algebras, Bull. Am. Math. Soc. **12**, 103 (1985).

[191] S. A. Wilkinson, Modelling supercoiled DNA knots and catenanes by means of a new regular isotopy invariant, Acta Applicandae Mathematica **25**, 1 (1991).

[192] L. H. Kauffman and S. J. Lomonaco Jr., Quantum entanglement and topological entanglement, New Journal of Physics **4**, 73.1 (2002).

[193] S. Nechaev, *Statistics of Knots and Entangled Random Walks* (World Scientific, Singapore, 1996).

[194] D. Aharonov and I. Arad, The BQP-hardness of approximating the Jones polynomial, New J. Phys. **13**, 035019 (2011).

[195] F. Jaeger, D. L. Vertigan, and D. J. A. Welsh, On the computational complexity of the Jones and Tutte polynomials, Math. Proc. Camb. Phil. Soc. **108**, 35 (1990).

[196] E. Artin, Theory of braids, Ann. Math. **48**, 101 (1947).

[197] J. W. Alexander, A lemma on systems of knotted curves, Proc. Nat. Acad. Sci. USA **9**, 93 (1923).

[198] L. H. Kauffman and S. J. Lomonaco Jr., A 3-Stranded Quantum Algorithm for the Jones Polynomial, Proc. of SPIE **6573**, 65730T (2007).

[199] S. J. Lomonaco Jr. and L. H. Kauffman, Topological Quantum Computing and the Jones Polynomial, Proc. of SPIE **6244**, 62440Z (2006).

[200] D. Aharonov, V. F. R. Jones, and Z. Landau, A Polynomial Quantum Algorithm for Approximating the Jones Polynomial, Algorithmica **55**, 395 (2009).

[201] L. H. Kauffman and S. J. Lomonaco Jr., Quantum Algorithms for the Jones Polynomial, Proc. of SPIE **7702**, 770203 (2010).

[202] T. Kobayashi, Experimental verification of the standard model of particle physics, Proc. Jpn. Acad., Ser. B **97**, 211 (2021).

[203] G. V. Dunne, *Self-Dual Chern-Simons Theories* (Springer-Verlag, Berlin, 1995).

[204] S. Scheel, and A. Szameit, A braid for light, Nat. Photon. **16**, 344 (2022).

[205] R. Marx, A. Fahmy, L. Kauffman, *et al.*, Nuclear-magnetic-resonance quantum calculations of the Jones polynomial, Phys. Rev. A **81**, 032319 (2010).

[206] P. Aliferis, Introduction to quantum fault tolerance, in *Quantum Error Correction* ed. by D. A. Lidar and T. A. Brun (Cambridge University Press, Cambridge, 2013).

[207] H. Wang, J. Qin, X. Ding, *et al.*, Boson Sampling with 20 Input Photons and a 60-Mode Interferometer in a $10^1$4-Dimensional Hilbert Space, Phys. Rev. Lett. **123**, 250503 (2019).

[208] A. W. Harrow and A. Montanaro, Quantum computational supremacy, Nature (London) **549**, 203 (2017).

[209] H.-S. Zhong, H. Wang, Y.-H. Deng, Quantum computational advantage using photons, Science **370**, 1460 (2020).

[210] G. F. Xu, D. M. Tong, and E. Sjöqvist, Path-shortening realizations of nonadiabatic holonomic gates, Phys. Rev. A **98**, 052315 (2018).

[211] P. Shen, T. Chen, and Z.-Y. Xue, Ultrafast Holonomic Quantum Gates, Phys. Rev. Applied **16**, 044004 (2021).

[212] P. Boross, J. K. Asboth, G. Szechenyi, *et al.*, Poor man's topological quantum gate based on the Su-Schrieffer-Heeger model, Phys. Rev. B **100**, 045414 (2019).

[213] H. Zimmermann, Non-Adiabatic Holonomic Quantum Gates in High-Index Materials, Master thesis, University of Rostock, (2021).

Acknowledgements

I would like to thank my advisor Prof. Stefan Scheel for the opportunity to pursue a Ph.D. in his group. His guidance and mentorship throughout the years shaped my understanding of physics and certainly influenced the style of this thesis. I further want to thank my colleagues at the Institute for Physics, in particular Lucas Teuber, for numerous illuminating discussions and collaborations in the first year of my Ph.D. Moreover, I owe gratitude to Prof. Alexander Szameit who endorsed experimental collaboration with his group. Here, Vera Neef deserves particular mention. It is due to her effort, that the theory, developed in this thesis, was successfully verified in experiment. Finally, I like to thank my family and friends for their support throughout the years.

Selbständigkeitserklärung

Ich gebe folgende Erklärung ab:

1. Die Gelegenheit zum vorliegenden Promotionsvorhaben ist mir nicht kommerziell vermittelt worden. Insbesondere habe ich keine Organisation eingeschaltet, die gegen Entgelt Betreuerinnen/Betreuer für die Anfertigung von Dissertationen sucht oder die mir obliegenden Pflichten hinsichtlich der Prüfungsleistungen für mich ganz oder teilweise erledigt.
2. Ich versichere hiermit an Eides statt, dass ich die vorliegende Arbeit selbstständig angefertigt und ohne fremde Hilfe verfasst habe. Dazu habe ich keine außer den von mir angegebenen Hilfsmitteln und Quellen verwendet und die den benutzten Werken inhaltlich und wörtlich entnommenen Stellen habe ich als solche kenntlich gemacht.

Rostock, den